Unveiling the Primary Quenching Mechanisms in Galaxies through Large Spectroscopic Surveys

James Anthony Allen Trussler

Jesus College

Department of Physics

University of Cambridge

This thesis is submitted for the degree of

Doctor of Philosophy

June 2020

Declaration

This thesis is the result of my own work and includes nothing which is the outcome of work done in collaboration except as declared in the Preface and specified in the text. It is not substantially the same as any that I have submitted, or, is being concurrently submitted for a degree or diploma or other qualification at the University of Cambridge or any other University or similar institution except as declared in the Preface and specified in the text. I further state that no substantial part of my thesis has already been submitted, or, is being concurrently submitted for any such degree, diploma or other qualification at the University of Cambridge or any other University or similar institution except as declared in the Preface and specified in the text. It does not exceed the prescribed word limit for the Degree Committee for the Faculty of Physics & Chemistry.

This thesis is based on material that has been submitted/published in:

- *Both starvation and outflows drive galaxy quenching*, Trussler, J., Maiolino, R., Maraston, C., Peng, Y., Thomas, D., Goddard, D., Lian, J., 2020, MNRAS, 491, 5406.
- *The weak imprint of environment on the stellar populations of galaxies*, Trussler, J., Maiolino, R., Maraston, C., Peng, Y., Thomas, D., Goddard, D., Lian, J., 2020, arXiv: 2006.01154.

The work in these articles was conducted in collaboration with the listed co-authors.

Summary

Unveiling the Primary Quenching Mechanisms in Galaxies through Large Spectroscopic Surveys

James Anthony Allen Trussler

Star-forming galaxies can be transformed into passive systems through a multitude of mechanisms that quench star formation, such as the halting of cold gas accretion (known as starvation) and the rapid removal of gas in AGN-driven winds. However, it remains unclear which mechanism is the most significant, primary driver of the star-forming–passive bimodality. Leveraging on the statistical power of the Sloan Digital Sky Survey, we have investigated how galaxy quenching depends on both the internal properties of galaxies (i.e. stellar mass) and external factors (i.e. environment), how galaxy quenching has evolved across cosmic time and how quenching operates within galaxies. Building upon an innovative technique for assessing the relative impact of different quenching mechanisms through comparisons of the levels of chemical enrichment in star-forming, green valley and passive galaxies, we have analysed the chemical properties of tens of thousands of galaxies in the local Universe to unveil the primary quenching mechanisms in galaxies. We find that the significant difference in stellar metallicity between passive galaxies and their star-forming progenitors implies that for galaxies at all masses, quenching must have involved an extended phase of starvation. In order to best match the observed properties of local passive galaxies, some form of gas ejection has to be introduced in our models, with outflows becoming increasingly more important with decreasing stellar mass. Through an analysis of the local population of green valley galaxies, we find that quenching operates more slowly in the local Universe than at high redshift. By separating star-forming, green valley and passive galaxies, we further find that the environment leaves a much weaker imprint on the stellar populations of galaxies than was previously thought. Satellite galaxies are only marginally more metal-rich and older than central galaxies of the same stellar

mass, with stellar metallicities that show only a weak dependence on halo mass, local overdensity and projected distance from their central. Finally, we find, using integral field spectroscopy from the SDSS-IV MaNGA galaxy survey, that passive galaxies are substantially more metal-rich than star-forming galaxies at all radii, with the stellar metallicity difference decreasing with increasing radial distance. Therefore, starvation is a primary driver of quenching at all radii in galaxies, playing a prominent role in quenching the central regions of galaxies, but playing an increasingly less important role in quenching their outskirts.

Acknowledgements

To my loving Mother, thank you so much for always believing in me, for always supporting me, for always praying for me, for always being there for me. You have sacrificed everything for me, all to provide me with the ultimate Gift, the true Freedom to pursue my own path in this life. All thanks to you, I now live your Dream. I am truly grateful for all the miracles that you have blessed my life with. I will always remember you for your gentle spirit, the purity of your soul and your everlasting Faith in Heaven. And here I now stand, reaching out for the stars, as I search for the mysteries hidden in the eternal beauty of the heavens.

To my dear Father, thank you so much for imparting in me your strength and wisdom, and the courage and will to live my life to the fullest. I know that you are always there, watching over me, guiding me every step of the way in my journey through life. From the bottom of my heart, I thank you for all the dreams that you have allowed us to live and your everlasting support that I feel within my soul which beckons me ever forward.

I would like to thank Jesus College and the University of Cambridge for blessing me with the opportunity to study in Cambridge. It is so special for me, truly a Dream, to be able to follow in my Father's footsteps, to share such a lovely connection with him. I am so grateful for all the wonderful opportunities I have had during my time here, and I know that he is looking down on me with a smile, proud of what his son has achieved.

To my dear doggies Benji, Honey and Barkley, thank you for being a part of my life. I can always count on you to bring a smile to my face and fill my heart with happiness.

To my loving British grandparents Andma and Opa, and my dear Dutch grandmother Oma, thank you so much for opening the door of opportunity for me, for providing me with the means to pursue my dreams. I am forever grateful for all of your love and support and the kindness that you have always blessed me with.

I would like to thank my good friend Mark for the many fun times we have had together and for inspiring me to always remain courageous and strong, no matter the circumstances that life presents us with. With your unwavering determination and your will to overcome any adversity, I know that you will win your current battle, emerging stronger than ever before.

I would like to thank my good friend and fellow Jesuan Vijay for all the entertaining and

enlightening discussions we have had while eating at your favourite restaurant in Cambridge, and for always being so eager and excited to be hear about my latest research. Your healthy enthusiasm always encouraged me to work hard to find a new highlight to share.

To my good friend and great office mate Andrin, I would like to thank you for all the lively and humorous chats we had in the office while we probably should have been working, as well as the many fun and refreshing coffee break walks over the years. No doubt they brought many a smile to my face and I am so grateful to have been working in such a happy, friendly, and banter-filled atmosphere.

I would also like to extend out my thanks to all the other students at the Kavli. It was so lovely to be part of such a tight-knit and friendly community, meeting each other for the daily coffee or braving the elements during our daily trek for lunch at Churchill.

I would like to thank my supervisor Roberto for the unique opportunity to work on such a fascinating project in such an incredible place. I have truly enjoyed and been grateful for every moment of it. Your enthusiasm and encouraging words always helped lift my spirit, inspiring and motivating me to always persevere.

Finally, I would like to thank everyone. Those named and also those unnamed. Without you I would not be where I am today, nor be the man I have grown to be. Thank you for your support, your guidance and your kindness. I am truly grateful for it all and I will strive to make the most out of this life that I have been blessed to live.

Contents

Chapter 1

Introduction

1.1 Island universes

Exactly a century ago, a Great Debate had caused a great divide in the astronomical community. Telescopic observations of the past two centuries had discovered great numbers of 'spiral nebulae', but their identity and (literal) place in the Universe remained unknown. One side, led by Harlow Shapley, argued that these spiral nebulae were located within the Milky Way, much like e.g. the Orion Nebula. The other side, led by Heber Curtis, instead maintained that these spiral nebulae were in fact distant island universes, completely separate from the Milky Way. So what was the true identity of spiral nebulae? This profound question demanded but a simple answer, which could only be provided by accurate measurements of the scale of the cosmos.

Peering through the largest telescope in the world at the time—the Hooker telescope at Mount Wilson Observatory—Hubble measured the distance to these nebulae using the newly-calibrated Cepheid variable distance scale. In doing so, Hubble made two groundbreaking discoveries. First, Hubble found that the recessional velocities of spiral nebulae increased linearly with their distance from us (Hubble 1929; Hubble & Humason 1931). This relation, now known as Hubble's law, revolutionised our understanding of the cosmos, as it provided strong evidence that the Universe was expanding, rather than existing in a static, steady state. Second, Hubble's distance measurements clearly showed that many of these nebulae were well over a Mpc away (Hubble 1926), and thus far beyond the limited confines of our Milky Way (which was estimated to be roughly 70 kpc in size at the time, Shapley 1918). And thus the debate was settled. Hubble had conclusively demonstrated that these enigmatic nebulae were

in fact distant island universes, much like our very own Milky Way.

And so the realm of extragalactic astronomy was born. These island universes, which we now refer to as galaxies, were extensively studied by Hubble. Through observations of hundreds of galaxies, Hubble found a clear pattern emerging in the galaxy population, which motivated him to arrange galaxies on to the so-called Hubble Sequence (also known as the Hubble tuning fork diagram, Hubble 1926, 1936), which we show in Fig. 1.1. On the right-hand side are the so-called late-type galaxies, which are characterised by spiral arms and disc-like morphologies. Labelled with an S, these late-type galaxies are further subdivided according to the properties of their spiral arms, which become both more prominent (relative to the nuclear region) and less tightly wound as one moves from the Sa to the Sc classification. In addition, late-type galaxies that exhibited bar-like features in their central regions were denoted with the SB label (e.g. an Sb late-type galaxy with a bar would be labelled as SBb). On the left-hand side are the so-called early-type galaxies, which are characterised by elliptical morphologies and are generally featureless. Labelled with an E, these early-type galaxies are further subdivided according to their ellipticity $\epsilon = 1 - b/a$, which specifies the ratio of their semi-minor to semi-major axis ratios, ranging from E0 (circular) to E7 (highly elliptical). Hubble placed the so-called lenticular galaxies at the branching point between spirals and ellipticals. Denoted by S0, these galaxies have bright central bulges, a disc-like morphology and no spiral arms. Finally, Hubble also defined a population of so-called irregular galaxies, which each had truly unique morphologies that did not fall under the late-type and early-type classifications.

Thus, galaxies, despite their plethora of properties, diverse shapes and sizes and the myriad of cosmic environments in which they reside, could be broadly divided into two classes: late-type and early-type. As we shall see, thanks to the remarkable insights brought about with the advent of large galaxy surveys in the late 20^{th} and 21^{st} century, this dichotomy manifests itself in a multitude of properties beyond just simple morphology alone.

1.2 Galaxy formation and evolution

Our understanding of the formation and evolution of galaxies has advanced tremendously since the pioneering discoveries of Hubble a century ago, which we owe to giant leaps forward in the observational, theoretical and computational study of galaxies.

On the observational side, telescopes have become vastly more powerful, being able to detect the faintest glimmers of light: from hidden dwarf galaxies in the Local Group (e.g. Koposov et al. 2015; Torrealba et al. 2019) out to the rise of the first galaxies during Cosmic Dawn (e.g. Zheng et al. 2012; Oesch et al. 2016; Bañados et al. 2018; Hashimoto et al. 2018). No longer held to our Earthly confines, we now have telescopes both in space and on the ground,

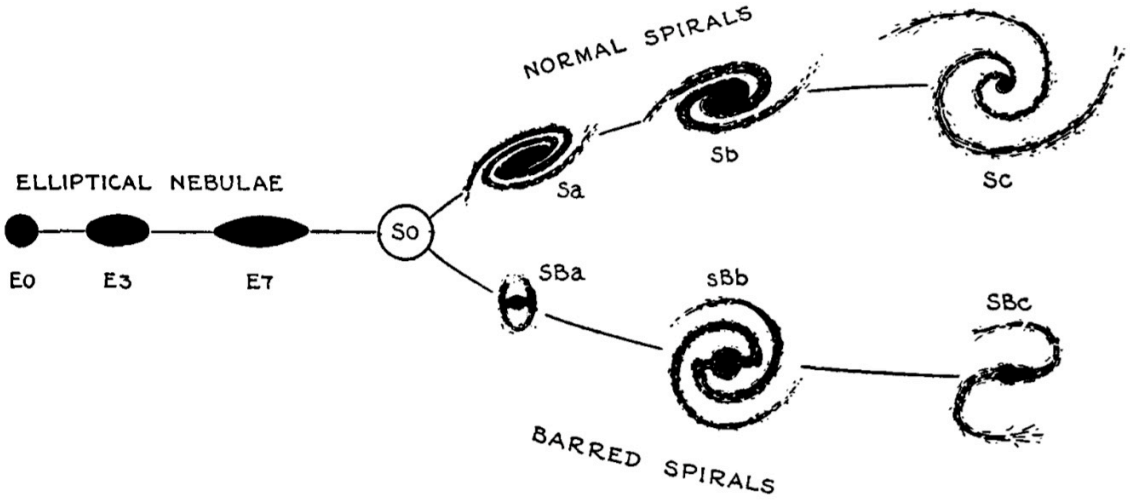

Figure 1.1. A diagram of the Hubble Sequence, reproduced from Hubble (1936). Early-type galaxies are on the left of the diagram, ranging from E0 (circular) to E7 (highly elliptical). Late-type galaxies are on the right of the diagram, and are divided into two branches: normal (i.e. non-barred) spirals and barred spirals. The spirals are further subdivided according to the properties of their spiral arms, which become both more prominent and less tightly wound as one moves from the Sa to the Sc classification. Lenticular galaxies, labelled by S0, are placed at the branching point between spirals and ellipticals.

collectively surveying over the entire range of the electromagnetic spectrum: from gamma-rays all the way through to the radio. Modern-day telescopes are used to study not only the stars, but also the gas in galaxies across a range of phases: from the cold and dense molecular gas out of which stars form to the hot and tenuous gas filling enormous clusters of galaxies. Using sophisticated instrumentation and cutting-edge techniques, we are now able to probe both the kinematical and chemical properties, as well as the physical conditions and energetics of the gas and stars in galaxies on a spatially-resolved manner (e.g. the CALIFA, SAMI and MaNGA surveys, Sanchez et al. 2012; Bryant et al. 2015; Bundy et al. 2015). Thus the observational study of galaxies has truly transformed since the days of Hubble. While Hubble himself was only able to study several hundred galaxies in his lifetime, his observational pursuit of the heavens continues to live on through large and advanced telescopes, both on ground and in space, such as the *Hubble Space Telescope*, which has demonstrated, through ultra deep observations (e.g. Beckwith et al. 2006), that there are in fact several hundred *billion* galaxies in the observable universe, see Fig. 1.2. It is only with the advent of the large galaxy surveys of the 21st century that we are beginning to draw upon this enormous population of galaxies, with current surveys sampling millions (e.g. the Sloan Digital Sky Survey, York et al. 2000), and surveys in the near future sampling billions of galaxies (e.g. *Euclid*, *Nancy Grace Roman Space Telescope* and the

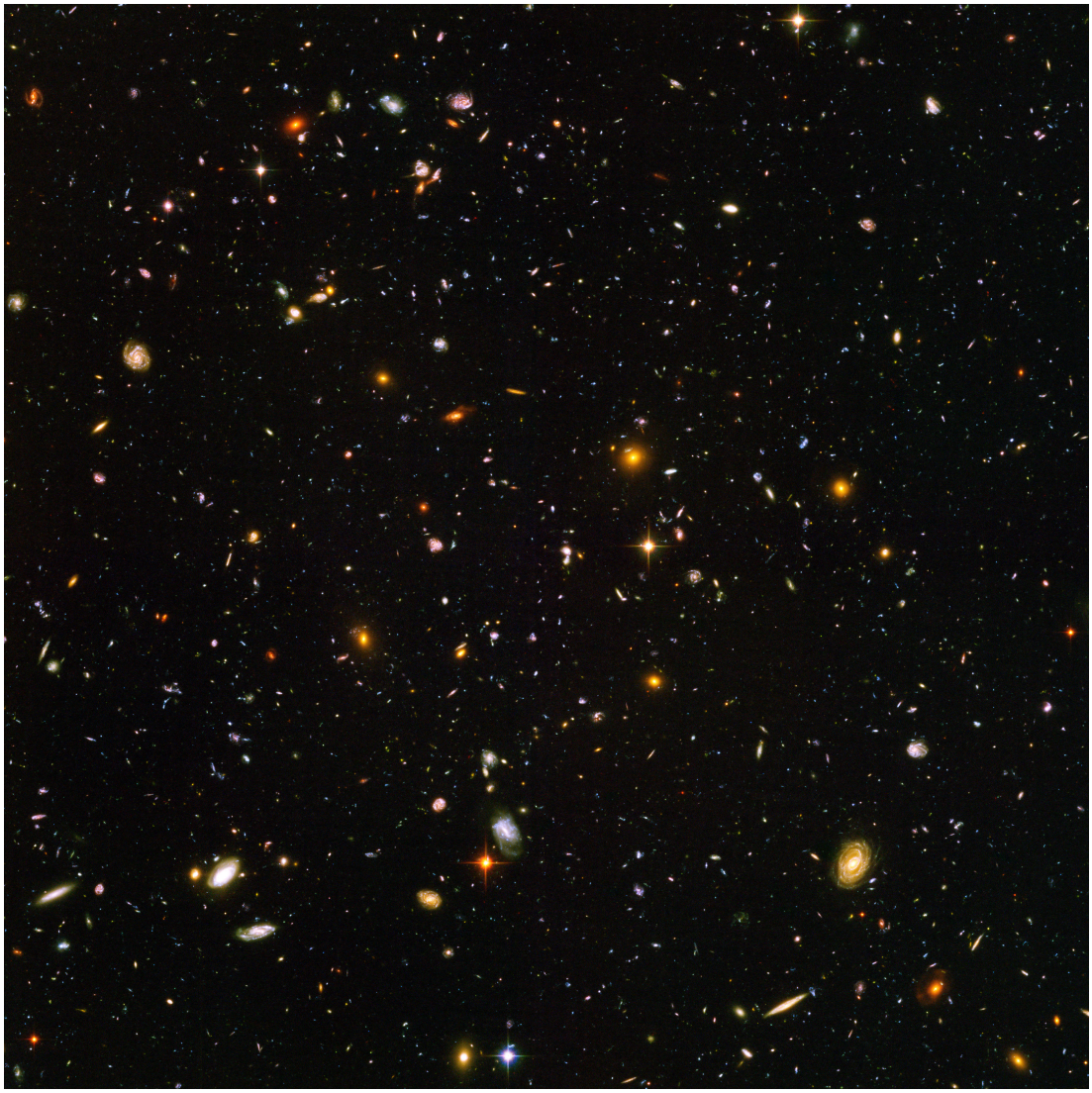

Figure 1.2. A colour rendition of the Hubble Ultra Deep Field image, a one million second exposure of an 11 arcmin^2 region taken with the Advanced Camera for Surveys on the Hubble Space Telescope, reproduced from Beckwith et al. (2006). There are roughly 10 000 galaxies in the image, ranging from galaxies in the local Universe ($z = 0$) to distant galaxies that are seen as they were less than one billion years after the Big Bang ($z = 7$).

Vera C. Rubin Observatory, Amendola et al. 2013; Spergel et al. 2015; Ivezić et al. 2019).

Significant advancements have also been made in our theoretical understanding of galaxies. We now know that galaxies are gravitationally bound collections of stars, gas, dust and dark matter (Zwicky 1933, 1937; Rubin et al. 1980): the result of structure formation under the action of gravity in an expanding Universe. Following the Big Bang, primordial dark matter density fluctuations were amplified by gravity, resulting in increasingly overdense and under-

dense regions. These overdense regions collapsed to form gravitationally bound dark matter haloes, which subsequently grew through the accretion of additional dark matter and through mergers with other dark matter haloes, in a process known as hierarchical merging (see e.g. Cole et al. 2002). Driven by gravity, this continuous merging of smaller structures resulted in the formation of successively larger structures, with dark matter collecting into clusters, superclusters, filaments and sheets, and the emergence of enormous cosmic voids that were largely lacking any material. Thus the cosmic web was formed, a complex foam-like arrangement of dark matter in a network of interconnected filaments located at the boundaries of immense voids (see e.g. Springel et al. 2005; Boylan-Kolchin et al. 2009).

Unlike dark matter, which is affected only by gravity, baryonic matter—the material that can emit and interact with radiation—initially oscillated in space as its gravitational collapse was halted by scattering off of photons. Following the epoch of recombination, the density of this baryonic gas quickly grew through gravitational instability, as it began rapidly collapsing onto the dense dark matter structures that were beginning to form (see e.g. White & Rees 1978; Fall & Efstathiou 1980). Thus, dark matter haloes served as the seeds of galaxy formation, with the baryonic gas being shock-heated as it accreted onto the dark matter haloes, resulting in the formation of a hot gaseous halo that was stabilised against gravitational collapse. The temperature of this halo gas slowly decreased through radiative cooling, causing the gas pressure support to diminish, with the halo gas thus collapsing further to form the gaseous disc out of which stars would eventually be born.

On the computational side, long gone are the days of using human computers to calculate the orbits of celestial objects or to analyse the spectra of stars. In today's modern era, powerful supercomputers are used to simulate the evolution of the Universe itself. Incorporating key physical processes such as gravity, star formation, black hole accretion, supernova feedback, active galactic nucleus (AGN) feedback and more, the formation and evolution of galaxies is followed from the era of recombination to the present day Universe. State-of-the-art hydrodynamical simulations are able to qualitatively reproduce many of the observed properties of galaxies, such as the local stellar mass function (e.g. Puchwein & Springel 2013; Vogelsberger et al. 2014a; Schaye et al. 2015) and galaxy sizes (e.g. Oser et al. 2012; Aumer et al. 2013). However, these simulations currently lack both the spatial and temporal resolution needed to properly capture the complex structure and evolution of the multi-phase interstellar medium. Indeed, key baryonic processes in galaxy evolution, such as star formation and black hole accretion, are implemented using so-called sub-grid models, which are incorporated by hand and only provide approximate descriptions of the baryonic physics taking place below the resolution limit of the simulations. Since different simulations implement these recipes differently, and because the key parameters in the recipes are tuned to best match the observations, it is not yet

completely clear whether the recent successes of simulations are attributable to the implementation of the relevant physics, or the appropriate adjustment of parameters (see e.g. Somerville & Davé 2015; Naab & Ostriker 2017).

Thus, while the formation and evolution of dark matter haloes—the hidden, non-luminous, enigmatic seeds of galaxy formation—are relatively well understood, it is the formation and evolution of the galaxies themselves and the luminous baryonic matter of which they are composed that ironically remains elusive and still requires much further consideration.

1.3 Star formation

Galaxies are the cosmic cities within which stars are born. Gas is accreted from the cosmic web, which then settles and cools in the galactic disc. Stars in the galaxy are then formed out of cold and dense clouds of molecular gas that collapse under their own gravity. Indeed, Jeans (1902) showed that a spherically symmetric gas cloud becomes unstable to gravitational collapse when its mass exceeds the Jeans mass $M_{\rm J}$, which scales as

$$M_{\rm J} \propto \frac{T^{3/2}}{\rho^{1/2}}, \tag{1.1}$$

where T and ρ are the temperature and mass density of the gas cloud, respectively. Thus, stars generally form out of cold (low T), dense (high ρ) gas because the Jeans mass threshold is relatively low.

In reality, star formation is much more complex than this simple description. Observations of stellar nurseries have shown that stars form with a wide range of masses, with the relative number of stars formed at each mass following an empirical distribution known as the initial mass function (IMF, see e.g. Salpeter 1955; Kroupa 2001; Chabrier 2003). Massive stars are rarer, hotter (i.e. bluer), more luminous and more short-lived than their cooler (i.e. redder), fainter, long-lived low-mass counterparts, with the light from massive stars dominating the spectrum of young stellar populations.

Star formation rates (SFRs) can be determined by measuring, either directly or indirectly, the amount of radiation produced by these young, massive, short-lived stars. Nebular Hα emission is commonly used as a SFR tracer, as the UV radiation from massive stars ionises the surrounding interstellar medium, which radiates strongly in Hα as electrons and protons recombine to form neutral hydrogen. Alternatively, either the UV continuum emission itself, or the FIR dust-reprocessed emission are used as SFR tracers (for more details, see e.g. Kennicutt & Evans 2012).

Given that stars form out of interstellar gas, Schmidt (1959) posited whether the star

formation rates and gas masses of galaxies are related through a star formation law of the form:

$$\Sigma_{\rm SFR} = A\Sigma_{\rm gas}^{N}, \tag{1.2}$$

where $\Sigma_{\rm SFR}$, $\Sigma_{\rm gas}$ and A are the star formation rate surface density, gas mass surface density and 'efficiency' of star formation, respectively. Indeed, observations of several dozen star-forming galaxies by Kennicutt (1998) later confirmed that the SFRs and gas masses of galaxies are tightly connected, being well-described by a power law (now known as the Schmidt-Kennicutt law), extending over several orders of magnitude in SFR and gas density, with $N = 1.4$.

In addition to the relation between star formation rate and gas mass, observational studies have also shown that there is a tight relation (sometimes referred to as the star-forming 'Main Sequence') between the global star formation rates and stellar masses of star-forming galaxies, that holds up to at least $z \sim 2$ (see e.g. Daddi et al. 2007; Elbaz et al. 2007; Noeske et al. 2007; Renzini & Peng 2015). The small scatter in the star formation rate–stellar mass relation suggests that merger-driven starbursts do not play a significant role in galaxy evolution, but rather that slow, secular processes dominate the star formation process in galaxies.

As depicted in Fig. 1.3, the currently accepted scenario is that the majority of galaxies increase in stellar mass while they are continuously being fed fresh and pristine gas accreted along filaments from the cosmic web. The cold and dense molecular gas in galaxies gravitationally collapses to form stars, which subsequently enrich the surrounding interstellar medium (ISM) with heavy elements produced during nucleosynthesis. In addition, galactic winds, launched either by supernova explosions or by actively accreting supermassive black holes, eject material out of the galactic disc, depositing heavy elements into the circumgalactic medium (CGM) and the wider intracluster/intergalactic medium (ICM/IGM). This ejected material may reaccrete onto the galaxy at later times, being recycled in the form of a galactic fountain.

Under smooth and steady gas accretion, the gas reservoirs of star-forming galaxies tend towards an equilibrium state (see e.g. Davé et al. 2012; Lilly et al. 2013; Peng & Maiolino 2014b), where the rates of gas depletion (due to star formation and outflows) and gas replenishment (due to gas accretion) are balanced. Thus, the star formation rates and gas accretion rates in galaxies are closely connected, with the evolution of the star-forming Main Sequence largely mirroring the evolution of gas accretion onto galaxies. Owing to the elevated gas accretion rates at higher redshift, as predicted by both cosmological simulations (see e.g. Genel et al. 2008; Faucher-Giguère et al. 2011; Dekel et al. 2013) and the analytical extended Press-Schechter theory of gravitational clustering (see e.g. Press & Schechter 1974; Lacey & Cole 1993; Neistein & Dekel 2008), the star formation rates of high-z star-forming galaxies were much higher, with the normalisation of the star-forming Main Sequence increasing with redshift (see e.g. Daddi et al. 2007; Elbaz et al. 2007; Noeske et al. 2007). Indeed, observations have shown that these

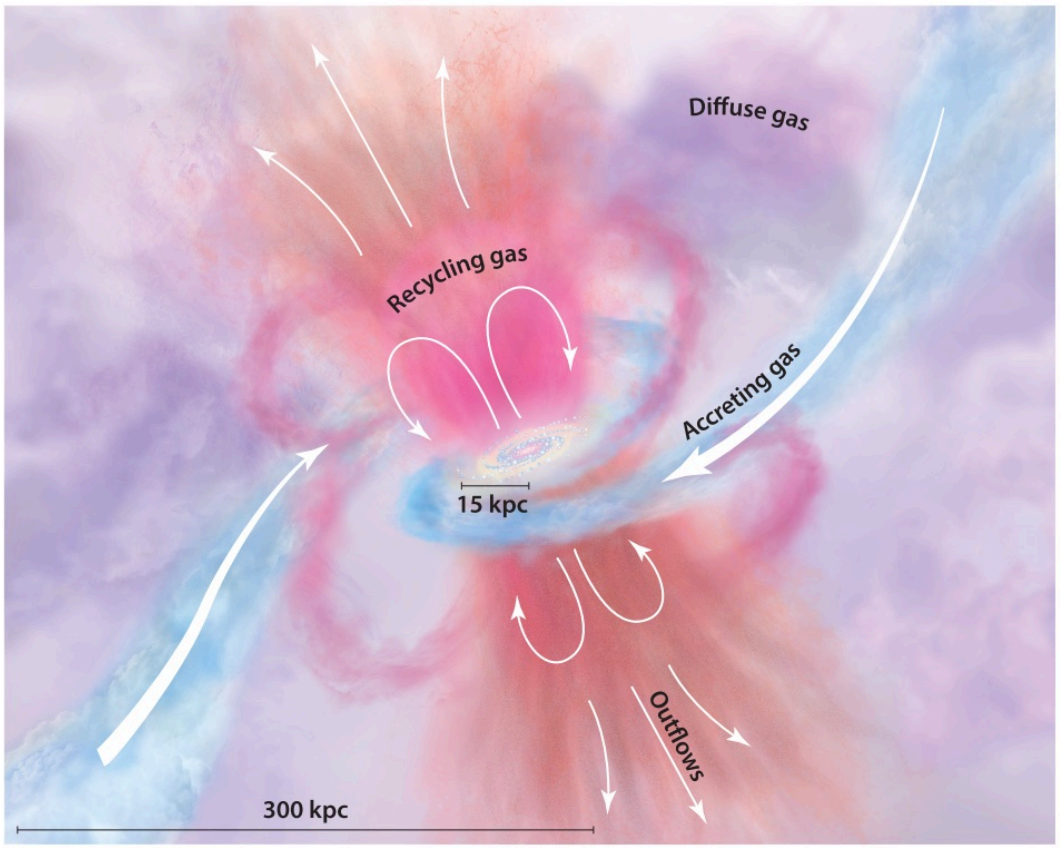

Figure 1.3. A diagram of the baryon cycle in galaxies, reproduced from Tumlinson et al. (2017). The galaxy's central bulge (coloured red) and gaseous disc (blue) are fed by filamentary accretion from the IGM (blue). The cold and dense gas in the galaxy gravitationally collapses to form stars. Outflows emerge from the disc (pink and orange), whereas gas that was previously ejected is recycled.

distant galaxies were both more gas-rich and more efficient at converting gas into stars than their local counterparts (see e.g. Tacconi & Genzel 2010; Genzel et al. 2015; Schinnerer et al. 2016; Scoville et al. 2017; Tacconi et al. 2018; Freundlich et al. 2019), with the typical star formation rate in galaxies at $z = 2$ being a factor of ~20 larger than at $z = 0$.

1.4 Bimodality

Our discussion so far has been centred on the population of galaxies that are actively forming stars. However, as alluded to almost a century ago by the late-type–early-type dichotomy on the Hubble Sequence, there exists a second population of galaxies whose morphological properties are seemingly very different from those of the actively star-forming, spiral arm wielding, disc-dominated galaxies. Indeed, as we shall see, this dichotomy manifests itself in a plethora of

galaxy properties beyond just simple morphology alone.

The advent of large galaxy surveys has heralded in a new era of discovery in the field of galaxy formation and evolution. In particular, it was found that galaxies are bimodally distributed in the colour–stellar mass plane (and also the colour–magnitude plane, see e.g. Strateva et al. 2001; Baldry et al. 2004, 2006; Schawinski et al. 2014), which we show in Fig. 1.4. Thus, galaxies can broadly be separated into two distinct populations: low-mass blue galaxies and high-mass red galaxies, which are referred to as the 'blue cloud' and 'red sequence', respectively. The relative dearth of galaxies between the red and blue peaks is thought to constitute a minor third population of galaxies that is currently transitioning from the blue cloud to the red sequence, referred to as the 'green valley'. Hearkening back to the late-type–early-type dichotomy discovered by Hubble, blue cloud galaxies were found to typically have late-type morphologies, while red sequence galaxies were found to typically have early-type morphologies. Thus, not only is there also a blue–red dichotomy of galaxies, but, more importantly, the colours (and therefore star formation histories) and morphologies of galaxies are clearly intimately connected, indicating that the same physical processes that give rise to these two distinct populations are also responsible for their starkly different properties.

Later studies revealed that this bimodality extends to many more of the key properties of galaxies, such as star formation rate (e.g. Noeske et al. 2007; Mcgee et al. 2011; Wetzel et al. 2012), stellar age (e.g. Kauffmann et al. 2003b; Gallazzi et al. 2008, 2014), stellar metallicity (e.g. Gallazzi et al. 2014; Peng et al. 2015), size/structure (e.g. Wuyts et al. 2011; van der Wel et al. 2014), gas content (e.g. Saintonge et al. 2011; Catinella et al. 2012; Boselli et al. 2014) and kinematics (e.g. Cappellari 2016a).

Galaxies are therefore broadly divided into two main classes: star-forming and passive. Star-forming galaxies typically have blue colours, young stellar populations, spiral arms, late-type morphologies, rotation-supported kinematics and are gas rich. In contrast, passive galaxies do not actively form stars and typically have red colours, old stellar populations, early-type morphologies, dispersion-dominated kinematics and are gas poor.

Deeper observations have revealed evidence for galaxy bimodality up to $z \sim 4$ (see e.g. Brammer et al. 2009; Muzzin et al. 2013), with the galaxy population clearly separating into two distinct regions of the UVJ plane (a UV-optical-NIR colour–colour diagram): corresponding, again, to a blue cloud and a red sequence of galaxies. Thus, these ancient passive systems must have assembled their mass very quickly and then shut down their star formation rapidly over a short timescale.

While it was initially thought that the Hubble Sequence constituted an evolutionary sequence, with early-type galaxies evolving into late-type galaxies, we now know that the converse is in fact true: star-forming galaxies evolve into passive galaxies, through the shutting down of

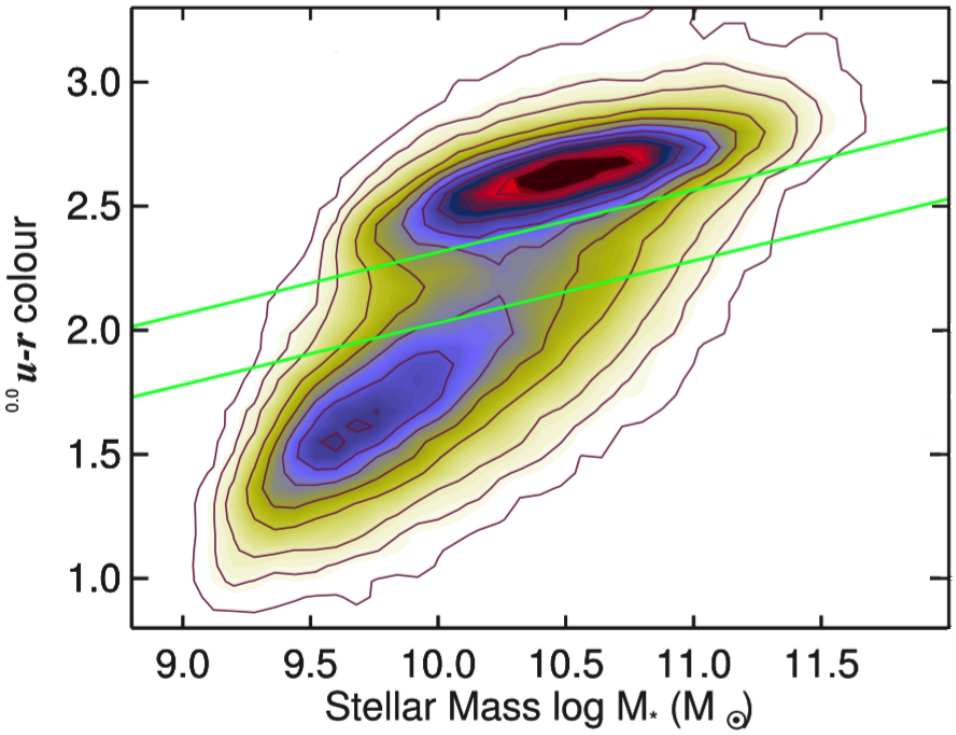

Figure 1.4. Galaxy bimodality in the $u - r$ colour–stellar mass plane, adapted from Schawinski et al. (2014). The galaxy population is clearly divided into two distinct peaks, corresponding to the low-mass blue cloud and the high-mass red sequence. The two green lines mark the boundary of the green valley galaxy region on the colour–mass plane, which corresponds to a relatively small population of galaxies that are thought to be currently transitioning from the blue cloud to the red sequence. The colour shown reflects the number of galaxies in each colour–mass bin, ranging from low (white) to intermediate (yellow/blue) to high (red) counts.

star formation, commonly referred to as 'quenching'. It is this transition from star-forming to passive, and the morphological, kinematical, structural and chemical transformation that seems to accompany it, that lies at the heart of galaxy evolution research today. In particular, much effort is being undertaken to understand how the starkly different properties of these two distinct populations are related to the processes taking (or not taking) place during the quenching process.

1.5 Quenching

Since stars form out of cold and dense clouds of gas that collapse under their own gravity, any physical process that either ejects gas from the galaxy (i.e. outflows or stripping), halts the accretion of fresh cold gas onto the galaxy (known as starvation) or stabilises the gas against

gravitational collapse can reduce the amount of star formation in a galaxy. Thus, there are a multitude of mechanisms that can quench star formation in galaxies.

In order to determine the relative role that different mechanisms play in shutting down star formation, and how this depends on key parameters such as galaxy mass (which traces internal processes), the environment in which galaxies reside (which traces external processes), and redshift, studies of large samples of star-forming and passive galaxies across a range of masses, environments and cosmic epochs have been undertaken. Since different galaxy evolutionary processes operate over different mass regimes and environments, the mass- and environment dependence of galaxy quenching can therefore reveal the relative importance of different quenching mechanisms.

In particular, the environment in which galaxies form has long been thought to play an important role in shaping their evolution, as observations of galaxy clusters in the local Universe had revealed that early-type galaxies are preferentially found in dense environments, while late-type galaxies dominate the galaxy population in low density environments (Dressler 1980). However, this prevalence of late-type galaxies in low-density environments could also be a mass-dependent effect, as late-type galaxies are preferentially low-mass (e.g. Wuyts et al. 2011), and there are more low-mass galaxies in low density environments (e.g. Kauffmann et al. 2004; Yang et al. 2009).

Later studies (e.g. Baldry et al. 2006; Peng et al. 2010; Woo et al. 2013), leveraging on the statistical power of large spectroscopic galaxy surveys, were able to disentangle the effects of mass and environment. As shown in Fig. 1.5, the quenched fraction of galaxies clearly increases with both stellar mass and with local overdensity, indicating that both mass and environment contribute to the quenching of galaxies. Red, quiescent, early-type galaxies are indeed more likely to be found in dense regions, close to the centres of massive haloes in large galaxy clusters, while blue star-forming late-type galaxies tend to be found in underdense regions, in the outskirts of low-mass haloes. Similarly, it is clear that for a given environment (galaxy overdensity), massive galaxies are more likely to be quenched than low-mass galaxies.

The role of the environment in galaxy quenching has also been investigated further through comparisons of the quenched fractions of central galaxies (usually defined to be the most massive and/or luminous galaxy in the group/cluster) and satellite galaxies (i.e. all the other galaxies in the group/cluster). These studies have shown that the quenched fraction for satellite galaxies is higher than that for centrals of the same stellar mass (see e.g. Peng et al. 2012; Wetzel et al. 2012, 2013; Wang et al. 2018). As discussed in Wang et al. (2018), this offset between centrals and satellites can be for two reasons. First, environmentally-driven quenching mechanisms either preferentially act, or only act (i.e. they are 'satellite-specific' mechanisms) on satellites. Second, these environmentally-driven quenching mechanisms can act on both

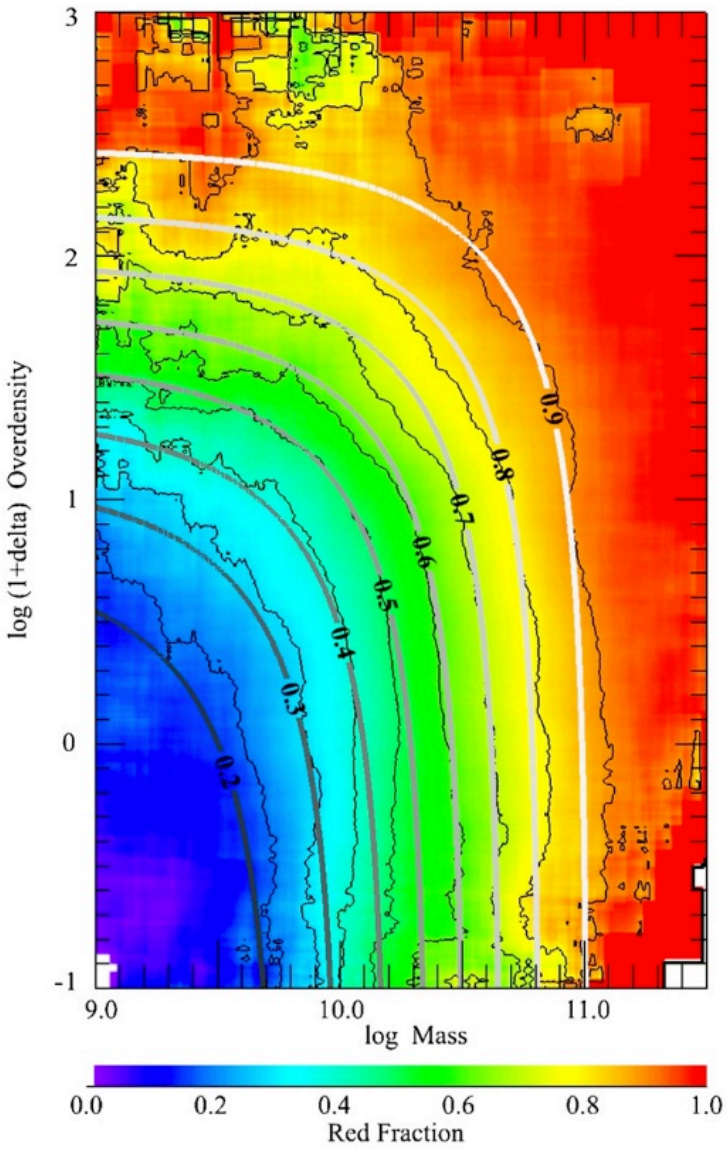

Figure 1.5. The red fraction (i.e. the quenched fraction) of galaxies in the SDSS (for $0.02 < z < 0.085$) as a function of stellar mass and environment (as measured by the local overdensity $1 + \delta$), reproduced from Peng et al. (2010).

centrals and satellites, but, because satellites tend to be in denser environments (i.e. higher local overdensity $1 + \delta$ and higher halo mass $M_{\rm h}$) than centrals of the same stellar mass, the impact of these processes are stronger on the satellite population than on the central population. Indeed, Wang et al. (2018) find, after matching centrals and satellites in both stellar mass and halo mass, that the quenched fractions of centrals and satellites become very similar. Thus they conclude that their findings strongly support the latter scenario, where centrals and satellites of similar masses experience similar quenching processes in their host haloes.

Finally, Peng et al. (2010) showed, for galaxies in the Sloan Digital Sky Survey (SDSS, $z < 0.1$) and zCOSMOS ($0.3 < z < 0.6$), that the effects of mass and environment are largely separable, implying that there are two distinct quenching processes at work: processes that depend on galaxy mass ('mass quenching', which is mostly independent of environment) and processes that depend on environment ('environmental quenching', which is mostly independent of mass).

Mass quenching corresponds to internal processes that quench star formation, with the effectiveness of the quenching mechanisms mainly depending on total galaxy mass. In the low-mass regime, outflows driven by stellar feedback (stellar radiation, stellar winds, or supernova explosions) are thought to be effective at reducing star formation, although they may not be sufficient to completely quench star formation (e.g. Larson 1974; Dekel & Silk 1986). The shallower potential wells of these low-mass galaxies mean that the gas is less strongly bound and hence escapes more easily in the form of outflows. On the other hand, AGN feedback is thought to be more effective at quenching massive galaxies. As massive galaxies tend to host more massive black holes which can reach larger AGN luminosities, these galaxies drive more powerful outflows that can clean the galaxy of its gas content (ejective feedback) and/or heat the surrounding circumgalactic medium via energy injection through radio jets and winds, which in turn results in diminished cold gas accretion, hence quenching by starvation (e.g. Fabian 2012; Cicone et al. 2014; King & Pounds 2015; Fluetsch et al. 2019). In addition, it is thought that infalling gas from the intergalactic medium is shock-heated as it accretes onto galaxies with halo masses above 10^{12} $M_{\odot}$, resulting in the heating of the halo gas, hence suppressing cold accretion onto the galaxy, therefore halting the supply of the fuel for star formation in galaxies ('halo quenching', e.g. Birnboim & Dekel 2003; Kereš et al. 2005; Dekel & Birnboim 2006).

Environmental quenching corresponds to external processes that quench star formation, through interactions between a galaxy and other galaxies, with the intracluster medium and the gravitational potential of the dark matter halo of the group/cluster in which the galaxy is embedded. These physical processes preferentially operate in dense environments and therefore will be more important for galaxies residing in groups/clusters than for galaxies in the field. Satellite galaxies falling into a cluster can have the gas in their ISM rapidly removed as they move through the hot ICM, which can result in rapid quenching in a process known as ram pressure stripping (e.g. Gunn & Gott, J. Richard 1972; Abadi et al. 1999). Furthermore, strong, frequent tidal interactions between two close companion galaxies can also lead to the removal of gas ('harassment', e.g. Farouki & Shapiro 1981; Moore et al. 1996). Stripping of the circumgalactic medium, i.e. the hot halo gas surrounding galaxies, will halt the accretion of cold gas onto the galaxy, therefore shutting down the supply of fuel for star formation, in a process known as 'strangulation' (e.g. Larson et al. 1980; Van Den Bosch et al. 2008). Similarly,

galaxies plunging into a group/cluster and interacting with the group dark matter halo are likely to become detached from the cosmic filaments that feed galaxies with fresh gas from the IGM (e.g. Kereš et al. 2005; Dekel & Birnboim 2006; Dekel et al. 2009), which again, shuts down the fuel supply for star formation, in a process known as 'cosmological starvation' (e.g. Feldmann & Mayer 2015; van de Voort et al. 2017; Aragon Calvo et al. 2019).

1.6 Metallicity

Further insights on the role that different physical processes play in galaxy evolution, during both the star-forming Main Sequence phase and during the quenching process, have been obtained by studying the chemical enrichment of galaxies. Since the abundance of heavy elements in the ISM results from stellar nucleosynthesis, and is further affected by the ejection of heavy elements by galactic winds and the accretion of gas from the IGM, the chemical enrichment level of a galaxy traces both the star formation history and the flow of baryons into and out of the galaxy. Thus, measurements of the chemical enrichment levels of the gas (known as gas-phase metallicities) and stars (known as stellar metallicities) in galaxies can serve as a powerful method to constrain galaxy evolutionary processes and the relative importance of different quenching mechanisms.

Metals are defined to be any elements heavier than hydrogen or helium. Thus, metals are the non-primordial elements that are produced by stars: either through stellar nucleosynthesis, supernova nucleosynthesis or in neutron-star–neutron-star mergers. In general, the more star formation that has taken place in a galaxy, the greater the metal content of the galaxy, since more stars being formed means that more metal production has taken place. Thus, measurements of the level of chemical enrichment in galaxies can yield powerful constraints on their star formation histories.

The level of chemical enrichment in a galaxy is measured through the so-called metallicity Z, which measures the relative abundance of metals in the gas and stars of the galaxy.

The metallicity is often given in terms of the relative number abundance of oxygen to hydrogen ($n_{\rm O}/n_{\rm H}$), where the solar oxygen abundance is $12+\log({\rm O/H})_\odot = 8.69$ (Asplund et al. 2009).

Alternatively, the metallicity can also be given in terms of the ratio of the mass of metals relative to the total mass of baryons, i.e.

$$Z = \frac{M_{\rm Z}}{M_{\rm b}}, \tag{1.3}$$

where $M_{\rm Z}$ is the mass of metals and $M_{\rm b}$ is the total mass in baryons (i.e. including hydrogen, helium and metals together). Both definitions can be applied to either the gas phase (in which

case M_b refers to the total gas mass) or to the stellar population (in which case M_b refers to the total mass in stars). Throughout this work, we assume that solar metallicity $Z_\odot = 0.02$.

1.6.1 Gas-phase metallicity

Gas-phase metallicities are determined by measuring the nebular emission of gas in galaxies. In particular, since the physical conditions in the ISM, such as metallicity, determine the intensity of the emission lines emitted by the ISM, the metallicity of the ISM is determined by measuring the intensity, or rather, the relative intensity of different emission lines, such as R_{23} = ([O II] $\lambda\lambda$3727, 3729 + [O III] $\lambda\lambda$4959, 5007)/Hβ (see e.g. Pagel et al. 1979; Pilyugin 2001, 2005). As these metallicity indicators are calibrated either empirically through observations of H II regions in the Milky Way or extragalactic H II regions (e.g. Pilyugin 2001; Pettini & Pagel 2004), or theoretically (e.g. Kewley & Dopita 2002; Kobulnicky & Kewley 2004) through the use of photoionisation models where nebular gas is photoionised by the radiation from young stars (e.g. Sutherland & Dopita 1993; Ferland et al. 1998), these calibrations can only be applied to determine the metallicity of gas within the star-forming regions of galaxies. As the nebular emission in passive galaxies is often too weak (due to the lack of gas) and not powered by active star formation, the gas-phase metallicities of passive galaxies have not yet been studied in detail, although this is expected to change in the future as metallicity calibrations for non-star-forming regions have recently become available (Kumari et al. 2019). Therefore, gas-phase metallicity measurements have primarily been used to better understand the role of different physical processes during the Main Sequence evolution of star-forming galaxies.

Observations have revealed that local galaxies follow a clear correlation between stellar mass and gas-phase metallicity, with the more massive galaxies being more metal enriched (e.g. Lequeux et al. 1979; Tremonti et al. 2004; Lee et al. 2006; Kewley & Ellison 2008; Andrews & Martini 2013). Although it is not entirely clear what physical processes drive the mass–metallicity relation (MZR), it has been suggested to primarily arise from supernova-driven galactic outflows of metal-rich gas which are preferentially expelled from low-mass galaxies (e.g. Larson 1974; Tremonti et al. 2004). Furthermore, observations of distant galaxies have revealed that the MZR holds at least out to $z \sim 3$ (e.g. Savaglio et al. 2005; Erb et al. 2006; Maiolino et al. 2008; Mannucci et al. 2009; Zahid et al. 2011, 2014; Onodera et al. 2016), with the normalisation of the MZR decreasing with redshift, which we show in Fig. 1.6. Thus, galaxies at high-redshift were more metal-poor than their local counterparts, which could potentially be indicating that high-redshift galaxies were more strongly accreting pristine (i.e. low metallicity) gas from the IGM, or perhaps that these galaxies are less evolved, and so have transformed less of their gas into stars, resulting in a lower amount of metals and hence a lower metallicity.

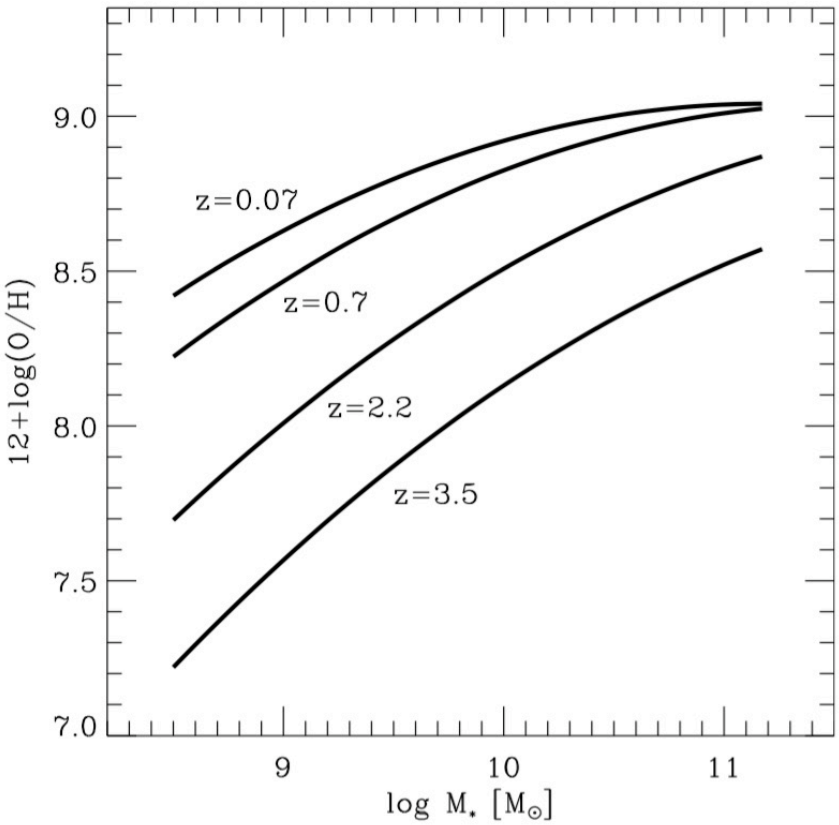

Figure 1.6. The evolution of the mass–metallicity relation, reproduced from Maiolino et al. (2008). The gas-phase metallicities of galaxies tend to increase with stellar mass and decrease with redshift.

Studies investigating the scatter in the MZR have revealed that the gas-phase metallicity also has a secondary dependence on SFR. This three-dimensional relationship between stellar mass, gas-phase metallicity, and SFR is known as the fundamental metallicity relation (FMR; Mannucci et al. 2010). For galaxies of a given stellar mass, the metallicity decreases with increasing SFR. This anticorrelation has been seen in observations (e.g. Ellison et al. 2008b; Lara-López et al. 2010; Mannucci et al. 2010; Cresci et al. 2012; Stott et al. 2013; Hunt et al. 2016a; Almeida & Sanchez-Menguiano 2019), as well as simulations/semi-analytical models (e.g. Yates et al. 2012; De Rossi et al. 2015; Lagos et al. 2016; De Rossi et al. 2017; Torrey et al. 2018, 2019) and has also been investigated using gas regulator models (e.g. Dayal et al. 2013; Lilly et al. 2013; Forbes et al. 2014; Peng & Maiolino 2014b; Hunt et al. 2016b). The anticorrelation is thought to be primarily driven by inflows of pristine gas, where the accreted gas dilutes the gas metallicity but also boosts the SFR by increasing the gas content. In addition to explaining the scatter in the MZR, the FMR also naturally explains, and is consistent with, the redshift-evolution of the MZR. Since galaxies at high-redshift had significantly higher SFRs

(due to the elevated gas accretion rates onto galaxies) than local galaxies, then, according to the FMR, these high-redshift galaxies should also be more metal-poor (due to the enhanced dilution), which is indeed the case. Finally, the small scatter in the FMR suggests that there is a smooth secular connection between star formation and gas flows.

The environmental dependence of the gas-phase metallicity of galaxies has also been extensively investigated. Observations of galaxies in the local Universe have revealed that satellite galaxies tend to be more metal-rich than central galaxies of the same stellar mass (Pasquali et al. 2012; Peng & Maiolino 2014a) and that cluster galaxies tend to be more metal-rich than field galaxies (Ellison et al. 2009). Furthermore, at a fixed stellar mass, the gas-phase metallicity tends to increase with increasing galaxy overdensity (e.g. Mouhcine et al. 2007; Cooper et al. 2008; Ellison et al. 2009; Peng & Maiolino 2014a; Wu et al. 2017), with increasing halo mass (e.g. Pasquali et al. 2012) and with decreasing projected distance from the central galaxy (for massive clusters, e.g. Petropoulou et al. 2012; Maier et al. 2016, 2019). However, the dependence of gas-phase metallicity with environment is typically rather weak, with most studies finding a ∼0.05 dex (at most ∼0.1 dex) environmental effect. Indeed, some studies do not even find a trend between gas-phase metallicity and environment (e.g. Hughes et al. 2013). Thus the environment only has a subtle impact on the chemical content of galaxies in the local Universe.

1.6.2 Stellar metallicity

Stellar metallicities are obtained from the analysis of the stellar continuum emission in galaxies. In particular, the observed stellar continuum and stellar absorption features are fit using combinations of known stellar spectra, yielding constraints on the stellar populations, i.e. the stellar metallicities, stellar ages and abundance ratios of the stars in the galaxy (see e.g. Bruzual & Charlot 2003; Maraston & Strömbäck 2011; Conroy 2013; Wilkinson et al. 2017).

Since a galaxy is composed of many stars, that formed at different times and under different conditions, the stars in any given galaxy typically have a range of metallicities. Therefore, the typical metallicity of the stars in the galaxy, known as the stellar metallicity, is given by the weighted average of the metallicities of the individual stars (or stellar populations) in the galaxy. The mass-weighted stellar metallicity $Z_{\rm MW}$ is given by weighting each star/stellar population i by their mass M_i:

$$Z_{\rm MW} = \frac{\sum_i M_i Z_i}{\sum_i M_i}, \tag{1.4}$$

where Z_i is the metallicity of star/stellar population i. In contrast, the light-weighted stellar

metallicity $Z_{\rm LW}$ is given by weighting each star/stellar population by their luminosity L_i:

$$Z_{\rm LW} = \frac{\sum_i L_i Z_i}{\sum_i L_i}. \tag{1.5}$$

Since young stellar populations are much brighter (per unit mass) than older stellar populations, they contribute relatively much more strongly to the light-weighted average. Hence the mass-weighted and light-weighted stellar metallicities are complementary, with the mass-weighted stellar metallicities tracing the cumulative evolution of the galaxy, while the light-weighted stellar metallicities primarily trace the properties of the young stellar populations in the galaxy.

Unlike gas-phase metallicities, stellar metallicities can be measured for both star-forming and passive galaxies (e.g. Thomas et al. 2005, 2010; Gallazzi et al. 2014; Lonoce et al. 2015; Onodera et al. 2015; Kriek et al. 2016; Toft et al. 2017). Thus, measurements of the stellar metallicities in galaxies have been used to better understand the role of different physical processes during both the Main Sequence evolution of star-forming galaxies and during the quenching process.

Much like the gas-phase mass–metallicity relation, studies of local galaxies have shown the existence of a stellar mass–stellar metallicity relation (e.g. Gallazzi et al. 2005; Thomas et al. 2005; Panter et al. 2008; Thomas et al. 2010), where more massive galaxies typically have higher stellar metallicities. While gas-phase metallicities trace the current chemical conditions in the gas, as discussed above, stellar metallicities represent a weighted average over all the stellar populations in the galaxy, with comparisons of gas and stellar metallicities showing that the stellar metallicities are typically 0.25 dex lower than the metallicity of the gas (e.g. Finlator & Dave 2008; Halliday et al. 2008; Peng & Maiolino 2014b; Pipino et al. 2014). Lian et al. (2018a,b) simultaneously analyse the gas and stellar MZR of local star-forming galaxies and find that, due to the relatively low stellar metallicity in low-mass galaxies, both MZRs can only be reproduced simultaneously if the metal-enrichment in low-mass galaxies is suppressed at early times in their evolution. This suppression can be achieved with either a time-dependent metal outflow with larger metal loading factors in galactic winds at early times (i.e. less metal retention), or through a time-dependent IMF, with steeper IMF slopes at early times (i.e. less metal production).

More recent observations have begun to probe the stellar metallicities of high-redshift star-forming galaxies (e.g. Halliday et al. 2008; Sommariva et al. 2012; Gallazzi et al. 2014; Cullen et al. 2019). Although these studies at high-redshift currently lack the statistics to confirm the existence of a tight MZR, they have found the stellar metallicities of high-redshift star-forming galaxies to be lower than those of local galaxies, which is similar to what has been seen using gas-phase metallicities.

Studies of the stellar populations of several dozen passive galaxies at intermediate redshifts ($z \sim 0.7$ and $z \sim 1.6$, Gallazzi et al. 2014; Lonoce et al. 2015; Onodera et al. 2015) and individual passive galaxies at high-redshift ($z \sim 2$, Kriek et al. 2016; Toft et al. 2017) have shown that these distant passive galaxies have comparable stellar metallicities to local passive galaxies, with their stellar ages being younger by an amount roughly equal to their lookback times. Thus, these quenched galaxies are likely to have evolved passively (i.e. with no episodes of rejuvenated star formation) to $z = 0$, with mergers only having a minor effect on the observed properties of their stellar populations.

The environmental dependence of the stellar metallicities of galaxies has also been studied, with Pasquali et al. (2010) having extensively investigated the dependence of stellar metallicity on the central–satellite dichotomy, as well as on group halo mass. They found that satellite galaxies tend to have higher stellar metallicities than central galaxies of the same stellar mass, with the stellar metallicity difference between centrals and satellites decreasing with increasing mass. Furthermore, they also found that the stellar metallicities of satellite galaxies tend to increase with increasing halo mass, with the slope of the stellar mass–stellar metallicity relation becoming shallower with increasing halo mass.

One significant benefit of studying stellar metallicities is that the chemical content of star-forming and passive galaxies can be compared, which can yield valuable insights on the amount of chemical enrichment (and thus star formation) that takes place during quenching. Indeed, Peng et al. (2015) pioneered the idea that the stellar metallicity difference between star-forming and passive galaxies can be used to determine the nature of the primary quenching mechanism in the Universe. As depicted in Fig. 1.7, during the Main Sequence evolution of a star-forming galaxy, gas is converted into stars and metals are continuously released into the ISM. As a result, subsequent generations of stars that form have progressively higher metallicities. However, due to the diluting effect of the accreting (pristine/low metallicity) gas, the metallicity increase (per unit stellar mass increase) is modest. If at some point star formation is rapidly halted because of gas removal (ejective mode), then few metals and few stars are formed in the quenching phase and the resulting passive galaxy has the same stellar mass and stellar metallicity as its star-forming progenitor. If, instead, gas accretion onto the galaxy is halted by some mechanism (e.g. halo heating), hence resulting in quenching by starvation, then the galaxy keeps forming stars out of the gas reservoir still available in the ISM. Since the dilution effect from the accreting gas is no longer present, the metallicity (of both the gas and the newly formed stars) increases much more steeply during the quenching phase: the result is a passive galaxy with a slightly higher stellar mass and a much higher stellar metallicity than its star-forming progenitor.

In their study, Peng et al. (2015) analysed the stellar metallicities of 26 000 galaxies in the Sloan Digital Sky Survey Data Release 4 (SDSS DR4; Adelman-McCarthy et al. 2006).

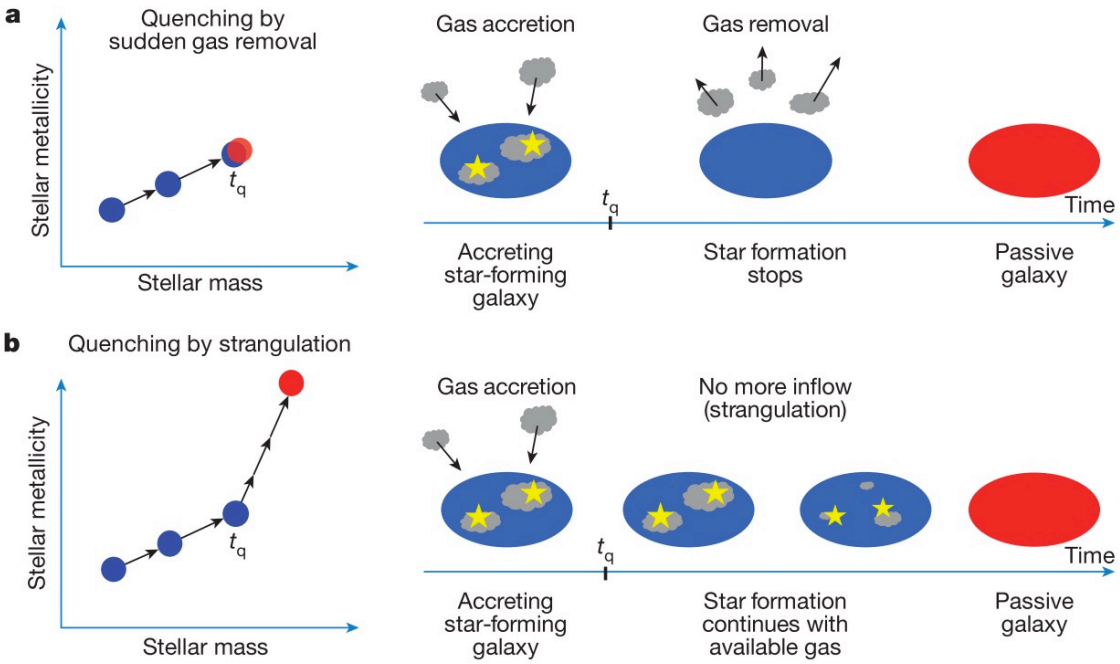

Figure 1.7. Illustration of two different quenching scenarios and their effect on stellar metallicities, reproduced from Peng et al. (2015). Top panel (a): Rapid and complete removal of the gas reservoir of the galaxy (for example, from strong outflows or ram pressure stripping) results in a passive galaxy with the same stellar mass and the same stellar metallicity as its star-forming progenitor. Bottom panel (b): In the starvation/strangulation scenario, the galaxy continues to form stars out of the available enriched ISM and, as a consequence, increases its stellar mass and significantly increases its stellar metallicity during the quenching process.

As shown in Fig. 1.8, at $M_* < 10^{11}$ $M_\odot$ passive galaxies were found to have a systematically larger stellar metallicity than star-forming galaxies of the same stellar mass, indicating that galaxies typically undergo significant chemical enrichment during quenching, a clear signature of quenching by starvation. In order to put quantitative constraints on the possible quenching mechanisms and timescales, the observed differences in stellar metallicity between star-forming and passive galaxies were then compared with the predictions of gas regulator models. Their analysis confirmed that starvation (i.e. the halting of the supply of cold gas) is the primary mechanism responsible for shutting down star formation in galaxies with stellar masses below 10^{11} $M_\odot$. Peng et al. (2015) inferred a typical mass-independent quenching timescale of 4 Gyr. They further found that their models are unable to reproduce the observed stellar metallicity differences when outflows are included, suggesting that outflows play a minor role in quenching galaxies. In order to distinguish between different origins for the starvation mechanism (e.g. halo quenching, strangulation or cosmological starvation), an analysis of the environmental dependence of the stellar metallicity difference was also undertaken. Satellite galaxies were

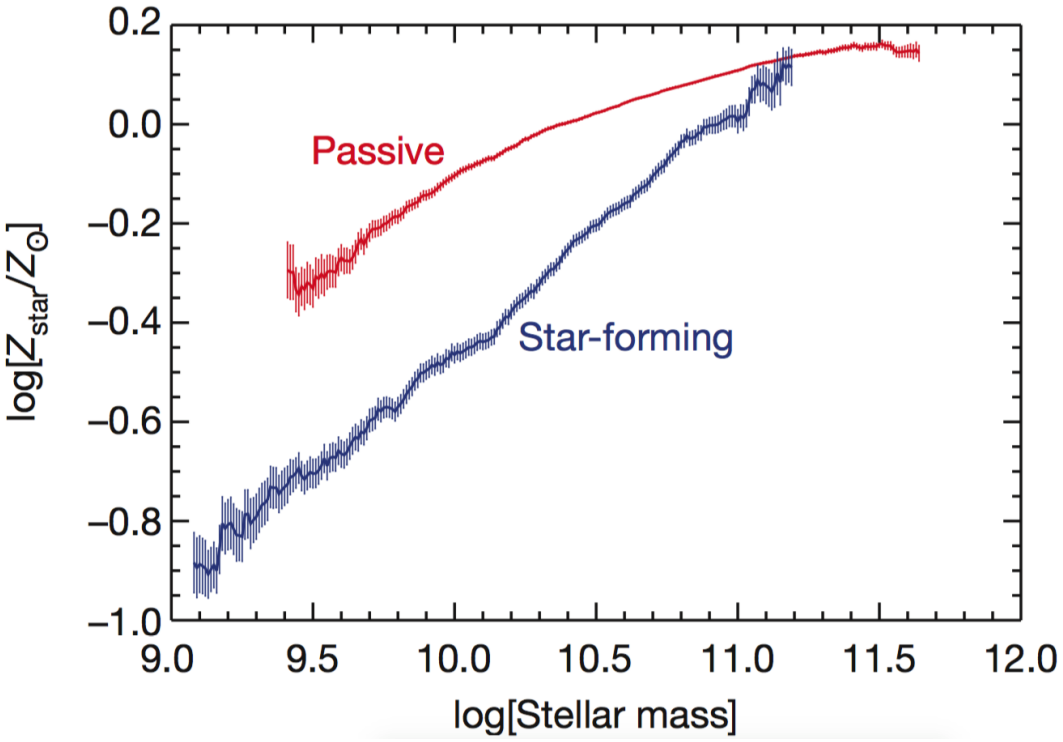

Figure 1.8. The stellar mass–stellar metallicity relation for star-forming (blue) and passive galaxies (red), adapted from Peng et al. (2015). Passive galaxies are significantly more metal-rich than star-forming galaxies of the same stellar mass, indicating that considerable chemical enrichment takes place during quenching, which is a clear signature of quenching by starvation.

found to have slightly higher stellar metallicity differences than central galaxies at stellar masses below 10^{10} $M_{\odot}$, suggesting an environmental origin for the starvation mechanism in this low-mass regime. However, at stellar masses above 10^{10} $M_{\odot}$ no difference was found between centrals and satellites, suggesting that in this higher mass range environmental effects do not contribute significantly to the quenching.

1.7 Thesis motivation and outline

In this thesis, we build upon the innovative, powerful and promising new technique pioneered by Peng et al. (2015), that assesses the relative impact of different quenching mechanisms through comparisons of the levels of chemical enrichment in star-forming and passive galaxies. In particular, by utilising the enhanced statistics available in Sloan Digital Sky Survey Data Release 7 (SDSS DR7, Abazajian et al. 2009), by further developing and refining the chemical evolution model by properly taking into account the effect of different progenitors of local galaxies, by delving deeper into the imprint of environment on the stellar populations of

galaxies, and by harnessing the spatially-resolved power of the integral field spectra from the SDSS-IV MaNGA galaxy survey, we intend to push the Peng et al. (2015) technique ever further, as we investigate how galaxy quenching depends on both the internal properties of galaxies (i.e. stellar mass) and external factors (i.e. environment), how galaxy quenching has evolved across cosmic time and how quenching operates within galaxies. Thus, by leveraging on the statistical power of large spectroscopic galaxy surveys and focussing on the chemical transformation that takes place during quenching, we aim to unveil the primary quenching mechanisms in galaxies.

More specifically, in Chapters 3 and 4, we build upon the original analysis by Peng et al. (2015), using stellar metallicity differences to determine the primary mechanism responsible for quenching star formation. We focus on the role of mass in galaxy quenching and the similarities and differences between the quenching of galaxies at high-redshift and the quenching of galaxies in the local Universe. Our analysis in this chapter improves upon the original study in several ways. Firstly, we undertake a more extensive comparison between models and observations, deriving stronger constraints on the mass-dependent role of outflows in quenching star formation, by simultaneously reproducing the stellar metallicities and the star formation rates observed in local passive galaxies in our models, which results into a revision of the relative role of starvation and outflows in different mass ranges. Secondly, using the much larger spectroscopic sample of galaxies (930 000 cf. 566 000 in the original work) available in SDSS DR7, we now also study the quenching of star formation in local green valley galaxies, in addition to the quenching of passive galaxies that was studied in the original work. Thirdly, we have introduced a more sophisticated treatment of the progenitor–descendant comparison to allow for a better assessment of the amount of chemical enrichment during the quenching phase. We now compare the stellar metallicity difference between local passive galaxies and their high-z star-forming progenitors, rather than the difference between local passive and local star-forming galaxies. This new comparison results in a widening of the gap in stellar metallicity between star-forming and passive galaxies, which qualitatively strengthens the case for starvation. Fourthly, we use the mass-weighted stellar ages of local galaxies derived in this work to provide a more empirically-motivated estimation of the redshift associated with the onset of quenching in the models. Finally, we adopt a consistent treatment of stellar metallicity in this chapter, comparing mass-weighted metallicity predictions from models with mass-weighted stellar metallicities from observations, rather than comparing against light-weighted stellar metallicities from observations like in Peng et al. (2015).

Furthermore, in Chapter 5, we study the imprint of the environment on the stellar populations of galaxies. We build upon the original environment analysis of Peng et al. (2015), by again leveraging on the greatly improved statistics in SDSS DR7 to delve deeper into the contribution of environmental effects to the quenching of galaxies, now also studying the green valley galaxy

population, as well as investigating trends with halo mass, overdensity and projected distance from the central galaxy. We also build upon the analysis of the environmental dependence of the stellar populations of galaxies by Pasquali et al. (2010), by investigating, for the first time observationally, how the stellar mass–stellar metallicity and the stellar mass–stellar age relations for star-forming, green valley and passive galaxies depend on environment.

In Chapter 6, we utilise the spatially-resolved spectra from the SDSS-IV MaNGA integral field spectroscopic galaxy survey to study the global stellar population parameters of galaxies, as well as the radial variation of these parameters. By studying the global stellar population properties, we aim to determine whether the key mass- and environment-dependent trends found in this thesis apply only to the central regions of galaxies, or instead hold true globally: from the innermost to the outermost regions in galaxies. Furthermore, by studying the radial variation of the stellar population parameters of galaxies, we aim to extend the analysis of galaxy quenching even further. In particular, we aim to address how quenching operates within galaxies, by investigating how the stellar metallicity difference between star-forming and passive galaxies varies with radial distance.

This thesis is structured as follows. In Chapter 2, we introduce the Sloan Digital Sky Survey data that we use in our analysis, discussing both the single fibre spectra from the SDSS Legacy Survey and the spatially-resolved spectra from the SDSS-IV MaNGA integral field spectroscopic galaxy survey. In Chapter 3, we introduce the chemical evolution model that is used in our analysis. In particular, we discuss how the relative levels of chemical enrichment in star-forming and passive galaxies can be used to assess the relative impact of different quenching mechanisms, the differential equations that we have developed to describe the evolution during quenching, our method for estimating the mass-dependent epoch $z_{\rm q}$ associated with the onset of quenching, and the initial properties of the star-forming progenitors at the onset of quenching. In Chapter 4, we utilise the statistical power of SDSS DR7 to investigate the role of mass in galaxy quenching. In particular, we analyse the chemical properties of tens of thousands of star-forming, green valley and passive galaxies in the local Universe to assess the relative role of starvation and outflows in driving galaxy quenching. We investigate the quenching of star formation both at high-redshift and in the local Universe by analysing the stellar metallicity differences between local passive galaxies and their high-redshift star-forming progenitors, and local green valley galaxies and local star-forming galaxies, respectively. In Chapter 5, we continue our analysis of the SDSS DR7 dataset, which we now use to investigate the role of environment in galaxy evolution and galaxy quenching. In particular, we study the dependence of the stellar populations of galaxies on environment, both in terms of the central–satellite dichotomy, as well as on further measures of environment: halo mass, local overdensity and projected distance. Furthermore, we use our chemical enrichment-based method to investigate

environmental quenching, analysing the environmental dependence of the stellar metallicity difference between star-forming and passive galaxies to determine whether environmental effects contribute to the starvation of galaxies. In Chapter 6, we utilise the spatially-resolved spectra from the SDSS-IV MaNGA galaxy survey to study both the global stellar population parameters, as well as the radial variation of these parameters in galaxies. First, we aim to verify whether the key mass- and environment-dependent findings from Chapters 4 and 5 hold true globally or only apply to the central regions in galaxies. Second, we investigate how quenching operates on a radial basis within galaxies. Finally, in Chapter 7 we conclude, as we summarise the main findings from this thesis and discuss our outlook for the future.

Chapter 2

Sloan Digital Sky Survey and Initial Data Analysis

2.1 Introduction

In this chapter we describe the Sloan Digital Sky Survey data that will be used throughout the analysis in this thesis, the methodology adopted to extract stellar population parameters (specifically stellar metallicities and stellar ages) from the stellar continuum emission of galaxies, as well as other information, such as the parameters describing the environment in which galaxies reside. In Section 2.2, we discuss the data from the SDSS Legacy Survey, which has obtained single fibre spectra targeting the central 3″ of ∼one million galaxies in the local Universe. In Section 2.3, we discuss the data from the SDSS-IV MaNGA integral field spectroscopic galaxy survey, which aims to obtain spatially-resolved spectral measurements for 10 000 galaxies in the local Universe.

More specifically, in Sections 2.2.1 and 2.3.1, we briefly introduce the two galaxy surveys. In Sections 2.2.2 and 2.3.2, we discuss the general survey data that is used in our analysis. In Sections 2.2.3 and 2.3.3, we outline how we have used spectral fitting to derive the stellar population parameters of SDSS galaxies. In Sections 2.2.4 and 2.3.4, we discuss the galaxy group catalogues and measures of environment that are used in our analysis. Finally, in Sections 2.2.5 and 2.3.5 we discuss how we use the bimodality in the SFR-M_* plane to classify galaxies as star-forming, green valley and passive.

2.2 SDSS Legacy Survey

2.2.1 Survey and sample

We use the spectroscopic sample of galaxies in the SDSS DR7 (York et al. 2000; Abazajian et al. 2009) dataset from the SDSS Legacy Survey, obtained using the Sloan 2.5 m telescope at Apache Point Observatory (APO) in New Mexico, United States (Gunn et al. 2006). The SDSS DR7 dataset includes five-band photometry (u, g, r, i, z; Gunn et al. 1998; Doi et al. 2010) for 357 million distinct objects and spectroscopy (Smee et al. 2013) for over 1.6 million sources, including 930 000 galaxies which we study in our analysis. The spectroscopic sample of galaxies is substantially larger than the 566 000 galaxies in DR4 (Adelman-McCarthy et al. 2006) that were studied by Peng et al. (2015).

The galaxies chosen for spectroscopic follow-up consist of two main samples. First, a sample complete to a Petrosian (1976) magnitude limit of $r = 17.77$ ('Main Galaxy Sample', Strauss et al. 2002). Second, two smaller and deeper samples of luminous red ellipticals up to $r = 19.2$, corresponding to an approximately volume-limited sample to $z = 0.38$ and $z = 0.55$, respectively ('Luminous Red Galaxy Sample'; Eisenstein et al. 2001). Spectroscopic observations are in the optical/NIR (3800–9200 Å), have a spectral resolution $R \sim 2000$ and a typical signal-to-noise ratio (S/N) ~ 10 for galaxies near the main sample flux limit. Each set of spectroscopic observations used a specially-designed plate, which had a unique set of holes drilled into it that matched the positions of the targeted galaxies on the sky. Optical fibres were placed at the holes in the plate, which fed the gathered light into the SDSS spectrograph, thus enabling the spectra of up to 640 galaxies to be taken at the same time. Each optical fibre had a width of 3″ and was positioned at the centre of the galaxy being observed. Thus, the spectra from the SDSS Legacy Survey only probe the central 3″ of galaxies.

Since the SDSS sample suffers from incompleteness at $M_* < 10^{10}$ $M_\odot$, we apply the V_{max} weightings from Blanton et al. (2003) to correct for volume incompleteness, allowing our analysis to be safely extended down to $M_* = 10^9$ $M_\odot$. However, we do note that these V_{max} corrections only have a very minor effect on our stellar mass–stellar metallicity and stellar mass–stellar age relations, and so do not affect the results from our study.

Similar to Peng et al. (2015), we restrict our analysis to galaxies with reliable spectroscopic redshifts in the range $0.02 < z < 0.085$. This redshift cut was applied for several reasons. Firstly, to reduce the effect of cosmological evolution on the analysis ($z_{max} \sim 0.55$ in the full SDSS sample corresponds to roughly 40 per cent of the age of the Universe). Secondly, to reduce the impact of aperture effects associated with the projected physical aperture of the SDSS spectroscopic fibre. If a broader redshift range were used, then the more distant galaxies would be studied over larger effective radii than nearby galaxies, which could result in unwanted

biases in the analysis. Finally, to ensure that the $V_{\rm max}$ correction remains reliable for the sample studied.

We also restrict our study to galaxies for which reliable stellar metallicities and stellar ages can be derived, requiring that the median signal-to-noise ratio per spectral pixel is higher than 20. Such a high S/N cut could potentially introduce biases into our analysis as low surface brightness galaxies are preferentially removed from the sample. However, we find that the trends seen in our results do not change significantly with the chosen S/N criterion. Hence we have selected a S/N threshold of 20, since this provides a healthy balance between good statistics and reliability of measurements. After applying these cuts on redshift and S/N, our sample consists of 86 066 galaxies.

2.2.2 Data

We make use of the publicly available MPA-JHU DR7 release of spectral measurements[a], which provides derived galaxy parameters for all galaxies in SDSS DR7. Stellar masses are obtained from fits to the photometry, using the Bayesian methodology of Kauffmann et al. (2003a). Star formation rates within the spectroscopic fibre aperture are computed from the Hα emission (Brinchmann et al. 2004), which are then aperture-corrected using photometry (Salim et al. 2007) to obtain total SFRs which extends beyond the spectroscopic fibre aperture. We use the total SFRs in our analysis. For AGN or galaxies with faint emission lines, such as passive galaxies, SFRs are derived from the strength of the 4000 Å break (D4000). It should be noted that the SFRs derived for passive galaxies are most likely upper limits. Furthermore, we also make use of the BPT classifications of Brinchmann et al. (2004), who used the [N II]-BPT diagnostic diagram to classify SDSS galaxies by the primary excitation source for their nebular emission.

2.2.3 Stellar population parameters

In this section we discuss the stellar population parameters (stellar metallicities and stellar ages) that are used throughout the analysis in this thesis. In Section 2.2.3.1, we outline the physical basis behind the spectral fitting process, motivating why the stellar population parameters of a galaxy can be extracted by fitting its observed spectrum, as well as the general technical procedures behind the spectral fitting process. In Section 2.2.3.2, we discuss the two-step spectral fitting procedure we adopt to derive stellar population parameters, and also discuss the performance of the FIREFLY spectral fitting code at recovering stellar population parameters.

[a]The MPA-JHU data release is available at https://wwwmpa.mpa-garching.mpg.de/SDSS/DR7/.

2.2.3.1 Physical motivation and technical aspects of general spectral fitting procedures

Firstly, we outline the physical basis behind the spectral fitting process, describing the physical principles behind why the spectrum of a galaxy is sensitive to the ages and metallicities of the stars in the galaxy, therefore motivating why the stellar population parameters of a galaxy can be extracted by fitting its observed spectrum.

The spectra of galaxies contain a wealth of information, with both the shape and normalisation of the stellar continuum, as well as the strength of various absorption features being dependent on the ages and metallicities of the stellar populations present in the galaxy. Firstly, there are numerous age-sensitive absorption features in optical galaxy spectra, with notable examples being D4000 and H$\delta_{\rm A}$. D4000, commonly referred to as the 4000 Å break, is an absorption feature around ~4000 Å, that is usually quite prominent in the spectra of passive galaxies. This absorption feature is brought about by the absorption of light by singly ionised calcium (Ca II) and other ionised metals in the atmospheres of stars (see e.g. Bruzual & Charlot 2003; Kauffmann et al. 2003a; Conroy 2013) The absorption feature is particularly strong for low-mass stars as these are relatively cool and therefore harbour a relatively large amount of singly ionised calcium in their atmospheres, but is relatively weak for high-mass stars as these are too hot (and therefore too ionised) to exhibit this absorption feature. Therefore, as a stellar population ages, the relatively bright and short-lived high-mass stars that dominate the spectrum of the stellar population fade away, and the stellar emission of the relatively faint and long-lived low-mass stars begins to dominate, with the strength of the D4000 absorption feature increasing as a stellar population ages, making it a useful indicator for the age of a stellar population. The H$\delta_{\rm A}$ absorption feature is another commonly used age-indicator, that is primarily brought about by Balmer absorption in the atmospheres of A-type stars (see e.g. Bruzual & Charlot 2003; Kauffmann et al. 2003a; Conroy 2013). These stars are sufficiently cool (with respect to the hotter O- and B-type stars) such that the hydrogen in their stellar atmospheres is neutral (rather than ionised), but sufficiently hot (with respect to the cooler F-, G-, K-, M-type stars) such that this hydrogen is in the $n = 2$ (rather than the $n = 1$) state, so that a relatively large amount of Balmer absorption takes place in the stellar atmosphere. As a result, as a stellar population ages, the strength of the H$\delta_{\rm A}$ absorption feature increases, as the O- and B-type stars begin to fade and the A-type stars begin to dominate the spectrum, reaching a peak, and then begins to fall in strength as the A-type stars begin to fade and leave the main sequence. Thus, the H$\delta_{\rm A}$ absorption feature is sensitive to stellar populations of intermediate stellar ages and is often used to identify galaxies that have had a recent (within the past ~0.1–1 Gyr, Kauffmann et al. 2003a) burst of star formation.

Secondly, there are numerous metallicity-sensitive absorption features in optical galaxy

spectra, such as the G-band feature at ~4300 Å due to neutral iron and CH, the Mg *b* triplet of magnesium at ~5175 Å and the Fe5270 feature of iron at 5270 Å (see e.g. Bruzual & Charlot 2003; Gallazzi et al. 2005). Unsurprisingly, these spectral features are all associated with metals in the atmospheres of stars, with the strength of the absorption feature increasing as the abundance of metals (and therefore the relative number of absorbers) increases.

The stellar population parameters are then derived by fitting the observed galaxy spectrum with a combination of stellar spectra. Typically the spectra associated with a coevolved population of stars of a given age and stellar metallicity, known as a simple stellar population (SSP), are used in the spectral fitting process, though other stellar spectra, such as those of individual stars (often in earlier works, see e.g. Spinrad & Taylor 1971; Faber 1972; Pritchet 1977) as well as groupings of stars with similar spectra (see e.g. Westfall et al. 2019) are also sometimes used. The SSP spectra are produced using stellar population synthesis models, which have three main ingredients: the IMF adopted, the stellar tracks used and the stellar spectral library that is used (for more details, see e.g. Bruzual & Charlot 2003; Maraston 2005; Maraston & Strömbäck 2011; Conroy 2013). Stars are initially populated (with a zero age main sequence and a given stellar metallicity) in the colour–magnitude (or the more theoretical $T_{\rm eff}$–g effective temperature–surface gravity) diagram according to the IMF that is adopted. The location of the stars in the colour–magnitude diagram (known as an isochrone) is then evolved in time, following so-called stellar tracks that are given by stellar evolution models. For each time step (i.e. stellar age), each star in the stellar population is assigned a spectrum, dependent on its position in the colour–magnitude diagram, where the spectra that are assigned are taken from libraries of stellar spectra of individual stars (known as stellar libraries). The spectra in these stellar libraries are either empirical, theoretical or a combination of empirical and theoretical spectra. The spectra of the individual stars in the colour–magnitude diagram are then combined together to give the spectrum of the SSP of that particular age and stellar metallicity.

Since different stellar population synthesis models use different IMFs, stellar tracks and stellar libraries, the spectra associated with the SSPs that they produce are also different. Therefore the stellar population parameters that are derived from fitting observed galaxy spectra are sensitive to the stellar population synthesis model used, with the choice of SSP adopted in the fitting process likely introducing systematic uncertainties in the values of the stellar population parameters that are obtained (see e.g. Conroy et al. 2009, 2010; Conroy & Gunn 2010; Conroy 2013). Furthermore, different stellar population synthesis models make different assumptions about uncertain aspects of the stellar evolutionary process (typically regarding the post main sequence evolution), such as the contribution of thermally-pulsating asymptotic giant branch stars or the colour ("morphology") of horizontal branch stars, as well as aspects related to the evolution of the stellar population itself, such as the incidence rate of blue stragglers, which

can lead to further systematics in the derived stellar population parameters (see e.g. Conroy et al. 2009, 2010; Conroy & Gunn 2010; Conroy 2013). A promising new approach that aims to reduce these systematics was introduced in the Flexible Stellar Population Synthesis (FSPS) model by Conroy et al. (2009) and Conroy & Gunn (2010). Unlike other models, which make fixed assumptions about these uncertain aspects of stellar (population) evolution, the FSPS model makes no fixed assumptions and is instead more flexible, as it is informed by the data currently being fit, with the data therefore demanding and determining which assumptions are appropriate for that particular spectrum. This approach reduces systematics but increases the degeneracy in the solution space.

These SSPs are then used to fit the observed galaxy spectrum so that the stellar population parameters can be determined. This fitting process is typically done in one of two ways. Traditionally, SSPs were used to simultaneously fit a series of age-sensitive and metal-sensitive absorption features (such as those mentioned earlier, see e.g. Gallazzi et al. 2005). More recently, SSPs are used to perform a full spectral fit, where both the shape and normalisation of the observed stellar continuum is matched, in addition to the various absorption features in the spectra (see e.g. Sanchez et al. 2016a; Cappellari 2017; Wilkinson et al. 2017). In order to carry out any individual iteration of a spectral fit, a star formation history (SFH) has to be assumed, which is given either parametrically or non-parametrically (see e.g. Conroy 2013; Lower et al. 2020). In the former scenario, the star formation history is given analytically by a simple, but physically-motivated parameterisation, such as a constant SFH ($\Psi(t) = c$), a declining SFH ($\Psi(t) \propto e^{-t/\tau}$) or a rising-and-falling SFH ($\Psi(t) \propto te^{-t/\tau}$). In the latter scenario, where the SFH is given non-parametrically, the observed spectrum is fit using a linear combination of SSPs of different ages and stellar metallicities, i.e. the SFH is given by a series of sequential bursts of star formation, producing distinct populations of stars of different ages and metallicities. As non-parametric SFHs are more flexible, they are typically better at recovering the true SFHs in galaxies than the more-constrained parametric SFHs, with spectral fitting processes that adopt non-parametric SFHs being better able to recover the stellar masses of galaxies (see Lower et al. 2020). Since each iteration of the spectral fitting process assumes a different SFH and stellar metallicity combination, the stellar population parameters (ages and metallicities) derived by any individual iteration of the fitting process will be different. The reported age and metallicity derived by the spectral fitting code is normally obtained by averaging over the ages and metallicities given by the various iterations of the spectral fitting process, where the spectral fits that better match the observed data (in terms of having a smaller χ^2), are weighted more strongly than the spectral fits that poorly match the observed data (see e.g. Wilkinson et al. 2017).

Finally, we discuss further technical aspects of the spectral fitting process. Firstly, the stellar

spectra in empirical stellar libraries are obtained by observing stars in the solar neighbourhood, which have solar-like abundance ratios (α/Fe). However, the stars in other galaxies likely do not have solar-like abundance ratios, so this mismatch between the stellar templates and the observed galaxy spectra can lead to further systematic uncertainties (see e.g. Bruzual & Charlot 2003; Thomas et al. 2003; Gallazzi et al. 2005). In spectral fitting procedures that simultaneously fit a series of age-sensitive and metallicity-sensitive absorption features, this problem is avoided by creating and fitting composite absorption features, which are obtained by combining individual absorption features together, in a way such that the strength of the absorption of the composite absorption feature is insensitive to the abundance ratio of the stars in the stellar population (see e.g. Bruzual & Charlot 2003; Thomas et al. 2003). In contrast, the stellar population parameters derived from a full spectral fit are less affected by this abundance ratio effect (see e.g. Maraston & Strömbäck 2011). Secondly, SSPs of different ages and stellar metallicities can have comparable spectra. Known as the age–metallicity degeneracy, this effect qualitatively comes about because the spectra of a given SSP becomes redder when its stellar metallicity is increased and also when its age is increased (see e.g. Bruzual & Charlot 2003; Maraston 2005; Maraston & Strömbäck 2011; Conroy 2013). By definition, the age–metallicity degeneracy is mostly avoided/minimised in methods that simultaneously fit a series of age- and metallicity-sensitive spectral indices. In the case of the full spectral fitting process, ages and metallicities can be well-recovered by modern spectral fitting codes such as FIREFLY, provided that the spectra are of sufficiently high S/N and that there is only a moderate amount of dust extinction (see Wilkinson et al. 2017). Indeed, the age–metallicity degeneracy is further compounded by dust reddening, which also reddens galaxy spectra. Extragalactic dust extinction is accounted for in the spectral fitting process, where either the dust extinction curve is assumed, or is determined in the spectral fitting process, along with the strength of the colour excess $E(B-V)$ (see e.g. Conroy 2013). Finally, while spectral fitting codes derive stellar population parameters by fitting the observed stellar continuum and absorption features, galaxy spectra typically also contain nebular emission lines which are superimposed on the stellar continuum. Traditionally, these nebular emission lines were masked, so that only the emission-line-free regions of the observed spectrum were fit. However, one key limitation of this approach is that the nebular emission lines often overlap with important absorption features in the stellar continuum, such as H$\delta_{\rm A}$, which can provide strong constraints on the ages and metallicities of the stellar populations in the galaxy (see discussion in e.g. Sarzi & Falcón Barroso 2006), but are also masked in this procedure. More recently, spectral fitting codes are adopting a new approach, where both the stellar continuum and the nebular emission are fit simultaneously (see e.g. Sarzi & Falcón Barroso 2006; Westfall et al. 2019). This spectral fitting procedure is usually carried out through an iterative process, where the nebular emission

lines are initially masked so that the stellar kinematics can be constrained, and then both the stellar continuum and nebular emission are fit simultaneously, going through a sequence of iterations until the fits in each iteration converge.

2.2.3.2 Spectral fitting procedure

We derive the stellar population parameters (i.e. the stellar metallicities and stellar ages) of SDSS galaxies through a two-step spectral fitting procedure. First, we fit the SDSS spectrum with the spectral fitting code pPXF (Cappellari & Emsellem 2004; Cappellari 2017) to determine the stellar velocity dispersion σ_*. Second, we use the measured stellar velocity dispersion to broaden the stellar templates in the FIREFLY (Comparat et al. 2017; Goddard et al. 2017b; Wilkinson et al. 2017) spectral fitting code. We then fit the SDSS spectrum with FIREFLY to obtain both the mass-weighted and light-weighted stellar metallicities and stellar ages of the galaxy. Both of the spectral fitting codes and their respective spectral fitting procedures will be described in more detail later in this section.

In both steps of the spectral fitting procedure, we mask the following nebular emission lines in the galaxy rest-frame: all the Balmer lines from Hα to H9, as well as [O II] $\lambda\lambda$3727, 3729, [Ne III] λ3869, [O III] $\lambda\lambda$4959, 5007, He I λ5876, [O I] $\lambda\lambda$6300, 6364, [N II] $\lambda\lambda$6548, 6583, [S II] $\lambda\lambda$6716, 6730 and [Ar III] λ7136. We also mask the following skylines in the observed frame: [O I] λ5577, Na D $\lambda\lambda$5890, 5896 and [O I] $\lambda\lambda$6300, 6364. Any wavelength channels that fall within $\pm$1000 km s^{-1} of the line centres of the aforementioned lines are ignored during the spectral fitting procedure.

While we have personally used this procedure to derive the stellar population parameters for galaxies in the SDSS-IV MaNGA survey (see Section 2.3), we do note that the stellar population parameters for galaxies in the SDSS Legacy Survey (that we study in this section) were instead derived by collaborators at Portsmouth (Daniel Goddard and Jianhui Lian), following the same spectral fitting procedure outlined here.

The spectral fitting procedures with pPXF and FIREFLY are discussed in more detail in Sections 2.2.3.3 and 2.2.3.4, respectively.

2.2.3.3 pPXF

The Penalized Pixel-Fitting method (pPXF, Cappellari & Emsellem (2004); Cappellari (2017)) uses a maximum penalised likelihood approach to extract the stellar kinematics (as well as the stellar populations, gas kinematics and gas emission) from galaxy spectra. We fit the SDSS spectra using the Vazdekis et al. (2010) stellar templates, which were derived from the MILES stellar library (Sanchez-Blazquez et al. 2006) and have metallicities [Z/H] =

−1.71, −1.31, −0.71, −0.4, 0.0, 0.22 and ages that range from 63 Myr to 16 Gyr. The spectral resolution is 2.51 Å FWHM and the wavelength coverage is 3540–7409 Å. An additive polynomial of order 12 is used in the fitting process to correct for slight template mismatches (by changing the strength of individual absorption lines).

2.2.3.4 FIREFLY

We use the spectral fitting code FIREFLY (Comparat et al. 2017; Goddard et al. 2017b; Wilkinson et al. 2017) to obtain stellar metallicities and stellar ages for each galaxy in the SDSS sample. Briefly, FIREFLY is a χ^2 minimisation fitting code that fits input galaxy spectra using an arbitrarily weighted, linear combination of simple stellar populations (SSPs) which can have a range of metallicities and ages. The weighted sum of metallicities and ages of each of the SSPs is used to derive the stellar metallicity and stellar age of the galaxy. The code returns both light-weighted and mass-weighted stellar ages and stellar metallicities. The light-weighted properties are obtained by weighting each SSP by its total luminosity across the fitted wavelength range (3500–7429 Å). On the other hand, mass-weighted properties are obtained by weighting each SSP by its stellar mass contribution. We primarily study the mass-weighted ages and metallicities in our analysis, as these are directly comparable with our simple gas regulator models. This is in contrast with the light-weighted ages and metallicities, which in the model would have to be computed using detailed stellar population synthesis modelling, that assesses the evolution of the relative light contributions from different stellar populations across the fitted wavelength range.

FIREFLY fits the observed galaxy spectra using the stellar population models of Maraston & Strömbäck (2011), together with input stellar spectra from the empirical stellar library MILES (Sanchez-Blazquez et al. 2006) and a Kroupa IMF (Kroupa 2001). We have chosen to use MILES in our analysis as it had the most comprehensive sampling range in stellar metallicity and stellar age out of the empirical libraries that were available. The MILES library has metallicities $[Z/\mathrm{H}] = -2.3,\ -1.3,\ -0.3,\ 0.0,\ 0.3$ and ages that span from 6.5 Myr to 15 Gyr. The spectral resolution is 2.5 Å FWHM and the wavelength coverage is 3500–7429 Å. We have also repeated our analysis using the Salpeter (Salpeter 1955) and Chabrier (Chabrier 2003) IMFs and find that the results throughout this thesis are essentially unchanged.

The performance of FIREFLY has been extensively tested in Wilkinson et al. (2017). We summarise the main findings here. Mock galaxies, with a wide range of star formation histories (short, intermediate and extended), dust content and S/N, were constructed. FIREFLY was able to recover stellar population properties such as age, metallicity and stellar mass remarkably well down to a S/N $\sim$ 20 (which is the S/N cut used in this chapter), for moderately dusty systems. When using a lower S/N ($\sim$5), metallicity may be underestimated by roughly 0.3 dex,

but this depends on the reddening of the system, which may alter the age determination and hence the metallicity. The accurate recovery of the stellar population parameters indicates that the full spectral fitting approach with no additional prior over the wide model grid of ages and metallicity is able to remove most degeneracies. However, it should be noted that there are residual degeneracies between age and dust especially, and between different star formation histories, for systems with a substantial amount of dust ($E(B-V) = 0.75$) and an extended star formation history (~10 Gyr), but these properties should pertain only to a minority of galaxies. Still, even in these very dusty systems FIREFLY is able to distinguish between short and extended formation histories, albeit with less precision. The effect of the adopted wavelength range on the derivation of metallicity was also studied, for two mock galaxies with very different ages (55 Myr and 7 Gyr). The input solar metallicities were recovered to within ±0.02 dex, with not too much dependence on the adopted wavelength range.

The performance of FIREFLY at recovering the ages and metallicities of Milky Way globular clusters was also tested. Wilkinson et al. (2017) found a very good match between the ages and metallicities derived by FIREFLY, and the ages and metallicities determined via CMD fitting, and stellar spectroscopy, respectively, with no bias in the derivation of metallicity over a wide range ($-2 < [Z/\mathrm{H}] < 0$). Furthermore, the ages and metallicities derived by FIREFLY were also compared with those obtained by Koleva et al. (2008), who used a different fitting code (NBURSTS, Chilingarian et al. 2007) and models (Pegase-HR, Le Borgne et al. 2004). Overall, the results are consistent, but Wilkinson et al. (2017) note that the FIREFLY results do not contain artificially low ages and display a smaller scatter around the resolved ages and metallicities.

The loci of SDSS DR7 galaxies on the age-metallicity plane using FIREFLY was also compared with the results obtained using other fitting codes, namely VESPA (Tojeiro et al. 2007, 2009) and STARLIGHT (Cid Fernandes et al. 2005). The comparison with VESPA is performed using their calculations based on the Maraston (2005) models. Wilkinson et al. (2017) find that the distributions of galaxies are broadly similar (most galaxies peak at old ages and high metallicity), but the exact age and metallicity solution will of course depend on what the model grid allows. In FIREFLY the models are not restricted, hence the solutions appear more spread than what is obtained with VESPA, who construct model vectors with a more restricted range of input properties. The comparison with STARLIGHT is performed using their calculations based on the Bruzual & Charlot (2003) models. Wilkinson et al. (2017) find that the main density of age and metallicity points cluster around 8 Gyr in age and 0.1 to 0.3 dex in $[Z/\mathrm{H}]$ for both fitting codes and model setup. Hence for the total sample, the codes agree very well. Differences are seen at the edges of the galaxy distribution in age and metallicity, which is attributable to the assumed model grid in the codes. Goddard et al. (2017b) further investigate the impact that different spectral fitting codes, stellar population synthesis models and stellar libraries can

have on the derived ages and metallicities in the context of radial gradients. They find that the systematic uncertainties introduced can be of a similar size to the signal being measured, which may help explain the variety in the age and metallicity gradients that have been obtained from various IFU studies (e.g. Gonzalez Delgado et al. 2015; Goddard et al. 2017b; Zheng et al. 2017; Li et al. 2018).

Outside of the spectral fitting code, stellar population model and stellar library used, the manner in which the average of a stellar population parameter is calculated also affects the derived stellar metallicities and ages. Using a linear average, one sums the linear quantities, e.g.

$$\langle Z_* \rangle = \sum_i w_i Z_{*,i}, \tag{2.1}$$

where w_i and $Z_{*,i}$ are the weight (e.g. light-weight or mass-weight) and stellar metallicity of SSP i, respectively. On the other hand, using a logarithmic average, one sums the logarithmic quantities, e.g.

$$\langle \log Z_* \rangle = \sum_i w_i \log Z_{*,i}. \tag{2.2}$$

The inequality of the arithmetic and geometric means implies that $\langle \log Z_* \rangle \leq \log \langle Z_* \rangle$, as the more metal-poor stellar populations are weighted more strongly when using the logarithmic average (see also the discussion in Sánchez-Blázquez et al. 2011; Gonzalez Delgado et al. 2015). As the stellar metallicities in our simple analytical model (see Section 3.3) are calculated using the linear average, we have chosen to use linearly-averaged ages and metallicities from FIREFLY in our analysis to ensure a consistent treatment of metallicity across the models and the observations. However, other works advocate using the logarithmic average (e.g. Sánchez-Blázquez et al. 2011; Gonzalez Delgado et al. 2015), because, for example, this results in values for the average that are more similar to the SSP-equivalent parameters. We note that the gap in stellar metallicity between star-forming and passive galaxies is likely to widen when using a logarithmic average, especially at the low-mass end, due to the greater prevalence of metal-poor stars in star-forming galaxies.

2.2.4 Environment measures

In order to study the dependence of stellar metallicities and stellar ages on environment, we divide the galaxy population into centrals and satellites, using the galaxy group catalogue of Yang et al. (2005, 2007). Briefly, the catalogue is constructed using an iterative Friend-of-Friends algorithm that has been calibrated on mock catalogues (Yang et al. 2005). Galaxies that are sufficiently close in projected distance and redshift are initially assigned into tentative groups. The properties of the dark matter halo (e.g. halo mass, virial radius, velocity dispersion) associated with each tentative group are determined and this information is then used to update

group memberships. The halo properties are recomputed, and this procedure is repeated until there are no further changes to the group membership. There are three different group samples that are constructed from these galaxies. We make use of Sample I, which contains 599 451 galaxies with SDSS redshifts only. In addition, for each sample, two group catalogues are constructed from the 'Petrosian' and 'Model' absolute magnitudes of the galaxies in the NYU Value-Added General Catalog (NYU-VAGC, Blanton et al. 2005), respectively. We use the 'Model' magnitudes in our analysis. We find that using the other sample and magnitude combinations has no significant effect on our results.

Having established groups and group membership, we then determine whether galaxies are centrals or satellites. Central galaxies are defined to be the most massive in their group. All other members of the group are defined to be satellite galaxies. We do not take the galaxy's spatial position in the group into account in our central–satellite classification system. Under the central–satellite definitions that we have used, isolated galaxies are always classified as centrals. Since there are a large number of groups with only a single galaxy (421 067 out of 472 504) in the Yang et al. (2007) group catalogue, a significant fraction of the central galaxies in our study are isolated centrals.

We also make use of the Yang et al. (2007) group halo masses $M_{\rm h}$. These halo masses were estimated using abundance matching applied in two different ways. First, by ranking the galaxy groups according to their total luminosity. Second, by ranking the galaxy groups according to their total stellar mass. Since stellar mass estimates are less strongly affected by recent star formation activity than luminosity, we have chosen to use the stellar-mass ranked halo masses in our analysis. We note that for some small groups (in terms of group size; and stellar mass of the central galaxy); no halo masses are assigned. We exclude these groups from our halo mass analysis. This cut preferentially removes low-mass centrals (since these tend to be in small groups) from the sample, but only has a relatively minor effect on the satellite subsample.

We also investigate how the properties of satellites are affected by their distance from the group centre, which we define to be the position of the central galaxy in the group. For each satellite galaxy, the projected distance $d_{\rm proj}$ from the central in its group is computed. This distance is then normalised by the virial radius $R_{\rm vir}$ of the group, which is given by $R_{\rm vir} = 120(M_{\rm h}/10^{11}\ M_{\odot})^{1/3}$ kpc (Dekel & Birnboim 2006). We exclude satellites that reside in groups with no assigned halo mass from our projected distance analysis, as it is not possible to determine the virial radius of the group in this case.

To further investigate the role environment plays in galaxy evolution, we study the local overdensity, which is a dimensionless density contrast given by $\delta_i = (\rho_i - \rho_{\rm m})/\rho_{\rm m}$, where δ_i is the overdensity around the $i^{\rm th}$ galaxy, ρ_i is an estimate of the local density around the $i^{\rm th}$ galaxy and $\rho_{\rm m}$ is the mean density at that redshift. We use the overdensities estimated by Peng et al.

(2010), which were computed following the methodology developed by Kovač et al. (2010). For each galaxy, the projected distance to the fifth nearest neighbour d_5 that lies within ±1000 km s^{-1} of that galaxy is determined. The local density ρ_i is then calculated by dividing the number of neighbouring galaxies (5) by the volume of a cylinder of radius d_5 and with length (in the radial direction) ±1000 km s^{-1}.

After matching the SDSS DR7 subsample discussed in Section 2.2.2 with both the Yang et al. (2007) catalogue and the overdensity dataset, our sample consists of 43 538 centrals and 16 805 satellites. For our halo mass and projected distance analysis, the sample size is further reduced to 35 440 centrals and 16 434 satellites, as groups that do not have halo masses assigned are excluded.

We show the distribution functions for all the centrals (purple) and satellites (orange) in our sample, in terms of group halo mass M_h (left panel), local overdensity $1+\delta_5$ (middle panel) and projected distance $d_\mathrm{proj}/R_\mathrm{vir}$ (only for satellites, right panel) in Fig. 2.1. The projected distances for centrals are not shown since they are, by definition, at the centres of their respective groups. We find that satellites tend to be, on average, in more massive haloes and denser regions than centrals. The same trends hold when comparing centrals and satellites in a narrow range of stellar mass (not shown). These trends come about because centrals of a given stellar mass occupy a narrow range in halo mass (see e.g. Yang et al. 2008, 2009, 2012). By our central–satellite definition, satellites with that stellar mass will have to have an even more massive central, and hence will occupy a group with a higher halo mass. Since the local overdensity tends to increase with halo mass (e.g. Woo et al. 2013), satellites will therefore also tend to be in denser regions than centrals of the same stellar mass.

2.2.5 Galaxy classification

We use the bimodality in the star formation rate–stellar mass (SFR–M_*) plane to classify galaxies as either star-forming, green valley or passive. In a similar fashion to Renzini & Peng (2015), we define the boundary of the star-forming (quenched) region in the SFR–M_* plane by the locus of points, given by a best straight-line fit, where the number of star-forming (quenched) galaxies per SFR–M_* bin has dropped below some threshold with respect to the peak value at a given mass. In this way, the SFR-M_* plane is partitioned into three regions, which correspond to star-forming, green valley and passive galaxies, respectively. The adopted boundary between star-forming and green valley galaxies is given by

$$\log \mathrm{SFR} = 0.70 \log M_* - 7.52 \tag{2.3}$$

and the adopted boundary between green valley and passive galaxies is given by

$$\log \mathrm{SFR} = 0.70 \log M_* - 8.02. \tag{2.4}$$

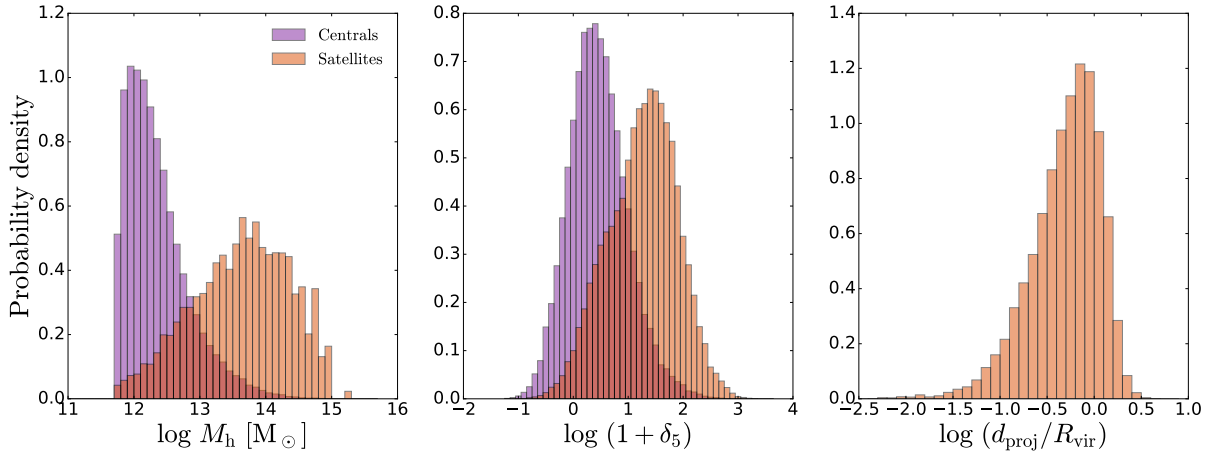

Figure 2.1. Distribution functions for all the centrals (purple) and satellites (orange) in our sample, in terms of group halo mass $M_{\rm h}$ (left panel), local overdensity δ_5 (middle panel) and projected distance $d_{\rm proj}/R_{\rm vir}$ (only for satellites, right panel). The projected distances for centrals are not shown since they are, by definition, at the centres of their respective groups.

This selection criterion is illustrated in Fig. 2.2, where we show the subsample of SDSS DR7 galaxies in the redshift range $0.02 < z < 0.085$. It should be noted that the results from our analysis do not change significantly when the slopes or intercepts of the boundaries between the star-forming, green valley and passive regions are moderately changed.

Star-forming galaxies are also required to have their BPT classification set to 'star-forming' according to the [N II]-BPT diagnostic diagram (Brinchmann et al. 2004). This excludes objects hosting an AGN, ensuring that we only analyse true star-forming galaxies in our study (as the presence of the AGN may affect the estimation of the star formation rate, through its additional contribution to the nebular line emission, and may also affect the determination of the stellar metallicity through the additional contribution to the continuum emission). This cut removes an additional 8060 star-forming galaxies (i.e. 32.8% of all star-forming galaxies) from our sample. After applying our cuts on redshift, S/N and this selection criterion, our final sample consists of 16 685 star-forming galaxies, 8445 green valley galaxies and 53 661 passive galaxies. All of these galaxies have reliable stellar masses, star formation rates, stellar metallicities and stellar ages.

Note that the relative fraction of star-forming, green valley and passive galaxies does not reflect the real relative census of these different populations of galaxies as their relative number is also convolved with our selection criteria (in particular the requirement of high S/N on the continuum, to reliably measure the stellar metallicities).

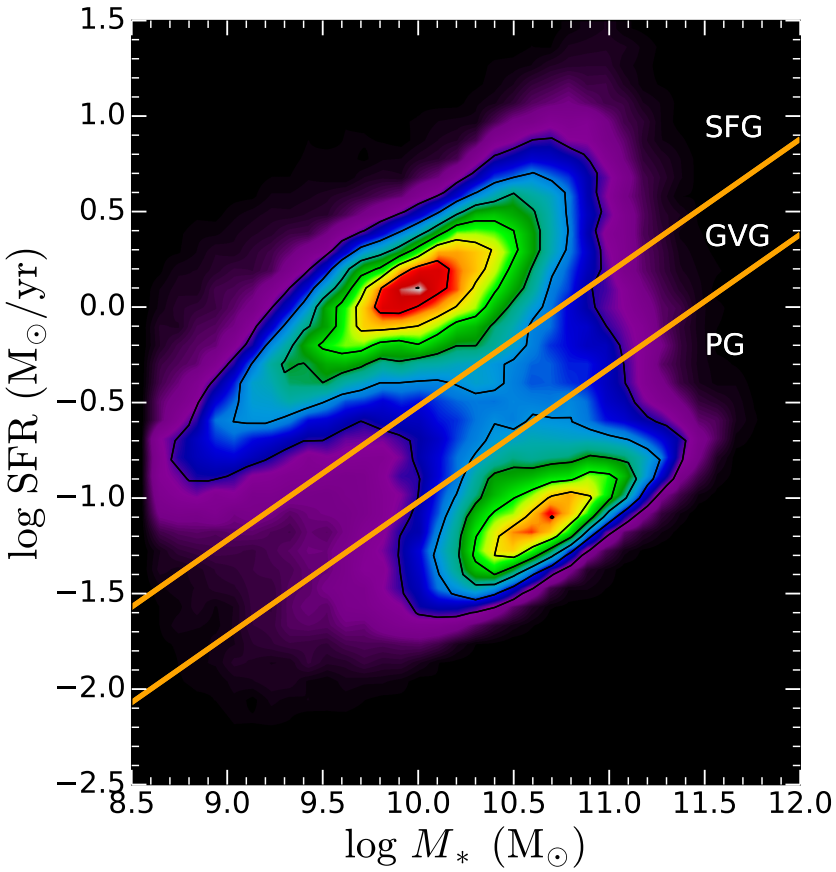

Figure 2.2. The bimodality of local galaxies in the star formation rate–stellar mass (SFR–M_*) plane. We only show the subsample of SDSS DR7 galaxies in the redshift range $0.02 < z < 0.085$. The colour shown reflects the number of galaxies in each SFR–M_* bin, ranging from low counts (purple) to high counts (red). The orange lines mark the boundaries of the star-forming, green valley and passive regions of the plane. Galaxies in the upper left are classified as star-forming (SFG), intermediate galaxies are classified as green valley (GVG), and galaxies in the lower right are classified as passive (PG).

2.3 SDSS-IV MaNGA Survey

2.3.1 Survey and sample

The SDSS-IV Mapping Nearby Galaxies at APO (MaNGA) galaxy survey is an ongoing integral field spectroscopic survey with the 2.5 m Sloan telescope, which is aiming to obtain spatially-resolved spectra for 10 000 galaxies in the local Universe (Bundy et al. 2015; Yan et al. 2016). The MaNGA survey uses 17 bundles of optical fibres to simultaneously gather spatially-resolved spectra from 17 galaxies at once, thereby enabling a large sample of spatially-resolved galaxy spectra to be taken. These hexagonally arranged fibre bundles (known as integral field units,

IFUs), come in a range of sizes (19, 37, 61, 91 and 127 fibres), chosen to match the distribution of apparent sizes of galaxies in the MaNGA galaxy survey (Drory et al. 2015).

Observations are in the optical/NIR (3600–10 000 Å), at a spectral resolution $R \sim 2000$ and are carried out using a three point dithering pattern (Law et al. 2015). This allows for complete spatial coverage of the galaxies, compensating for light lost between individual fibres (which are 2″ in diameter, with 0.5″ gaps between adjacent fibres). The spectral measurements are then combined in the Data Reduction Pipeline (DRP, Law et al. 2016; Yan et al. 2016) to form a uniform grid of interlocking square spectral pixels (each 0.5″ × 0.5″ in size, corresponding to a typical spatial sampling of ∼1–2 kpc), which will be referred to as 'spaxels'. The result is a 3-dimensional spectral datacube (x, y, λ), which provides the spectral flux as a function of both position on the sky (x, y) and wavelength λ.

The galaxies in the MaNGA galaxy survey have been selected from the SDSS Legacy Survey and follow a roughly flat distribution in log M_*, with $M_* > 10^9$ $M_\odot$ (Wake et al. 2017). 67% of the galaxies in the MaNGA survey are in the so-called Primary+ sample. These galaxies are relatively nearby ($\langle z \rangle = 0.03$) and have spatially-resolved spectral measurements out to a radial distance of 1.5 R_e. The remaining 33% of galaxies are in the so-called Secondary sample. These galaxies are relatively more distant ($\langle z \rangle = 0.045$) and thus appear smaller on the sky, with spatially-resolved spectral measurements out to a radial distance of 2.5 R_e.

We make use of the sample of MaNGA galaxies available in MaNGA Product Launch 9 (MPL-9), which is the latest data release and contains spatially-resolved spectra for 8405 galaxies. Similar to our analysis with the SDSS Legacy survey, we restrict our MaNGA analysis to galaxies with reliable spectroscopic redshifts in the range $0.02 < z < 0.085$. We further restrict our study to galaxies with reliable stellar metallicities and stellar ages. As shall be discussed in more detail in Section 2.3.3, we use the spatially-resolved spectra from the MaNGA galaxy survey to investigate both the global stellar population properties of galaxies, as well as the radial variation of these properties. We require that the median S/N per spectral pixel is higher than 20 and 10, for the global spectra and 0.5 R_e-wide annular spectra, respectively. We use a less strict cut for the annular spectra as otherwise the statistics in the relatively faint outermost (i.e. 1.5–2 R_e and 2–2.5 R_e) annuli become too small to be able to reliably investigate any radial trends. After applying these cuts on redshift and S/N for the global spectra, our sample consists of 5636 galaxies.

2.3.2 Data

We make use of the spatially-resolved MaNGA galaxy parameters provided by both the MaNGA Data Analysis Pipeline (DAP, Law et al. 2016; Belfiore et al. 2019) and the Pipe3D pipeline (Sanchez et al. 2016a,b), which were derived from fits to the spectra (more specifically, the

emission lines and stellar continuum) in the MaNGA datacubes. In particular, we use the radial distance maps (obtained from galaxy photometry) and the stellar velocity maps provided by the DAP, as well as the emission line flux/error maps and the stellar mass maps provided by Pipe3D. In addition, we use the elliptical Petrosian axis ratios b/a provided by the NASA-Sloan Atlas (NSA, Blanton et al. 2011) catalogue, that were derived from galaxy photometry.

As the galaxies in the MaNGA survey are selected from the SDSS Legacy Survey, we again make use of the MPA-JHU stellar masses and Brinchmann et al. (2004) BPT classifications.

Rather than use the Brinchmann et al. (2004) SFRs, we instead use the spatially-resolved spectra available in MaNGA to compute global SFRs by summing the SFR contributions on a spaxel-by-spaxel basis following the hybrid Hα-D4000 approach of Bluck et al. (2020). Briefly, for spaxels in which the nebular emission is primarily powered by star formation (according to the [S II]-BPT diagram in Kewley et al. 2006) and the S/N in the Hα, Hβ, [O III] and [S II] emission lines are all > 3, we compute the SFR from the Hα emission using the relation from Kennicutt & Evans (2012), assuming the cosmological parameters from the Planck 2015 data release (Planck Collaboration et al. 2016). The observed Balmer decrements are used to deredden the Hα fluxes, assuming a Calzetti et al. (2000) dust law with $R'_V = 4.05$ and an intrinsic Hα/Hβ ratio of 2.86 (Osterbrock & Ferland 2006). For spaxels where the nebular emission is not primarily powered by star formation and/or the S/N of the emission lines are not all > 3, we instead use the Bluck et al. (2020) empirical relation between sSFR and D4000 to compute sSFRs, which are then converted into SFRs using the stellar mass maps provided by Pipe3D.

2.3.3 Stellar population parameters

We derive the stellar metallicities and stellar ages of MaNGA galaxies following the same spectral fitting procedure outlined in Section 2.2.3. However, one key difference is that we first coadd the spatially-resolved MaNGA spectra before beginning the spectral fitting procedure. This coaddition is performed in two different ways. In order to investigate the global stellar population properties of galaxies, we integrate all the light in each MaNGA galaxy out to 1.5–2.5 R_e. In order to investigate the radial variation of the stellar population properties of galaxies, we instead divide each MaNGA galaxy into a series of 0.5 R_e-wide annular rings ranging from the innermost (0–0.5 R_e) to the outermost (2–2.5 R_e) regions, coadding the flux from all the spaxels in each annulus.

In each MaNGA galaxy, the spectra are coadded as follows. We identify all spaxels in the appropriate radial distance range using the radial distance maps provided by the DAP, excluding any spaxels for which the spectral data is of a poor quality. We only select spaxels for which both the median S/N in the r-band is greater than 5 and in which less than 10% of the wavelength

channels are flagged (which indicates issues with the quality of the observations) in the masks provided by the DRP. The spectra in each spaxel are then realigned to the same rest-frame velocity by using the stellar velocity maps provided by the DAP, where we further exclude any spaxels which are flagged as having unreliable stellar velocities by the DAP. The various velocity-aligned spectra are then resampled onto a common wavelength sampling using linear interpolation. Finally, the velocity-aligned spectra are coadded. In each wavelength channel, we only include the contributions from spaxels that are not flagged in that wavelength channel and we scale the coadded flux/variance to account for spaxels that have been excluded. Any wavelength channels that are flagged in more than 50% of the coadded spaxels are ignored during the spectral fitting procedure. In addition, we correct for the covariance between spaxels in the MaNGA datacubes by scaling the coadded variances by the empirical covariance correction factor described in Law et al. (2016).

2.3.4 Environment measures

Since the galaxies in the MaNGA survey are selected from the SDSS Legacy Survey, we again make use of the environment measures discussed in Section 2.2.4. After matching with the Yang et al. (2007) group catalogue, the MaNGA sample consists of 3126 centrals and 1354 satellites.

2.3.5 Galaxy classification

The distribution of MaNGA galaxies (with $0.02 < z < 0.085$) in the SFR–M_* plane is shown in Fig. 2.3. Similar to Fig. 2.2, there is a clear bimodality in the SFR–M_* plane. However, since we have used a different method to determine the global SFRs of MaNGA galaxies, the positions of galaxies in the plane have changed. The locations of the boundaries of the star-forming, green valley and passive regions of the plane have therefore also changed. The adopted boundary (determined by eye) between star-forming and green valley galaxies is now given by

$$\log \mathrm{SFR} = 0.83 \log M_* - 9.33 \tag{2.5}$$

and the adopted boundary between green valley and passive galaxies is now given by

$$\log \mathrm{SFR} = 0.83 \log M_* - 10.33. \tag{2.6}$$

Similar to Section 2.2.5, star-forming galaxies are also required to have their BPT classification set to ‘star-forming’ according to the [N II]-BPT diagnostic diagram (Brinchmann et al. 2004). This cut removes an additional 711 star-forming galaxies (i.e. 24.6% of all star-forming galaxies) from our sample.

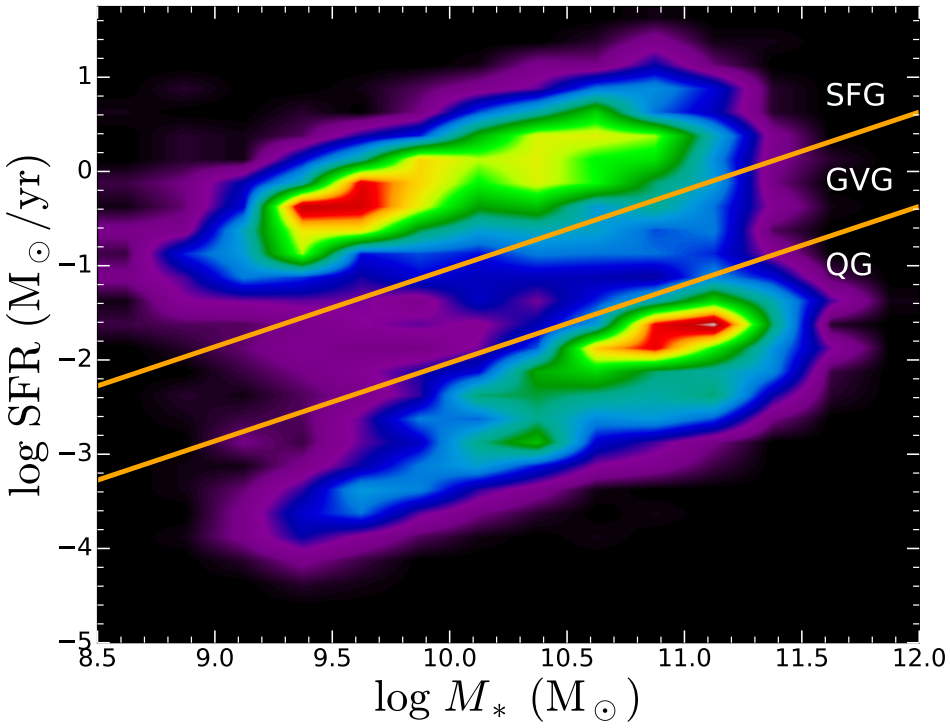

Figure 2.3. Similar to Fig. 2.2, but now showing the distribution of MaNGA galaxies (with $0.02 < z < 0.085$) in the star formation rate–stellar mass (SFR–M_*) plane. Since we have used a different method to determine the global SFRs of MaNGA galaxies, the positions of galaxies in the plane have changed. Therefore, the boundaries of the star-forming, green valley and passive regions of the plane are different to those in Fig. 2.2.

After applying our redshift cut, a cut of 20 on the median S/N of the coadded global spectra, and this selection criterion, our final MaNGA sample consists of 2182 star-forming galaxies, 615 green valley galaxies and 2128 passive galaxies.

Chapter 3

Chemical Evolution Model

3.1 Motivation and general methodology

In order to determine the role that different quenching mechanisms play in shutting down star formation, we compare the observed stellar metallicity differences between star-forming and passive (or green valley) galaxies with the predictions made by analytical models for galaxy evolution. In this chapter we discuss the models that we have developed to determine how the stellar metallicity of a galaxy changes during quenching. There are three key factors that influence our model predictions. First, our results depend on the differential equations that we solve to determine the evolution of the mass and metallicity of gas and stars in the galaxy. Second, we must estimate the cosmic epoch when the progenitors of local passive (or green valley) galaxies began quenching. Finally, we must specify the initial properties these star-forming progenitors had at the onset of quenching. We discuss the key principle behind our method, the differential equations that we use, our estimates for the onset of quenching and the initial properties of the star-forming progenitors in our models in Sections 3.2, 3.3, 3.4 and 3.5, respectively.

3.2 Unveiling the primary quenching mechanisms in galaxies

Peng et al. (2015) pioneered the idea that stellar metallicities can be used to distinguish between different quenching mechanisms. We build upon this idea in our analysis. Although already briefly mentioned in the introduction, here we discuss the basic idea behind the approach in

more detail.

Consider a typical star-forming galaxy that is evolving along the Main Sequence, with its gas reservoir in near equilibrium, where gas depletion (e.g. through star formation and galactic winds) is balanced by gas replenishment through accretion. Over time, the stellar mass of the galaxy increases as new stars are formed out of the ISM. Furthermore, both the gas-phase metallicity and the stellar metallicity increase with time, as the elements produced through stellar nucleosynthesis enrich the ISM and increase the gas metallicity, which causes successively more metal-rich stars to form out of the gas, resulting in a steady increase in the stellar metallicity. While a galaxy evolves along the star-forming main sequence, it accretes an appreciable amount of gas from the IGM to fuel its star formation and maintain its gas reservoir in a rough equilibrium. Since this accreted gas is pristine (i.e. low metallicity), the metal content within the galaxy is diluted, and so the rate of metal enrichment is slowed down, with both the gas-phase metallicity and the stellar metallicity growing less steeply (per unit stellar mass formed) than would have been the case in the absence of any gas accretion. However, star-forming galaxies do not remain on the Main Sequence indefinitely. Indeed, the star-forming progenitors of passive galaxies must have been thrown off of the Main Sequence at some epoch, at which point their gas reservoir begins to decline, star formation shuts down, and a quiescent system is ultimately produced. We imagine that this quenching process begins at some epoch $z_{\rm q}$, when the galaxy is thrown out of equilibrium and begins quenching. During this quenching phase both the stellar mass (ΔM_*) and the stellar metallicity (ΔZ_*) of the galaxy grow with time, as new metal-rich stars form out of the gas.

The amount by which the stellar metallicity is enhanced during quenching depends on the quenching mechanism.

Galaxies that quench rapidly through powerful outflows driven by AGN-feedback or ram pressure stripping quickly deplete their gas reservoirs and so only a small number of metal-enriched stars are produced during the quenching phase. In this case the stellar metallicity is only enhanced by a small amount during quenching and the stellar mass increase is negligible. Hence ΔZ_* and ΔM_* are small.

On the other hand, galaxies that deplete their gas reservoirs over long timescales and quench slowly, e.g. through starvation (in the absence of outflows), produce a significant amount of metal-enriched stars during the quenching phase. In addition to this, in the starvation scenario the supply of cold gas has halted and there is therefore no longer any dilution of the ISM by pristine gas accreted from the IGM, so the stellar metallicity grows much more steeply (per unit stellar mass formed). Moreover, if the gas is not removed by outflows or ram pressure stripping, then more gas remains available for additional star formation and, thus, for more metal production. Therefore, as a result of the combination of all these effects, galaxies that

quench through starvation undergo a significant increase in stellar metallicity during quenching, resulting in a large ΔZ_*.

Since small stellar metallicity enhancements correspond to quenching by rapid gas removal and large enhancements correspond to starvation, it is possible to distinguish between the two quenching mechanisms by measuring the amount by which the stellar metallicity is increased (ΔZ_*) during the quenching phase. Of course, we cannot make this measurement directly as it is not possible to track the evolution of the stellar metallicity of an individual galaxy across cosmic time in real data. Instead, we can measure this enhancement indirectly by statistically studying the difference in stellar metallicity between star-forming and passive galaxies. Star-forming galaxies represent galaxies prior to quenching ($t < t_q$), while passive galaxies represent galaxies after quenching has completed. Hence the stellar metallicity enhancement during quenching can be inferred from the stellar metallicity difference between star-forming and passive galaxies. By measuring this stellar metallicity difference for many galaxies, we aim to put constraints on the nature of the primary mechanism responsible for shutting down star formation in galaxies. Our work therefore focusses on the chemical enrichment and decline in star formation that takes place during the quenching phase.

As discussed in Chapter 1, there is also a strong connection between star formation activity and morphology, with star-forming galaxies typically having late-type morphologies, while passive galaxies tend to have early-type morphologies, which may indicate that galaxies often undergo a morphological transformation during quenching as well (e.g. Wuyts et al. 2011). How star formation quenching is accompanied by a morphological transformation is currently an active area of investigation. Galaxies merging, which redistributes stellar orbits, produces a burst of star formation and then generates outflows (AGN- or starburst-driven) is one of the mechanisms that is currently most commonly invoked. It has also been suggested that the morphological transformation associated with quenching is simply an observational effect, where the fading of the star-forming disc results in the bulge emerging more prominently (e.g. Carollo et al. 2016). Alternatively, it has also been proposed that morphology itself can be at the origin of the cause of quenching. More specifically, more bulge-dominated/spheroidal galaxies tend to have more massive central supermassive black holes, which can result in stronger AGN feedback (either through ejective outflows or through more significant heating of the galaxy halo), therefore resulting in a higher probability of the galaxy being quenched (Bluck et al. 2019, 2020). Despite this potentially important connection between galaxy morphology and galaxy quenching, we acknowledge that our analysis and models do not take the star-formation–morphology correlation nor morphological transformation into account.

3.3 Differential equations

We make use of the analytical framework developed in the gas regulator model of Peng & Maiolino (2014b), which does not assume any equilibrium conditions for galaxy evolution. Star formation is regulated, near equilibrium by the mass of the gas reservoir, which itself is affected by ongoing star formation, gas accretion and gas outflows. Furthermore, the ISM is enriched by metals produced through stellar nucleosynthesis, it is diluted by accretion of gas from the IGM (assumed to be near pristine) and metals are removed from the galaxy in galactic winds.

We use the instantaneous recycling approximation (IRA), which assumes that massive stars instantly die upon formation, returning some fraction of their (chemically enriched) gas to the ISM. Furthermore, this enriched material is instantaneously mixed uniformly with the gas in the ISM. On the other hand, low-mass stars are assumed to remain on the main sequence indefinitely, returning zero material to the ISM. Our model only tracks the global evolution of the stars and gas in the galaxy, and does not consider the spatial dependence of gas flows, metal enrichment or star formation. We also assume that the IMF does not change with time.

We parametrise star formation through an integrated, linear ($n = 1$) Schmidt-Kennicutt law (Schmidt 1959; Kennicutt 1998), with the star formation rate Ψ directly proportional to the gas mass g. That is,

$$\Psi = \epsilon g, \tag{3.1}$$

where ϵ is the 'star formation efficiency'. Although there is still debate on whether the Schmidt-Kennicutt relation is linear or super-linear, we assume the linear approximation in our model. We use the total gas mass for g, which includes both the atomic and molecular components. Furthermore, we use the total star formation efficiency for ϵ. We assume that ϵ remains constant during quenching. The star formation efficiency is related to the total gas depletion timescale $t_{\rm depl}$, through $\epsilon = 1/t_{\rm depl}$. The depletion timescale is defined as the time needed to convert the entire reservoir of gas in the galaxy into stars, assuming that the star formation rate remains fixed at the current value. We explore how our model predictions change when only the molecular gas component is considered in Appendix A.2.

We assume that the mass outflow rate Λ is directly proportional to the star-formation rate,

$$\Lambda = \lambda_{\rm eff}\Psi, \tag{3.2}$$

where $\lambda_{\rm eff}$ is the so-called outflow 'effective' mass-loading factor. The term 'effective' refers to the outflowing mass that effectively escapes the galaxy (i.e. permanently removed from the system) or which is reaccreted by the galaxy only on very long timescales ($\geq$ Hubble time). Outflowing gas which is reaccreted on to the galaxy on short timescales is not accounted into

the outflowing budget, as it is effectively recycled for further star formation. Therefore, galaxies with prominent outflows, and with ('classical') outflow loading factor $\lambda > 0$, may still have $\lambda_{\rm eff} = 0$ if the outflow does not escape the galaxy or the halo (as seems to be the case for many massive galaxies, Fluetsch et al. 2019).

In our subsequent analysis we will be modelling quenching purely through starvation (no inflow and no 'effective' outflows, i.e. with $\lambda_{\rm eff} = 0$), as well as quenching through a combination of starvation and outflows (i.e. no inflow and $\lambda_{\rm eff} > 0$).

Gas flows and star formation can change the amount of gas contained within a galaxy. Star formation and galactic winds deplete the gas reservoir, while gas accretion replenishes it. For a galaxy forming stars at a rate Ψ, ejecting gas at a rate Λ and accreting material at a rate Φ, the evolution of the gas mass is given by

$$\frac{{\rm d}g}{{\rm d}t} = -(1-R)\Psi - \Lambda + \Phi. \tag{3.3}$$

Here R is the return fraction, which is the fraction of the mass of newly formed stars that is quickly returned (IRA) to the ISM through stellar winds and supernovae. $1 - R$ represents the fraction of mass that is locked up in long-lived stars and stellar remnants. The value of R is determined using stellar evolution models and is given by

$$R = \frac{\int_{m_{\rm long}}^{m_{\rm up}} (m - M_{\rm R}(m))\phi(m){\rm d}m}{\int_{m_{\rm low}}^{m_{\rm up}} m\phi(m){\rm d}m}, \tag{3.4}$$

where m is the initial mass of a star that has formed out of the stellar birth cloud, $\phi(m)$ is the IMF, $M_{\rm R}(m)$ is the mass of the stellar remnant left behind by a star of initial mass m, $m_{\rm long}$ is the maximum mass of the so-called long-lived stars which do not pollute the ISM, and $m_{\rm low}$ and $m_{\rm up}$ are the lower and upper mass cutoffs of the IMF, respectively. We assume $R = 0.425$ (Vincenzo et al. 2016a) in our analysis.

Gas flows and star formation also affect the metal content of a galaxy. The metals produced by stellar nucleosynthesis enrich the ISM, while the accretion of pristine gas dilutes it and galactic winds remove metals from the galaxy. In general, the evolution of the total mass of metals in the gas-phase $gZ_{\rm g}$ is given by (Tinsley 1980)

$$\frac{{\rm d}(gZ_{\rm g})}{{\rm d}t} = y(1-R)\Psi - (1-R)Z_{\rm g}\Psi - Z_\Lambda\Lambda + Z_\Phi\Phi, \tag{3.5}$$

where $Z_{\rm g}$ is the gas-phase metallicity and Z_Λ and Z_Φ are the metallicity of the outflowing and inflowing gas, respectively. y is the net yield, representing the amount of newly-forged metals released into the ISM per unit mass locked up in long-lived stars.

Using the product rule and equation (3.3), equation (3.5) can be rearranged to give the evolution of the gas-phase metallicity, which is

$$g\frac{\mathrm{d}Z_g}{\mathrm{d}t} = (1-R)y\Psi - (Z_\Lambda - Z_g)\Lambda - (Z_g - Z_\Phi)\Phi. \tag{3.6}$$

The net yield y is determined using stellar evolution models and is given by

$$y = \frac{1}{1-R}\frac{\int_{m_{\rm long}}^{m_{\rm up}} p(m)m\phi(m)\mathrm{d}m}{\int_{m_{\rm low}}^{m_{\rm up}} m\phi(m)\mathrm{d}m}, \tag{3.7}$$

where $p(m)$, known as the stellar yield, is the fractional mass of metals produced and released into the ISM by a star of mass m. Vincenzo et al. (2016a) showed that the value of the net yield is quite sensitive to the IMF, the IMF upper mass cutoff, as well as the set of stellar yields that are adopted. We assume the $y = 0.054$ value corresponding to the Kroupa (2001) IMF, as this is the same IMF that was used to determine the observed stellar metallicities in FIREFLY. We do note that using a smaller yield value will affect our model predictions, as chemical enrichment is slower and so it will take longer to reproduce the observed stellar metallicity differences, resulting in a longer quenching timescale. We will see that models using small y values that incorporate outflows will have more difficulty reproducing the observed stellar metallicity differences. In particular, the $\lambda_{\rm eff}$ values derived by our models that simultaneously reproduce both the stellar metallicities and star formation rates of local passive (and green valley) galaxies would become smaller if a smaller y value is used.

We will make the simplifying assumption that the metallicity of the outflowing gas and the metallicity of the ISM are equal ($Z_\Lambda = Z_{\rm g}$), i.e. we assume that outflows do not preferentially remove metals from the galaxy. However, this assumption may not be completely true for low-mass galaxies, as Lian et al. (2018a,b) find that some metal-loading in the outflow (relative to the ISM metallicity) is required to simultaneously match gas-phase and stellar metallicities. Vincenzo et al. (2016b) also find that preferential ejection of oxygen (and other core-collapse SNe products) provides a better description of the observed chemical abundances and metallicities. This is also observed in a few galactic outflows (e.g. Ranalli et al. 2008). However, this differential effect is not major and our simplified analysis, which does not include this effect, is expected to provide a good description of the overall metallicity evolution, especially, obviously, for the starvation scenario (in the outflow scenario the preferential ejection of metals makes an even stronger case for explaining the observed metallicity difference between passive and star-forming galaxies in terms of starvation).

Furthermore, we will be investigating the effect that starvation (the halting of gas accretion) has on the evolution of stellar metallicities. Hence we will assume that there is no gas accretion during the quenching period and we set the inflow rate $\Phi = 0$.

Under these set of assumptions, equations (3.3) and (3.6) are simplified. The evolution of the gas mass is now given by

$$\frac{\mathrm{d}g}{\mathrm{d}t} = -(1-R)\Psi - \Lambda. \tag{3.8}$$

Furthermore, the evolution of the gas-phase metallicity is now given by

$$\frac{\mathrm{d}Z_g}{\mathrm{d}t} = (1-R)y\epsilon, \tag{3.9}$$

which continues to grow with time as stars return their metal-enriched gas to the ISM.

The stellar mass of the galaxy continuously increases due to the conversion of gas into stars. The evolution of the stellar mass s is given by

$$\frac{\mathrm{d}s}{\mathrm{d}t} = (1-R)\Psi, \tag{3.10}$$

where $(1-R)\Psi$ is the net star formation rate that contributes to the stellar mass increase of the galaxy.

Finally, the mass-weighted stellar metallicity rises with time as increasingly more metal-rich stars form out of the enriched gas. The evolution of the total mass of metals locked up in stars sZ_* is given by

$$\frac{\mathrm{d}(sZ_*)}{\mathrm{d}t} = (1-R)Z_{\mathrm{g}}\Psi, \tag{3.11}$$

where Z_* is the mass-weighted stellar metallicity. Using the product rule and equation (3.10), equation (3.11) can be rearranged to give the evolution of the mass-weighted stellar metallicity, which is

$$\frac{\mathrm{d}Z_*}{\mathrm{d}t} = \frac{\Psi}{s}(1-R)(Z_g - Z_*). \tag{3.12}$$

The stellar metallicity is a weighted average of the metallicities of all the stars in the galaxy. Since galaxies consist of a mixture of old metal-poor stars that formed early on out of pristine gas, as well as young metal-rich stars that recently formed out of more enriched gas, the mass-weighted stellar metallicity traces the cumulative chemical evolution of the galaxy. On the other hand, the gas-phase metallicity only traces the current state of chemical enrichment. As a result, the mass-weighted stellar metallicity of a galaxy tends to lag behind the gas metallicity.

Equations (3.8), (3.9), (3.10) and (3.12) can be solved using standard methods to give the temporal evolution of the gas mass, gas-phase metallicity, stellar mass and mass-weighted stellar metallicity, respectively. We have carried out this procedure and the solutions are:

$$g(t) = g_0 e^{-\frac{t}{\tau_{\mathrm{q}}}} \tag{3.13}$$

$$Z_{\mathrm{g}}(t) = Z_{\mathrm{g},0} + (1-R)y\epsilon t \tag{3.14}$$

$$s(t) = s_0 + \frac{a}{b} g_0 (1 - e^{-\frac{t}{\tau_q}}) \tag{3.15}$$

$$Z_*(t) = \frac{s_0 Z_{*,0} + \frac{a}{b} g_0 Z_{g,0} (1 - e^{-\frac{t}{\tau_q}}) + (\frac{a}{b})^2 y g_0 (1 - e^{-\frac{t}{\tau_q}} (1 + \frac{t}{\tau_q}))}{s_0 + \frac{a}{b} g_0 (1 - e^{-\frac{t}{\tau_q}})} \tag{3.16}$$

where g_0, $Z_{g,0}$, s_0 and $Z_{*,0}$ are the initial gas mass, gas-phase metallicity, stellar mass and mass-weighted stellar metallicity, respectively. τ_q is the e-folding timescale over which the gas mass (and hence also the SFR through equation (3.1)) decreases by a factor of e, and is given by

$$\tau_q = \frac{1}{\epsilon(1 - R + \lambda_{eff})}. \tag{3.17}$$

Finally, for convenience we define a and b, which are given by $a = 1 - R$ and $b = 1 - R + \lambda_{eff}$, respectively.

3.4 Estimating the onset of quenching

Prior to the onset of quenching, the star-forming progenitors of local passive galaxies probably evolved along the star-forming Main Sequence, where their gas reservoir was kept relatively fixed due to the balance between the depletion of gas driven by star formation and galactic winds and the replenishment of gas by accretion. However, these progenitors must have started quenching at some cosmic epoch in order to form the passive galaxies we see in the local Universe. In our model we assume that these progenitors began quenching through starvation at a redshift z_q, which is the epoch when the accretion of gas is halted in the starvation scenario.

We assume that z_q depends on the stellar mass M_* of the local passive galaxies. Indeed, studies such as Thomas et al. (2005, 2010) have shown how the typical star formation epoch and timescale depend on galaxy mass, finding that the more massive galaxies tended to form the bulk of their stars earlier on in cosmic history than less massive galaxies. Hence we would expect the progenitors of the most massive passive galaxies to have started quenching at higher redshift than the progenitors of low-mass passive galaxies. We use the mass-weighted stellar ages of local passive galaxies $t_0(M_*)$ that we derived in this thesis (see Figs. 4.2 and 6.2) to estimate the epoch associated with the onset of quenching z_q. We make the simplifying assumption that a negligible amount of additional stellar mass is formed during the quenching phase, i.e. that the gas mass available for additional star formation is small compared with the mass of stars already assembled. Since galaxies that quench through starvation form additional stars during the starvation phase, the lookback times to the onset of quenching that we estimate here through the mass-weighted ages are actually underestimates. We will revisit this caveat in Section 4.3.3.1. Under this simplifying assumption there is a simple relationship between the

stellar age of a local passive galaxy $t_0(M_*)$ and the stellar age of its star-forming progenitor at the onset of quenching $t(z_q, M_*)$. The difference between these two ages is just given by the (mass-dependent) lookback time $t_{lb}(M_*)$ to the onset of quenching. We have that

$$t_0(M_*) = t(z_q, M_*) + t_{lb}(M_*). \tag{3.18}$$

As discussed earlier, the star-forming progenitors of the most massive passive galaxies will have begun quenching at an earlier epoch in cosmic history, so these galaxies will have the largest lookback times. We therefore need to determine the epoch when these progenitors began quenching, $z_q(M_*)$, which is equivalent to determining the lookback time to the onset of quenching, $t_{lb}(M_*)$.

For local passive galaxies, it is reasonable to assume that the ages of their star-forming progenitors were much smaller than the lookback time to the onset of quenching, i.e. $t(z_q, M_*) \ll t_{lb}(M_*)$, as the stellar ages of the progenitors are usually < 1 Gyr (see e.g. Reddy et al. (2012); Sklias et al. (2017) for massive galaxies at $z = 1$–3, and Gallazzi et al. (2014) for low-mass galaxies at $z \sim 0.7$ if the observed relation is extrapolated down to lower masses), while the lookback times are usually ∼10 Gyr. In this case, the lookback times (and therefore z_q) are simply given by $t_0(M_*)$, the stellar ages of the local passive galaxies. That is, we set $t_{lb}(M_*) = t_0(M_*)$.

For local green valley galaxies, we have to be more careful, as these are still in the quenching phase. In this case the ages of the progenitors are comparable to the lookback times, i.e. $t(z_q, M_*) \sim t_{lb}(M_*)$. We estimate the lookback time, $t_{lb}(M_*)$, by assuming that the ages of the star-forming progenitors of the same mass, $t(z_q, M_*)$, are given by the stellar ages of local star-forming galaxies, $t_{0,SFG}(M_*)$. The lookback time to the onset of quenching is then given by the stellar age difference (that we obtained in this thesis) between local green valley galaxies and local star-forming galaxies of mass M_*, i.e. $t_{lb}(M_*) = t_{0,GVG}(M_*) - t_{0,SFG}(M_*)$.

We show the redshifts z_q when the star-forming progenitors of local passive and local green valley galaxies began quenching through starvation in our models in Fig. 3.1. Note that these redshifts were derived from our analysis of galaxies in the SDSS Legacy Survey using FIREFLY following the methodology described in Sections 2.2.3 and 4.2. The redshifts derived from our analysis of galaxies in the SDSS-IV MaNGA survey are similar, but are not shown.

3.5 Initial conditions

In order to model the change in stellar metallicity during quenching, the initial state of the star-forming progenitor at the onset of quenching has to be specified. The key initial conditions in our model are the gas mass g, the gas metallicity Z_g, the stellar metallicity Z_* and the

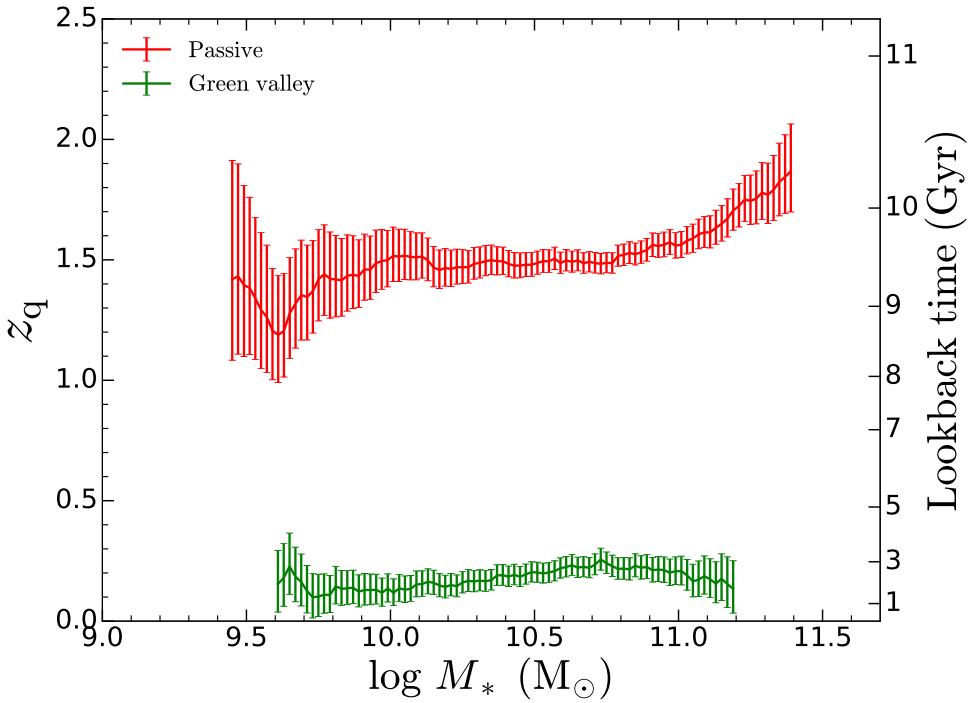

Figure 3.1. The redshift z_q when the star-forming progenitors of local passive galaxies (red) and local green valley galaxies (green) begin quenching through starvation, as a function of stellar mass, as inferred by our analysis of galaxies in the SDSS Legacy Survey. The onset of quenching for passive and green valley galaxies were estimated from the mass-weighted stellar ages of local passive galaxies, and the difference in mass-weighted stellar age between local green valley and local star-forming galaxies, respectively.

star formation efficiency ε. We use mass- and redshift-dependent scaling relations for star-forming galaxies, that span the stellar mass range $\log(M_*/\mathrm{M}_\odot) = 9.4$–$11.3$ and redshift range $0 \leq z \leq 2.0$, to determine the values for these quantities. We try, whenever possible, to use empirical scaling relations as opposed to theoretical scaling relations in our models. A summary of the initial conditions and other important quantities used in our gas regulator model is provided in Table 3.1.

In order to determine the total gas mass and star formation efficiency, we require measurements of both the molecular and atomic gas components. Tacconi et al. (2018) used a combination of CO and dust measurements to determine the molecular gas properties of star-forming galaxies over a broad range in stellar mass $\log(M_*/\mathrm{M}_\odot) = 9.0$–$11.9$ and redshift $z = 0$–4.4. We use their relations for molecular gas fractions (giving molecular gas masses) and molecular gas depletion timescales (giving molecular star formation efficiencies) in our model. Due to the intrinsic faintness of H I in emission, there are currently no atomic gas measurements for star-forming galaxies at high redshift (see e.g. Rhee et al. 2016; Cortese et al. 2017).

Table 3.1. Summary of the initial conditions and other key quantities used in the gas regulator model.

Quantity	Description	Passive galaxies	Green valley galaxies
g	Initial total gas mass (molecular + atomic)	Molecular gas mass: Tacconi et al. (2018) Atomic gas mass: Popping et al. (2014) Redshift-evolution: Tacconi et al. (2018)	Molecular gas mass: Boselli et al. (2014) Atomic gas mass: Boselli et al. (2014) Redshift-evolution: Tacconi et al. (2018)
$t_{\rm depl}$ $(=\epsilon^{-1})$	Total gas depletion time (molecular + atomic)	Molecular gas depletion time: Tacconi et al. (2018) Atomic gas depletion time: Popping et al. (2014) Redshift-evolution: Tacconi et al. (2018)	Molecular gas depletion time: Boselli et al. (2014) Atomic gas depletion time: Boselli et al. (2014) Redshift-evolution: Tacconi et al. (2018)
Z_*	Initial mass-weighted stellar metallicity	Local Z_*: $Z_{\rm MW}$ for star-forming galaxies derived in this thesis Redshift-evolution: Maiolino et al. (2008)	Local Z_*: $Z_{\rm MW}$ for star-forming galaxies derived in this thesis Redshift-evolution: Maiolino et al. (2008)
$Z_{\rm g}$	Initial gas-phase metallicity	0.25 dex larger than Z_*	0.25 dex larger than Z_*
$z_{\rm q}$	Redshift when the star-forming progenitor began quenching through starvation (i.e. when the accretion of gas is halted)	Given by the mass-weighted age of local passive galaxies derived in this thesis	Given by the mass-weighted age difference between local green valley and star-forming galaxies derived in this thesis
$t_{\rm quench}$	Duration of quenching (i.e. how long a star-forming progenitor must quench before its stellar metallicity is equal to the stellar metallicity of local passive/green valley galaxies)	Given by the time elapsed since the onset of quenching when $Z_{*,\rm model} = Z_{*,\rm passive}$ Represents the time required to complete quenching	Given by the time elapsed since the onset of quenching when $Z_{*,\rm model} = Z_{*,\rm green\ valley}$ Represents the time elapsed since the onset of quenching (since green valley galaxies have not yet completely quenched)
$\tau_{\rm q}$	e-folding time for quenching (i.e. the typical timescale over which most of the star formation and metal enrichment takes place)	Using equation (3.17), together with the $\lambda_{\rm eff}$ required to simultaneously reproduce the observed Z_* and SFR in local passive galaxies	Using equation (3.17), together with the $\lambda_{\rm eff}$ required to simultaneously reproduce the observed Z_* and SFR in local green valley galaxies

We have chosen to use theoretical relations between the molecular and atomic components of galaxies to estimate atomic gas masses and atomic gas depletion times in our model, which are supported by indirect measurements. We use the results from Popping et al. (2014), who used pressure-based H_2 formation recipes to determine the evolution of the molecular-to-atomic gas mass ratio $R_{\rm mol}$ across cosmic time, indicating that at high redshift, at least out to $z \sim 3$, most of the gas in a galaxy is in the molecular phase. These results are in agreement with HI constraints given by the (lack of) evolution of damped Ly α absorption systems (Prochaska & Wolfe 2009), indicating that the amount of H I in galaxies remains roughly constant out to $z \sim 3$, while the amount of molecular gas increases substantially (Tacconi et al. 2018). We estimate the atomic gas mass a in our model galaxies from the molecular gas mass m and $R_{\rm mol}$ by computing $a = m/R_{\rm mol}$. In a similar fashion, the atomic depletion time $t_{\rm depl,a}$ is obtained from the molecular depletion time $t_{\rm depl,m}$ through $t_{\rm depl,a} = t_{\rm depl,m}/R_{\rm mol}$.

In contrast with local passive galaxies, which are thought to have mostly begun quenching at higher redshift, local green valley galaxies are a transitionary population that have only recently begun quenching. Therefore, in our analysis that investigates the quenching of star formation in local green valley galaxies, we use the local relations (Boselli et al. 2014) for the total gas mass and total gas depletion time measured for star-forming galaxies in our models. Since our models estimate that the star-forming progenitors of these green valley galaxies began quenching between $0.15 \leq z_{\rm q} \leq 0.25$ (based on the stellar age difference between local star-forming and green valley galaxies), we evolve the local relations to this redshift range, using the redshift-dependence of the gas mass and gas depletion timescale measured by Tacconi et al. (2018).

Deep observations of galaxies have begun to probe the stellar mass–stellar metallicity relation at high redshift, such as the works by Choi et al. (2014) at $z \sim 0.4$, Gallazzi et al. (2014) at $z = 0.7$, Lonoce et al. (2015) and Onodera et al. (2015) at $z \sim 1.5$, Halliday et al. (2008) at $z = 2$, Sommariva et al. (2012) and Cullen et al. (2019) at $z = 3$ and Lian et al. (2018c). However, current studies of the stellar metallicity relation at high redshift do not yet have the broad coverage in stellar mass and redshift, nor the statistics (resulting in very large scatter or the need to use stacking) that is required by our models. In addition, and more importantly, the stellar metallicities currently measured at high redshift use the rest-frame UV stellar continuum, where opacity in the stellar atmospheres is dominated by iron. Therefore these studies mostly measure the iron abundance. In contrast, the metallicity measured in the optical in local galaxies includes absorption features from many elements and therefore provides a more comprehensive view of the stellar metallicity. Therefore, we do not use the observed stellar mass–stellar metallicity relations at high redshift to determine the initial stellar metallicities in our model. Instead, we make the assumption that the gas MZR and stellar MZR

of star-forming galaxies evolve similarly across cosmic time (Peng & Maiolino 2014b). In that case the evolution of stellar metallicity with redshift is simply given by the evolution of the gas metallicity. We have used the redshift evolution of the gas MZR measured by Maiolino et al. (2008) to evolve the local relation for the mass-weighted stellar metallicities of star-forming galaxies (that we derived in this thesis) to higher redshift, and this is shown in Figs. 4.4 and 6.3. We investigate the validity of our assumed evolution of the stellar MZR in Section 4.4.2.

Studies of gas-phase metallicities can suffer from calibration issues, where different diagnostics can yield significantly different metallicities, resulting in mass–metallicity relations with different shapes and different normalisations (e.g. Kewley & Ellison 2008; Curti et al. 2017). We wish to avoid any issues associated with metallicity calibrations in our analysis. We could in principle use the stellar metallicities from FIREFLY and the gas-phase metallicities from Maiolino et al. (2008), who estimated the evolution of the MZR as a function of redshift by using consistent calibrations within the gas-phase metallicity diagnostics. However, we would then be using two separate metallicity calibrations for gas and stars, which are likely to be inconsistent with one another. We restrict our analysis to a single calibration scheme and do not directly use the gas-phase metallicities from Maiolino et al. (2008) in our model. Instead, we use only the metallicity evolution (i.e. $\Delta \log Z_g / \Delta z$) inferred by Maiolino et al. (2008) and renormalise it locally using the stellar metallicities obtained by FIREFLY.

Observational and theoretical studies have shown that there is typically a 0.2–0.3 dex difference between the gas-phase metallicity and stellar metallicity in star-forming galaxies (e.g. Finlator & Dave 2008; Halliday et al. 2008; Yates et al. 2012; Yates & Kauffmann 2014; Peng & Maiolino 2014b; Pipino et al. 2014; Ma et al. 2016; De Rossi et al. 2017; Lian et al. 2018c). This result seems to apply across a broad range in stellar mass and in redshift. Hence we set the initial gas metallicity to be 0.25 dex larger than the initial mass-weighted stellar metallicity in our models.

For local descendants (i.e. passive or green valley galaxies) of stellar mass M_*, we make the simplifying assumption that their progenitors also had a stellar mass M_* at the onset of quenching. We investigate how the assumed stellar mass offset (which will affect the initial properties of the star-forming progenitors) between progenitors and descendants can affect our results in Section 4.4.3. The initial state $[g, \epsilon, Z_g, Z_*]$ of a star-forming progenitor of stellar mass M_* that begins quenching at z_q is then given by evaluating the scaling relations discussed above at (M_*, z_q).

Chapter 4

Both Starvation and Outflows Drive Galaxy Quenching

4.1 Introduction

In this chapter we utilise the statistical power of the SDSS Legacy Survey to investigate the role of mass in galaxy quenching. In particular, we analyse the chemical properties of 80 000 galaxies in the local Universe, comparing the observed stellar metallicities of star-forming, green valley and passive galaxies with the predictions from our chemical evolution model to assess the relative role of starvation and outflows in driving galaxy quenching. We investigate the quenching of star formation both at high-redshift and in the local Universe by analysing the stellar metallicity differences between local passive galaxies and their high-redshift star-forming progenitors, and local green valley galaxies and local star-forming galaxies, respectively.

This chapter is structured as follows. In Section 4.2 we discuss the stellar mass–stellar metallicity relations (and also the stellar mass–stellar age relations) which form the basis for all of our subsequent analysis. In Section 4.3, we compare the observed stellar metallicity differences with the predictions from our chemical evolution model to put constraints on the relative role of different quenching mechanisms, as well as the associated quenching timescale. In Section 4.4, we discuss assumptions and modelling techniques that need to be taken into account when comparing our results to the literature. Finally, in Section 4.5, we summarise our main findings and conclude.

The content in this chapter has been adapted from our published article: *Both starvation and*

outflows drive galaxy quenching, Trussler, J., Maiolino, R., Maraston, C., Peng, Y., Thomas, D., Goddard, D., Lian, J., 2020, MNRAS, 491, 5406 (Trussler et al. 2020a), where all of the work in the article was conducted by the author of this thesis, in collaboration with the listed co-authors.

4.2 Scaling relations

We apply the cuts in redshift and S/N, as well as the SFR-M_* classification criterion discussed in Section 2.2 to investigate relations between stellar mass and stellar metallicity, as well as stellar mass and stellar age, for star-forming, green valley and passive galaxies. All galaxies of a particular class (e.g. star-forming) are binned in stellar mass bins of 0.02 dex and the median stellar metallicity and stellar age in each mass bin is determined. Error bars on the median stellar metallicities and stellar ages are given by the 1σ uncertainty on the median ($1.253\sigma/\sqrt{N}$). We also apply a running average of 0.2 dex to smooth the data. These scaling relations in stellar mass–stellar metallicity and stellar mass–stellar age will form the basis for all of our subsequent analysis. The differences in stellar age between star-forming and passive (green valley) galaxies, will be used to estimate the epoch when the progenitors of local passive (green valley) galaxies began quenching. Furthermore, the differences in stellar metallicity between star-forming and passive (green valley) galaxies will enable us to put constraints on the role that different quenching mechanisms played in quenching the progenitors of local passive (green valley) galaxies.

4.2.1 Stellar metallicity

The mass-weighted stellar mass–stellar metallicity relations for star-forming (blue), green valley (green) and passive galaxies (red) are shown in the top panel of Fig. 4.1. We find that the stellar metallicity increases with stellar mass for star-forming, green valley, and passive galaxies alike. This result is qualitatively similar to what has been seen in previous studies, where the stellar metallicity tends to increase with stellar mass. For example, Gallazzi et al. (2005) studied the light-weighted stellar mass–stellar metallicity relation for the total galaxy population (i.e. without distinguishing between star-forming, green valley and passive galaxies) in SDSS DR4 and found that more massive galaxies typically have larger stellar metallicities. Peng et al. (2015) further divided the Gallazzi et al. (2005) sample into star-forming and passive galaxies, and found that the stellar metallicity tends to increase with stellar mass for both of these subpopulations. Similar to Peng et al. (2015), but using mass-weighted rather than light-weighted stellar metallicities in our study, we also find that at a given stellar mass the stellar metallicity of passive galaxies is systematically larger than that of star-forming galaxies.

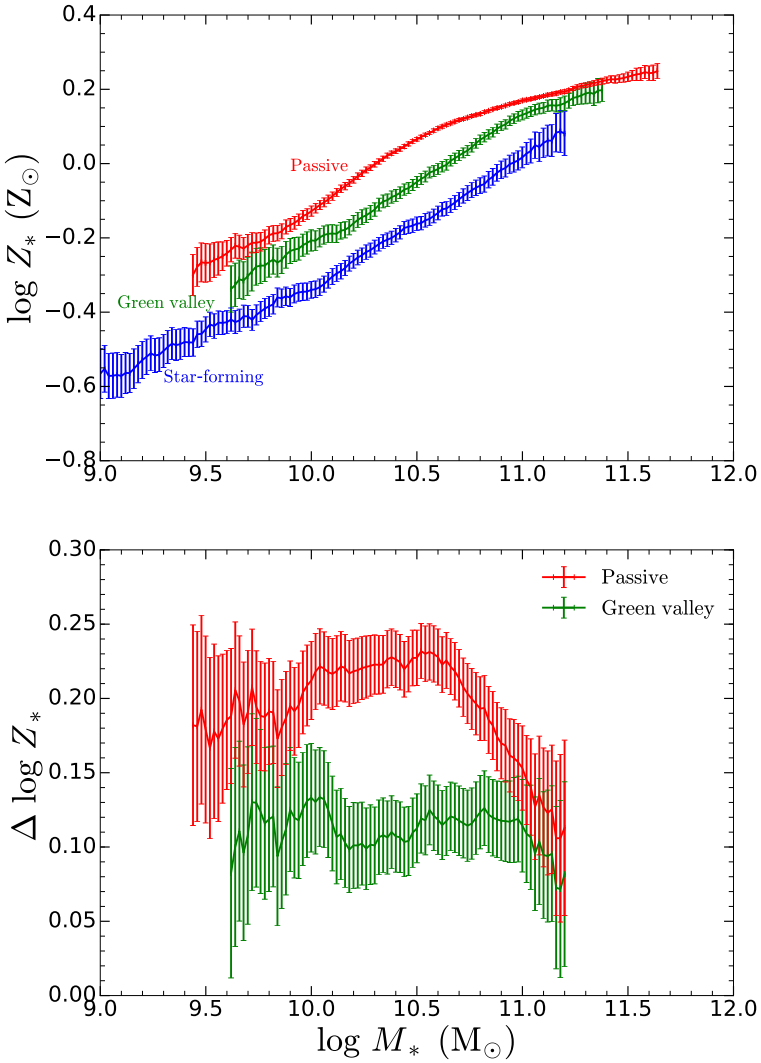

Figure 4.1. Top panel: The stellar mass–stellar metallicity relation for star-forming (blue), green valley (green) and passive (red) galaxies. Galaxies are binned in 0.02 dex stellar mass bins and the median stellar metallicity in each bin is plotted. Error bars correspond to the 1σ uncertainty on the median. Bottom panel: The observed difference in stellar metallicity between star-forming and passive galaxies (red), as well as the difference between star-forming and green valley galaxies (green). Error bars represent the 1σ error on the stellar metallicity difference.

In addition to this, we find that green valley galaxies typically have metallicities that are intermediate between those of star-forming and passive galaxies.

The difference in stellar metallicity between star-forming and passive galaxies (red), as well as the difference between star-forming and green valley galaxies (green) is shown in the bottom panel of Fig. 4.1. The stellar metallicity differences are computed by determining the logarithmic difference between the appropriate populations for each stellar mass bin. For

example, the stellar metallicity difference between star-forming and passive galaxies is given by $\log Z_{\rm PG}(M_*) - \log Z_{\rm SFG}(M_*)$. We find, similar to Peng et al. (2015), that the stellar metallicity difference between star-forming and passive galaxies decreases with increasing stellar mass. As we shall see later on, this metallicity difference is even higher if one compares the metallicity of passive galaxies with the metallicity of their star-forming progenitors at high redshift. Our results therefore suggest that galaxies typically undergo significant chemical enrichment during the quenching phase. This significant difference in stellar metallicity between star-forming and passive galaxies is qualitatively consistent with quenching through starvation, and inconsistent with quenching through simple gas removal (ejective mode). Within the starvation scenario, the decrease in stellar metallicity difference can be attributed to the smaller gas fractions present in more massive galaxies, which therefore have relatively smaller amounts of gas available to convert into metals during starvation.

In contrast to the Peng et al. (2015) study, we find that there is a non-zero difference in stellar metallicity above 10^{11} $M_\odot$ (which becomes even larger when comparing passive galaxies with their high-z star-forming progenitors). This enables us to investigate the nature of the primary quenching mechanism for massive galaxies in this study, which is something that was not possible in the original Peng et al. (2015) analysis. Furthermore, we find that, at the low-mass end, the stellar metallicity differences between star-forming and passive galaxies found in this chapter is 0.2 dex smaller than what was found in Peng et al. (2015) (who used the metallicity measurements from Gallazzi et al. 2005). We discuss the similarities and differences between the stellar metallicities and ages derived using FIREFLY and those derived by Gallazzi et al. (2005), as well as the implications this has on our results, in more detail in Section 4.4.1.

4.2.2 Stellar age

We show the mass-weighted stellar mass–stellar age relation for star-forming, green valley and passive galaxies in Fig. 4.2. The stellar ages of the different galaxy subpopulations tend to increase with increasing stellar mass. Furthermore, passive galaxies and green valley galaxies are always systematically older than star-forming galaxies of the same stellar mass. Combined, Figs. 4.1 and 4.2 indicate that green valley galaxies are intermediate between star-forming and passive galaxies in both metallicity and age. Their intermediate properties are perhaps to be expected for the simple reason that, if we assume one-way evolution (i.e. ignoring rejuvenation), green valley galaxies are currently making the transition from star-forming to passive. We note that the mass-weighted ages for star-forming and passive galaxies in our study are typically 2–4 Gyr higher than the light-weighted ages in Peng et al. (2015). We discuss this point in more detail in Section 4.4.1, but briefly remark that this is mostly due to the fact that mass-weighted ages tend to be larger than light-weighted ages, but we also acknowledge that the different

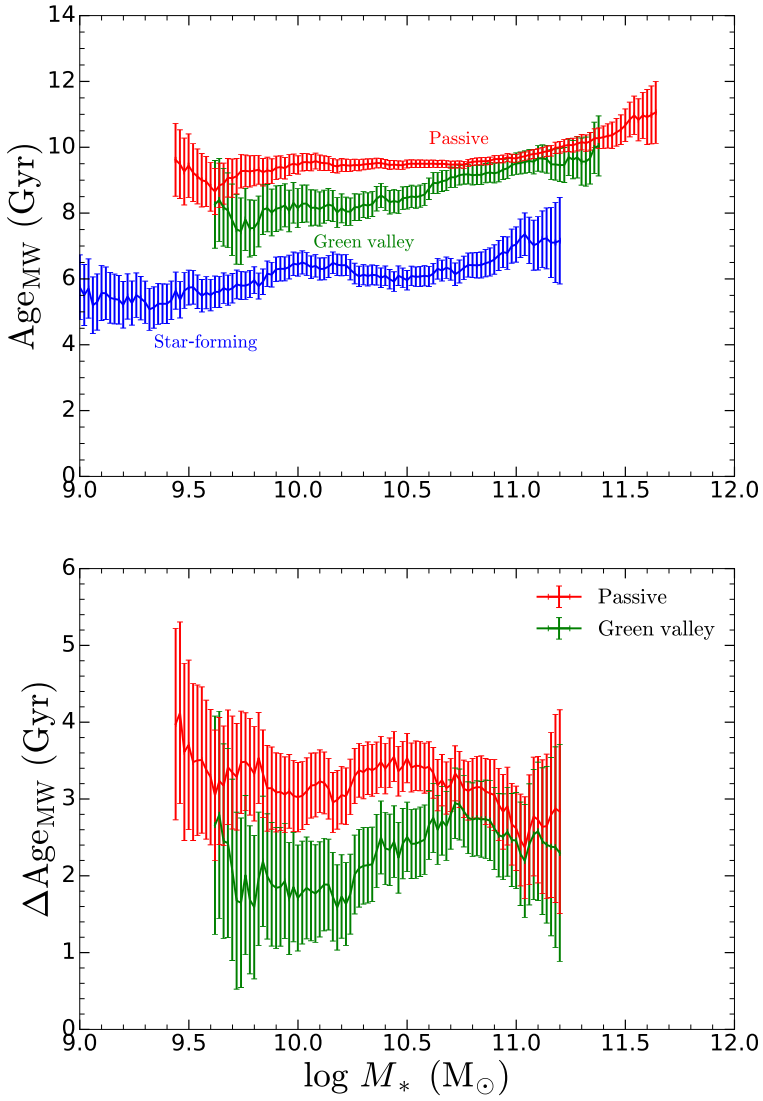

Figure 4.2. Top panel: The stellar mass–stellar age relation for star-forming (blue), green valley (green) and passive (red) galaxies. Bottom panel: The observed difference in stellar age between star-forming and passive galaxies (red), as well as the difference between star-forming and green valley galaxies (green).

modelling and fitting techniques adopted in the two works likely also play a role.

Fig. 4.2 also shows the stellar age difference Δt between star-forming and passive galaxies, as well as the age difference between star-forming and green valley galaxies. We find that the star-forming–passive age difference is typically between 2.5–4 Gyr and seems to be roughly constant within the error bars, with perhaps a weakly declining trend with increasing stellar mass. This is different to the roughly mass-independent ~4 Gyr that was found in Peng et al. (2015), perhaps due to the reasons mentioned earlier. The star-forming–green valley age difference is smaller, typically between 1.5–3 Gyr, with perhaps a weakly increasing trend with

increasing stellar mass.

4.3 Quenching mechanisms

In this section we compare the observed differences in stellar metallicity between star-forming and passive (or green valley) galaxies with the predictions from gas regulator models to put constraints on the relative role of different quenching mechanisms. We will investigate closed-box models, where galaxies quench purely through starvation and with no outflows ($\lambda_{\rm eff} = 0$), but will also consider leaky-box models, where galaxies quench through a combination of starvation and outflows ($\lambda_{\rm eff} > 0$). This will allow us to study how the relative role of different quenching mechanisms, as well as the associated quenching timescale depends on stellar mass. On the one hand, we will study how the star-forming progenitors of local passive galaxies quenched, providing insights into the processes responsible for shutting down star formation at high redshift ($z \sim 1$–2). On the other hand, we will also address the quenching of star formation in the local Universe, by studying local green valley galaxies that are currently in the process of quenching. Combined, these two studies enable us to probe the evolution of galaxy quenching across cosmic time.

4.3.1 Evolution of SFR and Z_* during the quenching phase

In this subsection, we briefly introduce and highlight the differences between the closed-box and leaky-box models that will be explored in the remainder of this section.

We will consider two different leaky-box models. In Sections 4.3.2.2 and 4.3.3.2, we assume that $\lambda_{\rm eff} = 1$ for galaxies of all stellar masses. In Section 4.3.2.3 (Section 4.3.3.3), we instead find the values of $\lambda_{\rm eff}$ for which our model simultaneously reproduces the Z_* and SFR seen in passive (green valley) galaxies.

We schematically show the evolution of the star formation rate and the evolution of the logarithmic stellar metallicity during the quenching phase in our models in Fig. 4.3. The main aspects of these two quenching models are summarised in the following. Prior to the onset of quenching, the galaxy evolves along the star-forming main sequence, where its gas reservoir is in quasistatic equilibrium, so the star formation rate increases slowly, and the stellar metallicity increase is modest due to dilution by accretion of pristine gas. At a time $t(z_{\rm q})$, the accretion of cold gas is halted and the galaxy begins quenching through starvation. The blue curve shows the evolution in the case of pure starvation ($\lambda_{\rm eff} = 0$) that we will explore in Section 4.3.2.1, while the red curve shows the evolution in the case of starvation with outflows ($\lambda_{\rm eff} > 0$) which we will explore in Sections 4.3.2.2 and 4.3.2.3. In the absence of gas accretion, the star formation

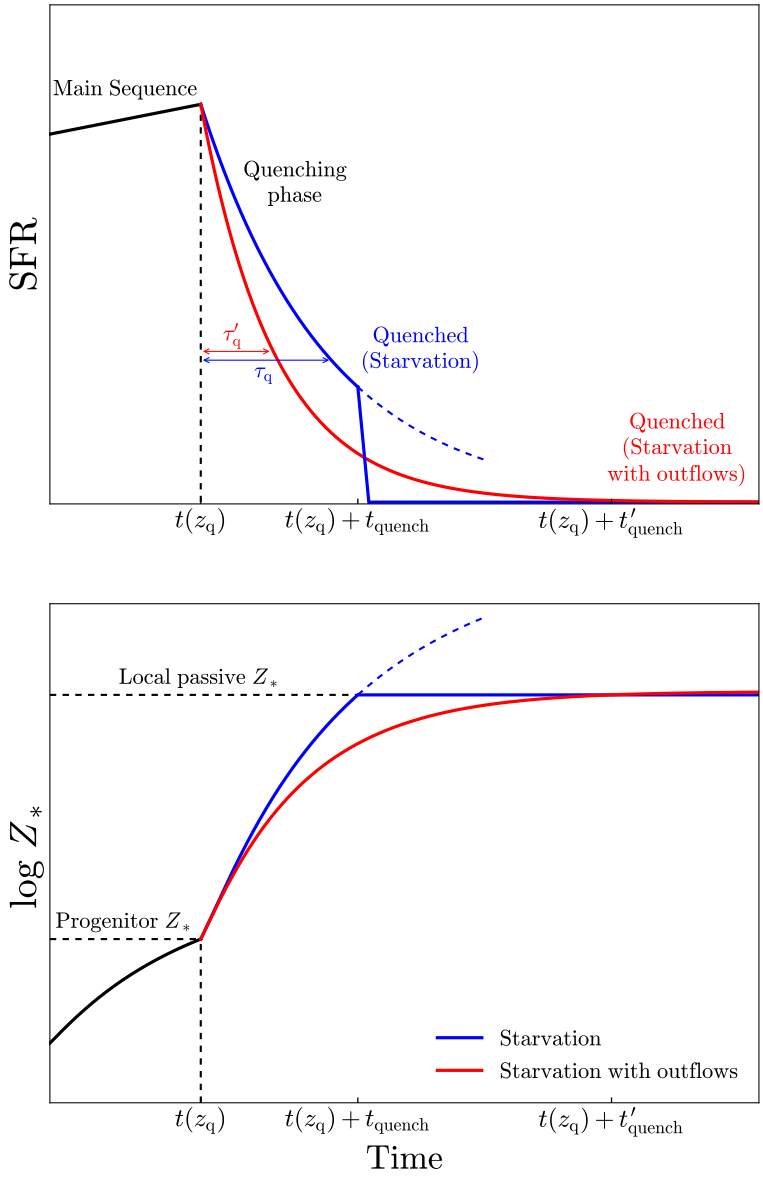

Figure 4.3. A schematic illustration of the evolution of the star formation rate (SFR, top panel) and the evolution of the logarithmic stellar metallicity (log Z_*, bottom panel) during the quenching phase in our models. The galaxy initially evolves along the star-forming main sequence. At a time $t(z_q)$, the accretion of cold gas is halted and the galaxy begins quenching through starvation ($\lambda_{eff} = 0$, blue) or through starvation with outflows ($\lambda_{eff} > 0$, red). In the starvation scenario, the galaxy quenches for a timescale t_{quench} before it reaches the level of chemical enrichment seen in local passive galaxies, at which point the onset of an ejective or heating mode prevents any further star formation and chemical enrichment, and the galaxy is quenched. In the starvation with outflows scenario, after a time t'_{quench} has elapsed the galaxy has completed quenching, and, for our analysis in Section 4.3.2.3, both its stellar metallicity and star formation rate are similar to that seen in local passive galaxies. τ_q and τ'_q represent the e-folding timescales in the starvation, and starvation with outflows scenarios, respectively.

rate declines exponentially according to

$$\Psi(t) = \Psi_0 e^{-\frac{t}{\tau_q}}, \tag{4.1}$$

as gas is converted into stars and removed in galactic winds. Therefore, τ_q represents the e-folding timescale over which the star formation rate decreases by a factor of e, and is given by

$$\tau_q = \frac{1}{\epsilon(1 - R + \lambda_{\rm eff})}. \tag{4.2}$$

The e-folding timescale for the model incorporating outflows τ_q' is shorter than for the model including only starvation τ_q, as the additional gas that is lost through galactic winds causes the star formation rate to decline more quickly. In the pure starvation scenario, the galaxy quenches for a timescale $t_{\rm quench}$ before it has a stellar metallicity that matches the stellar metallicity observed for a local passive galaxy of the same stellar mass. However, as we shall see in Section 4.3.2.1, these galaxies still harbour a relatively large gas reservoir, and so continued star formation beyond $t = t(z_q) + t_{\rm quench}$ in our model would result in a galaxy that is too metal-rich (as shown by the dashed blue curves). In order to prevent further star formation and chemical enrichment, an ejective or heating mode is required, which completely quenches the galaxy, reducing the star formation rate to zero and keeping the stellar metallicity constant at a fixed value. In the starvation with outflows scenario, the quenching phase has a duration $t'_{\rm quench}$, at which point, for the model explored in Section 4.3.2.3, both the stellar metallicity and the star formation rate of the galaxy are similar to those seen in local passive galaxies of the same stellar mass.

4.3.2 Passive galaxies (quenching at high-z)

We begin by investigating the processes responsible for quenching the star-forming progenitors of local passive galaxies. Since these passive systems stopped forming stars early on in cosmic history, our analysis in this subsection addresses the quenching of star formation at high redshift. We focus on reproducing the observed stellar metallicity differences ΔZ_* between star-forming and passive galaxies with our models. The observed ΔZ_* that we will use in the subsequent analysis corresponds to the stellar metallicity difference between local passive galaxies and their star-forming progenitors at high redshift, rather than the observed ΔZ_* between local passive galaxies and local star-forming galaxies. It should be noted that our approach is different to what was done in Peng et al. (2015), who instead analysed the observed ΔZ_* between local passive galaxies and local star-forming galaxies. As was discussed in Section 3.5, the stellar metallicities of the star-forming progenitors are estimated by evolving the stellar metallicities of local star-forming galaxies to higher redshift using the cosmic evolution of the mass-metallicity

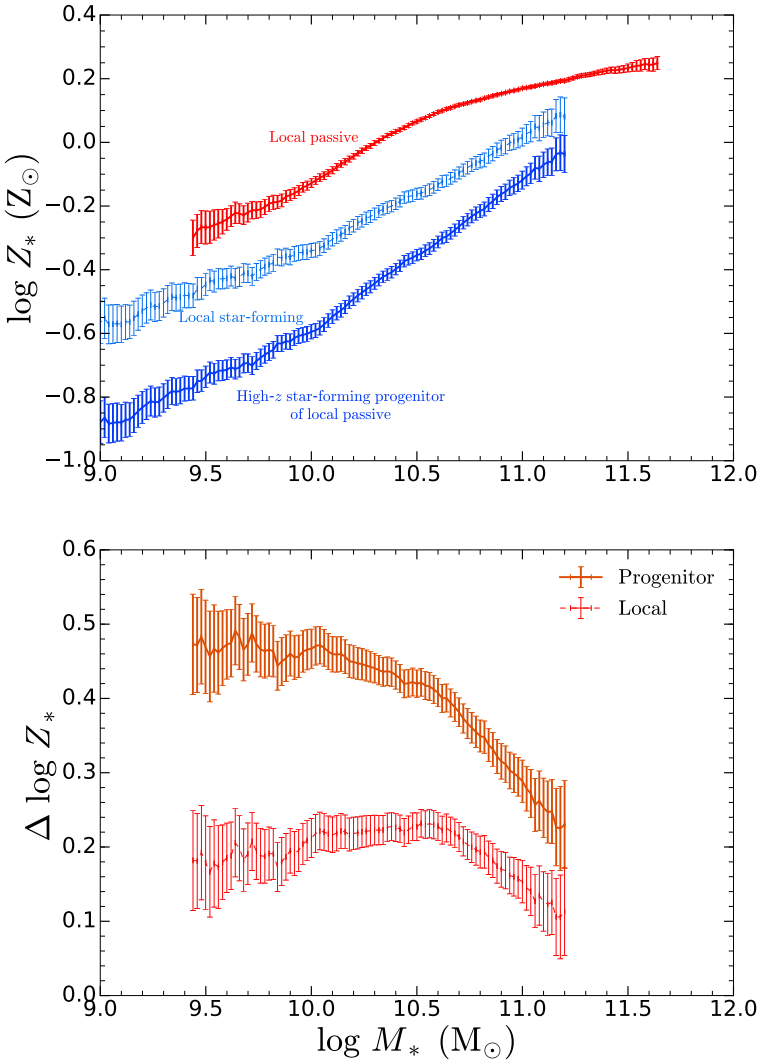

Figure 4.4. Top panel: The stellar mass–stellar metallicity relation observed for local passive galaxies (red) and local star-forming galaxies (light blue), as well as our estimates for the stellar metallicities for the star-forming progenitors of local passive galaxies (dark blue). Bottom panel: The observed difference in stellar metallicity between local star-forming and local passive galaxies (red) and the estimated difference in stellar metallicity between local passive galaxies and their star-forming progenitors at higher redshift (orange).

relation described by Maiolino et al. (2008). The observed stellar metallicities of local passive galaxies and our estimates for the stellar metallicities of their star-forming progenitors are shown in Fig. 4.4. Since star-forming galaxies at higher redshift are less metal-rich than their local counterparts, the observed stellar metallicity differences between local passive galaxies and their progenitors that are studied in this section are even larger than the metallicity differences between local passive and local star-forming galaxies seen in Fig. 4.1.

4.3.2.1 Pure starvation

We first consider closed-box models for galaxy evolution, where galaxies quench purely through starvation and no outflows are included ($\lambda_{\rm eff} = 0$). A comparison between the observed and model-predicted stellar metallicity differences is shown in the top panel of Fig. 4.5. The horizontal axis refers to the initial stellar mass M_* of the star-forming progenitor. The observed stellar metallicity difference between star-forming and passive galaxies of the same stellar mass is given by the dashed black curve. If galaxies formed a negligible amount of additional stellar mass ΔM_* during the quenching phase (i.e. if galaxies followed a ∼vertical trajectory in the top panel of Fig. 4.4), then this would be the amount of chemical enrichment that takes place during the quenching phase. However, star-forming galaxies at high-redshift are gas rich, and, if they quench through starvation, can convert a considerable portion of this gas into new stars, resulting in a non-negligible increase in stellar mass during quenching (i.e. galaxies actually follow a diagonal trajectory in Fig. 4.4). Hence the actual increase in stellar metallicity during the quenching phase is larger than in the $\Delta M_* = 0$ case, since the stellar metallicity of passive galaxies increases with increasing stellar mass. In our models, the quenching phase ends when the metallicity of the model galaxy $Z_{*,\rm model}$ with stellar mass $M_* + \Delta M_*$ is the same as that of a local passive galaxy with that same mass, i.e. when $Z_{*,\rm model}(M_*+\Delta M_*) = Z_{*,\rm PG}(M_*+\Delta M_*)$. The black solid curve shows the difference in stellar metallicity between star-forming progenitors and their local passive descendants, after taking the increase in stellar mass that occurs during the quenching phase into account.

Fig. 4.5 also shows the model-predicted stellar metallicity enhancements at various times Δt after the onset of quenching, given by the coloured curves. The stellar metallicity enhancements grow with time as successively more metal-rich stars form out of the ISM, which increases the average mass-weighted stellar metallicity of the galaxy. Our models predict that the rate of stellar metallicity enrichment ($\Delta \log Z_*/\Delta t$) decreases with increasing mass, where the change in stellar metallicity in a given time step is smallest for the most massive galaxies. This is primarily because gas fractions decrease with increasing stellar mass, so the most massive galaxies have the smallest gas fractions. As a result, these massive galaxies form relatively fewer new stars compared to the population of stars already present, and so their stellar metallicity increases more slowly.

From Fig. 4.5, we see that closed-box models are easily able to reproduce the observed stellar metallicity differences represented by the solid black curve. The models typically take about 2–3 Gyr to reach the level of chemical enrichment seen in local passive galaxies (following a diagonal trajectory in Fig. 4.4), which suggests that the progenitors of local passive galaxies up to $M_* \sim 10^{11.2}$ $\rm M_\odot$ that quenched purely through starvation did so over a 2–3 Gyr timescale.

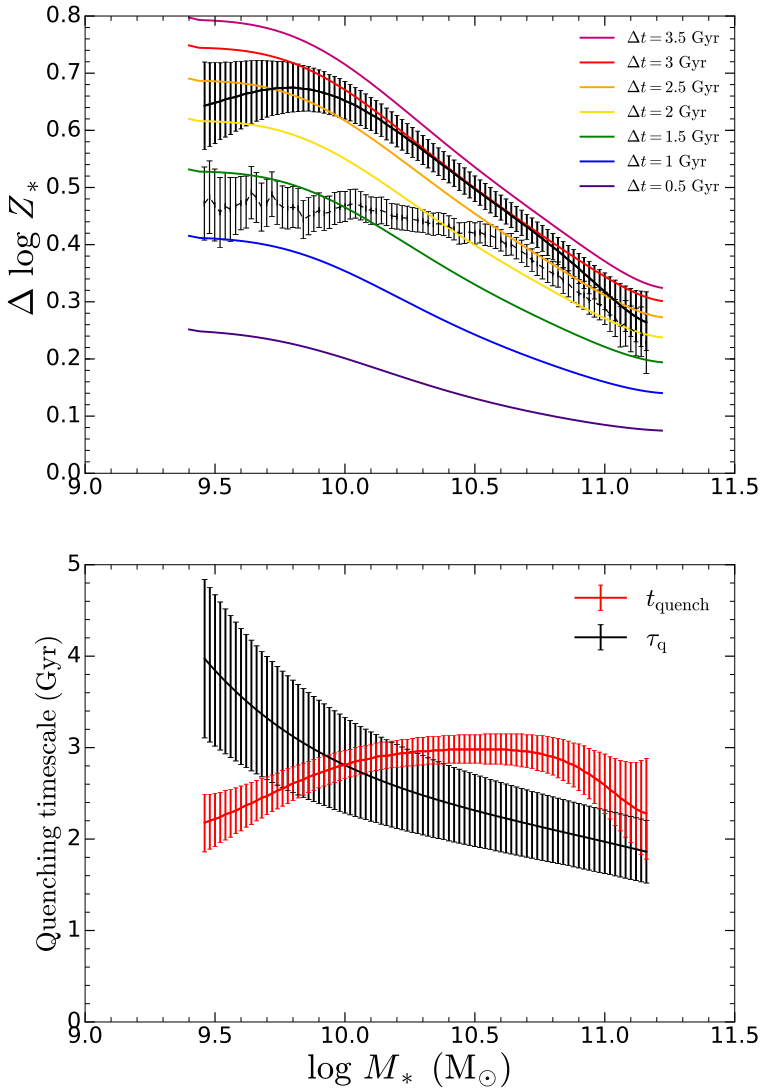

Figure 4.5. Top panel: The dashed black curve shows the observed stellar metallicity difference between local passive galaxies and their star-forming progenitors of the same stellar mass. The solid black curve shows the actual increase in stellar metallicity during the quenching phase (taking into account the increase in stellar mass of the galaxy during quenching). The coloured lines show the stellar metallicity difference predicted by a closed-box model ($\lambda_{\rm eff} = 0$) at different times after the onset of starvation. The horizontal axis refers to the initial stellar mass of the star-forming progenitor. Bottom panel: The quenching timescales $t_{\rm quench}$ derived from the stellar metallicity difference between star-forming and passive galaxies are shown in red, where the error bars take into account the 1σ errors on the stellar metallicity differences. The e-folding timescales for star-formation $\tau_{\rm q}$ during quenching are shown in black, where the error bars are due to the uncertainties on the depletion times from Tacconi et al. (2018).

We study this mass-dependence of the duration of quenching in more detail in the bottom panel of Fig. 4.5. We define the duration of quenching $t_{\rm quench}$ as the timescale over which a galaxy quenching through starvation enriches in stellar metallicity by an amount equal to the observed stellar metallicity difference between star-forming and passive galaxies, after accounting for the increase in stellar mass during quenching. In other words, $t_{\rm quench}$ is the time when our model-predicted enrichment equals the observed stellar metallicity difference. We find that the duration of quenching (shown in red) is between 2–3 Gyr, growing for $\log(M_*/{\rm M}_\odot) < 10.5$ and then declining. The error bars on $t_{\rm quench}$ reflect the 1σ error on the stellar metallicity differences. We also show (in black) the e-folding timescale for star-formation $\tau_{\rm q}$, which decreases with increasing mass due to the increase of total star formation efficiency ϵ with mass in our models (which also matches observations, e.g. Boselli et al. 2014). The error bars are due to the uncertainties on the depletion times from Tacconi et al. (2018).

Thomas et al. (2010) measured the α-enhancements in local early-type galaxies and used this information to put constraints on the typical timescale over which the progenitors of these local passive galaxies formed the bulk of their stars. They find that the progenitors of more massive galaxies formed most of their stars at earlier epochs and over shorter timescales than their less massive counterparts, which is qualitatively consistent with the trend shown by $\tau_{\rm q}$. However, at the low-mass end, we find that quenching ends even before one e-folding timescale has elapsed, which is rather inconsistent with the continuously declining star formation histories in Thomas et al. (2010). Furthermore, the 2 Gyr timescale is substantially shorter than the star formation timescales in Thomas et al. (2010). These results potentially suggest that the progenitors of low-mass passive galaxies did not quench purely through starvation. We explore alternative scenarios, where galaxies quench through a combination of starvation and outflows later in this section.

We note that the quenching timescales $t_{\rm quench}$ of 2–3 Gyr that we obtain are smaller than the 4 Gyr that was found by Peng et al. (2015). There are a number of reasons for this. On the observational side, we use a different set of stellar metallicities to the original work. We explore this point in more detail in Section 4.4. On the modelling side, we utilise different scaling relations to specify the initial conditions of the star-forming progenitors in our model, as well as an alternative method to estimate the cosmic epoch when these progenitors begin quenching. In addition, we also distinguish between quenching timescale $t_{\rm quench}$ and epoch of the quenching onset $z_{\rm q}$. In our model, the quenching timescale refers to the duration of quenching i.e. our findings suggest that galaxies quench purely through starvation for 2–3 Gyr, at which point quenching has completed. On the other hand, in Peng et al. (2015), the quenching timescale refers to the amount of time that has elapsed since the onset of quenching through starvation, i.e. their results suggest that we are typically seeing passive galaxies 4 Gyr after the

onset of quenching through starvation.

Peng et al. (2015) also compared their timescale of 4 Gyr from the stellar metallicity analysis with the difference in stellar age Δage between star-forming and passive galaxies. If one assumes that a negligible amount of stars are formed (i.e. passive evolution) during the starvation phase, then this stellar age difference represents the time elapsed since the onset of quenching (which is exactly what $t_{\rm quench}$ measures in the Peng et al. (2015) model). They find this age difference to be mass-independent at ∼4 Gyr, which is consistent with the timescale that was obtained from the stellar metallicity difference analysis. We do not make this comparison between $t_{\rm quench}$ and Δage for passive galaxies in our work. This is because our $t_{\rm quench}$ measures the timescale required to complete quenching, whereas Δage measures the time elapsed since the onset of quenching, so these two quantities trace different timescales and are therefore not comparable. To clarify, after a galaxy completes quenching (i.e. it becomes passive), $t_{\rm quench}$ remains fixed, but its Δage continues to increase indefinitely as more time elapses, and so these two quantities begin to diverge. We note that we will make a comparison between $t_{\rm quench}$ and Δage for green valley galaxies in Section 4.3.3. Unlike passive galaxies, green valley galaxies are still in the process of quenching and so $t_{\rm quench}$ actually measures the time since the onset of quenching (rather than the time to complete quenching), so a meaningful comparison between $t_{\rm quench}$ and Δage can be made.

Our closed-box model suggests that the progenitors of local passive galaxies quenched through starvation for 2–3 Gyr, as that is the time required to reproduce the observed stellar metallicity differences. However, we can see from Fig. 4.5 that the model-predicted curves can exceed the observed stellar metallicity differences, as they continue to grow even after 2 Gyr of quenching through starvation has elapsed. There is clearly still a substantial increase in the stellar metallicity enhancement ΔZ_* during the subsequent timesteps Δt after the observed stellar metallicity difference has been reached. If these galaxies were actually quenched, then there should only be a residual amount of chemical enrichment after 2–3 Gyr as all the gas has been exhausted, and there is only a marginal amount of star formation remaining. Evidently, the 'quenched' galaxies in our closed-box model still have a relatively large gas reservoir and are still forming a considerable number of stars. This point is made clearer when comparing the duration of quenching $t_{\rm quench}$ with the e-folding timescale $\tau_{\rm q}$. At most, only ∼1 e-folding timescale has elapsed, with roughly $e^{-0.5} \approx 60\%$ and $e^{-1} \approx 37\%$ of the initial gas reservoir still present for galaxies of $\log(M_*/{\rm M}_\odot) = 9.5$ and 11.0, respectively. The properties of the 'quenched' galaxies in our models are therefore in stark contrast with the observed properties of local passive galaxies, which have small gas reservoirs and are not actively forming stars. Furthermore, since the 'quenched' galaxies in our model continue to form stars and become progressively more enriched, their stellar metallicities begin to exceed the stellar metallicities

seen in local passive galaxies, as shown by the top panel in Fig. 4.5.

In order to prevent this prolonged chemical enrichment in our closed-box model, an additional mechanism must kick in, when the observed stellar metallicity difference has been reached (~2–3 Gyr), which abruptly stops any further star formation and enrichment. This mechanism could be some form of an ejective mode or heating mode that starts to play a role near the end of the starvation phase, to prevent further chemical enrichment from taking place. There are a number of mechanisms that could eject the remaining gas in the galaxy at the end of the starvation phase. For example, an AGN that is being activated could clear or heat the gas (e.g. Ciotti & Ostriker 2007; Ciotti et al. 2009). Satellite galaxies plunging through the hot ICM could rapidly lose their gas through ram pressure stripping, and this may happen only when the galaxy enters deep into the cluster (Muzzin et al. 2014). However, it should be noted that our sample of SDSS galaxies consists mostly of centrals, see Yang et al. (2007). Alternatively, the integrated feedback from many Type Ia supernovae could eject or heat the remaining gas (Pipino & Matteucci 2004; Matteucci et al. 2006; Pipino & Matteucci 2006; Pipino et al. 2008). Since supernovae are more effective at driving away material in low density conditions, this mechanism is especially effective at ejecting gas at the end of the starvation phase, when the gas content has diminished and the densities have fallen. Moreover, Type Ia SNe have a well defined timescale (~1–2 Gyr) before they start contributing significantly to the energy injection into the ISM, which would explain well why the additional ejective/heating mode kicks in only around 2.5 Gyr after the last episode of major star formation, i.e. after the onset of quenching.

To summarise, using a closed-box model we find that the progenitors of local passive galaxies quenched purely through starvation over a timescale of 2–3 Gyr, and then additional star formation and additional chemical enrichment was abruptly halted by the onset of an ejective or heating mode. However, as an alternative, our results may also suggest that the progenitors of local passive galaxies did not quench purely through starvation. Indeed, other models, such as a combination of starvation and outflows during the quenching, may potentially provide a better description of the quenching process as discussed in the following sections.

4.3.2.2 Starvation with outflows

We now study leaky-box models for galaxy evolution, where galaxies quench through a combination of starvation and outflows. In this section we assume the outflow mass loading factor of one classically assumed by many models, i.e. $\lambda_{\rm eff} = 1$. Our results are shown in Fig. 4.6. The main effect of introducing outflows in our model is that the gas reservoir depletes faster than in the closed-box case, as now both star formation and galactic winds drain the gas content. This has two main consequences for our model predictions. Firstly, since the gas reservoir depletes more rapidly, the star formation rate also declines faster and less stars are formed within a

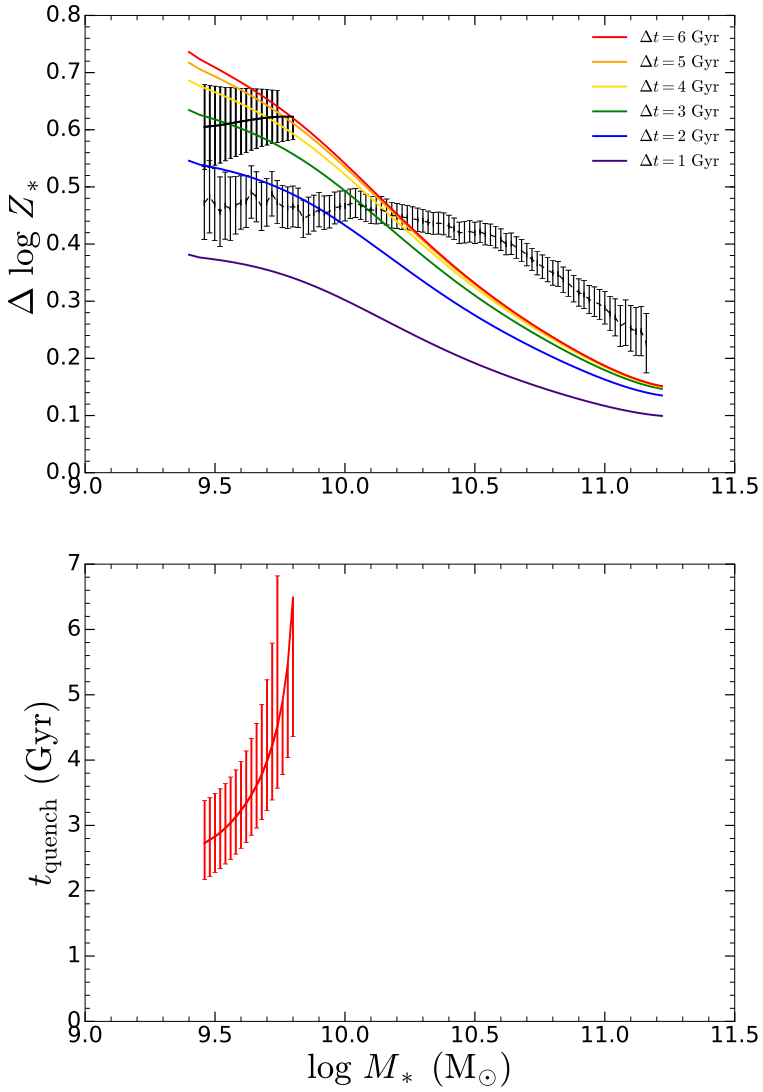

Figure 4.6. Similar to Fig. 4.5, but we now consider a leaky-box model, incorporating outflows with $\lambda_{\rm eff} = 1$. Also note that the timesteps in our model are now 1 Gyr (instead of the 0.5 Gyr used in Fig. 4.5). We omit the upper limit on the increase in stellar metallicity during quenching ΔZ_* (given by the solid black curve) when it cannot be reproduced by our model, and in that case we only show the lower limit on the duration of quenching $t_{\rm quench}$.

given time interval. As a result, the stellar metallicity increases more slowly in the leaky-box model. Hence any quenching timescales we derive in our analysis (i.e. the time derived to match ΔZ_*) will be longer than in the closed-box model. Secondly, only a fraction of the initial gas reservoir is now converted into new, metal-rich stars. The rest of the gas is expelled, so the amount of material that is actually available to increase the stellar metallicity of the galaxy has been reduced. As a result, the maximum stellar metallicity increase of the galaxy, which

occurs when the gas reservoir is completely depleted, is lower in the leaky-box models. Hence it may become more difficult for our model to reproduce the stellar metallicity differences that have been observed.

We find that models incorporating outflows are also capable of reproducing the observed stellar metallicity differences seen in low-mass galaxies, with $\log(M_*/\mathrm{M}_\odot) < 9.8$. These low-mass systems have sufficiently large gas fractions so that the observed stellar metallicity enhancement can be achieved, even if a substantial amount of gas is removed by outflows. Due to the reduced rate of chemical enrichment caused by the removal of gas, the typical quenching timescales are longer than those found with the closed-box model. In the specific case of $\lambda_{\mathrm{eff}} = 1$, the bottom panel of Fig. 4.6 shows that the duration of quenching is 3–6 Gyr for galaxies with $\log(M_*/\mathrm{M}_\odot) < 9.8$. Since both closed-box models (pure starvation) and leaky-box models (starvation with outflows) are consistent with the observations, we conclude that outflows could have potentially played an important role in shutting down the star formation in the progenitors of low-mass passive galaxies. Lian et al. (2018a,b) also find that outflows could potentially be more important in driving evolution in low-mass galaxies, as they show that either strong, time-dependent outflows with large metal-loading factors, or a time-varying IMF must be invoked to simultaneously reproduce both the gas MZR and the stellar MZR in local low-mass star-forming galaxies.

On the other hand, the predictions from our leaky-box model are inconsistent with the stellar metallicity differences observed in high-mass galaxies with $\log(M_*/\mathrm{M}_\odot) > 9.8$. Outflows with $\lambda_{\mathrm{eff}} = 1$ remove too much gas in these massive systems, preventing sufficient chemical enrichment during quenching. Our findings suggest that powerful outflows played a minor role in quenching the progenitors of high-mass passive galaxies. These massive galaxies either quenched purely through starvation for 2–3 Gyr before any future star formation was abruptly halted by the onset of an ejective or heating mode, or through a combination of starvation and weak outflows, with $\lambda_{\mathrm{eff}} < 1$. Note that this does not mean that outflows are not present in massive galaxies, but that most of the outflowing gas does not escape and is being recycled (i.e. the 'classical' loading factor can be $\lambda \sim 1$ even if $\lambda_{\mathrm{eff}} < 1$).

4.3.2.3 Constraints on λ_{eff} from observed Z_* and SFR

Until now, we have only been using the observed stellar metallicity differences to put constraints on the nature of quenching. We have investigated whether given models can reproduce the observed stellar metallicity enhancement and we have determined the timescale required to achieve this. So far we have only been considering models consisting of pure starvation ($\lambda_{\mathrm{eff}} = 0$) and models incorporating a combination of starvation and outflows ($\lambda_{\mathrm{eff}} = 1$). As we have seen, increasing λ_{eff} decreases the rate of stellar metallicity enrichment and lengthens

the timescale required to reproduce the observed ΔZ_*. At any mass, if $\lambda_{\rm eff}$ is set too large, outflows become too prominent and remove a significant fraction of the available gas, rendering it impossible to enrich by ΔZ_*. Therefore, there is a range of $\lambda_{\rm eff}$ values that can reproduce the observed stellar metallicity differences, each with different quenching timescales. Hence there is a level of degeneracy in our analysis, as the quenching timescale that is derived depends on the value of $\lambda_{\rm eff}$ that is assumed.

A further, important constraint that should help break the $\lambda_{\rm eff} - t_{\rm quench}$ degeneracy comes from analysing the star formation rates of these galaxies that are being quenched. At the moment when ΔZ_* enrichment is achieved, our model galaxy has a stellar metallicity that is comparable to that of local passive galaxies. In principle this galaxy should therefore also have a star formation rate that is consistent with those of local passive galaxies. However, as was found in 4.3.2.1, the 'quenched' galaxies in our $\lambda_{\rm eff} = 0$ model still had a non-negligible star formation rate. Rather than invoke a second, abrupt quenching phase (as was done in Section 4.3.2.1), we aim, in this subsection, to simultaneously reproduce both the observed stellar metallicity and the star formation rate in local passive galaxies, by using a non-zero time-independent mass loading factor $\lambda_{\rm eff}$. We require that when the galaxy's stellar metallicity enrichment equals the observed stellar metallicity difference ΔZ_*, its current SFR and M_* place it in the passive region of the SFR-M_* plane in Fig. 2.2. Since galaxies that quench with different $\lambda_{\rm eff}$ values will have different star formation rates at the moment ΔZ_* enrichment is satisfied, if $\lambda_{\rm eff}$ is chosen to be too small, then the star formation rate will still be too large. On the other hand, if $\lambda_{\rm eff}$ is too large, then too much gas is removed and it is impossible for the galaxy to ever satisfy the enrichment criterion. Hence there will only be a range of $\lambda_{\rm eff}$ values that can simultaneously reproduce both the observed stellar metallicity and star formation rate in local passive galaxies.

We show the duration of quenching derived from our joint metallicity-SFR analysis in the top panel of Fig. 4.7. We find that $t_{\rm quench}$ is typically 5–7 Gyr, which is considerably larger than the timescales we found in the $\lambda_{\rm eff} = 0$ scenario. In the middle panel we show the e-folding timescales for star formation $\tau_{\rm q}$ during the quenching phase. We find that $\tau_{\rm q} \sim 1$ Gyr. While the star formation efficiency ϵ and the 'effective' mass-loading factor $\lambda_{\rm eff}$ depend on stellar mass (see bottom panel), we find that $\tau_{\rm q}$ is mostly mass-independent. Although the duration of quenching $t_{\rm quench}$ is long, the typical timescale over which the bulk of the stellar metallicity enrichment occurs is considerably shorter (2–$3\tau_{\rm q}$). This point is demonstrated more clearly by inspecting the model-predicted curves in the top panel of Fig. 4.6. We can see that the stellar metallicity initially increases quite rapidly, but quickly slows down as it asymptotically approaches its limiting value.

We show the mass-loading factors required to simultaneously reproduce the stellar metallicity and SFR of passive galaxies in the bottom panel of Fig. 4.7. We find that the mass-loading

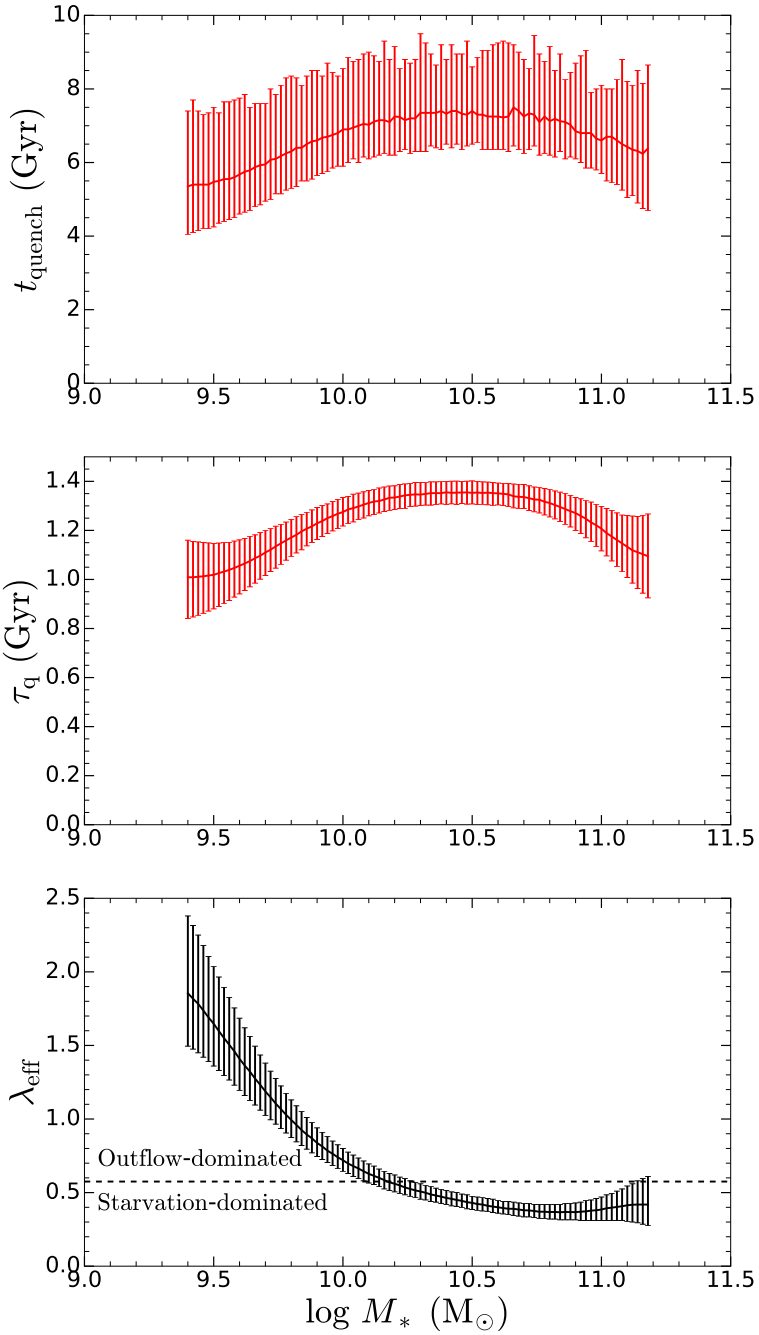

Figure 4.7. Top panel: Similar to the bottom panel in Fig. 4.5, but we now apply our joint metallicity-SFR analysis. Middle panel: The e-folding timescales $\tau_{\rm q}$, which indicate the typical timescale over which the star formation rate declines and the stellar metallicity enriches, as a function of stellar mass. Bottom panel: The mass-loading factors $\lambda_{\rm eff}$ required to simultaneously satisfy the ΔZ_* and the SFR quenching criteria. The horizontal dashed line is the $\lambda_{\rm eff}$ value for which the outflow rate ($\lambda_{\rm eff}\Psi$) is the same as the net gas consumption rate ($(1-R)\Psi = 0.575\Psi$). Galaxies with $\lambda_{\rm eff}$ above (below) this boundary are considered to be outflow-dominated (starvation-dominated). We show the median e-folding timescale and mass-loading factor in each stellar mass bin, with the error bars representing the standard deviation.

factor strongly decreases with increasing stellar mass. This anti-correlation between stellar mass and $\lambda_{\rm eff}$ is qualitatively consistent with the mass dependence in theoretical models, which predict that $\lambda \propto M_*^{-1/3}$ (Murray et al. 2005) for momentum-driven winds and $\lambda \propto M_*^{-2/3}$ for energy-driven winds (e.g. Dekel & Silk 1986), as well as other observational evidence (e.g. Heckman et al. 2015; Chisholm et al. 2017; Fluetsch et al. 2019). Our results indicate that 'effective' outflows (which are capable of permanently removing gas from the galaxy) are, together with starvation, of increasing importance in low-mass galaxies. In particular, since the rate at which gas is locked up into long-lived stars is given by $(1-R)\Psi = 0.575\Psi$, and the rate at which gas is ejected from the galaxy is given by $\lambda_{\rm eff}\Psi$, then, for galaxies with $\log(M_*/{\rm M}_\odot) < 10.2$, the rate at which gas is lost through galactic winds is roughly 1–3 times larger than the rate at which gas is locked up into long-lived stars. Clearly outflows play an essential role in depleting the gas reservoir of low-mass galaxies during the quenching phase. Outflows are relatively weaker ($\lambda_{\rm eff} \leq 0.6$) in more massive galaxies ($\log(M_*/{\rm M}_\odot) > 10.2$), with starvation becoming the dominant quenching mechanism, as illustrated in Fig. 4.7. However, outflows still play an important role in quenching star formation, as comparable amounts of gas are removed through galactic winds and through the formation of long-lived stars. Although these massive galaxies may be ejecting large amounts of gas in the form of outflows (i.e. a large λ), our results suggest that these ejection events are short-lived and/or most of the outflowing gas does not escape the galaxy and is instead recycled (i.e. a relatively small $\lambda_{\rm eff}$).

4.3.3 Green valley galaxies (quenching in the local Universe)

We now investigate the processes responsible for quenching star formation in galaxies in the local Universe, by studying the green valley galaxy population. Our analysis is similar to Section 4.3.2, but we now consider the stellar metallicity difference between star-forming galaxies and green valley galaxies. Since green valley galaxies have only recently begun quenching (if we assume that all green valley galaxies follow a one-way evolution with little contribution from rejuvenation), the stellar metallicities of their progenitors are only slightly smaller than the stellar metallicities of local star-forming galaxies. Hence the stellar metallicity differences between green valley galaxies and their star-forming progenitors are only slightly larger than the differences seen in Fig. 4.1.

4.3.3.1 Pure starvation

A comparison between the observed and model-predicted stellar metallicity differences is shown in the top panel of Fig. 4.8. We find that our closed-box model is able to reproduce the observed stellar metallicity differences, which could potentially suggest that the majority of green valley

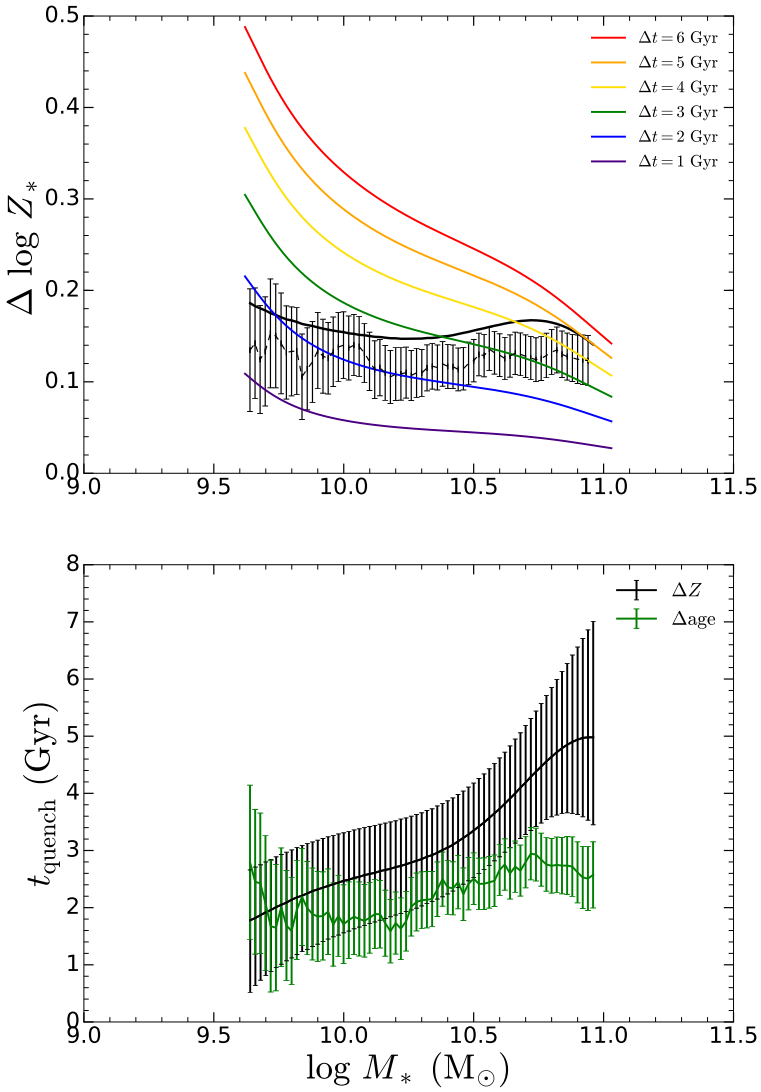

Figure 4.8. Top panel: The dashed black curve shows the observed stellar metallicity difference between local green valley galaxies and their star-forming progenitors of the same stellar mass. The solid black curve shows the actual increase in stellar metallicity during the quenching phase (taking into account the increase in stellar mass of the galaxy during quenching), with error bars omitted for clarity. The coloured lines show the stellar metallicity difference predicted by a closed-box model ($\lambda_{\rm eff} = 0$) at different times after the onset of starvation. Bottom panel: Duration of quenching derived from the stellar metallicity difference (ΔZ) between star-forming galaxies and green valley galaxies (black), as well as the quenching timescales obtained from the stellar age difference (Δage) between star-forming and green valley galaxies (green). The error bars on the ΔZ-derived and Δage-derived quenching timescales are due to the 1σ errors on the stellar metallicity and stellar age differences, respectively.

galaxies are quenching through starvation. However, this model is not constrained to match the gas content in green valley galaxies. We will explore models that simultaneously reproduce both the chemical content and star formation rates in green valley galaxies in Section 4.3.3.3. The closed-box models typically require 2–5 Gyr of quenching to reach the level of enrichment seen in observations, which implies that we are typically seeing these green valley galaxies 2–5 Gyr after the onset of quenching. These quenching timescales for local green valley galaxies are comparable to, or even longer than the quenching timescales of ∼2–3 Gyr that were found for the progenitors of local passive galaxies in Section 4.3.2. Coupled with the fact that passive galaxies have completed quenching, while green valley galaxies are still in the process of quenching (and so would take even longer to fully complete quenching), galaxies in the local Universe must be quenching much more slowly than their counterparts at higher redshift. This increase in quenching timescale is mostly due to the fact that gas depletion timescales in the local Universe are longer than at high redshift (e.g. Tacconi et al. 2013; Santini et al. 2014; Genzel et al. 2015; Schinnerer et al. 2016; Scoville et al. 2017; Tacconi et al. 2018), so it takes more time for galaxies to exhaust their gas reservoir during starvation.

The mass-dependence of the time elapsed since the onset of quenching $t_{\rm quench}$ is shown more clearly in the bottom panel of Fig. 4.8, where the quenching timescale obtained from our stellar metallicity difference analysis is shown by the black curve. We find that the duration of quenching increases with increasing stellar mass, i.e., on average, more massive green valley galaxies began quenching at an earlier epoch than less massive green valley galaxies. This result mostly comes about because the stellar metallicity difference between star-forming and green valley galaxies is roughly mass-independent, while the rate of chemical enrichment is slower in more massive systems due to the smaller gas fractions present.

We also estimate the time elapsed since the onset of quenching from the observed stellar ages of star-forming and green valley galaxies. If we make the simplifying assumption that galaxies evolve passively (i.e. no additional stars are formed) during the quenching phase, then from equation (3.18) and the discussion that followed, the time since the onset of quenching is just given by the difference in the stellar ages of star-forming and green valley galaxies. These stellar age differences then provide an alternative, independent estimate for the duration of quenching. The quenching timescales derived from the stellar age differences (Δage) are shown by the green curve in the bottom panel of Fig. 4.8. The typical stellar age difference between star-forming and green valley galaxies is within 2–3 Gyr, indicating that we are witnessing green valley galaxies roughly 2.5 Gyr after the onset of quenching. We find that, for $\log(M_*/\mathrm{M}_\odot) < 10.5$, the quenching timescales derived from our stellar metallicity analysis are roughly consistent with the timescales obtained from the stellar age differences. However, at the high-mass end, there is a significant offset between these two estimates for the time elapsed since the onset of

quenching, which we shall discuss further.

We made the simplifying assumption that galaxies evolve passively during quenching. Of course, young, metal-rich stars will be formed during quenching which will increase the average stellar metallicity and also decrease the average stellar age of the galaxy. Hence the observed stellar age of real green valley galaxies, which do not evolve passively, will be smaller than the idealised, passively-evolving green valley galaxies that we were considering. As a result, the age difference between star-forming and green valley galaxies that we observe will be smaller than the actual duration of quenching. In other words, the quenching timescales from our Δage analysis are likely underestimated. Furthermore, since the onset of quenching $z_{\rm q}$ in our models is estimated using Δage, any uncertainties related to the onset of quenching will also affect the ΔZ-derived estimates for the duration of quenching. At the high-mass end, relaxing the assumption of passive evolution will result in a larger $z_{\rm q}$ and therefore higher initial gas fractions and shorter depletion times, resulting in a smaller ΔZ-derived estimate for $t_{\rm quench}$, hence further narrowing the gap between our two estimates for the duration of quenching. However, while this point does potentially help to explain the offset between the estimates for the duration of quenching at the high-mass end, we do note that it will worsen the agreement between the ΔZ ages and Δages at the low-mass end. We will investigate whether models that include outflows can provide better agreement between these two timescales at the low-mass end later in this section.

Numerous works have also studied the typical timescales over which galaxies in the local Universe quench. For example, Wetzel et al. (2013) and Fossati et al. (2017) used N-body simulations/semi-analytic models to track satellite orbits, and subsequently determined the quenching timescales that were needed to match the quenched fraction of local satellite galaxies observed in SDSS DR7. They find that the typical quenching timescale decreases with increasing mass, with Wetzel et al. (2013) finding the timescale to decrease from 4 Gyr at $M_* = 10^{10}$ M$_\odot$ to 2 Gyr at $M_* = 10^{11}$ M$_\odot$, while Fossati et al. (2017) find that the timescale decreases from 8 Gyr at $M_* = 10^{10}$ M$_\odot$ to 6 Gyr at $M_* = 10^{11}$ M$_\odot$. Fillingham et al. (2015) argue that the quenching timescales derived for massive satellites ($M_* \sim 10^{8\text{–}11}$ M$_\odot$) are broadly consistent with being driven by starvation, with the quenching timescale corresponding to the cold gas depletion time. Fillingham et al. (2015) also undertake a similar analysis to the aforementioned works, but instead study the much lower mass ($M_* = 10^{6\text{–}8}$ M$_\odot$) dwarf satellites in the Local Group. They find substantially shorter quenching timescales of $\sim$ 1–1.5 Gyr, which they posit may be due to ram pressure stripping (see also Fillingham et al. 2016), which is likely to be more effective at removing gas in these low-mass systems. In addition, Wheeler et al. (2014) studied the quenched fractions of intermediate mass ($M_* = 10^{8.5\text{–}9.5}$ M$_\odot$) satellites and find that the quenching timescales are much longer (> 9.5 Gyr). These satellites are likely to be

too massive to quench through ram pressure stripping, so they instead quench through starvation (albeit very slowly due to the long depletion times in these low-mass galaxies, e.g. Boselli et al. 2014). In a similar vein, Guo et al. (2017) also determined estimates for the timescale upon which satellite galaxies must quench, following accretion into the group/cluster halo. Using dynamical arguments, they find that intermediate-mass ($9.5 < \log(M_*/\mathrm{M}_\odot) < 10.5$) galaxies typically quench over a timescale of 7 Gyr.

As is expected, the quenching timescales, t_{passive}, obtained from the aforementioned works (except the 2 Gyr from Wetzel et al. (2013)) are larger than the timescales, t_{green}, we derive in our analysis. This should be the case because t_{passive} measures the total time required to complete quenching (transforming a galaxy from star-forming to passive), while our timescales measure the time that green valley galaxies have been quenching for so far. Since green valley galaxies are still in the process of quenching and require additional time to complete the transformation into passive galaxies, $t_{\mathrm{green}} < t_{\mathrm{passive}}$. However, we do note that such a comparison between quenching timescales is complicated by the fact that the aforementioned works investigated the quenching of satellite galaxies, while our sample of SDSS galaxies consists mostly of centrals (see Yang et al. 2007). We separately analyse central and satellite galaxies in Chapter 5.

4.3.3.2 Starvation with outflows

A comparison between the observed stellar metallicity differences and the predictions from models with the 'classical' $\lambda_{\mathrm{eff}} = 1$ is shown in Fig. 4.9. We find that models incorporating outflows struggle to reproduce the observed stellar metallicity differences at the high-mass end, suggesting that powerful outflows play a minor role in quenching star formation in massive galaxies in the local Universe. In contrast, the stellar metallicity differences are still easily reproduced at the low-mass end, indicating that even stronger outflows may be required to quench these galaxies. We will investigate this in more detail in the next section.

4.3.3.3 Constraints on λ_{eff} from observed Z_* and SFR

Similar to Section 4.3.2.3, we determine the range of λ_{eff} such that both the ΔZ_* and the SFR quenching criteria are simultaneously satisfied. This means that when the galaxy's stellar metallicity enrichment in our model equals the observed stellar metallicity difference ΔZ_*, its SFR and M_* place it in the green valley galaxy locus of the SFR-M_* plane in Fig. 2.2.

The quenching timescales t_{quench} derived from our joint metallicity-SFR analysis are shown in the top panel of Fig. 4.10. We also show the e-folding timescales τ_{q} in the middle panel, and the associated mass-loading factors in the bottom panel. The quenching duration t_{quench} increases with increasing stellar mass from 4 to 6.5 Gyr. These timescales are not significantly

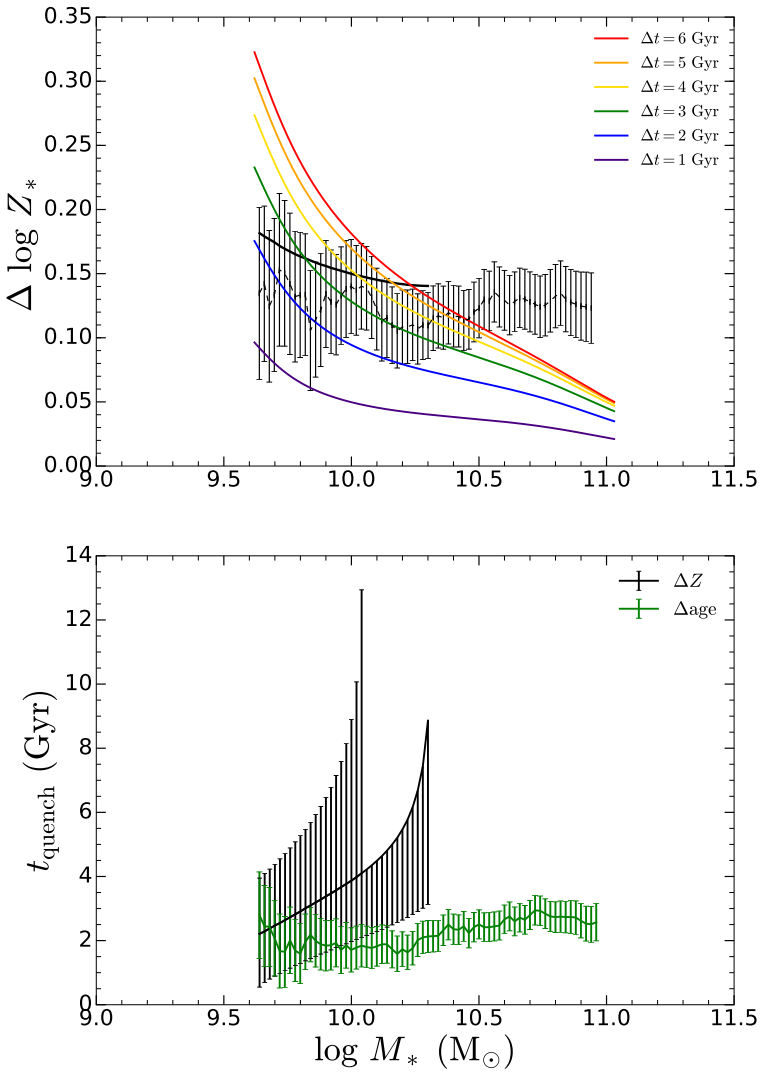

Figure 4.9. Similar to Fig. 4.8, but we now consider a leaky-box model, incorporating outflows with $\lambda_{\rm eff} = 1$. We omit the upper limit on the increase in stellar metallicity during quenching ΔZ_* (solid black curve in the top panel) when it cannot be reproduced by our model, and in that case we only show the lower limit on the ΔZ-derived duration of quenching $t_{\rm quench}$ (black curve in the bottom panel).

different from what was seen for passive galaxies in Fig. 4.7. As mentioned earlier, since local green valley galaxies are still in the process of quenching, this means that the total time required to complete the quenching phase and fully transition to the passive sequence will be longer than the $t_{\rm quench}$ that has been obtained, indicating that local green valley galaxies quench more slowly than their counterparts at higher redshift. This is illustrated more clearly by the e-folding timescales $\tau_{\rm q}$, which increase with mass in the range from 1.5 to 2.5 Gyr, and are larger than what was obtained in our study of local passive galaxies ($\sim$1 Gyr). Furthermore, we

find that the mass-loading factors $\lambda_{\rm eff}$ are similar to those at high-z, indicating that outflows in the local Universe are, on average, likely to be comparable in power and frequency to those at higher redshift. Similar to our study of passive galaxies, we find that the typical mass-loading factor decreases with increasing mass, indicating that 'effective' outflows play an important role in quenching local low-mass galaxies, with 1–3 times more gas lost through outflows than through gas consumption for $\log(M_*/\mathrm{M}_\odot) < 10.4$. Outflows become relatively less important and sub-dominant relative to starvation at high masses (but still eject comparable amounts of gas to what is lost through gas consumption), likely indicating that the outflowing gas in local massive galaxies does not escape and is instead reaccreted and/or that these ejection events are short-lived.

However, we do note that the long quenching timescales $t_{\rm quench}$ that we have derived are substantially larger than the timescales obtained from the stellar age difference analysis (Fig. 4.10), while our e-folding timescales $\tau_{\rm q}$ are more comparable. As discussed in 4.3.3.1, our estimates for the onset of quenching $z_{\rm q}$ based off of the age difference Δage may be inaccurate, which is likely to result in underestimates and overestimates for the duration of quenching from the Δage and ΔZ_* methods, respectively. It is also possible that our model which assumes continuous outflows, with a constant, large mass-loading factor does not provide an adequate description of how star formation is shut down in local green valley galaxies. This would suggest that another mechanism, which together with starvation, allows for a significant increase in stellar metallicity together with a rapid reduction in the star formation rate.

In addition, the inconsistency between quenching timescale inferred from the metallicities and the age differences observed in Fig. 4.10 may reflect the limits of the dataset. Indeed, the SDSS Legacy Survey fibre only probes the central region of galaxies. While this is not a major problem for star-forming galaxies and passive galaxies (which have mild metallicity and age gradients, Belfiore et al. 2017a; Goddard et al. 2017a) it is a potential issue for green valley galaxies, which often have a quenched central region and an outer (much younger) star-forming disc (Belfiore et al. 2017b, 2018). The physical properties in green valley galaxies that vary rapidly with galactocentric radius are not properly probed by the single-fibre SDSS data, and may likely introduce some inconsistencies in our analysis. It will be possible to further investigate the quenching of green valley galaxies, overcoming the limitations of a single fibre, by analysing the spatially-resolved spectral data provided by integral field spectroscopic galaxy surveys, such as SDSS-IV MaNGA (although at the expense of statistics), which we do in Chapter 6.

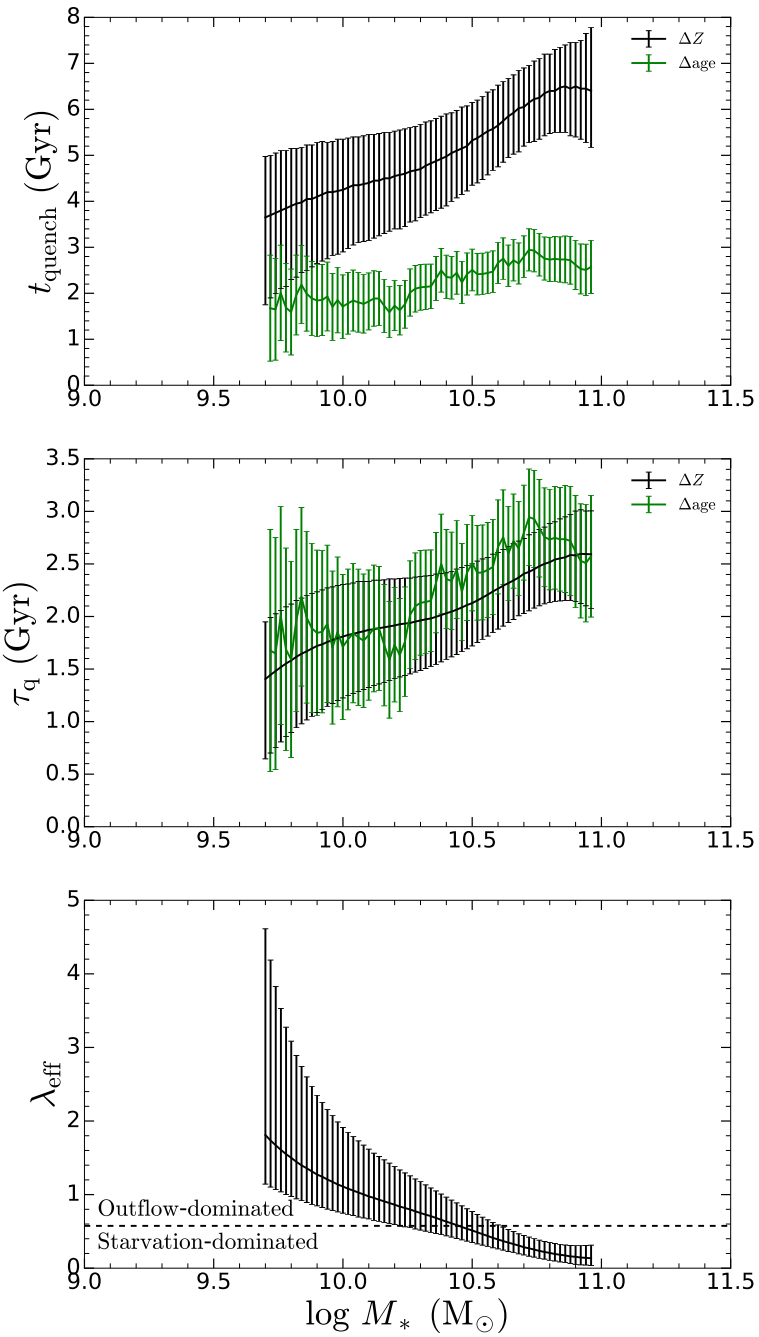

Figure 4.10. Top panel: Similar to the bottom panel in Fig. 4.8, but we now apply our joint metallicity-SFR analysis. Middle panel: The e-folding timescales $\tau_{\rm q}$, which indicate the typical timescale over which the star formation rate declines and the stellar metallicity enriches, as a function of stellar mass. Bottom panel: The mass-loading factors $\lambda_{\rm eff}$ required to simultaneously satisfy the ΔZ_* and the SFR quenching criteria. The horizontal dashed line is the $\lambda_{\rm eff}$ value for which the outflow rate ($\lambda_{\rm eff}\Psi$) is the same as the net gas consumption rate ($(1-R)\Psi = 0.575\Psi$). Galaxies with $\lambda_{\rm eff}$ above (below) this boundary are considered to be outflow-dominated (starvation-dominated). We show the median e-folding timescale and mass-loading factor in each stellar mass bin, with the error bars representing the standard deviation.

4.4 Assumptions and caveats

In this section we clarify modelling assumptions and also discuss caveats regarding our work. In particular, in Section 4.4.1 we investigate how the stellar metallicities and ages that are derived are affected by the fitting technique and stellar population synthesis model used, and the impact this may have on our results. In Section 4.4.2 we study the validity of our simplifying assumption regarding the evolution of the stellar MZR in our models. In Section 4.4.3 we investigate how our results are affected by introducing a mass offset between star-forming progenitors and local passive galaxies in our models. Finally, in Section 4.4.4 we investigate how modifications to the amount of mass return to the ISM in our models can affect our results.

4.4.1 Stellar population modelling techniques

In this subsection we compare the stellar-mass–stellar metallicity and stellar-mass–stellar age relations that are obtained using mass-weighted and light-weighted quantities from FIREFLY with those obtained using the metallicities and ages derived by Gallazzi et al. (2005) which were used in Peng et al. (2015).

In Fig. 4.11, we show the stellar mass–stellar metallicity relation (top panel) and stellar mass–stellar age relation (bottom panel) for star-forming, green valley and passive galaxies, using both the mass-weighted (which have been used throughout this chapter, solid) and light-weighted (dashed) values from FIREFLY, as well as the ages and metallicities derived by Gallazzi et al. (2005, dotted). The median error bars for each galaxy type are shown in the bottom right corner of both panels. We briefly note that the relative ordering of the star-forming, green valley and passive galaxies is preserved, independent of which stellar populations values are used, i.e. star-forming galaxies are always the youngest and most metal-poor, and green valley galaxies are always intermediate in metallicity and age between star-forming and passive galaxies.

First we will focus on the comparison between the mass- and light-weighted quantities from FIREFLY. As expected, the light-weighted metallicities tend to be higher than the mass-weighted metallicities (with a typical difference of 0.05–0.20 dex for star-forming galaxies that appears to decrease with mass), and the light-weighted ages tend to be younger than the mass-weighted ages. Interestingly, we find that for massive passive ($\log M_* > 10.5$) and massive green valley ($\log M_* > 10.8$) galaxies, the light-weighted metallicities are in fact slightly lower than the mass-weighted metallicities. This may perhaps be an indication that the gas in these passive galaxies has been gradually diluting (e.g. Yates et al. 2012; Yates & Kauffmann 2014), or that some of the high-mass green valley galaxies are in fact rejuvenated systems, rather than galaxies currently in the act of quenching. However, since the offset between mass- and light-weighted metallicities is small we will not explore this point any further.

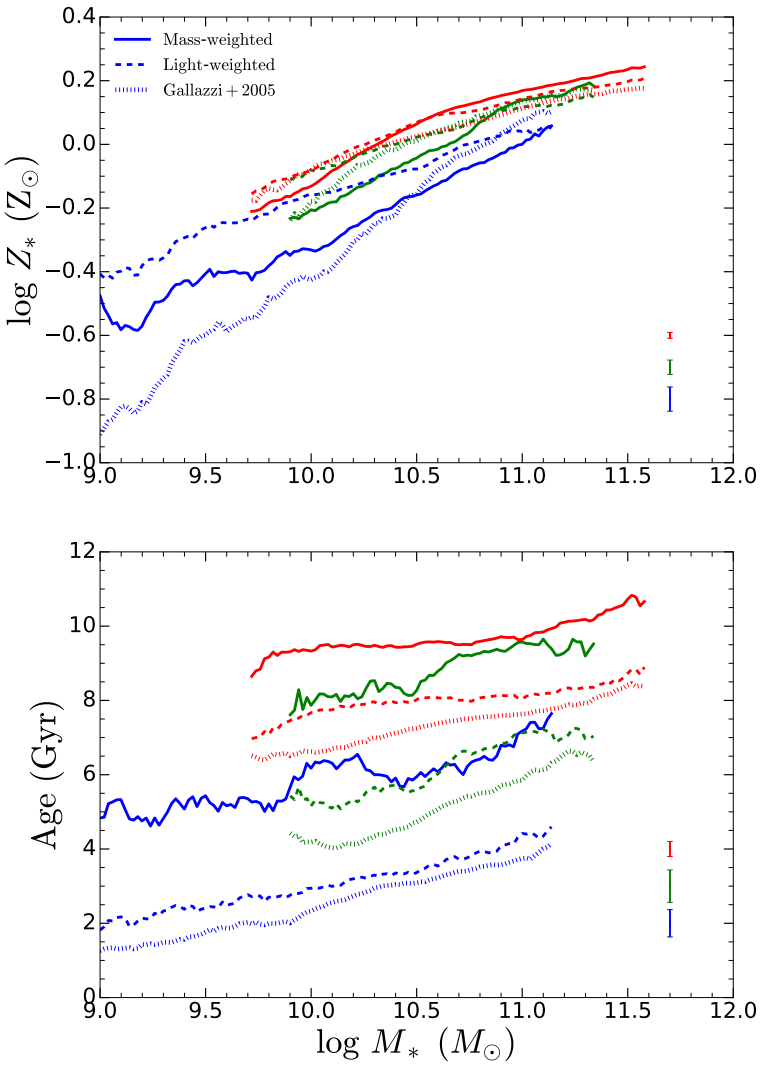

Figure 4.11. The stellar mass–stellar metallicity relation (top panel) and stellar mass–stellar age relation (bottom panel) for star-forming (blue), green valley (green) and passive (red) galaxies, using mass-weighted (solid) and light-weighted (dashed) metallicities/ages from FIREFLY, and metallicities/ages from Gallazzi et al. (2005, dotted). The median error bars for each galaxy type are shown in the bottom right corner of both panels. Note that the mass-weighted stellar metallicities and ages from FIREFLY have been used throughout this chapter.

Since the ages and metallicities derived by Gallazzi et al. (2005) were obtained by simultaneously fitting five spectral absorption features in the optical SDSS spectra, their quantities are light-weighted and we will compare them with the light-weighted quantities from FIREFLY. We find that there is excellent agreement between the stellar ages derived from the two works. The Gallazzi et al. (2005) ages are consistently younger, with a typical age offset of 0.25–1 Gyr from the FIREFLY ages. In order to compensate for the younger (and therefore bluer) stellar

populations in Gallazzi et al. (2005), one might expect their metallicities to be higher (to produce a redder spectrum) than the FIREFLY metallicities, due to the age–metallicity degeneracy. However, we can see from the figure that this is not always the case, especially not for low-mass star-forming galaxies, where the Gallazzi et al. (2005) metallicities are substantially smaller than the light-weighted metallicities from FIREFLY, and, surprisingly, are also smaller than the mass-weighted metallicities as well. We suspect that the aforementioned systematics associated with the choice of stellar population model and stellar library (discussed in Section 2.2.3.2) play an important role in driving this difference between the measured metallicities, as Gallazzi et al. (2005) used the Bruzual & Charlot (2003) models with STELIB, while we use the Maraston & Strömbäck (2011) models with MILES. This is likely further exacerbated by the fact that the techniques used to derive ages and metallicities are different: FIREFLY uses a full spectral fit of the optical spectrum, while Gallazzi et al. (2005) derive stellar populations by simultaneously fitting multiple optical spectral indices. Maraston & Strömbäck (2011) compared the metallicities obtained via full spectral fitting and via indices with those from resolved spectroscopy. They found that metallicities derived via indices depend strongly on which exact indices are used, whereas the full spectral fitting method, by using the full spectrum, provides a better match to the actual metallicity. We further note that, while the metallicities in Gallazzi et al. (2005) are averaged logarithmically (see discussion in Gonzalez Delgado et al. 2015), we instead use their median stellar metallicities, which are not affected by the averaging scheme used. Hence the large offset between the FIREFLY and Gallazzi et al. (2005) metallicities that we see are not due to this effect (which was discussed in detail in Section 2.2.3.2).

We acknowledge that the quantitative aspects of our results are affected by the set of stellar population parameters that are adopted in the analysis. On the one hand, the stellar age differences are not greatly affected by the choice of stellar population parameter set, so our estimations for the onset of quenching in the models will be largely unchanged. However, at least from Fig. 4.11, the stellar metallicities appear to be rather sensitive to the parameter set that is adopted. We note however that the difference in stellar metallicity between star-forming and passive galaxies is rather substantial, especially when comparing against the high-z star-forming progenitors, even when using the mass-weighted metallicities from FIREFLY. Our results suggest that the stellar metallicity of a galaxy typically increases by a factor of 2–3 during the quenching phase (see Fig. 4.4). The gap in metallicity widens even further when using the Gallazzi et al. (2005) data, which will result in longer quenching timescales in our closed-box models, and smaller $\lambda_{\rm eff}$ values in our joint SFR-Z_* analysis in Section 4.3.2.3, further strengthening the case for starvation as a necessary component of quenching.

Finally, we reiterate that the qualitative aspects of our results seem to be less strongly affected by the set of stellar population parameters used. As noted earlier, we find that star-

forming galaxies are more metal-poor and younger than passive galaxies of the same stellar mass, independent of the three stellar population parameter sets that were investigated in Fig. 4.11. We further note that, in addition to this chapter and Peng et al. (2015), a wide gap in stellar metallicity between star-forming and passive galaxies has also been seen in other works (using different spectral fitting codes, stellar population models and libraries), albeit indirectly. Gonzalez Delgado et al. (2015); Scott et al. (2017); Li et al. (2018) studied the global and, with the exception of Scott et al. (2017), also the spatially-resolved stellar population properties for galaxies in the CALIFA (Sanchez et al. 2012), SAMI (Bryant et al. 2015), and MaNGA (Bundy et al. 2015) surveys, respectively. Using visual morphology, or, in some cases, also Sércic indices (Sérsic 1963), each work finds that early-type/elliptical galaxies have larger stellar metallicities than late-type/spiral galaxies of the same stellar mass. Given the correlation between galaxy morphology and star formation rate (e.g. Wuyts et al. 2011), early- and late-type galaxies roughly correspond to passive, and star-forming galaxies, respectively, so the finding of a stellar metallicity difference between different galaxy populations in those works is qualitatively consistent with what has been found in this chapter.

4.4.2 Evolution of the stellar mass–stellar metallicity relation

In our model, the initial stellar metallicities of the high-z progenitors of local passive galaxies were estimated by assuming that the stellar MZR evolves in the same way as the gas MZR in Maiolino et al. (2008). This method was adopted because observations of the stellar metallicities of star-forming galaxies beyond $z = 0$ currently lack sufficient statistics and coverage in stellar mass and redshift to adequately constrain the evolution of the stellar MZR. In this subsection we compare our predicted redshift evolution with determinations of stellar metallicity and stellar mass from data available in the literature. Given that those determinations depend on a range of assumptions regarding stellar population models and fitting techniques it is quite hard to quantitatively interpret any agreement or disagreement. We note upfront however that the overall picture seems to be consistent and we provide some general statements to aid the interpretation.

The redshift-evolution of the stellar mass–stellar metallicity relation is shown in Fig. 4.12. The solid curves represent the stellar MZR that is used in our model, evaluated at various redshifts. The $z = 0$ (indigo) relation corresponds to the mass-weighted stellar metallicities of star-forming galaxies shown in Fig. 4.1, while the higher redshift relations were obtained by evolving the local relation in redshift according to the evolution of the gas MZR in Maiolino et al. (2008). Since the gas-phase metallicities of high-redshift star-forming galaxies tend to be lower than local galaxies of the same stellar mass, the normalisation of the stellar MZR decreases with redshift in our model. Furthermore, since the evolution of the gas MZR is stronger for

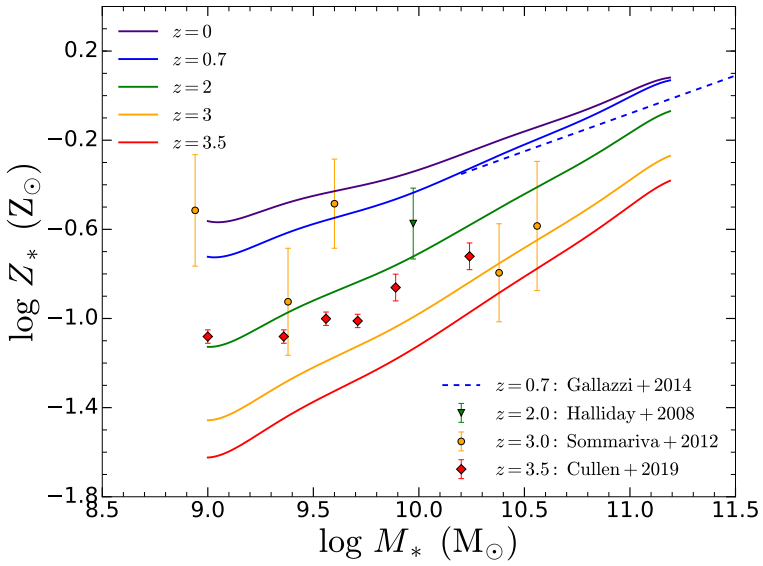

Figure 4.12. The redshift-evolution of the stellar mass–stellar metallicity relation in our model is shown by the solid curves, evaluated at $z = 0$ (indigo), $z = 0.7$ (blue), $z = 2$ (green), $z = 3$ (orange) and $z = 3.5$ (red). The $z = 0$ curve corresponds to the mass-weighted stellar metallicities of star-forming galaxies shown in Figure 4.1. The $z > 0$ curves were obtained by evolving the $z = 0$ curve in redshift according to the evolution of the gas MZR in Maiolino et al. (2008). We also show the stellar metallicities of star-forming galaxies observed at $z = 0.7$ (Gallazzi et al. 2014, blue dashed curve), $z = 2$ (Halliday et al. 2008, green triangle), $z = 3$ (Sommariva et al. 2012; Cullen et al. 2019, orange circles) and $z = 3.5$ (Cullen et al. 2019, red diamonds).

lower-mass galaxies in Maiolino et al. (2008), the stellar MZR steepens with redshift, which is qualitatively consistent with the findings of Lian et al. (2018c), who used a chemical evolution model to investigate the evolution of the gas and stellar MZR from z~3.5 to 0.

On Fig. 4.12, we also show the stellar metallicities of star-forming galaxies modelled from data at high-redshift, which follow the same colour coding as our model estimates for the stellar MZR. We show the $z = 0.7$ stellar MZR measured from 40 galaxies by Gallazzi et al. (2014, blue dashed curve), the stellar metallicity of a stack of 75 galaxies at $z = 2$ from Halliday et al. (2008, green triangle), the stellar metallicities of $z = 3$ galaxies from Sommariva et al. (2012, orange circles) and the $z \sim 3.5$ stacks of galaxies from Cullen et al. (2019, red diamonds). Note that the stellar metallicities from the high-redshift observations are all light-weighted, while our model estimates of the stellar MZR are mass-weighted. Mass-weighted stellar metallicities tend to be lower than light-weighted metallicities, with the offset between them depending on the star formation history (but is typically 0.1–0.2 dex (e.g. Zahid et al. 2017)). This offset needs to be taken into account when comparing the model estimates with the observations.

From inspection of Fig. 4.12, we find that there is good agreement between our model estimates and the results from Gallazzi et al. (2014) at $z = 0.7$, with at most a 0.09 dex dis-

agreement at the high-mass end. However, this disagreement becomes worse when accounting for the mass-weight–light-weight offset. We note that Gallazzi et al. (2014) adopted Bruzual & Charlot (2003) models and obtained an estimate of stellar metallicity from solar-scaled Lick indices. This modelling approach is substantially different from the one we adopt here, where the Maraston & Strömbäck (2011) models and full spectral fitting were used to obtain metallicities and ages. We also find reasonable agreement (0.15 dex offset) between our model and the $z = 2$ Halliday et al. (2008) results, which is further improved when accounting for the mass-weight–light-weight offset. There is significant scatter in the stellar metallicities for the $z = 3$ galaxies obtained by Sommariva et al. (2012). While our model estimates provide a reasonable agreement with the two high-mass measurements, there is considerable disagreement with the three low-mass measurements, even when accounting for the mass-weight–light-weight offset. We also find some disagreement between our model estimates and the $z \sim 3.5$ results from Cullen et al. (2019), with our models consistently underestimating the stellar metallicities of these galaxies. Indeed, Cullen et al. (2019) find that there is little evolution in the stellar MZR for $2.5 < z < 5.0$. These results suggest that our assumed evolution of the stellar MZR may become inaccurate at $z = 3$. However, this inaccuracy is not a significant issue, since the maximum redshift that we use for our quenching epochs z_q is $z \sim 2$ (see Fig. 3.1), and up to that redshift the stellar MZR evolution in our models provides reasonable agreement with the observations. Moreover, for what concerns the residual discrepancies, one should also take into account that the metallicity measurements based on the rest-frame UV spectrum of distant galaxies mostly probe the iron abundance, while the optical spectra of local galaxies probe a mixture of iron and alpha-elements, while gas phase mostly traces the oxygen (or alpha-element) abundance, so it should not be surprising that there is some residual disagreement.

Finally, we note that the shape and normalisation of the gas MZR is affected by the calibration used (e.g. Kewley & Ellison 2008). Hence different calibrations may predict stronger or weaker evolution of the gas MZR with redshift. The strong evolution of the gas MZR in Maiolino et al. (2008) agrees well with the predictions of several hydrodynamical simulations (e.g. Ma et al. 2016; Davé et al. 2017). However, other simulations predict a weaker evolution of the gas MZR (e.g. Davé et al. 2011; De Rossi et al. 2015, 2017; Torrey et al. 2019), which agrees better with the weaker evolution of the gas MZR observed by Hunt et al. (2016a), who used a different metallicity calibration to Maiolino et al. (2008) in their analysis. We note that assuming a weaker evolution of the gas MZR in our analysis will result in narrowing the metallicity gap between local passive galaxies and their high-z star-forming progenitors. This will result in shorter quenching timescales in our closed-box analysis in Section 4.3.2.1. For our analysis in Section 4.3.2.3, the narrower metallicity gap means that galaxies can afford to lose more gas in the quenching process and therefore our $\lambda_{\rm eff}$ values will increase.

4.4.3 Progenitor–descendant stellar mass offset

In our model we assume that high-z progenitors have the same stellar mass as their local passive descendants. In the absence of stellar mass loss (e.g. through tidal stripping, Chang et al. 2013; Tollet et al. 2017; Wang et al. 2017), this implies that galaxies form a minor amount of additional stellar mass during the quenching phase. However, high-z star-forming galaxies have large gas fractions (e.g. Daddi et al. 2010; Genzel et al. 2015; Tacconi et al. 2018), and, if they quench through starvation, are able to convert a significant portion of this gas into new stars. This results in a non-negligible increase in stellar mass during quenching, which is inconsistent with the assumption of progenitors and descendants having the same stellar mass in our model. In this subsection, we investigate how introducing a stellar mass offset between progenitors and descendants affects the timescales and mass-loading factors predicted by our model.

In principle, the stellar mass increase increment during quenching could be mass-dependent, because, for instance, gas fractions are mass-dependent (e.g. Genzel et al. 2015; Tacconi et al. 2018). Indeed, in our closed-box models from Section 4.3.2.1, we find that galaxies typically increase in mass by 0.2–0.6 dex (at the high-mass and low-mass ends, respectively), while for our models in Section 4.3.2.3 the mass increase range is 0.20–0.45 dex. Hence the stellar mass offset, defined as

$$\Delta \log M_* = \log M_{*,\mathrm{progenitor}} - \log M_{*,\mathrm{descendant}} \tag{4.3}$$

is mass-dependent. However, rather than assume a mass-dependent stellar mass offset between progenitors and descendants, we instead study the effect of using various fixed stellar mass offsets (that span the range of mass increases seen in our models) on our model predictions.

The effect of introducing a progenitor–descendant stellar mass offset is shown in Fig. 4.13 (which follows the format of Fig. 4.7). The different curves correspond to different stellar mass offsets, $\Delta \log M_*$, ranging from 0 to −0.6, in 0.2 dex increments. Error bars are omitted for clarity. We find that introducing a stellar mass offset between progenitors and descendants has a very minor effect on the quenching timescales (t_{quench} and τ_{q}) and mass-loading factors λ_{eff} obtained by our model, which indicates that our simplifying assumption that progenitors and descendants have the same stellar mass does not significantly affect our results. Note that the horizontal axis refers to the stellar mass of the progenitors, rather than the stellar mass of the descendants. For a given progenitor stellar mass, a more negative stellar mass offset corresponds to a descendant of higher stellar mass, which will tend to be older (see Fig. 4.2) and therefore have an earlier quenching epoch z_{q} in our model (see Fig. 3.1). However, since z_{q} is only weakly dependent on stellar mass, using a different stellar mass offset will only result in a small change in z_{q} and will therefore only introduce a small change in the initial gas mass, depletion time and stellar metallicity of the progenitor. Hence the results from our model are

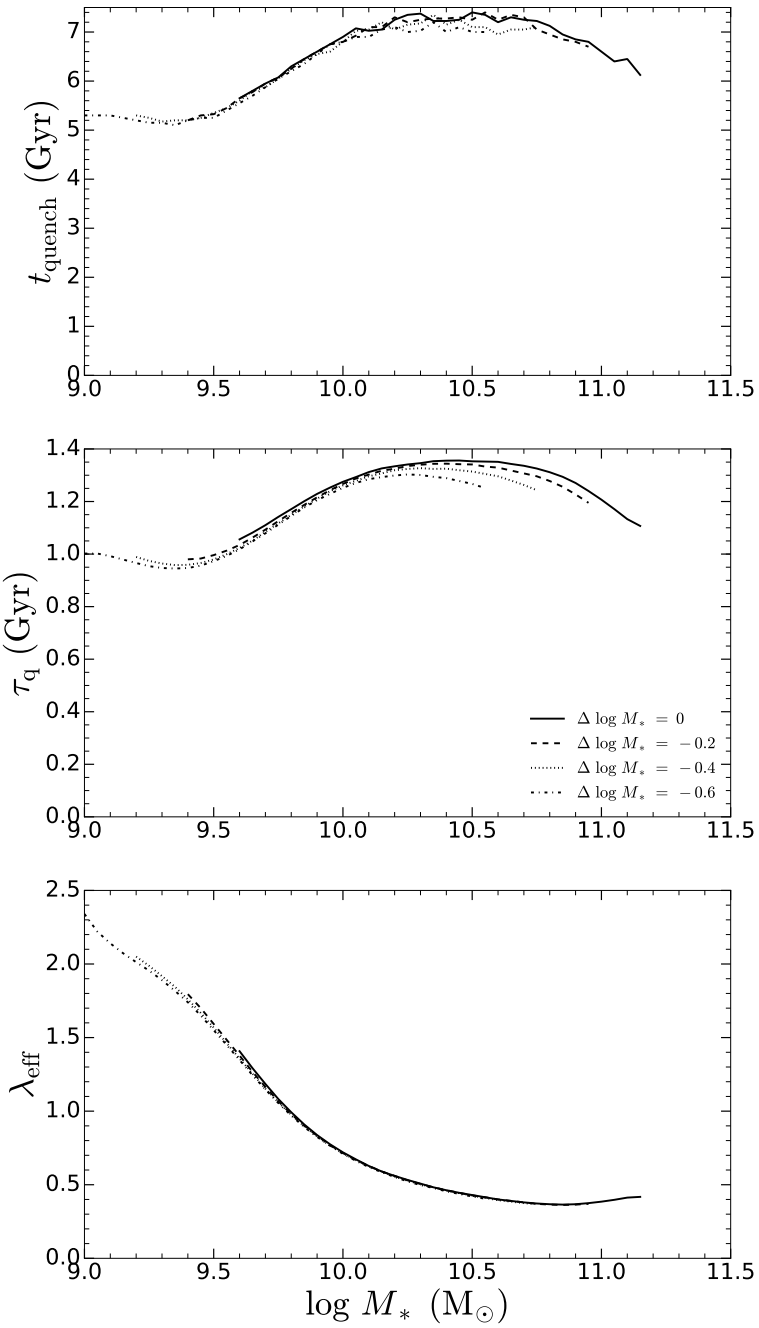

Figure 4.13. Similar in format to Fig. 4.7. The horizontal axis represents the stellar mass of the star-forming progenitors, which are assumed to be offset from the stellar mass of their local passive descendants by $\Delta \log M_*$ (defined in equation (4.3)). The model predictions for $\Delta \log M_*$ = 0 (solid), -0.2 (dashed), -0.4 (dotted), -0.6 (dot-dashed) are shown.

not strongly affected by the stellar mass offset that is assumed.

4.4.4 Mass return to the ISM

In our model we assume the instantaneous recycling approximation (IRA), where sufficiently massive stars instantly die upon formation, returning some of their stellar mass to the ISM. Massive stars, which recycle their gas quickly, significantly contribute to the return of stellar mass to the ISM. However, AGB stars (and to a much lesser extent Type Ia SNe) also return a considerable amount of gas to the ISM (e.g. Segers et al. 2016), albeit over much longer timescales than massive stars. The majority of this gas is returned over the first few Gyr, but there is still some mass return even after 10 Gyr (e.g. Maraston 2005; Leitner & Kravtsov 2011; Segers et al. 2016). This delayed recycling of gas will affect the evolution of the gas reservoir in the starvation scenario. In this subsection, we investigate how modifications to the return fraction R affect the timescales and mass-loading factors predicted by our model.

The return fraction R is weakly dependent on stellar metallicity ($\Delta R \sim 0.02$), but is sensitive to the IMF adopted ($\Delta R \sim 0.15$, Vincenzo et al. 2016a), with $R \sim 0.3$ for a more bottom-heavy IMF like Salpeter (1955) and $R \sim 0.45$ for a more bottom-light IMF like Kroupa (2001) and Chabrier (2003). Modifying the mass threshold used in the IRA to, for example, take into account the delayed recycling of gas from AGB stars, will also affect R. In this chapter, we assumed $R = 0.425$ (Vincenzo et al. 2016a). We now consider the impact of assuming different values of R, using values that are larger/smaller (±25%) and substantially larger/smaller (±50%) than our adopted value. Thus, the maximum variations in ΔR that we test are much greater than what is to be expected from adopting different IMFs or changing the mass threshold in the IRA.

The effect of modifying R is shown in Fig. 4.14. The various curves correspond to different values of R. Error bars are omitted for clarity. We find that the value of R that is adopted does not significantly affect the shape of the quenching timescale and mass-loading factor curves. However, the normalisation of these curves changes quite strongly (~50%) when substantial (±50%) variations in R are considered, while the effects are more minor (~25%) when smaller variations in R are used.

We find that increasing R results in longer quenching timescales and smaller mass-loading factors. The reason for this is that, for a given mass-loading factor $\lambda_{\rm eff}$, increasing R increases the amount of gas that is being lost through winds, $\lambda_{\rm eff}\Psi$, relative to the amount of gas that is being locked up in stars, $(1 - R)\Psi$. In order to still reproduce the observed ΔZ_* between star-forming and passive galaxies, $\lambda_{\rm eff}$ therefore has to decrease when R increases. Furthermore, by definition (see equation (6.1)), $\tau_{\rm q}$ therefore increases (and therefore also $t_{\rm quench}$ increases) with increasing R.

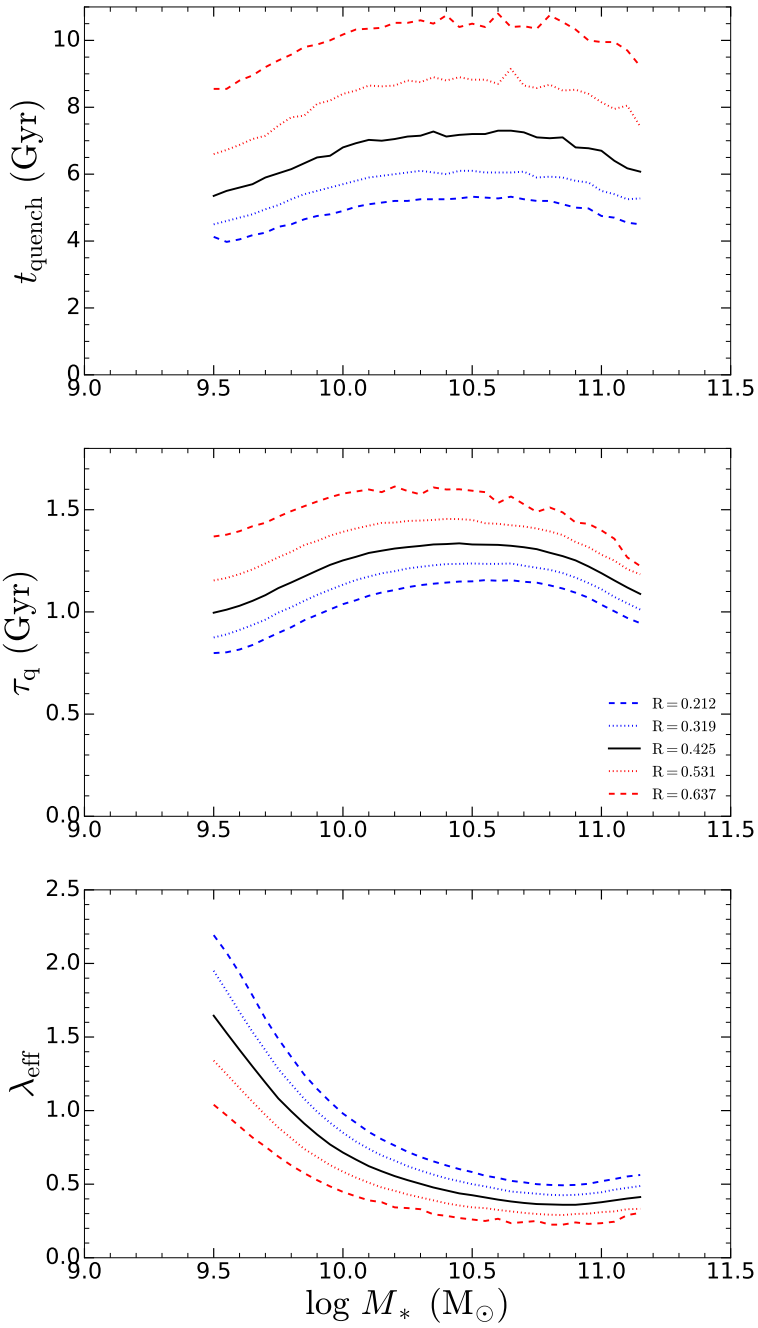

Figure 4.14. Similar in format to Fig. 4.7. Here we investigate how the adopted value of R affects our model predictions, for $R = 0.212$ (dashed blue), $R = 0.319$ (dotted blue), $R = 0.425$ (solid black), $R = 0.531$ (dotted red) and $R = 0.637$ (dashed red). Note that $R = 0.425$ was assumed throughout this chapter.

4.5 Summary and conclusions

We have investigated the mechanisms responsible for quenching star formation in galaxies across the cosmic epochs, i.e. the processes responsible for transforming star-forming galaxies into passive systems. We leverage on the method initially developed by Peng et al. (2015), who suggest that the stellar metallicity difference between local passive galaxies and their star-forming progenitors is a powerful tracer of the quenching process. We expand and improve upon the Peng et al. (2015) method in the following ways. We undertake a more extensive comparison between models and observations, deriving stronger constraints on the mass-dependent role of outflows in quenching star formation, by simultaneously reproducing the stellar metallicities and the star formation rates observed in local passive galaxies in our models. We use the much larger spectroscopic sample of galaxies available in SDSS DR7. Leveraging on the tripling in statistics that this new dataset has enabled, we now also study the quenching of star formation in local green valley galaxies. We have introduced a more sophisticated treatment of the progenitor–descendant comparison. We now compare the stellar metallicity difference between local passive galaxies and their high-z star-forming progenitors. This results in a widening of the gap in stellar metallicity between star-forming and passive galaxies, which qualitatively strengthens the case for starvation. In addition, we now also adopt the scaling relations, in terms of gas fractions and star formation efficiency, that have been observed for star-forming galaxies at high-redshift. We use the mass-weighted stellar ages of local galaxies to provide a more empirically-motivated estimation of the onset of quenching $z_{\rm q}$ in the models. We adopt a consistent treatment of stellar metallicity in this chapter, comparing mass-weighted metallicity predictions from models with mass-weighted stellar metallicities from observations.

We obtain the following observational results for local passive galaxies:

(i) The (mass-weighted) stellar metallicity of passive galaxies is always higher than the stellar metallicity of local star-forming galaxies of the same stellar mass.

(ii) Under the empirically- and theoretically-motivated assumption that the normalisation of the stellar mass–stellar metallicity relation for star-forming galaxies decreases with increasing redshift, then the metallicity difference becomes even larger if passive galaxies are compared with their star-forming progenitors at high-redshift.

(iii) The metallicity difference is a function of stellar mass, being highest at low masses and decreasing at high masses, but still remaining significant in the most massive galaxies analysed ($M_* \sim 10^{11}$ M$_\odot$).

(iv) The stellar metallicities of green valley galaxies (which probe the quenching process in the local Universe) are intermediate between those of star-forming and passive galaxies.

We investigated galaxy quenching using both closed-box models (where galaxies quench purely through starvation, with 'effective' outflow mass-loading factor $\lambda_{\rm eff} = 0$) and leaky-box models (where galaxies quench through a combination of starvation and outflows, with $\lambda_{\rm eff} > 0$). We explored two different leaky-box models in this chapter. Firstly, we investigated the case when $\lambda_{\rm eff} = 1$ for galaxies of all stellar masses. Secondly, we did not fix $\lambda_{\rm eff}$, but instead found the values of $\lambda_{\rm eff}$ for which our model simultaneously reproduced both the Z_* and SFR seen in local passive (and green valley) galaxies. By comparing the observed stellar metallicity difference between passive galaxies and their star-forming progenitors at high-redshift with the predictions from these simple analytical models of chemical evolution, we infer the following:

(i) The prominent metallicity difference between passive galaxies and their star-forming progenitors implies that for galaxies at *all* masses, quenching involved an extended phase of starvation, i.e. halting (or very substantial decrease) of gas accretion from the circumgalactic/intergalactic medium.

(ii) However, we find that some form of gas ejection has to be introduced into the models to best match the observed properties (i.e. stellar metallicities and SFRs) of local passive galaxies, indicating that outflows also play an important role in quenching star formation in galaxies. Thus we find that the combination of starvation together with outflows is responsible for quenching the majority of galaxies.

(iii) In our closed-box models we find that the duration of the quenching phase is 2–3 Gyr, with an e-folding time of 2–4 Gyr, after which a sudden ejection or heating of gas must have occurred to prevent further star formation and chemical enrichment of the galaxy. This delayed ejection/heating phase may have resulted from e.g. the cumulative energy of Type Ia SNe, AGN energy injection or the onset of ram pressure stripping.

(iv) In our leaky-box models which instead incorporate continuous (rather than invoke sudden) outflows, we find that the duration of quenching is longer at 5–7 Gyr, with an e-folding timescale for star formation of ∼1 Gyr.

(v) Furthermore, we find that the 'effective' mass loading factor decreases with increasing stellar mass, indicating that 'effective' outflows (which are capable of permanently removing gas from the galaxy) are, together with starvation, of increasing importance in low-mass galaxies. In particular, for galaxies with $\log(M_*/{\rm M}_\odot) < 10.2$, we find that the rate at which gas is lost through galactic winds is roughly 1–3 times larger than the rate at which gas is locked up into long-lived stars. Outflows become relatively less important and sub-dominant relative to starvation at high masses (but still eject comparable amounts of gas to what is lost through gas consumption), likely indicating that a significant fraction of the outflowing gas in these massive galaxies does not escape and is instead reaccreted and/or that these ejection events are short lived.

While passive galaxies have enabled us to explore the role of different quenching mechanisms at high redshift, when most of the star formation and quenching process took place, the analysis of green valley galaxies has offered us the opportunity of studying the quenching process in the local Universe. By comparing the observed stellar metallicity with simple models we infer the following:

(i) The stellar metallicity difference between green valley galaxies and local star-forming galaxies indicates that also locally the quenching process is likely to involve an extensive period of starvation.

(ii) The duration of quenching tends to increase with increasing stellar mass, indicating that, on average, more massive green valley galaxies began quenching at an earlier epoch than less massive green valley galaxies. However, this timescale is dependent on the contribution from outflows, with our closed-box model predicting 2–5 Gyr, while our leaky-box model that matches the Z_* and SFR in local green valley galaxies predicts 4–6.5 Gyr.

(iii) We find that the duration of quenching is comparable to, or larger than the timescales obtained for passive galaxies. Since green valley galaxies are still in the transition phase and have yet to quench completely, the timescales derived are in fact lower limits, suggesting that galaxies in the local Universe quench more slowly than their counterparts at higher redshift.

(iv) We also find that the *e*-folding timescales for star formation are longer in green valley galaxies (1.5–2.5 Gyr) than for passive galaxies (∼1 Gyr), which further supports the notion that, on average, the quenching of star formation occurs more slowly in the local Universe.

(v) We find that the effective mass-loading factors $\lambda_{\rm eff}$ decrease with increasing stellar mass, with a similar normalisation to the results obtained for our analysis of passive galaxies. This result suggests that the power and prevalence of outflows in galaxies in the local Universe are comparable to those in galaxies at higher redshift (z ∼1–2).

We note however some inconsistencies between the quenching timescale inferred from the metallicity difference between green valley and star-forming galaxies and the age difference between the two galaxy populations. There are various possible explanations for this inconsistency. One of the most important effects is that green valley galaxies are characterised by steep radial gradients in their properties (in particular age and star formation), while the SDSS DR7 single fibre captures only the central properties of these galaxies. Therefore, it is important to repeat this analysis by exploiting integral field spectroscopic galaxy surveys, which we shall do in Chapter 6.

Chapter 5

The Weak Imprint of Environment on the Stellar Populations of Galaxies

5.1 Introduction

In this chapter we leverage on the statistical power of the SDSS Legacy Survey to investigate the role of environment in galaxy evolution and galaxy quenching. In particular, we study the dependence of the stellar populations of galaxies on environment, both in terms of the central–satellite dichotomy, as well as on further measures of environment: halo mass, local overdensity and projected distance. Furthermore, we use our chemical enrichment-based method to investigate environmental quenching, analysing the environmental dependence of the stellar metallicity difference between star-forming and passive galaxies to determine whether environmental effects contribute to the starvation of galaxies.

This chapter is structured as follows. In Section 5.2, we investigate the dependence of the stellar populations of galaxies on environment, in terms of the central–satellite dichotomy, halo mass, overdensity and projected distance. In Section 5.3, we study how the stellar metallicity difference between star-forming and passive galaxies depends on the previously mentioned measures of environment, to investigate the role the environment plays in galaxy quenching, with emphasis on whether environmental effects contribute to the starvation of galaxies. In Section 5.4, we discuss the environmental trends that we have found for stellar metallicities, focussing on the comparison against environmental trends that previous studies have found for gas-phase metallicities. Finally, in Section 5.5, we summarise our main findings and conclude.

The content in this chapter has been adapted from our submitted article: *The weak imprint of environment on the stellar populations of galaxies*, Trussler, J., Maiolino, R., Maraston, C., Peng, Y., Thomas, D., Goddard, D., Lian, J., 2020, arXiv: 2006.01154 (Trussler et al. 2020b), where all of the work in the article was conducted by the author of this thesis, in collaboration with the listed co-authors.

5.2 The dependence of stellar populations on environment

In this section we investigate how the stellar populations (stellar metallicities and stellar ages) of galaxies depend on environment. Our analysis will be largely focussed on how the stellar mass–stellar metallicity relation is affected by the environment, but we will briefly also investigate the stellar mass–stellar age relation as well. We will explore the similarities and differences between centrals and satellites in Section 5.2.1, the dependence of the stellar mass–stellar metallicity relation on halo mass in Section 5.2.2, the dependence on the local overdensity in Section 5.2.3 and the dependence on projected distance in Section 5.2.4.

5.2.1 Central–satellite dichotomy

In this section, we study the dependence of the stellar mass–stellar metallicity relation and the stellar mass–stellar age relation on the central–satellite dichotomy. Galaxies are classified as either central or satellite using the definitions in Section 2.2.4, are subsequently binned in stellar mass, and both the median stellar metallicity and the error on the median ($1.253\sigma/\sqrt{N}$) are computed for each mass bin, where σ is the standard deviation of the stellar metallicity in the mass bin, and N is the number of galaxies in that mass bin.

5.2.1.1 Stellar metallicity

We show the mass-weighted stellar mass–stellar metallicity relation for centrals (dashed) and satellites (solid) in the left panel of Fig. 5.1. We find that satellites are typically more metal-rich than centrals of the same stellar mass, and that this metallicity difference is highly significant (i.e. multiple σ). Furthermore, the metallicity difference between centrals and satellites decreases with increasing stellar mass, from ~0.1 dex at the low-mass end down to ~0 at the high-mass end. Taken at face value, this large offset between centrals and satellites suggests that the gas flow and chemical enrichment histories of central and satellite galaxies may be different, with the environment playing a relatively more important role at shaping galaxy evolution at the low-mass end, and a relatively less important role at the high-mass end.

Our result is qualitatively consistent with Pasquali et al. (2010), who studied the stellar metallicities of centrals and satellites in SDSS DR4 (Adelman-McCarthy et al. 2006), which

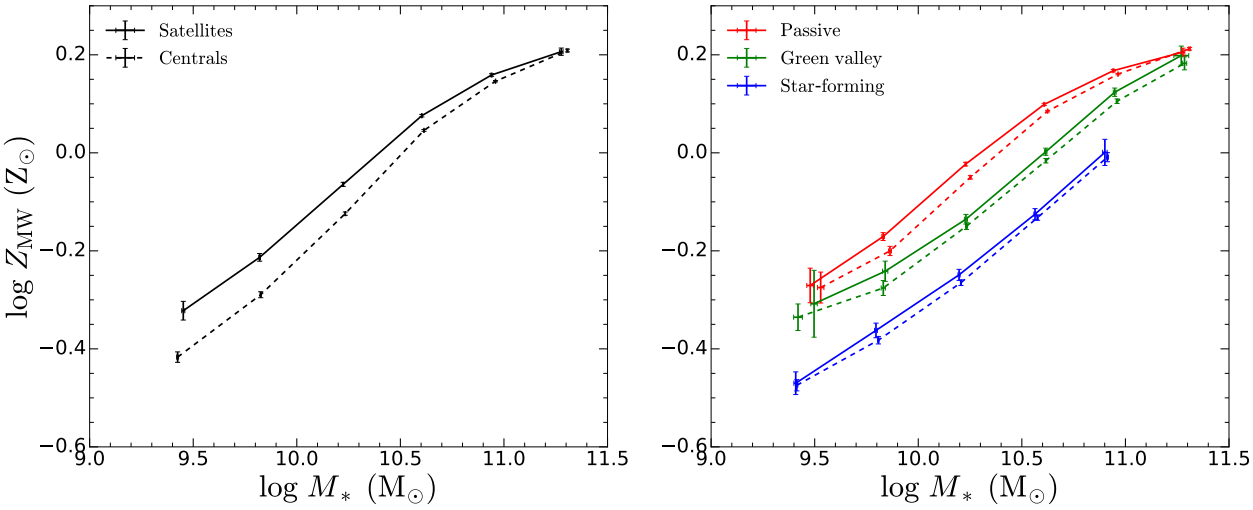

Figure 5.1. The mass-weighted stellar mass–stellar metallicity relation for centrals (dashed) and satellites (solid). Galaxies are binned in stellar mass and the median stellar metallicity in each mass bin is shown. Error bars correspond to the 1σ uncertainty on the median. Left panel: The mass-weighted stellar mass–stellar metallicity relation when including all galaxies (i.e. without splitting into star-forming, green valley and passive galaxies, black). Right panel: The mass-weighted stellar mass–stellar metallicity relation for star-forming (blue), green valley (green) and passive galaxies (red).

consists of a smaller sample of galaxies than our study of SDSS DR7. Although their results were based on light-weighted stellar metallicities (rather than the mass-weighted stellar metallicities used in our work), that were obtained using a different spectral fitting procedure (through simultaneous fitting of five metallicity- and age-sensitive optical spectral absorption features from Gallazzi et al. (2005), rather than through a full spectral fit of the optical continuum using FIREFLY), they also found that satellites are more metal-rich than centrals of the same stellar mass, with the difference between centrals and satellites decreasing with increasing stellar mass. We study the stellar mass–stellar metallicity relation for centrals and satellites using light-weighted metallicities from FIREFLY and from Gallazzi et al. (2005) in Appendix B.2. Briefly, we find similar qualitative trends to the results obtained using mass-weighted stellar metallicities (satellites are more metal-rich than centrals), although the quantitative details are slightly different.

However, as previously shown in Peng et al. (2015) and Chapter 4, and also depicted in the right panel of Fig. 5.1, passive galaxies (shown in red) and green valley galaxies (shown in green) are substantially more metal-rich than star-forming galaxies (shown in blue) of the same stellar mass. Hence, if the relative abundance of star-forming, green valley and passive galaxies (i.e. the quenched fraction, or non-SF fraction) is different for centrals and satellites, then one would

expect the average stellar metallicity for the overall populations (i.e. including star-forming, green valley and passive galaxies together) of centrals and satellites to be different, because they have different proportions of relatively metal-poor star-forming and relatively metal-rich green valley/passive galaxies. So, even if the stellar metallicity of star-forming centrals and satellites, green valley centrals and satellites, and passive centrals and satellites are the same, one would still expect to see a metallicity offset between the overall populations of centrals and satellites because of this effect. Thus, the large offset between the overall population of centrals and satellites (i.e. when including all types of galaxies) shown in the left panel of Fig. 5.1, may in fact be driven by a strong dependence of quenched fraction on environment, rather than a strong dependence of stellar metallicity on environment.

The dependence of quenched fraction on the environment has been extensively investigated in the literature (e.g. Peng et al. 2010, 2012; Woo et al. 2013; Wang et al. 2018). In particular, it has been found that, at a fixed stellar mass, the quenched fraction for satellites is higher than for centrals. For the sake of convenience, we show this result using our sample (which has been biased by cuts on S/N), but showing the non-SF fraction (i.e. including green valley and passive galaxies), rather than the quenched fraction, in Fig. 5.2. Since the non-SF fraction is higher for satellites than for centrals of the same stellar mass, the satellite population consists of relatively more green valley and passive galaxies, which have high stellar metallicities, and relatively fewer star-forming galaxies, which have lower stellar metallicities. Thus, at a given stellar mass, one would expect the overall satellite population to have a higher stellar metallicity than the overall central population, which is what was seen in the left panel of Fig. 5.1.

In order to disentangle the inherent dependence of stellar metallicity on environment from the trends brought about by the dependence of quenched fraction on environment, we further divide the central and satellite populations into star-forming, green valley and passive galaxies in the right panel of Fig. 5.1. We find that the stellar metallicity difference between centrals and satellites that was seen when considering the overall population is greatly reduced after separating into star-forming, green valley and passive galaxies. Evidently the dependence of quenched fraction on environment exaggerates the true stellar metallicity difference between central and satellite galaxies, which is actually much smaller. Nonetheless, there is still an indication, especially for green valley and passive galaxies, that satellites are more metal-rich than centrals of the same stellar mass, albeit to a lesser degree and with less significance (due to the smaller metallicity gap, as well as the lower statistics and hence larger error bars).

We show the stellar metallicity difference between centrals and satellites more clearly in Fig. 5.3. The typical metallicity difference for star-forming galaxies is 0.01–0.02 dex, for green valley galaxies is 0.02–0.03 dex and for passive galaxies is 0–0.03 dex, which are clearly much smaller than what is seen when simply comparing the overall central population

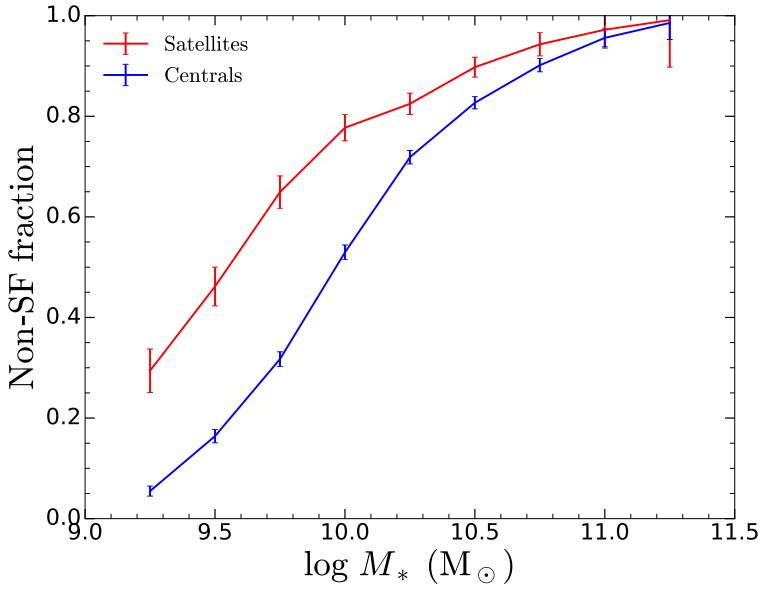

Figure 5.2. The non-SF fraction (i.e. the fraction of galaxies that are green valley or passive) for centrals (blue) and satellites (red) in our sample (which has been biased by cuts on S/N). The errors on the non-SF fractions were obtained by propagating the errors (assumed to be Poissonian) on the green valley + passive galaxy count and the total galaxy count in each mass bin.

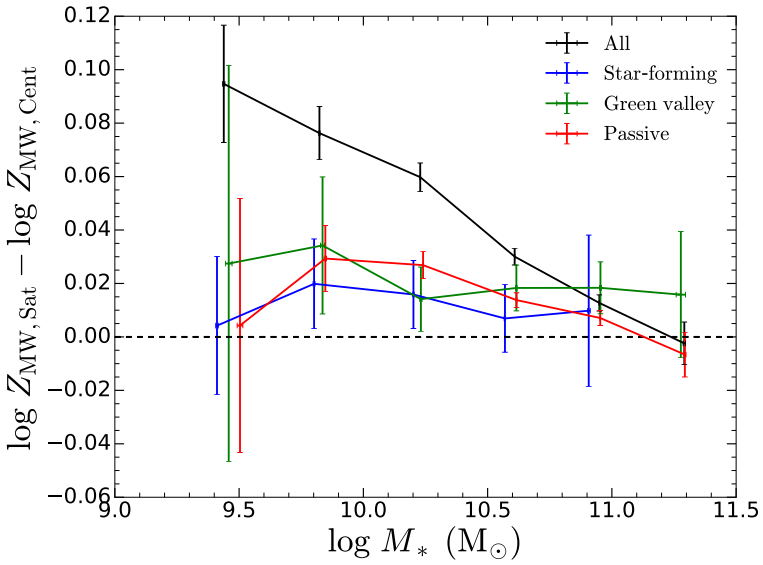

Figure 5.3. The mass-weighted stellar metallicity difference $\Delta \log Z_{MW} = \log Z_{MW,Sat} - \log Z_{MW,Cent}$ between centrals and satellites of the same stellar mass, including all galaxies (i.e. without splitting into star-forming, green valley and passive galaxies, black), for star-forming galaxies (blue), green valley galaxies (green) and passive galaxies (red). Error bars correspond to the 1σ error on the stellar metallicity difference.

against the overall satellite population (shown in black), except perhaps at the high-mass end ($\log(M_*/\mathrm{M}_\odot) \geq 11.0$). Our results for star-forming, green valley and passive galaxies are qualitatively consistent with the findings of Bahé et al. (2017), who used the cosmological hydrodynamical EAGLE simulation to study the stellar metallicities of > 3600 galaxies with $\log(M_*/\mathrm{M}_\odot) > 10$. Similar to this chapter, they find that star-forming satellites, green valley satellites and passive satellites are more metal-rich than star-forming centrals, green valley centrals and passive centrals of the same stellar mass, respectively.

However, there are quantitative differences with our work, as they typically find larger offsets between centrals and satellites, with a typical metallicity difference of 0.01–0.03 dex for star-forming galaxies, 0.05–0.07 dex for green valley galaxies and 0.01–0.08 dex for passive galaxies. In contrast to our results, they find that the metallicity difference between the overall population of centrals and satellites is intermediate between (rather than greater than) the metallicity differences for star-forming, green valley and passive galaxies, at 0.02–0.05 dex. This disagreement with our work is likely to be related to the quenched fraction effect. If, in the EAGLE simulation, either the stellar metallicities of star-forming, green valley and passive galaxies are very similar, or the quenched fractions of centrals and satellites are similar, then one should obtain the Bahé et al. (2017) result for the overall population of centrals and satellites.

In addition to exaggerating the stellar metallicity difference between centrals and satellites, a comparison between the overall central population against the overall satellite population also misrepresents the mass-dependence of the true metallicity difference between centrals and satellites. While the metallicity difference for the overall population clearly declines with increasing stellar mass, it is roughly independent of stellar mass for star-forming and green valley galaxies, and appears to decline more weakly with increasing stellar mass for passive galaxies (especially if one ignores the lowest stellar mass bin, for which the statistics are rather low). Thus, the strong mass dependence of the stellar metallicity difference for the overall population (shown in Figs. 5.1 and 5.3) is not driven by the inherent dependence of stellar metallicity on environment (i.e. centrals vs satellites), but rather on the relative mass dependence of the non-SF fractions for centrals and satellites (shown in Fig. 5.2).

At the low-mass end, there is a large difference between the non-SF fraction for centrals and satellites. In addition, the gap in stellar metallicity between star-forming, green valley and passive galaxies is at its widest at the low-mass end (which is shown more clearly in Chapter 4). As a result, the stellar metallicity difference between the overall populations of centrals and satellites is relatively large at the low-mass end, as the satellite population consists of a relatively high fraction of metal-rich green valley and passive galaxies with respect to the central population. However, as stellar mass increases, the difference between the non-SF fractions for centrals and satellites decreases, and the gap in stellar metallicity between

star-forming, green valley and passive galaxies narrows. Hence the overall stellar metallicity difference decreases with increasing mass. It is only at the high-mass end ($\log(M_*/\mathrm{M}_\odot) \geq 11.0$), where the non-SF fractions for centrals and satellites are identical, that the differences between the overall populations of centrals and satellites are purely driven by the inherent dependence of stellar metallicity on the central–satellite dichotomy, and we see that this effect is rather small.

To summarise, the stellar metallicity difference between the overall population of centrals and satellites is brought about by two effects. First, the inherent dependence of stellar metallicity on environment. That is, the stellar metallicity difference between star-forming centrals and star-forming satellites, green valley centrals and green valley satellites, and passive centrals and passive satellites. Second, the dependence of quenched fraction on environment. Since the stellar metallicities of star-forming, green valley and passive galaxies of the same stellar mass are different, the difference in quenched fraction between centrals and satellites also contributes to the stellar metallicity difference seen between the overall population of centrals and satellites. Owing to the large offset in stellar metallicity between star-forming, green valley and passive galaxies, the quenched fraction effect is much more prominent than the inherent environmental dependence in driving the apparent metallicity–environment relations.

We strongly suggest that the quenched fraction effect should be taken into account (by splitting into star-forming, green valley and passive galaxies) whenever investigating trends with environment (e.g. central–satellite dichotomy, halo mass, overdensity, projected distance) for scaling relations that are different for star-forming and passive galaxies, else the quenched fraction effect results in misrepresenting the true, inherent dependence on environment, as well as e.g. the stellar-mass dependence. Examples of such scaling relations are the stellar mass–stellar age relation, stellar mass–colour relation, stellar mass–star formation rate relation and the stellar mass–effective radius relation. We briefly study the mass-weighted stellar mass–stellar age relation in the next section to highlight how the aforementioned pitfalls apply.

5.2.1.2 Stellar age

We show the mass-weighted stellar mass–stellar age relation for the overall central population (dashed) and satellite population (solid) in the left panel of Fig. 5.4. We find that satellites are typically older than centrals of the same stellar mass, with the difference being highly significant (i.e. multiple σ) across the entire stellar mass range. In addition, the stellar age difference decreases with increasing stellar mass, from ~2 Gyr at $\log(M_*/\mathrm{M}_\odot) = 9.5$ to ~0.5 Gyr at $\log(M_*/\mathrm{M}_\odot) = 11.5$. Again, we find that our results are qualitatively consistent with the work of Pasquali et al. (2010), who obtained similar trends with SDSS DR4, using light-weighted ages and a different spectral fitting procedure (see Gallazzi et al. 2005). We

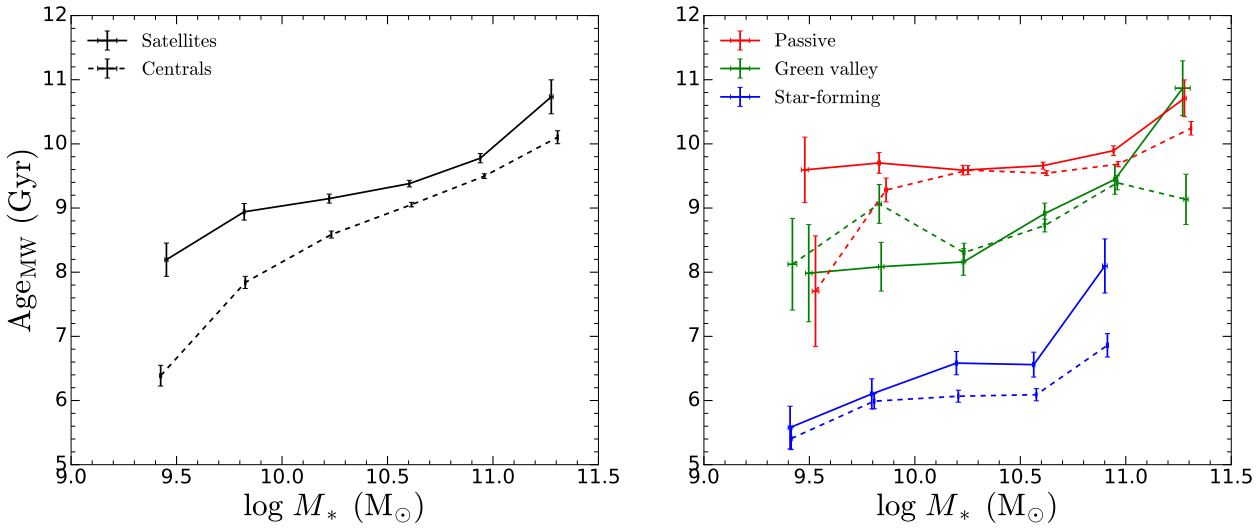

Figure 5.4. Similar to Fig. 5.1, but now showing the mass-weighted stellar mass–stellar age relation.

briefly study the light-weighted stellar mass–stellar age relation using light-weighted ages from FIREFLY and Gallazzi et al. (2005) in Appendix B.3, and find that the qualitative (but not the quantitative) trends obtained in this section are preserved. Taken at face value, the large age offset between centrals and satellites suggests that the star formation histories of central and satellite galaxies may be different, with the imprint of environment being strongest at the low-mass end and weaker at the high-mass end.

However, as shown in the right panel of Fig. 5.4, after splitting into star-forming, green valley and passive galaxies, the age differences between centrals and satellites tend to become much smaller and less significant than what was seen for the overall population. In some cases the age differences are still large, such as the lowest mass bin for passive galaxies and the highest mass bin for green valley galaxies, but it should be noted that the statistics in these mass bins are very low (with respect to the other mass bins), so the large offset that we see may partly be due to noise. Similar to what was seen for the overall population, star-forming satellites tend to be older than star-forming centrals, and passive satellites tend to be older than passive centrals of the same stellar mass. However, the trend for green valley galaxies is less clear, which may be because the statistics for green valley galaxies are relatively low with respect to star-forming and passive galaxies (see our sample description in Section 2.2.5). Neglecting the highest mass bin, we find that at high masses the ages of green valley satellites and green valley centrals are comparable. On the other hand, at the low-mass end there is even an indication that green valley centrals are older than green valley satellites, which is a reversal of the trend seen elsewhere (satellites are older than centrals). However, we do not find this result to be significant, since

the stellar mass–stellar age relation is, roughly speaking, a monotonically increasing relation, so the relatively high age for centrals in the second-lowest mass bin may be due to random scatter driven by the low-number statistics.

Furthermore, while the age difference between the overall population of centrals and satellites clearly decreases with increasing stellar mass, there are no clear trends for star-forming, green valley and passive galaxies. If anything, star-forming galaxies exhibit the opposite trend, with the age difference between centrals and satellites instead increasing with increasing stellar mass.

5.2.2 Halo mass

Having studied the dependence of the mass-weighted stellar mass–stellar metallicity relation on the central–satellite dichotomy, we now move on to further measures of the environment. In this section we study how the mass-weighted stellar mass–stellar metallicity relation depends on group halo mass $M_{\rm h}$ for both centrals and satellites.

We bin galaxies into quartiles of halo mass, which we refer to as Low, Mid-Low, Mid-High and High, for the 1st (i.e. the least massive haloes), 2nd, 3rd and 4th (i.e. the most massive haloes) quartiles, respectively. Since the distributions of centrals and satellites in halo mass are different (see Fig. 2.1), we use different halo mass quartiles for centrals and satellites to more clearly identify the trends with halo mass. To clarify, this means that the halo mass range associated with e.g. the Low quartile is different for centrals and satellites. Furthermore, since passive galaxies are more likely to reside in massive haloes, while star-forming galaxies are more likely to reside in low-mass haloes (e.g. Woo et al. 2013), the distributions for star-forming, green valley and passive galaxies in halo mass are different. Hence we also use different halo mass quartiles for star-forming galaxies, green valley galaxies, passive galaxies and the overall population of galaxies.

5.2.2.1 Satellites

We show the mass-weighted stellar mass–stellar metallicity relation for the overall population of satellites in different halo mass quartiles in the top-left panel of Fig. 5.5. We find that, at a fixed stellar mass, the stellar metallicity for the overall population of satellites tends to increase with increasing halo mass, and that this applies across the entire stellar mass range studied. Although the stellar metallicity difference between adjacent quartiles is small and perhaps marginally significant, there is a clear offset between the lowest and highest halo mass quartiles, that tends to decrease with increasing halo mass, from 0.1 dex at the low-mass end down to 0.05 dex at the high-mass end. As with our results mentioned earlier in this chapter,

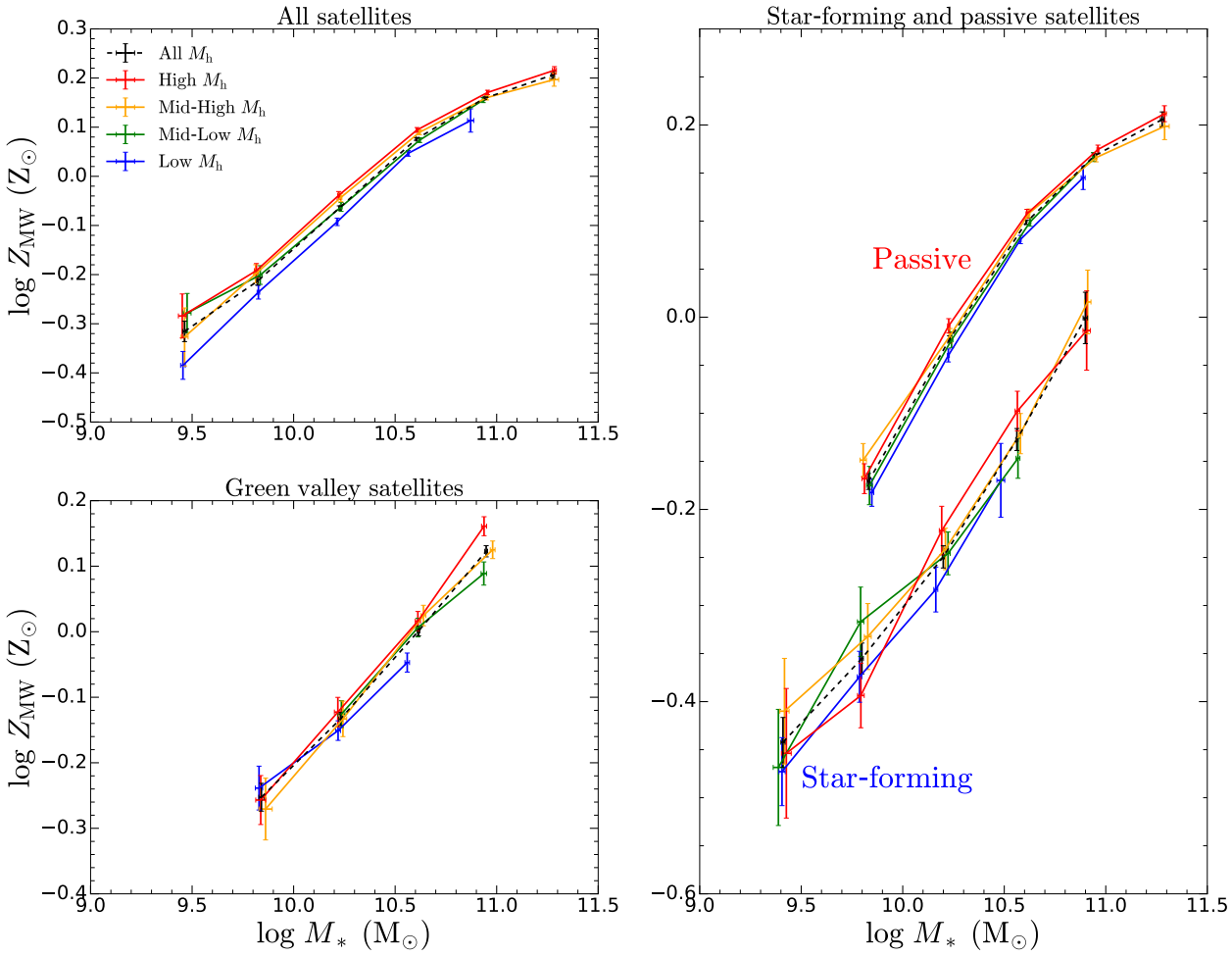

Figure 5.5. The mass-weighted stellar mass–stellar metallicity relation for satellites in different quartiles of halo mass M_h, which we refer to as Low (shown in blue), Mid-Low (green), Mid-High (orange) and High (red) for the 1st (i.e. the least massive haloes), 2nd, 3rd and 4th (i.e. the most massive haloes) quartiles, respectively, as well as the relation obtained without splitting into quartiles of halo mass (named All, in dashed black). Note that the vertical scale and range is different for each panel. Furthermore, the halo mass quartiles in the different panels correspond to different halo mass ranges. Top-left panel: all satellites (i.e. without splitting into star-forming, green valley and passive galaxies). Right panel: star-forming and passive satellites. Bottom-left panel: green valley satellites.

these findings are also qualitatively consistent with the study of Pasquali et al. (2010). Taken at face value, our result suggests that the environment plays an important role in shaping the chemical enrichment histories of satellites of all masses, with satellites in more massive haloes tending to be more metal-rich than satellites in less massive haloes.

However, as with the discussion of the stellar metallicity difference between the overall populations of centrals and satellites in Section 5.2.1.1, it is important to bear in mind the

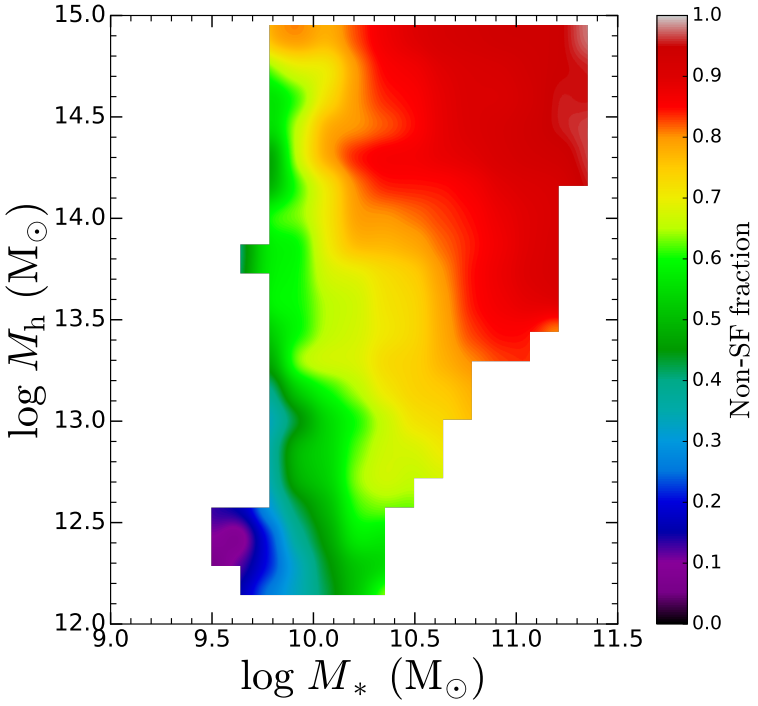

Figure 5.6. The non-SF fraction (i.e. the fraction of galaxies that are green valley or passive) for our sample of satellites (which has been biased by cuts on S/N), colour-coded as a function of stellar mass and halo mass.

quenched fraction effect when interpreting our results for the halo-mass dependence of the overall population of satellites in Fig. 5.5. Numerous studies (e.g. Woo et al. 2013) have shown that, at a fixed stellar mass, the quenched fraction of satellites increases with increasing halo mass. For convenience we show this result in Fig. 5.6, but displaying instead the dependence of the non-SF fraction on stellar mass and halo mass for our sample (which has been biased by cuts on S/N). Thus, the relative number of green valley and passive galaxies (which have higher stellar metallicities than star-forming galaxies of the same stellar mass) increases as one moves from the lower to the higher quartiles. As a result, the quenched fraction effect may be exaggerating the true, inherent dependence of the stellar metallicity of satellites on halo mass.

We show the dependence of the mass-weighted stellar mass–stellar metallicity relation on halo mass for star-forming, green valley and passive satellites in the right, bottom-left and right panels, respectively. Note that the vertical scale and range is different for each panel. In general, we find that the trends with halo mass are less clear, smaller, and less significant than what was seen when studying the overall population of satellites. This may be the case for two reasons. First, the inherent dependence of stellar metallicity on halo mass is weak, so the trend for the overall population is perhaps mostly driven by the quenched fraction effect. Second, due to the lower statistics (since the data is split between star-forming, green valley

and passive), the scaling relations have larger scatter, which complicates interpretation, and the error bars are larger, which makes it more difficult to distinguish between different quartiles. For star-forming satellites, we find that there is no clear trend with halo mass. The error bars on the stellar metallicities are relatively large because the dispersion in the stellar metallicities of star-forming galaxies is relatively high (see Chapter 4). For green valley satellites there is no trend at low stellar masses, but there is an indication that the stellar metallicity tends to increase with increasing halo mass at the high-mass end. Finally, for passive satellites, we find that there is a steady but small (∼0.04 dex between the Low and High quartiles) increase of stellar metallicity with halo mass (of low significance) across the entire stellar mass range studied.

5.2.2.2 Centrals

We show the mass-weighted stellar mass–stellar metallicity relation for centrals in different halo mass quartiles in Fig. 5.7. Given the correlation between the stellar mass of the central galaxy in a group and group halo mass (see e.g. Yang et al. 2008, 2009, 2012), centrals in the higher halo mass quartiles tend to have higher stellar masses. Therefore, there is little overlap in the stellar mass range covered between the different halo mass quartiles. In order to represent the trends with halo mass for centrals more clearly, we therefore use a different stellar-mass binning procedure, now instead choosing mass bins such that there are an equal number of centrals per bin.

Interestingly, for the passive centrals in the right panel of Fig. 5.7, there is an indication that, over the narrow range of stellar mass where there is overlap between subsequent quartiles, centrals of a given stellar mass are more metal-rich when they reside in lower mass haloes. There is perhaps also a similar trend for green valley centrals in the bottom-left panel but it is much weaker than what is seen for passive centrals.

A possible explanation for this effect is that it may be driven by a potential progenitor bias, where the stellar metallicities of passive centrals of a given stellar mass may also depend on their formation histories, which in turn may depend on halo mass (see Man et al. 2019). Since the stellar metallicity of a passive central depends on both the stellar metallicity of its star-forming progenitor and the amount of chemical enrichment that takes place during quenching, any potential halo mass dependence in either of these two factors will determine the halo mass dependence of the stellar metallicity of the passive central. If, as suggested by Man et al. (2019), at a fixed stellar mass, passive centrals with larger halo masses formed earlier, then their star-forming progenitors likely started quenching at a relatively higher redshift. Since the normalisation of the mass–metallicity relation decreases with redshift (see e.g. Maiolino et al. 2008; Lian et al. 2018c), then the stellar metallicities of the star-forming progenitors of passive centrals of a given stellar mass, but with larger halo masses, should be smaller. Conversely,

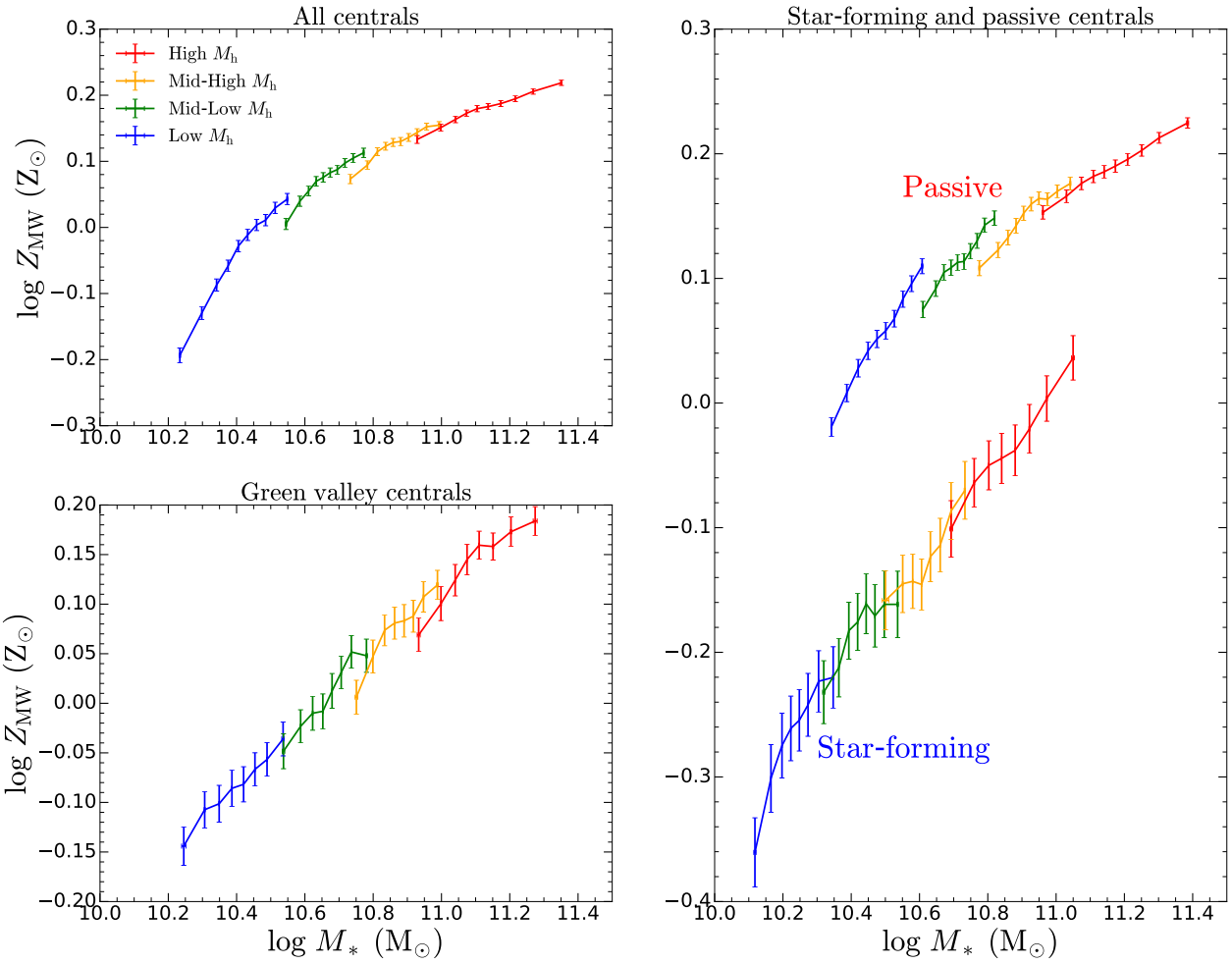

Figure 5.7. Similar to Fig. 5.5, but now showing the mass-weighted stellar mass–stellar metallicity relation for centrals.

however, since the typical gas fractions in galaxies increase with redshift (e.g. Schinnerer et al. 2016; Scoville et al. 2017; Tacconi et al. 2018), the gas fractions of the star-forming progenitors in more massive haloes should be larger. As the amount of chemical enrichment that takes place during quenching depends on how many additional metal-rich stars are formed, which in turn depends on the size of the available gas reservoir (and also the relative importance of different quenching mechanisms, namely starvation and outflows, for more details see Chapters 3 and 4) the star-forming progenitors of passive centrals in more massive haloes likely undergo more chemical enrichment during quenching. Therefore, there are two competing and opposing effects (progenitor metallicity and enrichment during quenching), that both potentially depend on halo mass, that influence the stellar metallicity of the passive central. Depending on which effect is stronger, progenitor bias may or may not explain the observed trend with halo mass, i.e. the vertical offset seen between subsequent halo mass quartiles in Fig. 5.7.

Alternatively, rather than being offset vertically (i.e. in metallicity), the halo mass quartiles for passive central galaxies may in fact be offset horizontally (i.e. in stellar mass). This scenario is depicted more clearly in the left panel of Fig. 5.8, which shows a schematic illustration for the evolution of central galaxies. Passive centrals, due to their lack of gas, subsequently evolve through dry mergers, where both their stellar mass and halo mass increase (causing them to move to the next halo mass quartile), but their stellar metallicity remains relatively unchanged. In fact, the stellar metallicity of the passive central will slightly decrease as it merges with another galaxy, as that galaxy must have a lower stellar mass than the central (otherwise the central would be a satellite, by definition) and thus, on average, has a lower stellar metallicity. Thus, passive central galaxies evolve along a ~horizontal/slightly downward trajectory on the stellar mass–stellar metallicity plane, with the normalisation of the stellar mass–stellar metallicity relation becoming progressively lower for the higher halo mass quartiles. In contrast, star-forming centrals evolve along the star-forming Main Sequence, following a diagonal trajectory in the stellar mass–stellar metallicity plane as they steadily accrete gas from the cosmic web and/or acquire gas in short bursts from wet mergers, causing both their stellar mass and stellar metallicity to increase as progressively more and more metal-rich stars are formed out of the gas reservoir. In addition, as shown in Peng et al. (2015) and Chapter 4, and depicted in Fig. 5.8, the large difference in chemical enrichment between star-forming and passive galaxies necessitates that most star-forming galaxies quench through an extended phase of starvation (a shut down of cold gas accretion). In addition, as discussed in Chapter 4, while starvation is likely to be the prerequisite of quenching, outflows can also contribute, with the combination of starvation and outflows being responsible for quenching the majority of galaxies.

In the right panel of Fig. 5.8 we show a schematic illustration for the evolution of satellite galaxies. The stellar metallicity of star-forming satellites has little dependence on halo mass (as already shown), as well as on overdensity or projected distance (as we will see later in this Section). Again, star-forming satellites typically quench through starvation to become passive satellites, though, given that environmental effects may be at play, we label this as ‘strangulation’ in this case. The stellar metallicity of passive satellites tends to increase with halo mass, as well as with increasing overdensity and decreasing projected distance (as will be shown later in this Section).

5.2.3 Overdensity

In this section we study the dependence of the mass-weighted stellar mass–stellar metallicity relation on the local overdensity, by binning galaxies in quartiles of the local overdensity. Since the distributions of centrals and satellites in local overdensity are different (see Fig. 2.1), and because passive galaxies are more likely to reside in overdense regions, while star-forming

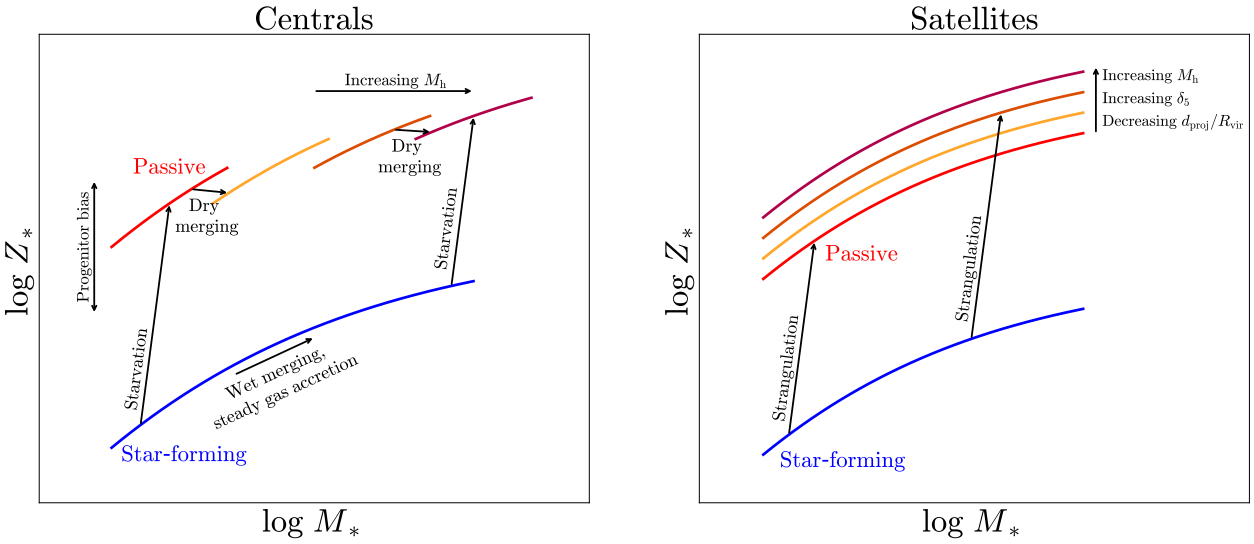

Figure 5.8. A schematic illustration showing how the evolution of galaxies in the stellar mass–stellar metallicity plane depends on environment. Left panel: The evolution of central galaxies is shown. Star-forming centrals (shown in blue) evolve along the Main Sequence, following a diagonal trajectory in the stellar mass–stellar metallicity plane, through steady accretion of gas from the cosmic web and/or by acquiring gas in short bursts from wet mergers. Passive centrals, split into quartiles in halo mass (shown in various shades of red), evolve through dry mergers, following a ∼horizontal/slightly downward trajectory in the stellar mass–stellar metallicity plane, where both their stellar mass (M_*) and halo mass ($M_{\rm h}$) increase (causing them to move to the next halo mass quartile), but their stellar metallicity (Z_*) remains relatively unchanged/decreases slightly as the satellite galaxy involved in the merger is, by definition, of a lower stellar mass and therefore has, on average, a lower stellar metallicity. Alternatively, a potential progenitor bias may also explain the trend with halo mass, where, at a fixed stellar mass, passive centrals in more massive haloes may potentially have lower stellar metallicities because they potentially quenched earlier. Given the correlation between the stellar mass of central galaxies and their group halo mass, there is limited overlap in the stellar mass range covered between the different halo mass quartiles. Star-forming centrals tend to quench through starvation to become passive centrals. Right panel: The evolution of satellite galaxies is shown. The stellar metallicity of star-forming satellites does not show much dependence on halo mass ($M_{\rm h}$), overdensity (δ_5) or projected distance from their central ($d_{\rm proj}/R_{\rm vir}$). In contrast, the stellar metallicity of passive satellites tends to increase with increasing halo mass, increasing overdensity and with decreasing projected distance. Given that environmental effects may be contributing to the starvation of satellites, we label the transition from star-forming to passive as being driven by strangulation.

galaxies are more likely to reside in underdense regions (see e.g. Baldry et al. 2006; Peng et al. 2010; Woo et al. 2013), we use separate quartiles for each of these populations.

5.2.3.1 Satellites

We show the mass-weighted stellar mass–stellar metallicity relation for the overall population of satellites in different overdensity quartiles in the top-left panel of Fig. 5.9. In a similar fashion to what was found in our halo mass analysis in Section 5.2.2, we find that, at a fixed stellar mass, the stellar metallicity for the overall population of satellites tends to increase with increasing overdensity. Furthermore, the offset between the lowest and highest overdensity quartiles also decreases with increasing stellar mass, from 0.1 dex at the low-mass end, down to 0.02 dex at the high-mass end. Again, this would be an indication for a strong dependence of stellar metallicity on environment, but, as with the halo masses, at a fixed stellar mass, the quenched fraction of satellites increases with increasing overdensity (see e.g. Peng et al. 2010; Woo et al. 2013). Thus the quenched fraction effect is likely exaggerating the true dependence of stellar metallicity on the overdensity.

We show the scaling relations for star-forming satellites, green valley satellites and passive satellites in the right, bottom-left and right panels, respectively. As with the halo mass analysis, the inherent dependence of stellar metallicity on overdensity is weaker than what is seen for the overall population of satellites. We do not find any trend for star-forming satellites with overdensity. Green valley satellites display an increasing trend of stellar metallicity with overdensity at the high-mass end. Finally, passive satellites tend to increase in stellar metallicity with increasing overdensity across the entire stellar mass range. Qualitatively, our findings for the overdensity analysis are very similar to what was found in the halo mass analysis. Given the correlation between halo mass and overdensity (see Woo et al. 2013), the similarity between our results using halo masses and overdensities is to be expected.

Interestingly, most of the variation of stellar metallicity with overdensity for the overall population, green valley and passive satellites comes about from the jump to the Mid-High and High quartiles, with little to no variation between the Low and Mid-Low quartiles. We suspect that this may be the case because of two reasons, which would affect the quenched fraction of satellites (relevant for the overall population) and which would affect the impact of environmentally-driven processes (relevant for green valley and passive galaxies). Small overdensities typically correspond to galaxies that are in groups with membership ≤ 5, (i.e. the $N = 5$ used in the calculation of the overdensity δ_5). As discussed in detail in Woo et al. (2013), this corresponds to the so-called cross-halo mode, where the fifth nearest neighbour is in another group and the overdensity is therefore characterising the density of galaxies between groups, rather than the density of galaxies within groups. Hence, in this regime, the overdensity

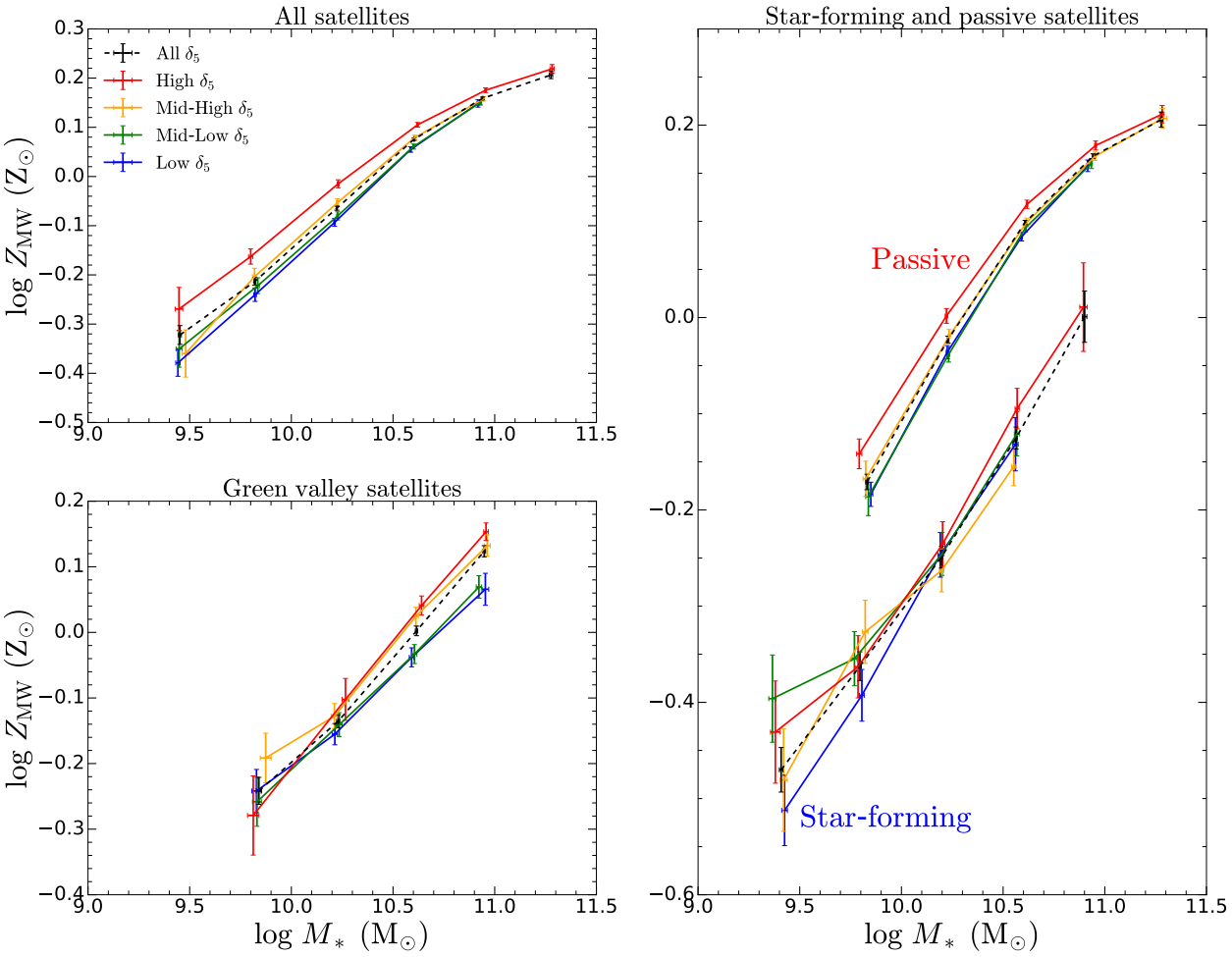

Figure 5.9. Similar to Fig. 5.5, but now binning in quartiles of overdensity δ_5.

is not a strong tracer of environmentally-driven processes and we do not expect to see strong correlations of stellar metallicity (as is the case for green valley and passive satellites) nor quenched fraction (which is shown quite clearly in Peng et al. 2010; Woo et al. 2013) with overdensity. Additionally, for groups with membership > 5, the fifth nearest neighbour is in the same group and the overdensity anti-correlates with the projected distance from the centre of the group (see e.g. Woo et al. 2013). In this regime, relatively small overdensities correspond to large projected distances, for which it is reasonable to expect that environmentally-driven processes have not yet become active and/or insufficient time has elapsed since the infall of the satellite into the group. Hence most of the variation of stellar metallicity (either due to the inherent environmental dependence or brought about by the quenched fraction effect) with overdensity comes about from the jump to the Mid-High and High quartiles.

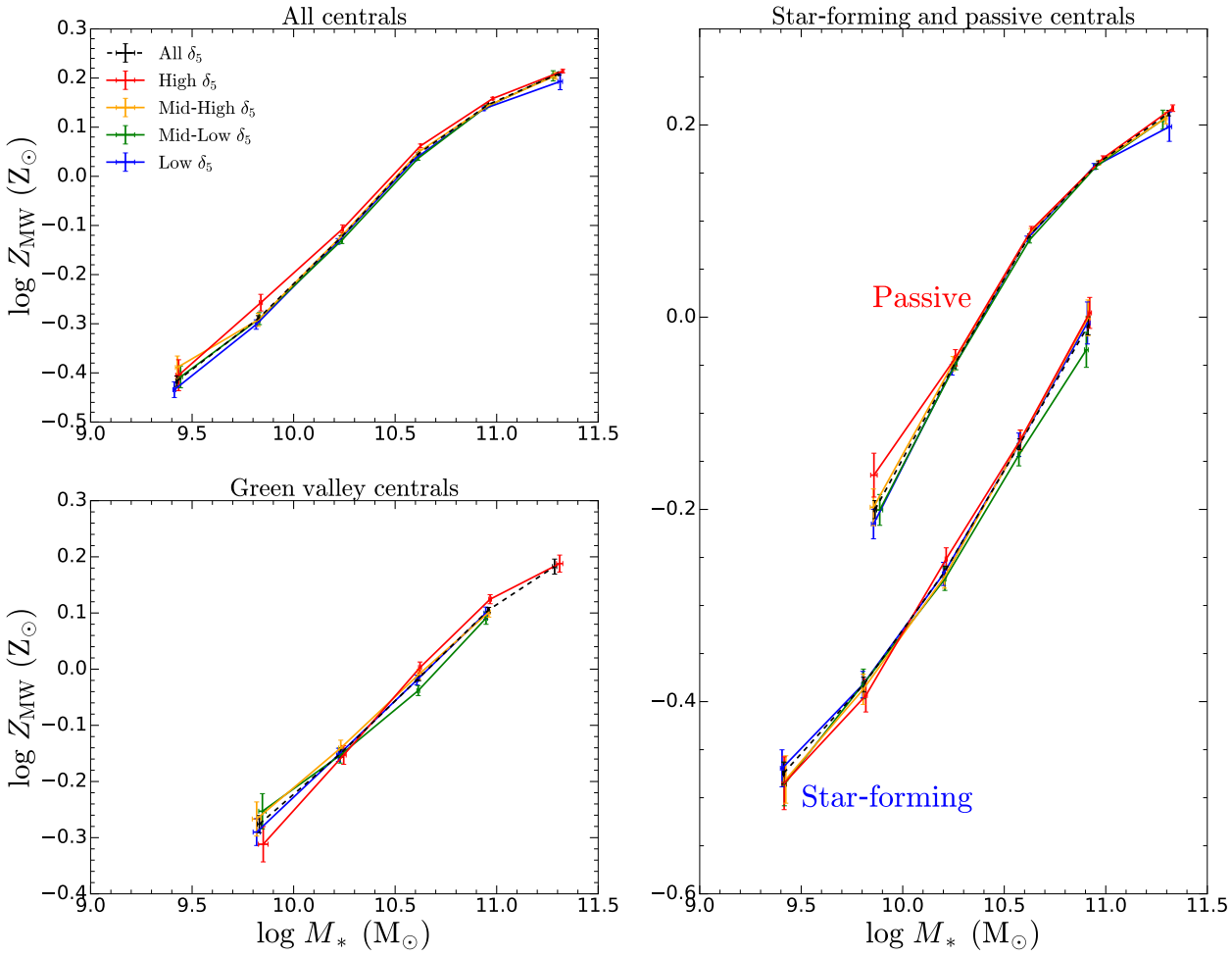

Figure 5.10. Similar to Fig. 5.9, but now showing the mass-weighted stellar mass–stellar metallicity relation for centrals.

5.2.3.2 Centrals

We show the mass-weighted stellar mass–stellar metallicity relation for centrals in different quartiles of overdensity in Fig. 5.10. We find, for the overall population of centrals in the top-left panel, that the stellar metallicity tends to increase slightly with increasing overdensity, but this is primarily due to the jump to the High δ_5 quartile. Since the quenched fraction of centrals increases weakly with overdensity (see e.g. Woo et al. 2013), this is likely to be driven by the quenched fraction effect. Indeed, we do not find any clear trend between stellar metallicity and overdensity for star-forming, green valley or passive centrals.

5.2.4 Projected distance

In this section we study the dependence of the mass-weighted stellar mass–stellar metallicity relation on projected distance (normalised by the virial radius of the galaxy group), by binning satellites in quartiles of projected distance. Our study of the dependence on projected distance is motivated by the fact that some physical processes, like e.g. ram pressure stripping, may only become active close to the centres of groups/clusters (i.e. at small projected distances), or that sufficient time may need to elapse following the infall of a satellite into a group/cluster before the impact of these processes becomes apparent (again, at small projected distances). As star-forming satellites are more likely to reside in the outskirts of galaxy groups, while passive satellites are more likely to reside closer to the centres of galaxy groups (see e.g. Woo et al. 2013), the distributions for star-forming, green valley and passive satellites in projected distance are different, so we use different quartiles for each of these populations.

We show the mass-weighted stellar mass–stellar metallicity relation for the overall population of satellites in different projected distance quartiles in the top-left panel of Fig. 5.11. We find that, at a fixed stellar mass, the stellar metallicity for the overall population of satellites tends to increase with decreasing distance to the central galaxy of the group, with the stellar metallicity difference between the highest and lowest projected distance quartiles decreasing with increasing stellar mass, from 0.08 dex at the low-mass end, down to ∼0 dex at the high-mass end. However, most of this variation of stellar metallicity with projected distance comes about from the jump to the Low $d_{\rm proj}/R_{\rm vir}$ quartile, with little variation with projected distance between the High, Mid-High and Mid-Low quartiles. Taken at face value, this may indicate that the physical processes that affect the chemical evolution of galaxies in galaxy groups/clusters only become active close to the centre of the group, or that sufficient time must have elapsed since the infall of the satellite into the group for the impact of these processes to become significant. However, it is important to bear in mind that the quenched fraction effect is likely exaggerating the true dependence of stellar metallicity on projected distance, as, at a fixed stellar mass, the quenched fraction of satellites increases with decreasing projected distance (see e.g. Woo et al. 2013).

We show the mass-weighted stellar mass–stellar metallicity relation for star-forming satellites, green valley satellites and passive satellites in the right, bottom-left and right panels, respectively. Again, the inherent dependence of stellar metallicity on projected distance is weaker than what was seen for the overall population of satellites, although still present. In addition, we do not find a clear trend with projected distance for star-forming satellites. There is perhaps a weak indication of a trend for green valley satellites, in the sense that the Low quartile tends to be more metal-rich than the other quartiles (except at the low-mass end). Finally,

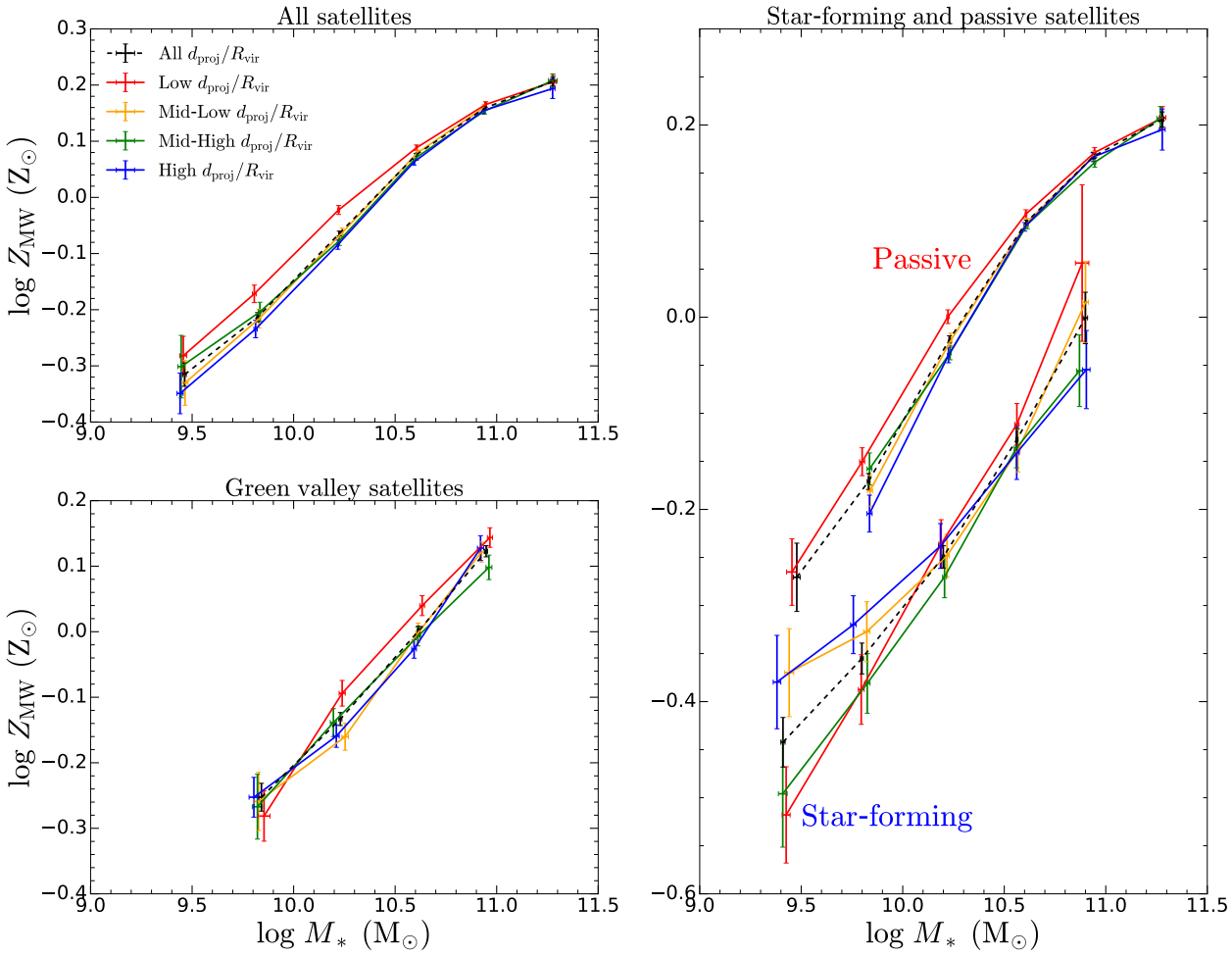

Figure 5.11. Similar to Fig. 5.5, but now binning in quartiles of projected distance $d_{\rm proj}/R_{\rm vir}$. Note that the order of the colour scheme for the quartiles has been reversed. The Low, Mid-Low, Mid-High and High quartiles are now coloured red, orange, green and blue, respectively.

the stellar metallicity of passive satellites tends to increase with decreasing projected distance across the entire stellar mass range, with the difference between the Low and High quartile decreasing with increasing stellar mass.

Overall, the trends seen for both the overall population of satellites, as well as the star-forming, green valley and passive subpopulations, are qualitatively consistent with what was seen in the halo mass and overdensity analysis, in the sense that the trends seen with increasing halo mass or overdensity are also seen with decreasing projected distance. This might be because, for groups with more than five galaxies (i.e. more than the $N = 5$ we use in the calculation of the overdensity δ_5), overdensity anti-correlates with projected distance (for more details, see Woo et al. 2013). However, we do find that the trends in this section are less clear

than what was found earlier, and this may perhaps be because each projected distance quartile is averaged over haloes of all masses. For example, the Low $d_{\rm proj}/R_{\rm vir}$ quartile contains both low-mass haloes (for which we expect the environmental influence to be relatively weak) and high-mass haloes (for which we expect the environmental influence to be relatively strong).

5.3 Environmental quenching

Our analysis thus far has focussed on the stellar mass–stellar metallicity relation. We now shift our attention to the stellar metallicity difference between star-forming and passive galaxies to investigate how the environment contributes to the quenching of galaxies. As discussed in detail in Peng et al. (2015) and Chapters 3 and 4, the stellar metallicity difference between star-forming and passive galaxies can be used to distinguish between different quenching mechanisms as the amount of chemical enrichment during the quenching phase depends on the mechanism. In the case of a galaxy quenching by sudden gas removal (e.g. outflows or rapid ram pressure), the stellar metallicity increase ΔZ_* during the quenching phase is small as relatively few additional stars are formed out of the available gas reservoir. On the other hand, galaxies quenching through starvation (the halting of cold gas accretion) no longer have their ISM diluted by the inflow of pristine gas and form relatively many additional metal-rich stars, so the increase in stellar metallicity during the quenching phase is large. Thus, if galaxies quench primarily through starvation, the stellar metallicity difference between star-forming and passive galaxies of the same stellar mass should be large. In contrast, if galaxies quench primarily through sudden gas removal, the stellar metallicity difference should be small. In reality, galaxies are likely to quench through a combination of starvation and gas removal processes, as indicated in Chapter 4.

We will use the stellar metallicity difference between star-forming and passive galaxies as a proxy for the prevalence of starvation as a mechanism for quenching star formation in galaxies. In particular, we wish to investigate whether environmental effects contribute to the starvation of galaxies, and if so, to put constraints on the physical origin of any environmentally-driven starvation. We will study this through a comparison between the stellar metallicity difference for centrals and satellites in Section 5.3.1, and a comparison between the stellar metallicity difference for centrals and satellites in different quartiles of halo mass, overdensity and projected distance in Section 5.3.2. If e.g. the stellar metallicity differences for satellites are larger than for centrals, this could be due to two effects. First, that starvation occurs more frequently for satellites. Second, that the typical chemical enrichment during starvation is larger for satellites. The latter would be the case if relatively more of the available gas reservoir is consumed in star formation rather than removed in galactic winds or gas stripping processes, i.e. if the ‘effective’

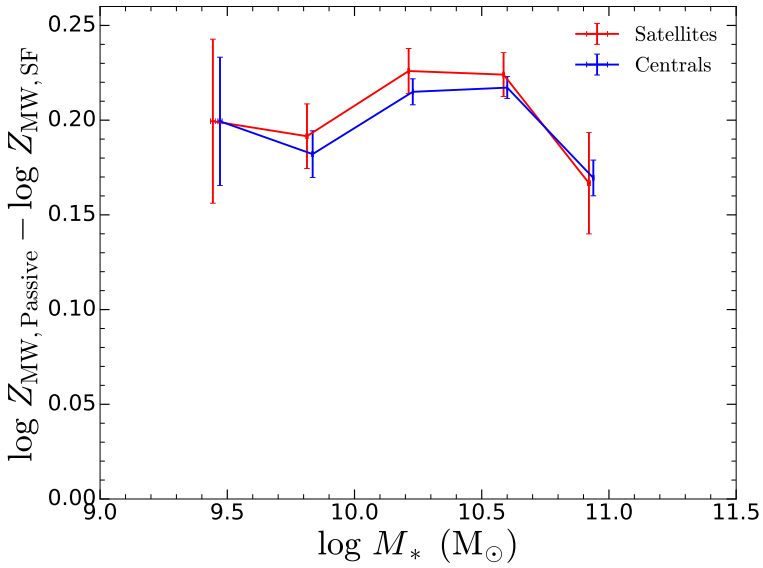

Figure 5.12. The mass-weighted stellar metallicity difference $\Delta \log Z_{\rm MW} = \log Z_{\rm MW,Passive} - \log Z_{\rm MW,SF}$ between star-forming and passive galaxies, for centrals (blue) and satellites (red). Error bars represent the 1σ error on the stellar metallicity difference.

mass-loading factor $\lambda_{\rm eff}$ of outflows and/or gas stripping is smaller in satellites than in centrals.

5.3.1 Central–satellite dichotomy

In this section we investigate whether the mass-weighted stellar metallicity difference between star-forming and passive galaxies differs for centrals and satellites. In particular, we study the stellar metallicity difference between star-forming centrals and passive centrals, as well as the difference between star-forming satellites and passive satellites.

In Fig. 5.12, we show the mass-weighted stellar metallicity difference between star-forming and passive galaxies, for both centrals (blue) and satellites (red). Although star-forming satellites and passive satellites are slightly more metal-rich than star-forming centrals and passive centrals of the same stellar mass, respectively (see Figs. 5.1 and 5.3), we do not find an indication for a significant offset between the stellar metallicity differences for centrals and satellites. This comes about because the offsets between star-forming satellites and centrals (0.01–0.02 dex) are comparable to the offsets between passive satellites and centrals (0.01–0.03 dex). Hence, when taking the stellar metallicity difference between star-forming and passive galaxies, there is only a ∼0.01 dex offset between centrals and satellites, as shown in Fig. 5.12.

Our lack of an offset between the stellar metallicity differences for centrals and satellites is not in line with the findings of Peng et al. (2015), who instead found an indication that the metallicity difference is larger for satellites at low masses ($\log(M_*/\rm M_\odot) = 9.5$). This

disagreement in the results may come about for a number of reasons. First, we use a different sample of galaxies, namely SDSS DR7 rather than DR4. Second, we classify galaxies as star-forming and passive using star formation rates, rather than galaxy colours. Third, we use stellar metallicities obtained using a different spectral fitting procedure, namely the mass-weighted stellar metallicities from FIREFLY rather than the light-weighted stellar metallicities from Gallazzi et al. (2005).

5.3.2 Dependence on other environmental parameters

In this section we study how the stellar metallicity difference between star-forming and passive galaxies depends on halo mass, overdensity and projected distance, for both centrals and satellites.

In Section 5.2 we found a subtle indication that the stellar metallicity of both green valley and passive satellites depends on environment, with the stellar metallicities tending to increase slightly with both increasing halo mass and overdensity, and with decreasing projected distance. In contrast, we found no strong evidence for a trend between stellar metallicity and environment for star-forming satellites, neither for halo mass, nor for overdensity or projected distance. Thus, in this section, when computing the stellar metallicity differences, we will make the assumption that the stellar metallicity of star-forming satellites (and star-forming centrals) does not depend on environment, i.e. we will not bin the star-forming satellite population into quartiles and instead use the relation for the entire population of star-forming satellites (given by the curves named 'All' in Figs. 5.5, 5.9 and 5.11). On the other hand, we will bin the green valley and passive satellites into quartiles of halo mass, overdensity and projected distance, in a similar fashion to what was done in Section 5.2. In Appendix B.4, we relax the assumption that the stellar metallicity of star-forming satellites is independent of environment, by also splitting the star-forming satellite population into quartiles of environment. Briefly, we find in that case that, given the scatter in the scaling relations for star-forming satellites and the relatively large error bars, any trends seen with environment are washed out.

We show how the mass-weighted stellar metallicity difference between star-forming and passive galaxies depends on group halo mass (top panels), overdensity (middle panels) and projected distance (bottom panel) for both centrals (left panels) and satellites (right panels) in Fig. 5.13. In the following we discuss these trends separately for centrals and satellites.

5.3.2.1 Centrals

For centrals, the analysis of the stellar metallicity difference on halo mass in the top-left panel is complicated by the fact that there is little overlap in stellar mass between subsequent halo

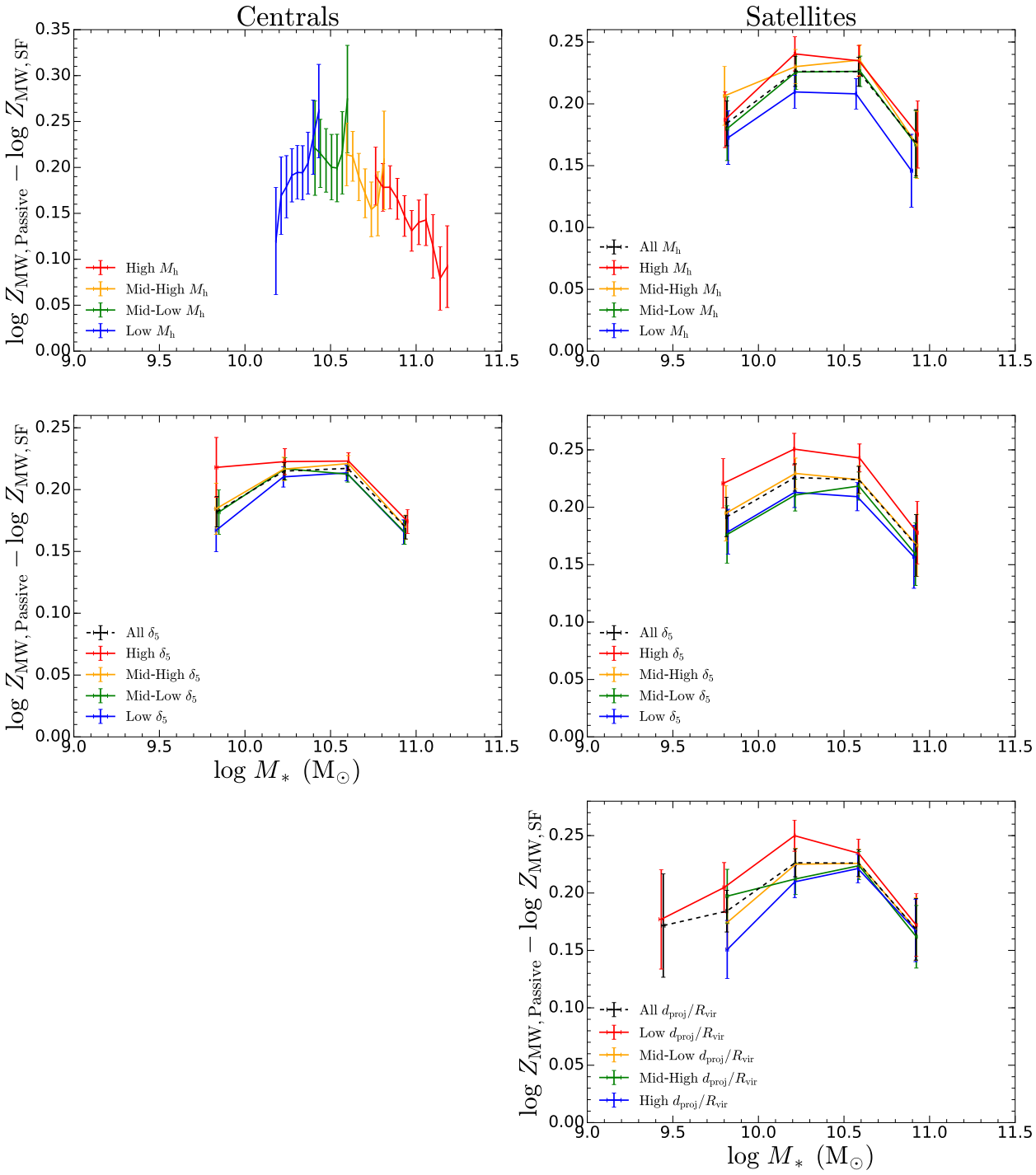

Figure 5.13. The mass-weighted stellar metallicity difference $\Delta \log Z_{\rm MW} = \log Z_{\rm MW,Passive} - \log Z_{\rm MW,SF}$ between star-forming and passive galaxies for centrals (left panels) and satellites (right panels) in quartiles of different environmental measures. The Low (blue), Mid-Low (green), Mid-High (orange) and High (red) quartiles correspond to the $0^{\rm th}$–$25^{\rm th}$, $25^{\rm th}$–$50^{\rm th}$, $50^{\rm th}$–$75^{\rm th}$ and $75^{\rm th}$–$100^{\rm th}$ percentiles, respectively. We reverse the order of the colour scheme for the projected distance quartiles. We assume that the stellar metallicities of star-forming satellites (and star-forming centrals) do not depend on environment, and therefore only use quartiles for the passive satellite (and passive central) population. It should be noted that the ranges associated with the quartiles for centrals and satellites are different. We also show the stellar metallicity differences obtained without splitting into quartiles (named All, shown in dashed black). Top panels: passive galaxies are split into quartiles of group halo mass $M_{\rm h}$. Middle panels: passive galaxies are split into quartiles of overdensity δ_5. Bottom panel: passive satellites are split into quartiles of projected distance from their central $d_{\rm proj}/R_{\rm vir}$.

mass quartiles. Thus, the only trend that we can comment on is that, where there is overlap between quartiles, the stellar metallicity difference is marginally larger for the lower quartile of the pair. In the middle-left panel, there is a subtle (but not significant) indication that the stellar metallicity difference perhaps increases with overdensity. Thus, if the environment affects the stellar metallicity difference between star-forming centrals and passive centrals, it has only a very marginal effect at most.

5.3.2.2 Satellites

For satellites, there is a relatively stronger (but still not significant) trend between the stellar metallicity difference and environment. In the top-right panel, the stellar metallicity difference tends to increase with halo mass, with a ~0.04 dex offset between the Low and High quartiles. Similarly, in the middle-right panel, the stellar metallicity difference tends to increase with overdensity, with a 0.02–0.04 dex offset between the Low and High quartiles. Finally, in the bottom-left panel, we find that the stellar metallicity difference also tends to increase with decreasing projected distance, with a 0.01–0.05 dex offset between the Low and High quartiles. Despite the excellent overall statistics in SDSS DR7, there are only a relatively small number of satellites (especially with respect to centrals) in our sample. Hence, although the trends for satellites appear to be stronger than for centrals, these trends are still only marginally significant: at most at the 2σ level in some mass bins. However, it should be noted that, given the relatively weak inherent dependence of stellar metallicity on environment (see Section 5.2), a study of stellar metallicity differences (which have larger error bars than stellar metallicities) is likely to only find marginally significant trends even if the statistics are high (as is the case with SDSS DR7).

5.3.3 Summary of environmental quenching

As discussed in Peng et al. (2015) and Chapter 4, and also outlined at the beginning of this section, the large stellar metallicity difference observed between the overall population of star-forming and passive galaxies provides strong evidence indicating that, for the majority of galaxies, quenching likely involved an extended phase of starvation, with gas removal through outflows or ram pressure stripping also contributing to the quenching. This starvation process is generally ascribed to two primary classes of phenomena: i) mass-dependent phenomena, in which the halo of the galaxy is heated by AGN feedback (via energy injection through jets or winds) or through gravitational shock-heating, resulting in the suppression of cold accretion onto the galaxy (e.g. Dekel & Birnboim 2006; Croton et al. 2006; Fabian 2012; Brownson et al. 2019); ii) environmental effects, often referred to as ‘strangulation’, that occur when satellite

galaxies plunge into the hot halo of a larger galaxy or an overdense region (i.e. a group or cluster) and have their circumgalactic medium stripped and/or become disconnected from the cosmic web, which prevents the satellite galaxy from accreting further fresh gas (e.g. Larson et al. 1980; Van Den Bosch et al. 2008; Feldmann & Mayer 2015; van de Voort et al. 2017; Aragon Calvo et al. 2019).

The lack of environmental dependence in the stellar metallicity difference between star-forming and passive central galaxies indicates, not surprisingly, that the starvation responsible for quenching central galaxies is not driven by environmental phenomena, but primarily by mass-related phenomena such as halo heating by AGN and halo gravitational shock heating, or the recently proposed angular momentum quenching (Peng & Renzini 2020; Renzini 2020), where a galaxy can be deprived of new molecular gas when the inflowing gas accreted from the IGM comes in with excessive angular momentum.

The presence of environmental effects (although only at the 2σ level) on the stellar metallicity difference between star-forming and passive satellite galaxies indicates that environmental 'strangulation' does play a role in the starvation process that quenches satellite galaxies. However, the stellar metallicity difference accounted for by environmental effects is small relative to the overall stellar metallicity difference for the entire satellite population. Specifically, while the overall stellar metallicity difference between star-forming and passive satellite galaxies ranges from 0.10 to 0.22 dex depending on mass (see also Chapter 4 where a slightly larger stellar mass range is investigated), the environmental contribution to this difference is less than 0.04 dex. Therefore, while environmental 'strangulation' does play a role in the quenching of satellite galaxies, the bulk of their starvation is still due to mass-related effects.

We also note that, as pointed out in Chapter 4, that gas removal processes can also contribute to the quenching of satellite galaxies, either in the form of outflows or ram pressure stripping, with the gas removal processes being less important in massive galaxies, but becoming progressively more important in lower mass galaxies. However, quantitatively constraining the role of these phenomena relative to strangulation would be challenging. This would demand an analysis similar to that performed in Chapter 4, which would require incorporating the stellar ages and stellar metallicities of satellites split by environment (i.e. halo mass, local overdensity and projected distance) into the analysis. However, the limited statistics would not allow us to provide meaningful constraints, as even our analysis in Chapter 4 struggled to obtain significant constraints in some mass bins, even when analysing the full population of galaxies in SDSS DR7.

Qualitatively, however, the increase in the stellar metallicity difference between star-forming and passive satellites with environment (i.e. with increasing halo mass, increasing local overdensity and decreasing projected distance) indicates that starvation becomes relatively more

prevalent, i.e. outflows become less important with increasing environment. In the context of our chemical evolution model, this therefore implies that the 'effective' mass-loading factor $\lambda_{\rm eff}$, which describes the net gas outflow rate $\Lambda = \lambda_{\rm eff} \times {\rm SFR}$ during quenching, decreases with increasing halo mass, increasing local overdensity and with decreasing projected distance. Thus, in addition to environmental 'strangulation', the larger stellar metallicity differences in denser environments may also be due to ram pressure confinement, where the denser and hotter gas found in denser environments (i.e. increasing δ_5) nearer to the centres (i.e. decreasing $d_{\rm proj}/R_{\rm vir}$) of more massive haloes (i.e. increasing $M_{\rm h}$) helps confine and prevent outflowing gas from escaping the satellite galaxy, thereby reducing $\lambda_{\rm eff}$ through the enhanced recycling of outflowing gas.

5.4 Comparison with gas-phase metallicity studies

In this section we discuss the environmental trends that we have found for stellar metallicities, focussing on the comparison against environmental trends that previous studies have found for *gas-phase* metallicities. It should be noted that while gas-phase metallicities have only been measured for star-forming galaxies, stellar metallicities can be measured for both star-forming and passive galaxies.

The environmental dependence of the stellar populations in galaxies has previously been investigated by Pasquali et al. (2010), who studied the overall populations of centrals and satellites and did not differentiate between star-forming, green valley and passive galaxies in their analysis. They found that the stellar metallicities of galaxies are strongly dependent on environment, with satellites being substantially more metal-rich (0–0.2 dex, decreasing with stellar mass) than centrals of the same stellar mass. In contrast, Pasquali et al. (2012) studied the gas-phase metallicities in star-forming galaxies, and found that the environmental dependence was much weaker, with satellites only being marginally more metal-rich (0-0.05 dex, decreasing with stellar mass) than centrals of the same stellar mass. Furthermore, after restricting their stellar metallicity analysis to a sample of galaxies for which gas-phase metallicities are available (i.e. only including star-forming galaxies and excluding passive galaxies), Pasquali et al. (2012) found that the stellar metallicity difference between centrals and satellites becomes much smaller (~0). Thus the large stellar metallicity differences between centrals and satellites found in Pasquali et al. (2010) were primarily driven by the environmental dependence of the quenched fraction of galaxies. As shown in this chapter (and implicitly by the findings of Pasquali et al. 2012), the true stellar metallicity difference between centrals and satellites is in fact much smaller (see Fig. 5.1).

In addition to Pasquali et al. (2012), numerous other works have also compared the gas-

phase metallicities of central and satellite galaxies (see e.g. Ellison et al. 2009; Peng & Maiolino 2014a), finding that satellites are typically more metal-rich than centrals of the same stellar mass. Interestingly, although this is qualitatively similar to our results for star-forming galaxies (as well as green valley and passive galaxies), we note that the *stellar* metallicity differences we find between star-forming centrals and satellites (0.01–0.02 dex) are smaller than the corresponding *gas-phase* metallicity differences (∼0.05 dex). This quantitative disagreement can come about for two reasons. First, systematic effects associated with the choice of metallicity calibration and the different methods for measuring gas-phase and stellar metallicities. Second, while gas-phase metallicities provide an instantaneous measure of chemical enrichment as they probe the current conditions in the ISM, stellar metallicities instead provide a cumulative measure of chemical enrichment that is averaged over longer timescales (especially for the mass-weighted metallicities we study in our analysis). As a result, stellar metallicities will react less promptly and therefore be less sensitive to recent or ongoing environmentally-driven processes that cause metal enrichment, due to the averaging effect over the entire stellar population.

The dependence of gas-phase metallicities on further environmental parameters has also been investigated, with studies finding that the gas-phase metallicities of star-forming satellites at a fixed stellar mass tends to increase with increasing halo mass (e.g. Pasquali et al. 2012), increasing local overdensity (e.g. Mouhcine et al. 2007; Cooper et al. 2008; Ellison et al. 2009; Peng & Maiolino 2014a; Wu et al. 2017) and decreasing projected distance from the central galaxy (for massive clusters, e.g. Petropoulou et al. 2012; Maier et al. 2016, 2019). In contrast, we find that the stellar metallicities of star-forming satellites do not depend on environment. This discrepancy between the trends for gas-phase and stellar metallicities is likely to be due to the fact that stellar metallicities react less promptly and are therefore less sensitive to recent metal enrichment (which is likely being driven by environmental processes). However, if the enrichment (process) persists on longer timescales, especially during the quenching process, then this environmental dependence should become observable in the stellar metallicities as well, especially for passive satellites and potentially also for green valley satellites. Indeed, we find that the stellar metallicities of passive satellites (and green valley satellites, although with less significance) increase with increasing halo mass, increasing local overdensity and decreasing projected distance, which is likely reflecting the aforementioned environmental trends for the gas-phase metallicities of star-forming satellites.

Furthermore, both Peng & Maiolino (2014a) and Lian et al. (2019) find that the environmental dependence (in terms of the local overdensity) of the gas-phase metallicities of star-forming satellites decreases with increasing stellar mass. Again, while we do not see this trend in the stellar metallicities of star-forming satellites, it is readily apparent for passive satellites. Indeed, we find that, for both the local overdensity and projected distance, the envir-

onmental dependence of the stellar metallicities of passive satellites decreases with increasing stellar mass.

Finally, similar to studies of the gas-phase metallicities of central galaxies (e.g. Peng & Maiolino 2014a), we find that the stellar metallicities of star-forming centrals (and also green valley and passive centrals) do not depend on local overdensity.

5.5 Summary and conclusions

We have utilised the statistical power of SDSS DR7 to investigate the environmental dependence of the stellar populations of galaxies, as well as environmental quenching. We obtain the following results:

(i) Similar to earlier works, such as Pasquali et al. (2010), we find that satellites are both more metal-rich (< 0.1 dex) and older (< 2 Gyr) than centrals of the same stellar mass, which has often been interpreted as an indication that the environment plays an important role in shaping both the chemical evolution and star formation histories of galaxies. However, after separating star-forming, green valley and passive galaxies, we find that the true environmental dependence is in fact much weaker, with star-forming, green valley and passive satellites being only marginally more metal-rich (< 0.03 dex) and older (< 0.5 Gyr) than star-forming, green valley and passive centrals of the same stellar mass.

(ii) The strong environmental effects (found by previous studies) when galaxies are not differentiated result from a selection effect brought about by the environmental dependence of the quenched fraction in galaxies, as both the stellar metallicities and stellar ages of passive galaxies are considerably larger than those of star-forming galaxies of the same stellar mass (with $\Delta \log Z_* \sim 0.15$ and $\Delta \mathrm{age} \sim 3$ Gyr). Thus, we strongly advocate for the separation of the star-forming, green valley and passive populations of galaxies when the environmental dependence of galaxy properties are investigated, as otherwise both the true environmental dependence of these properties will be exaggerated and the mass dependence of any environmental effects will be misrepresented, especially when the properties are starkly different for star-forming and passive galaxies (e.g. galaxy colours, SFRs, galaxy sizes).

(iii) We also investigate further environmental trends for both centrals and satellites separately, by dividing star-forming, green valley and passive galaxies into quartiles of halo mass, local overdensity and (for satellites only) projected distance from the central. We obtain the following results:

- We find no further environmental trends for star-forming galaxies, neither for centrals nor for satellites.

- In contrast, the stellar metallicities of green valley and passive satellites increase weakly with increasing halo mass, increasing local overdensity and decreasing projected distance.
- Furthermore, we find that the stellar metallicities of central galaxies do not depend on the local overdensity.
- We also find a unique feature in the stellar mass–stellar metallicity relation for passive centrals, where galaxies in more massive haloes have larger stellar mass at constant stellar metallicity. This effect is interpreted in terms of dry merging of passive central galaxies and/or progenitor bias.

(iv) Finally, we use the method of Peng et al. (2015) to investigate environmental quenching, using the stellar metallicity difference between star-forming and passive galaxies as a proxy for the prevalence of starvation as a quenching mechanism in galaxies. We find the following:

- Although satellites have slightly enhanced stellar metallicities with respect to centrals, we find that the stellar metallicity differences between star-forming and passive satellites, and star-forming and passive centrals are comparable.
- Furthermore, following the environmental trends in the stellar mass–stellar metallicity relations that we discussed earlier, the stellar metallicity differences between star-forming and passive centrals do not depend on halo mass nor on local overdensity, indicating that the starvation responsible for quenching central galaxies is not driven by environmental phenomena, but primarily by mass-related phenomena.
- In contrast, the stellar metallicity difference between star-forming and passive satellites increases weakly with increasing halo mass, increasing local overdensity and decreasing projected distance, which we interpret in terms of moderate environmental starvation ('strangulation') contributing to the quenching of satellite galaxies. Indeed, as the stellar metallicity difference accounted for by environmental effects (< 0.04 dex) is small relative to both the overall stellar metallicity difference for the entire satellite population (0.10–0.22 dex, see also Chapter 4) and the mass-dependence of this overall stellar metallicity difference, this indicates that, while environmental strangulation does play a role in the quenching of satellite galaxies, the bulk of their starvation is still due to mass-related effects.

Chapter 6

A Global and Spatially-Resolved View of Galaxy Quenching

6.1 Introduction

In this chapter we harness the spatially-resolved power of the SDSS-IV MaNGA integral field spectroscopic galaxy survey to investigate how quenching operates on a radial basis within galaxies. In particular, we study the global stellar population parameters for ~5000 galaxies in the local Universe to determine whether the key mass- and environment-dependent trends in galaxy quenching found in Chapters 4 and 5 using the single fibre SDSS Legacy Survey spectra hold true globally or only apply to the central regions in galaxies. Furthermore, we study the radial variation of the stellar population parameters of galaxies to address how quenching operates within galaxies, analysing how the stellar metallicity difference between star-forming and passive galaxies varies with radial distance to determine whether starvation is a primary driver of quenching at all radii in galaxies.

This chapter is structured as follows. In Section 6.2, we study the mass- and environment-dependence of the global stellar population parameters of galaxies, aiming to verify whether our key findings in Chapters 4 and 5 also hold true globally. In Section 6.3, we study the radial variation of the stellar population parameters of galaxies to investigate how quenching operates within galaxies. Finally, in Section 6.4 we summarise our main findings and conclude.

6.2 Quenching: a global view

In this section we study the global stellar population properties of star-forming, green valley and passive galaxies, obtained by integrating all the light in each MaNGA galaxy out to ∼1.5–2.5 R_e and fitting the resulting spectrum with FIREFLY, with our analysis focussing on the stellar mass–stellar metallicity and stellar mass–stellar age relations that are obtained using these integrated stellar metallicities and ages. Thus the stellar metallicities and ages that we study here truly represent the global properties of galaxies, as opposed to only the properties of the central regions that are probed by the individual 3″ SDSS Legacy Survey fibre in our analysis in Chapters 4 and 5, which may potentially be a cause for concern for those studies. Of course, the capability of studying such global properties with MaNGA comes at the cost of greatly reduced statistics with respect to the SDSS Legacy Survey data that was used in Chapters 4 and 5.

In Chapter 4, we found that passive galaxies are significantly more metal-rich (in the centre) than star-forming galaxies of the same stellar mass. Our models indicated that galaxies at all masses must quench through starvation, with outflows becoming increasingly important with decreasing stellar mass. In addition, in Chapter 5, we found that the environment only leaves a weak imprint on the stellar populations of galaxies, with satellites being only marginally more metal-rich and older than centrals of the same stellar mass. Using the global stellar metallicities and ages available from MaNGA we therefore wish to verify whether these key findings of Chapters 4 and 5 were affected by aperture effects and therefore only hold in the central regions of galaxies, or whether their conclusions instead hold true globally: from the innermost to the outermost regions of galaxies.

In Section 6.2.1, we study the global stellar mass–stellar metallicity and stellar mass–stellar age relations for star-forming, green valley and passive galaxies. In Section 6.2.2, we use chemical evolution models to put constraints on the relative importance of starvation and outflows in quenching star formation in the progenitors of local passive galaxies and in local green valley galaxies. Finally, in Section 6.2.3, we investigate the environmental dependence of the global stellar mass–stellar metallicity and stellar mass–stellar age relations, with emphasis on any underlying differences between central and satellite galaxies.

6.2.1 Global scaling relations

6.2.1.1 Stellar metallicity

We show the global mass-weighted stellar mass–stellar metallicity relation for star-forming (blue), green valley (green) and passive galaxies (red) in the top panel of Fig. 6.1. Similar to Chapter 4 (and also Peng et al. 2015), we find that the stellar metallicities of star-forming,

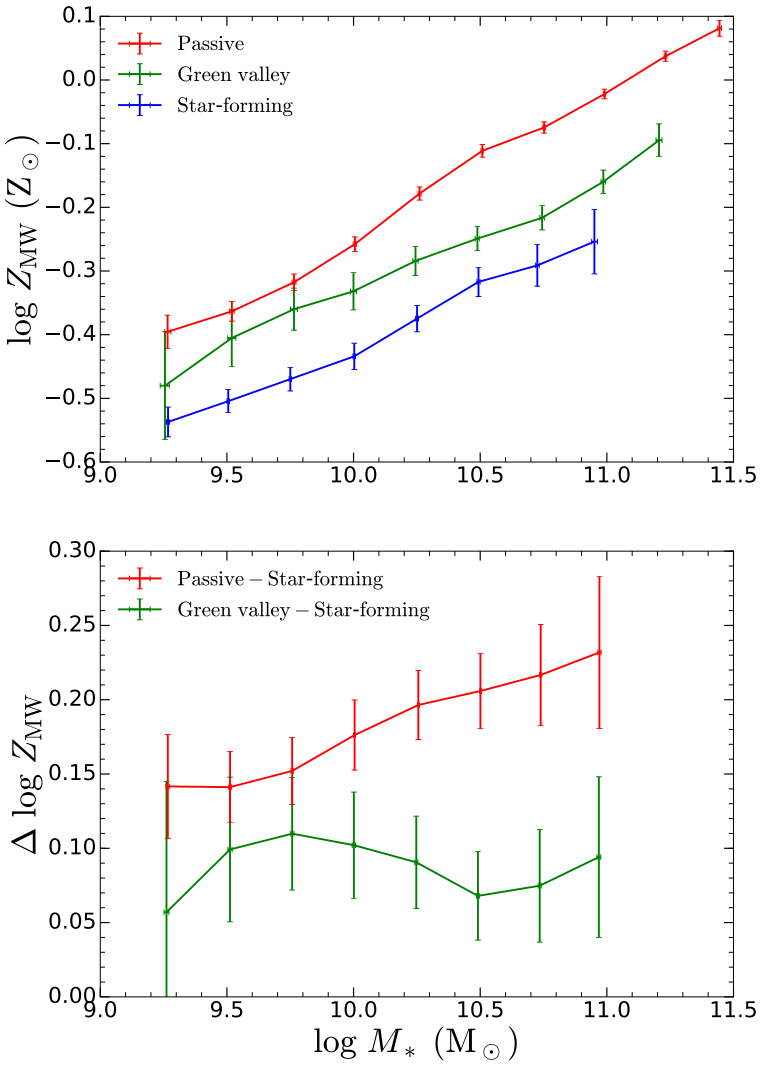

Figure 6.1. Top panel: The mass-weighted stellar mass–stellar metallicity relation for star-forming (blue), green valley (green) and passive (red) galaxies, using global stellar metallicities obtained by integrating all the light in each MaNGA galaxy out to ~1.5–2.5 R_e. Galaxies are binned in stellar mass and the median stellar metallicity in each mass bin is shown. Error bars correspond to the 1σ uncertainty on the median. Bottom panel: The stellar metallicity difference $\Delta \log Z_{\rm MW}$ between star-forming and passive galaxies (red) and between star-forming and green valley galaxies (green). Error bars correspond to the 1σ uncertainty on the stellar metallicity difference, obtained by adding in quadrature the errors on the metallicities for star-forming and green valley/passive galaxies.

green valley and passive galaxies tend to increase with stellar mass. Furthermore, passive galaxies tend to be more metal-rich than star-forming galaxies of the same stellar mass, with green valley galaxies having metallicities that are intermediate between those of star-forming and passive galaxies. Thus, the enhanced level of chemical enrichment of passive galaxies with respect to star-forming galaxies is not just confined to the central regions, but is instead a global property, indicating that starvation is likely to be driving the global quenching of star formation in galaxies.

However, we do find that there are some quantitative differences between the global stellar mass–stellar metallicity relation we study here and the innermost 3″ stellar mass–stellar metallicity relation studied in Chapter 4. First, the normalisation of the global stellar mass–stellar metallicity relation is lower, with the median stellar metallicities of star-forming, green valley and passive galaxies tending to be lower at any given stellar mass (by 0.05–0.25 dex) than what was found in Chapter 4. This result is to be expected however, as numerous studies have shown (e.g. Goddard et al. 2017a,b; Zheng et al. 2017; Li et al. 2018; Oyarzún et al. 2019) that stellar metallicity gradients in both star-forming and passive galaxies tend to be negative, with the stellar metallicity decreasing with increasing radial distance from the centre of the galaxy. Thus, our global stellar metallicities, which incorporate the light from the outer, more metal-poor stars in the galaxy, in addition to the light from the inner, more metal-rich stars (probed by the central 3″ fibre in Chapter 4), will tend to be lower.

Furthermore, we find, as shown in the bottom panel of Fig. 6.1, that the stellar metallicity difference between star-forming and passive galaxies tends to increase with increasing stellar mass. This is in contrast to our findings in Chapter 4 (and also Peng et al. 2015), where we instead find that the stellar metallicity difference tends to decrease with increasing stellar mass. Evidently this difference between our findings using the global stellar metallicities versus the innermost 3'' metallicities must be related to the relative stellar metallicity gradients in star-forming and passive galaxies, and how these depend on stellar mass. In particular, we believe this disagreement is driven by a mass-dependent aperture effect, which, when combined with the bulge–disc decomposition of star-forming galaxies, generates this discrepancy with the single-fibre result. Indeed, since the typical size of galaxies (as measured through e.g. the effective radius R_e) tends to increase with stellar mass (e.g. van der Wel et al. 2008; Cappellari et al. 2013; Cappellari 2013; van der Wel et al. 2014; Van Dokkum et al. 2015; Cappellari 2016b), the fixed 3″ aperture of the SDSS fibre captures light from a relatively smaller fraction of the entire galaxy for galaxies of a higher stellar mass. In addition, the central bulge in star-forming galaxies tends to be more metal-rich than the surrounding disc (see e.g. Johnston et al. 2012, 2017; Breda & Papaderos 2018; Tabor et al. 2019). Together, this means that in massive star-forming galaxies the 3″ fibre mostly only probes the central, metal-rich bulge, while in less

massive star-forming galaxies more of the surrounding relatively metal-poor disc is probed. Therefore, as stellar mass increases, the stellar metallicities for star-forming galaxies become more strongly biased towards the high value of the central metal-rich bulge. Since passive galaxies do not have a bulge–disc decomposition and also tend to have smaller effective radii than star-forming galaxies of the same stellar mass (see e.g. Cappellari et al. 2013; Cappellari 2013; van der Wel et al. 2014; Van Dokkum et al. 2015; Cappellari 2016b), this effect is smaller for passive galaxies. Thus the biased view of a 3″ aperture actually underestimates the actual stellar metallicity difference between massive star-forming and passive galaxies, which helps explain the opposite trends found in this chapter and in Chapter 4.

We study the global light-weighted stellar mass–stellar metallicity relation in Appendix C.2.1. Briefly, we find, similar to our findings in Chapter 4 (and also Peng et al. 2015), that the light-weighted stellar metallicities of star-forming, green valley and passive galaxies tend to increase with stellar mass, with both passive and green valley galaxies being more metal-rich than star-forming galaxies of the same stellar mass.

6.2.1.2 Stellar age

We show the global mass-weighted stellar mass–stellar age relation for star-forming, green valley and passive galaxies in the top panel of Fig. 6.2. Similar to our findings in Chapter 4, we find that the ages of star-forming, green valley and passive galaxies increase weakly with increasing stellar mass. Additionally, passive galaxies tend to be older than star-forming galaxies of the same stellar mass, with green valley galaxies having ages intermediate between star-forming and passive galaxies. The mass-weighted age difference between star-forming and green valley/passive galaxies is shown in the bottom panel of Fig. 6.2. The age differences are relatively flat with stellar mass, with the age difference between star-forming and green valley galaxies typically being 3.5–4 Gyr, while the age difference between star-forming and passive galaxies is typically 4–4.5 Gyr.

We study the global light-weighted stellar mass–stellar age relation in Appendix C.2.2. Again, we find similar qualitative trends between the global stellar ages studied here and the ages from the central 3″ studied in Chapter 4. Light-weighted stellar ages tend to increase with increasing stellar mass. Furthermore, green valley and passive galaxies tend to be older than star-forming galaxies of the same stellar mass.

6.2.2 Quenching mechanisms

In this section we revisit the quantitative analysis of stellar metallicity differences that were carried out in Chapter 4, now using the global mass-weighted stellar mass–stellar metallicity

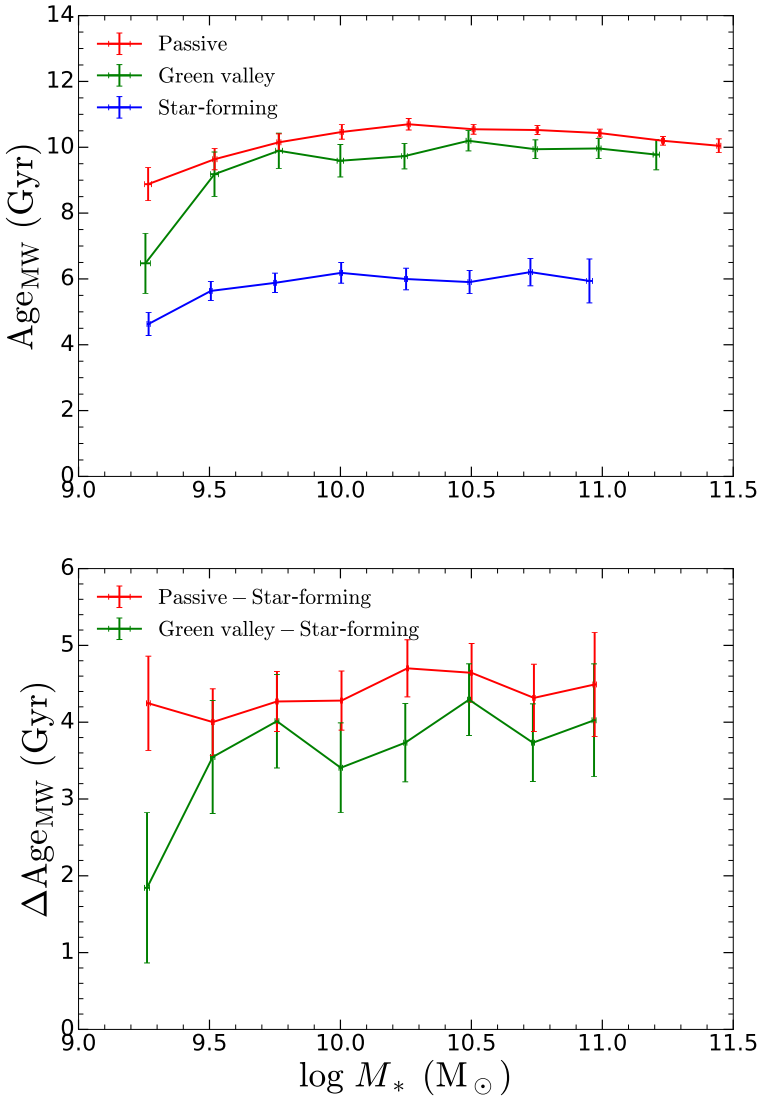

Figure 6.2. Similar to Fig. 6.1, but now showing the global mass-weighted stellar mass–stellar age relation.

relation obtained in this work. Since there are quantitative differences between the global and the central 3″ stellar metallicities, with the global stellar mass–stellar metallicity relation having a lower normalisation, we investigate here how these quantitative differences affect the main model-based conclusions that we obtained in Chapter 4. In particular, we wish to determine whether the conclusions from Chapter 4 can be extended to galaxies globally, rather than only holding in the central regions of galaxies.

The details of the model-based analysis are given in Chapter 4. Briefly, we compare the observed differences in stellar metallicity between star-forming and passive (or green valley) galaxies with the predictions of chemical evolution models to determine the relative importance

of starvation and outflows in quenching star formation in galaxies. Our models aim to simultaneously reproduce both the mass-weighted stellar metallicity and the star formation rates of local passive and local green valley galaxies, which puts constraints on the duration of quenching $t_{\rm quench}$ and the value of the 'effective' mass-loading factor $\lambda_{\rm eff}$ during the quenching phase.

In Section 6.2.2.1, we analyse the stellar metallicity difference between star-forming and passive galaxies, therefore determining how the star-forming progenitors of local passive galaxies quenched at high-redshift (z∼1–2). In Section 6.2.2.2, we instead study the quenching of star-formation in the local Universe, by analysing the stellar metallicity difference between local star-forming and local green valley galaxies.

6.2.2.1 Passive galaxies (quenching at high-z)

As discussed in Chapter 4, the progenitors of local passive galaxies are star-forming galaxies at high-redshift, rather than star-forming galaxies in the local Universe. Hence it is necessary to compare the stellar metallicity difference between local passive galaxies and their high-redshift star-forming progenitors, rather than the metallicity difference between local passive and local star-forming galaxies. Similar to our analysis in Chapter 4, we estimate the stellar metallicity of these high-redshift star-forming progenitors by evolving the global mass-weighted stellar mass–stellar metallicity relation for local star-forming galaxies to high-redshift. We assume that the stellar metallicity relation follows the same redshift-evolution as the gas-phase mass–metallicity relation in Maiolino et al. (2008), with the onset of quenching $z_{\rm q}$ given by the global mass-weighted stellar mass–stellar age relation for local passive galaxies found in this work.

We show the global mass-weighted stellar mass–stellar metallicity relation for the high-z star-forming progenitors of local passive galaxies (in dark blue) in the top panel of Fig. 6.3. Although both the global mass-weighted stellar mass–stellar metallicity and the global mass-weighted stellar mass–stellar age relations show quantitative differences with the central 3″ relations in Chapter 4, we find that the stellar mass–stellar metallicity relations for the high-redshift star-forming progenitors are qualitatively similar.

We show the stellar metallicity difference between local passive galaxies and their star-forming progenitors (in dark orange) in the bottom panel of Fig. 6.3. In contrast to our findings in Chapter 4, we find that this stellar metallicity difference is roughly flat with stellar mass, rather than decreasing with increasing stellar mass. This key difference is mostly brought about by the fact that the global stellar metallicity difference between local star-forming and local passive galaxies increases (rather than decreases) with stellar mass, which, as discussed in Section 6.2.1, is likely due to the biasing brought about by the 3″ SDSS Legacy Survey fibre.

The results obtained using our chemical evolution models are shown in Fig. 6.4. The duration of the quenching phase (i.e. the time required to transition from star-forming to

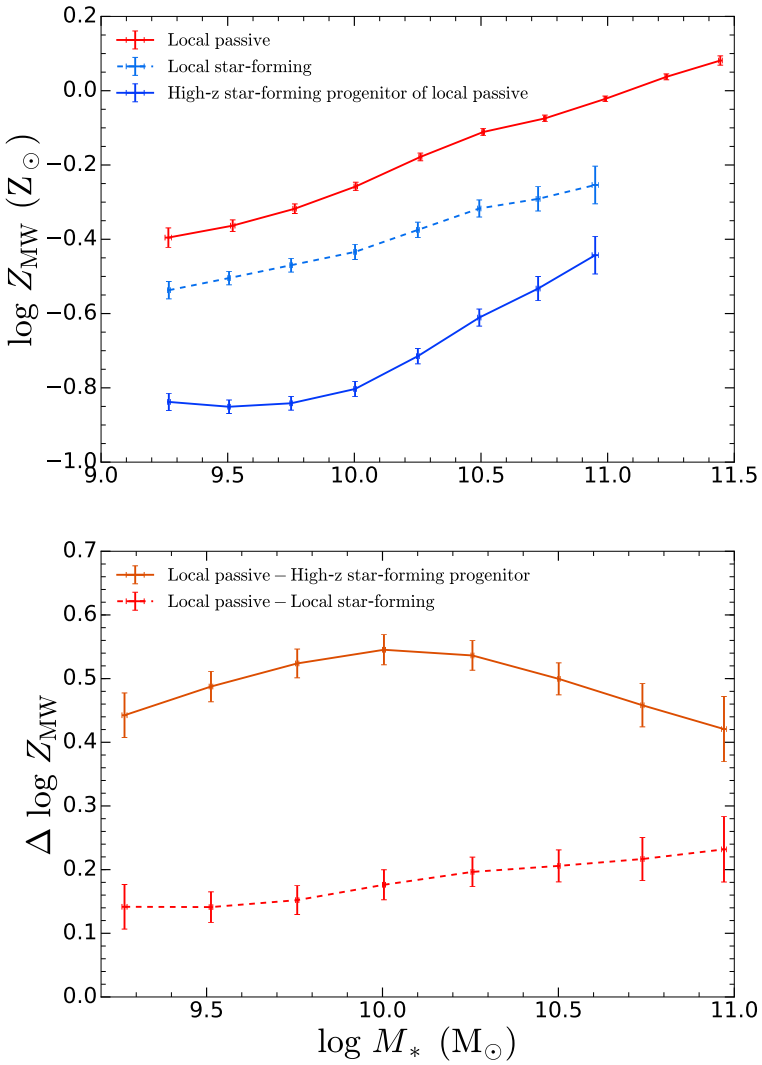

Figure 6.3. Top panel: The global mass-weighted stellar mass–stellar metallicity relation for local passive galaxies (red), local star-forming galaxies (dashed light blue) and the high-redshift star-forming progenitors of local passive galaxies (dark blue). The stellar metallicities of the high-redshift progenitors are estimated by evolving the global mass-weighted stellar mass–stellar metallicity relation for local star-forming galaxies to high-redshift. We assume the evolution is given by the evolution of the gas-phase mass–metallicity relation in Maiolino et al. (2008), with the onset of quenching $z_{\rm q}$ given by the global mass-weighted stellar mass–stellar age relation for local passive galaxies found in this work. Bottom panel: The mass-weighted stellar metallicity difference between local passive and local star-forming galaxies (dashed red) and the mass-weighted stellar metallicity difference between local passive galaxies and their high-redshift star-forming progenitors (dark orange).

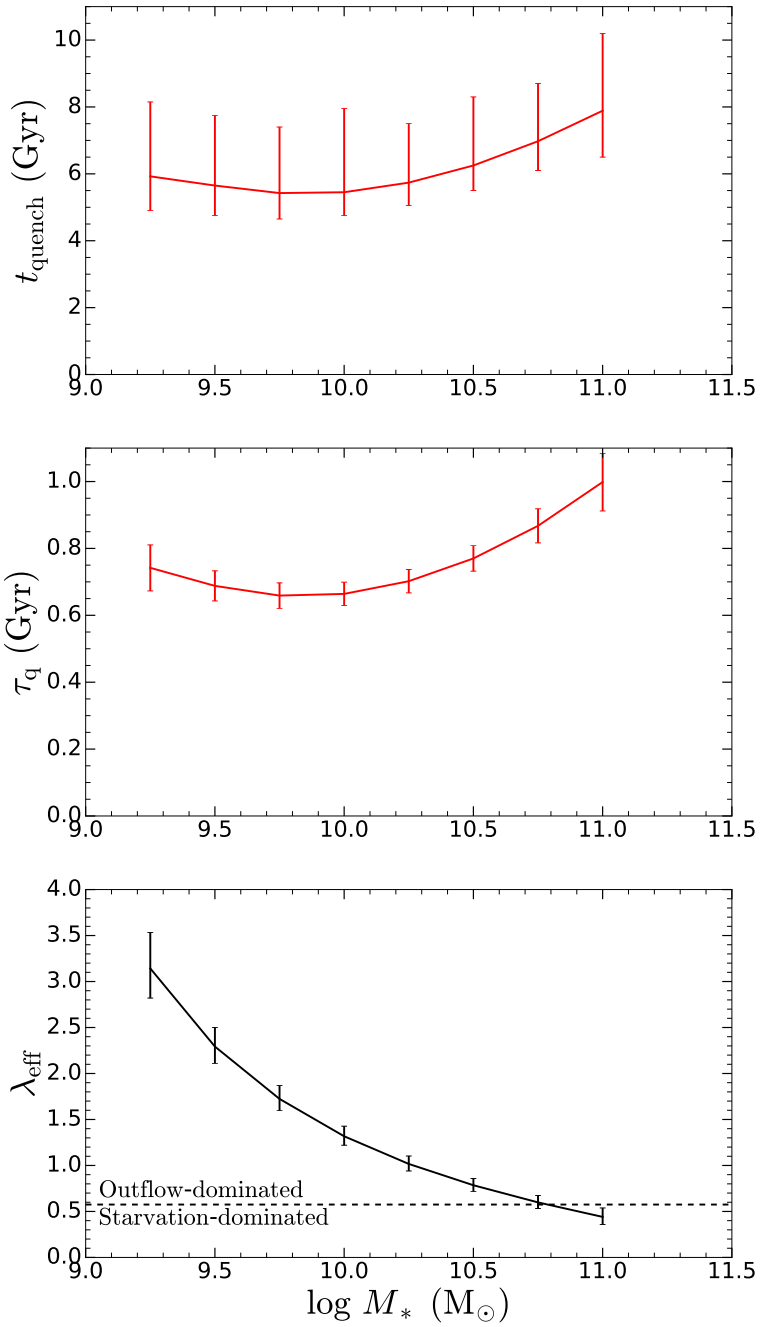

Figure 6.4. Constraints on the quenching of the high-redshift star-forming progenitors of local passive galaxies. Top panel: The duration of the quenching phase $t_{\rm quench}$. Middle panel: The e-folding timescales $\tau_{\rm q}$. Bottom panel: The 'effective' mass-loading factors $\lambda_{\rm eff}$ required to simultaneously reproduce both the global mass-weighted stellar metallicity and the star formation rates of local passive galaxies. The horizontal dashed line is the $\lambda_{\rm eff}$ value for which the outflow rate ($\lambda_{\rm eff}\Psi$) is the same as the net gas consumption rate ($(1-R)\Psi = 0.575\Psi$). Galaxies with $\lambda_{\rm eff}$ above (below) this boundary are considered to be outflow-dominated (starvation-dominated). We show the median duration of quenching, e-folding timescale and mass-loading factor in each stellar mass bin, with the error bars representing the standard deviation.

passive, simultaneously matching both the global mass-weighted stellar metallicity and the star formation rate of local passive galaxies) is shown in the top panel and is roughly flat with stellar mass at 6–7 Gyr. In addition, the *e*-folding timescales for quenching, shown in the middle panel and defined as

$$\tau_{\rm q} = \frac{1}{\epsilon(1 - R + \lambda_{\rm eff})}, \tag{6.1}$$

are also roughly flat with stellar mass at 0.7–0.9 Gyr. Finally, the 'effective' mass-loading factors $\lambda_{\rm eff}$, shown in the bottom panel, tend to decrease with increasing stellar mass. All of these results are qualitatively consistent with our findings in Chapter 4.

However, there are some quantitative differences between our results in Fig. 6.4 and our findings in Chapter 4 for the central (3″) region of galaxies. Although the *logarithmic* stellar metallicity differences between local passive galaxies and their high-redshift star-forming progenitors are similar in both works, the normalisation of the global mass-weighted stellar mass–stellar metallicity relation is lower. Therefore, the *linear* stellar metallicity difference is smaller for the global stellar metallicities studied in this work. This implies that less chemical enrichment actually takes place during the quenching phase. This has two important consequences for our model-based predictions. First, the duration of quenching $t_{\rm quench}$ will be shorter. Second, less gas needs to be consumed to reach the chemical enrichment level of local passive galaxies, so more of the initial gas reservoir can be ejected in outflows and $\lambda_{\rm eff}$ will therefore be larger. This also means that the *e*-folding timescale $\tau_{\rm q}$ will be shorter.

Indeed, we find that the mass-loading factors in this work tend to be larger. Most importantly, the transition from outflow-dominated to starvation-dominated occurs at a higher stellar mass: $\log(M_*/{\rm M}_\odot) = 10.75$ instead of $\log(M_*/{\rm M}_\odot) = 10.2$. Hence our analysis of the global properties of galaxies has revealed that outflows are more important than what we had inferred from our analysis of the central regions of galaxies. However, an extensive phase of starvation is still required to explain the substantial increase in metallicity during quenching. Thus, while starvation is likely to be the prerequisite for quenching, outflows are primarily responsible for depleting the gas reservoirs of galaxies at almost all masses during quenching. Additionally, the e-folding timescales are indeed slightly smaller: $\tau_{\rm q} \sim 0.8$ Gyr as opposed to $\tau_{\rm q} \sim 1$ Gyr.

However, our durations of quenching $t_{\rm quench}$ are comparable to the 5–7 Gyr found in Chapter 4. The reason for this is that we use a different SFR indicator to our analysis in Chapter 4. We calculate the global SFRs by summing, on a spaxel-by-spaxel basis, the SFRs estimated by the hybrid Hα-D4000 approach of Bluck et al. (2020). In contrast, in our analysis in Chapter 4 we used the global SFRs from Brinchmann et al. (2004) that were estimated by aperture-correcting the Hα/D4000-based in-fibre SFRs. Although the SFRs for star-forming galaxies are similar using both indicators, our SFR indicator estimates a lower SFR

for passive galaxies. For example, using our indicator, the boundaries of the passive region of the SFR-M$_*$ diagram at $\log(M_*/\mathrm{M}_\odot) = 10,\ 11$ are log SFR $= -2.5,\ -1$, as opposed to log SFR $= -1,\ -0.25$. Thus, using our indicator, the duration of quenching t_{quench} will tend to be longer, as the SFR that has to be reached in the models is lower. As shown in Appendix C.3.1, if we instead use the SFRs from Brinchmann et al. (2004), the durations of quenching t_{quench} are indeed lower, at 4–5 Gyr, while the e-folding timescales and mass-loading factors are essentially the same. Therefore our model-based estimates for the duration of quenching are sensitive to the SFR indicator used.

6.2.2.2 Green valley galaxies (quenching in the local Universe)

We show the results from our chemical evolution models for green valley galaxies in Fig. 6.5. Our model-based estimate for the time elapsed since the onset of quenching t_{quench}, using the stellar metallicity difference between local star-forming and local green valley galaxies (ΔZ), is shown in the top panel in black. We find that t_{quench} is roughly flat with stellar mass at ∼4 Gyr. We also show an alternative estimate for the time elapsed since the onset of quenching, given by the global mass-weighted stellar age difference between local star-forming and local green valley galaxies (Δage) in green. We find that the stellar age difference is also roughly flat with stellar mass, typically at 3.5–4 Gyr. Thus our two estimates for t_{quench} are in good agreement with each other. This is in contrast to our findings in Chapter 4, where we instead found more considerable (2–4 Gyr) disagreement between our two t_{quench} estimates.

The middle panel in Fig. 6.5 shows the e-folding timescale τ_{q}, which we find to be roughly flat with stellar mass at ∼1 Gyr. In Chapter 4 we instead found that τ_{q} increased with stellar mass, from 1.5 to 2.5 Gyr over the same stellar mass range. Given the relation between τ_{q} and λ_{eff}, these discrepancies in normalisation and variation with stellar mass are brought about by the larger 'effective' mass-loading factors λ_{eff} that are derived by our models using global stellar metallicities, which we show in the bottom panel of Fig. 6.5. Interestingly, we find that green valley galaxies are outflow-dominated at all stellar masses, rather than transitioning to starvation-dominated at $\log(M_*/\mathrm{M}_\odot) = 10.4$ as was found in Chapter 4. Thus we conclude, that for galaxies at all masses both in the local Universe and at high-redshift, starvation is likely to be the prerequisite for quenching, while outflows are primarily responsible for depleting the gas reservoirs of galaxies during quenching.

The results of our chemical evolution models, using the Brinchmann et al. (2004) global SFRs rather than the Bluck et al. (2020) SFRs are shown in Appendix C.3.2. Briefly, we find that the e-folding timescales and mass-loading factors are roughly the same, while the t_{quench} values are substantially smaller at ∼2–3 Gyr.

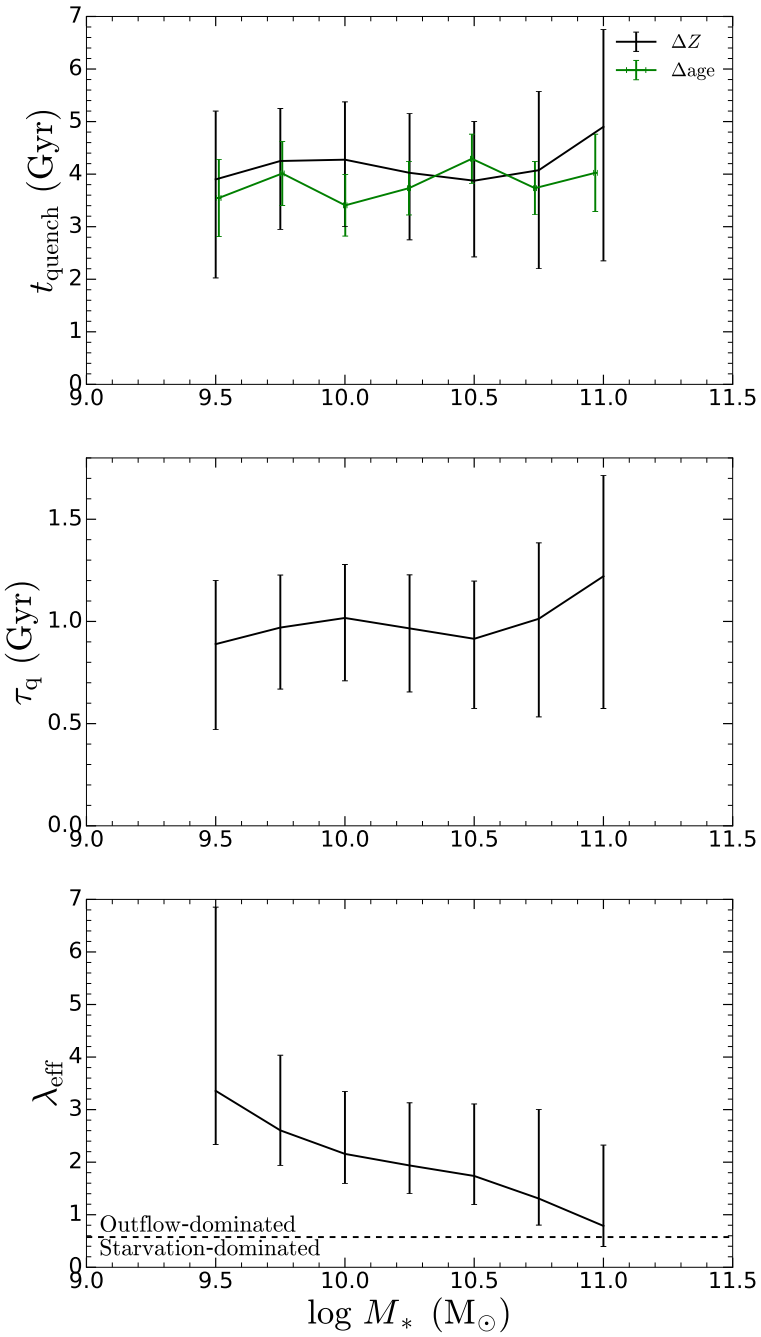

Figure 6.5. Similar to Fig. 6.4, but now showing constraints on the quenching of local green valley galaxies, obtained using models that simultaneously reproduce both the global mass-weighted stellar metallicity and the star formation rate of local green valley galaxies. Top panel: The model-based estimate (ΔZ) for the time elapsed since the onset of quenching $t_{\rm quench}$ is shown in black. An alternative estimate for $t_{\rm quench}$ (Δage), given by the global mass-weighted stellar age difference between local star-forming and local green valley galaxies, is shown in green.

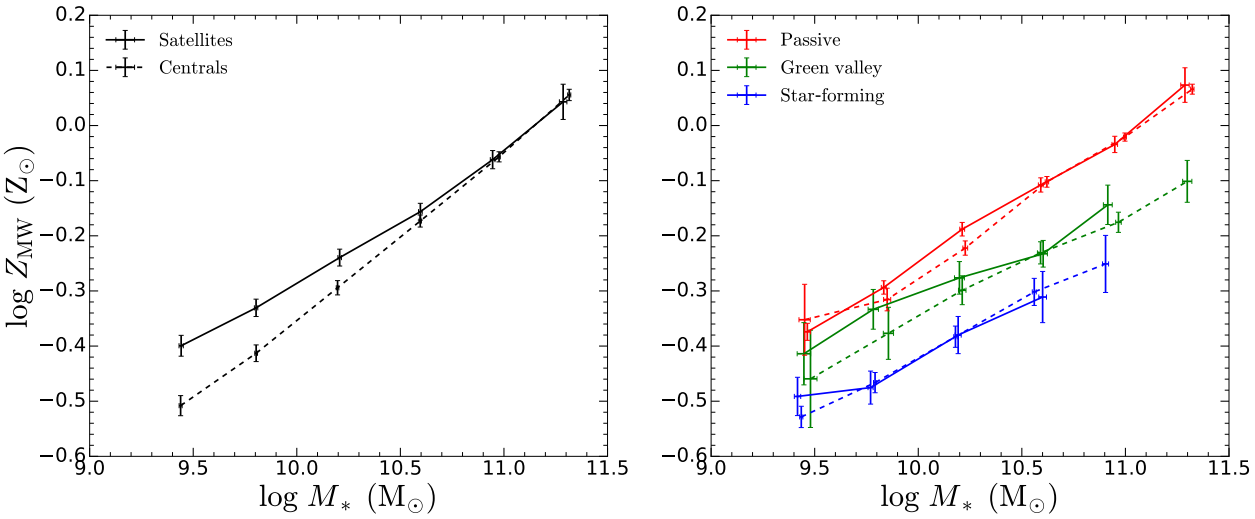

Figure 6.6. The global mass-weighted stellar mass–stellar metallicity relation for centrals (dashed) and satellites (solid). Left panel: The global mass-weighted stellar mass–stellar metallicity relation when including all galaxies (i.e. without splitting into star-forming, green valley and passive galaxies, black). Right panel: The global mass-weighted stellar mass–stellar metallicity relation for star-forming (blue), green valley (green) and passive galaxies (red).

6.2.3 Environmental dependence

6.2.3.1 Stellar metallicity

We show the global mass-weighted stellar mass–stellar metallicity relation for the overall populations (i.e. including star-forming, green valley and passive galaxies together) of centrals (dashed) and satellites (solid) in the left panel of Fig. 6.6. We find, similar to Chapter 5, that satellites tend to be more metal-rich than centrals of the same stellar mass, with the offset between centrals and satellites decreasing with stellar mass.

In the right panel we separate the overall populations of centrals and satellites into star-forming, green valley and passive galaxies, showing the global mass-weighted stellar mass–stellar metallicity relation for star-forming (blue), green valley (green) and passive galaxies (red). We find that the underlying stellar metallicity differences between centrals and satellites become much smaller after separating star-forming, green valley and passive galaxies. Thus, the key finding of Chapter 5, that the true, inherent dependence of stellar metallicity on environment (in terms of the central–satellite dichotomy) is much weaker than what is found when simply comparing the overall populations of centrals and satellites (which was done by other past works), applies not just to the central regions of galaxies but also holds true globally: from the innermost to the outermost regions in galaxies.

Similar to Chapter 5, we find that passive satellites and green valley satellites tend to be

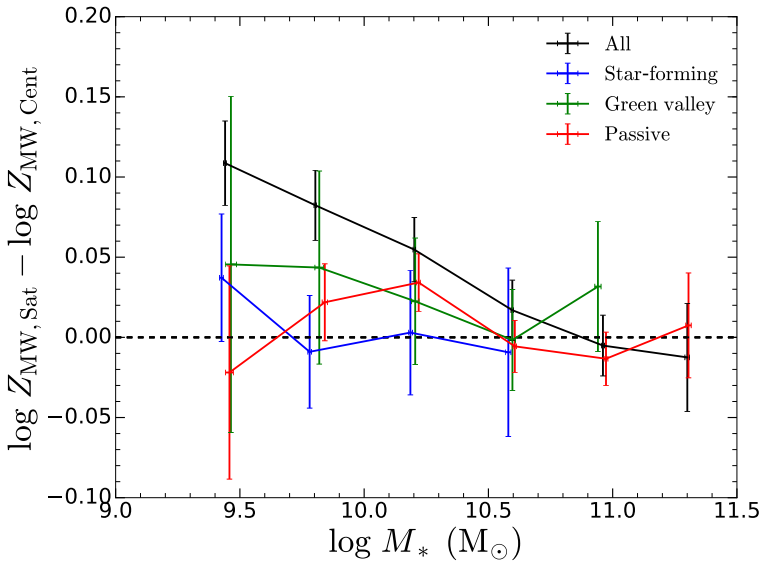

Figure 6.7. The global mass-weighted stellar metallicity difference $\Delta \log Z_{\rm MW}$ = $\log Z_{\rm MW,Sat} - \log Z_{\rm MW,Cent}$ between centrals and satellites of the same stellar mass, including all galaxies (i.e. without splitting into star-forming, green valley and passive galaxies, black), for star-forming galaxies (blue), green valley galaxies (green) and passive galaxies (red). Error bars correspond to the 1σ error on the stellar metallicity difference.

slightly more metal-rich than passive centrals and green valley centrals of the same stellar mass. However, in contrast to our findings in Chapter 5, we do not find star-forming satellites to be more metal-rich than star-forming centrals of the same stellar mass. This discrepancy is not too surprising, however, because the statistics available in MaNGA (~5000 galaxies) are roughly 7% of what was available in our SDSS Legacy Survey study (~80 000 galaxies) in Chapter 5. Since the inherent dependence of stellar metallicity on environment is weak (see Chapter 5) and the statistics in MaNGA are relatively low, we may not be sensitive enough to pick up on these weak effects as they become washed out by random scatter in the scaling relations.

The stellar metallicity differences between centrals and satellites are shown more clearly in Fig. 6.7. It is clear that the quenched fraction effect, i.e. the selection effect, brought about by the difference in quenched fraction between centrals and satellites, that applies when star-forming, green valley and passive galaxies are not separated (discussed in detail in Chapter 5), exaggerates and also misrepresents the mass-dependence of the global mass-weighted stellar metallicity differences between centrals and satellites. While the difference decreases with mass for the overall populations of centrals and satellites, there is no clear trend with mass for star-forming, green valley and passive galaxies.

We obtain qualitatively similar results for the global light-weighted stellar mass–stellar metallicity relation for centrals and satellites, which we show in Appendix C.4.1.

Similar to what was done in Chapter 5, we have also investigated how the global mass-weighted stellar mass–stellar metallicity relation depends on further measures of the environment: halo mass $M_{\rm h}$, local overdensity δ_5 and projected distance $d_{\rm proj}/R_{\rm vir}$. Our results using the global stellar metallicities largely echo what was found using the central 3″ metallicities in our analysis in Chapter 5, indicating that the imprint of environment on the stellar populations of galaxies is weak, not only in the central regions of galaxies but *globally*. However, it should be noted that, owing to the much lower statistics in MaNGA, these trends are weaker, with more scatter and less significance than was seen in our analysis in Chapter 5.

More specifically, we find (but do not show) that the stellar metallicities of satellites tend to increase with increasing halo mass, increasing local overdensity and decreasing projected distance, relatively strongly for the overall populations of satellites, but relatively weakly for green valley and passive satellites, and with no trends for star-forming satellites. In addition, we again find evidence for the dry merging of galaxies, with the overall population of centrals, as well as green valley and passive centrals exhibiting a horizontal offset between adjacent halo mass percentiles, as was seen in Chapter 5. Finally, similar to our findings in Chapter 5, while the stellar metallicities of the overall population of centrals increase weakly with local overdensity, we find no trend for star-forming, green valley and passive centrals.

6.2.3.2 Stellar age

We show the global mass-weighted stellar mass–stellar age relation for centrals (dashed) and satellites (solid) in the left panel of Fig. 6.8. Again, our findings are similar to our findings in Chapter 5, with satellites tending to be older than centrals of the same stellar mass.

After separating into star-forming, green valley and passive galaxies, we find, as shown in the right panel of Fig. 6.8, that the true offset in age between centrals and satellites is actually much smaller. Similar to our findings in Chapter 5, star-forming satellites and passive satellites tend to be older than star-forming centrals and passive centrals of the same stellar mass. In fact, we find that star-forming satellites at $\log(M_*/{\rm M}_\odot) = 9.75, 10.25$ are significantly older than their central counterparts, though we suspect that this is mostly driven by small number statistics, as this feature was not present in our study in Chapter 5. In contrast to Chapter 5, we do not find green valley satellites to be older green valley centrals of the same stellar mass.

We obtain qualitatively similar results for the global light-weighted stellar mass–stellar age relation for centrals and satellites, which we show in Appendix C.4.2.

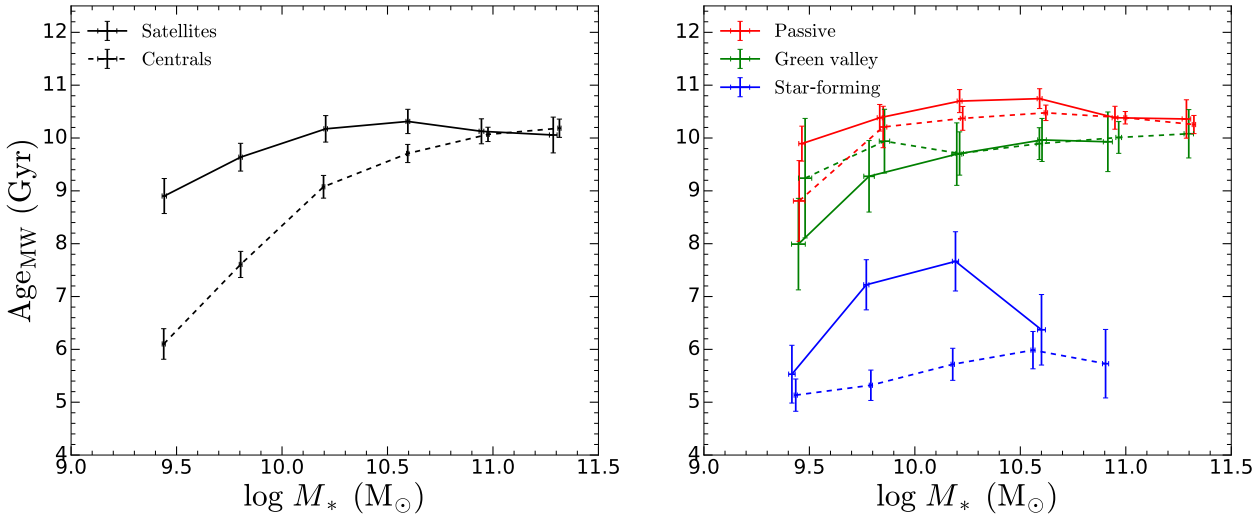

Figure 6.8. Similar to Fig. 6.6, but now showing the global mass-weighted stellar mass–stellar age relation.

6.3 Quenching: a spatially-resolved view

In this section we study the radial variation of the stellar metallicities and stellar ages in star-forming, green valley and passive galaxies. In particular, we aim to put constraints on how the quenching of star formation varies with radial distance in galaxies. Rather than integrate all the light out to ~1.5–2.5 R_e as was done in Section 6.2, here we instead partition each MaNGA galaxy into 0.5 R_e wide annuli: ranging from the innermost regions ($0 < R/R_e < 0.5$) to the outermost regions ($2 < R/R_e < 2.5$) in galaxies. The light from all the spaxels within each annulus are combined and the resulting spectrum is fit using FIREFLY.

We investigate the general radial variation of the stellar metallicities and stellar ages in Section 6.3.1. In Section 6.3.2 we study the environmental dependence of these radial variations, splitting the MaNGA sample into centrals and satellites.

6.3.1 Spatially-resolved scaling relations

6.3.1.1 Stellar metallicity

We show the spatially-resolved mass-weighted stellar mass–stellar metallicity relation for star-forming (blue), green valley (green) and passive (red) galaxies in Fig. 6.9, with each panel corresponding to a different radial interval, ranging from the innermost regions ($0 \leq R/R_e < 0.5$, top-left panel) to the outermost regions ($2 \leq R/R_e < 2.5$, bottom-left panel) in galaxies. We can clearly see that the stellar metallicities of star-forming, green valley and passive galaxies all tend to increase with stellar mass within each radial interval. Furthermore, the stellar

metallicities of passive galaxies are higher than those of star-forming galaxies within each radial interval and at all masses, with green valley galaxies having stellar metallicities that are intermediate between those of star-forming and passive galaxies. Thus, not only are passive galaxies more chemically-enriched than star-forming galaxies in the central regions (see Chapter 4 and Peng et al. 2015) and globally (see Section 6.2.1), but we can now make an even stronger statement: passive galaxies are substantially more metal-rich than star-forming galaxies at *all* radii, indicating that starvation is likely to be driving the quenching of star formation at *all* radii in galaxies.

Similar to what was found using the global stellar metallicities in Section 6.2.1, the stellar metallicity difference between star-forming and passive galaxies tends to increase with stellar mass. This effect is most notable in the innermost regions of galaxies, as can be seen in the top-left ($0 \leq R/R_{\rm e} < 0.5$) and top-right ($0.5 \leq R/R_{\rm e} < 1$) panels, but is also marginally present at intermediate radial distances ($1 \leq R/R_{\rm e} < 1.5$, middle-left panel).

Fig. 6.9 also shows that the normalisation of the mass-weighted stellar mass–stellar metallicity relation for star-forming, green valley and passive galaxies decreases with radial distance, with the typical stellar metallicities becoming smaller as we move from the innermost regions (top-left panel) to the outermost regions in galaxies (bottom-left panel). Furthermore, the typical stellar metallicity difference between star-forming and passive (and also green valley) galaxies tends to decrease with increasing radial distance.

We show the radial-dependence of the stellar metallicities of star-forming, green valley and passive galaxies more clearly in Fig. 6.10. Galaxies are now binned in radial distance (in units of the effective radius $R_{\rm e}$), with each panel now corresponding to a different stellar mass interval, ranging from low stellar masses ($9 \leq \log(M_*/{\rm M}_\odot) < 9.5$, top-left panel) to high stellar masses ($11 \leq \log(M_*/{\rm M}_\odot) < 11.5$, bottom-left panel). We can see that star-forming, green valley and passive galaxies all exhibit negative stellar metallicity gradients, with the stellar metallicities tending to decrease with radial distance, indicating that the outskirts of galaxies tend to be more metal-poor than the inner regions. Furthermore, we find that the stellar metallicity gradients in passive and green valley galaxies tend to be steeper than those of star-forming galaxies. As a result, the stellar metallicity difference between star-forming and passive (and also green valley) galaxies tends to decrease with radial distance (except perhaps in the lowest stellar mass bin).

We show the light-weighted radial stellar metallicity relations in Appendix C.6.1. Briefly, we find the same key trends as with the mass-weighted stellar metallicities. Green valley and passive galaxies are more metal-rich than star-forming galaxies at *all* radii, with the stellar metallicity difference between star-forming and green valley/passive galaxies decreasing with radial distance.

It should be noted that we have not applied any inclination cuts to the MaNGA sample in

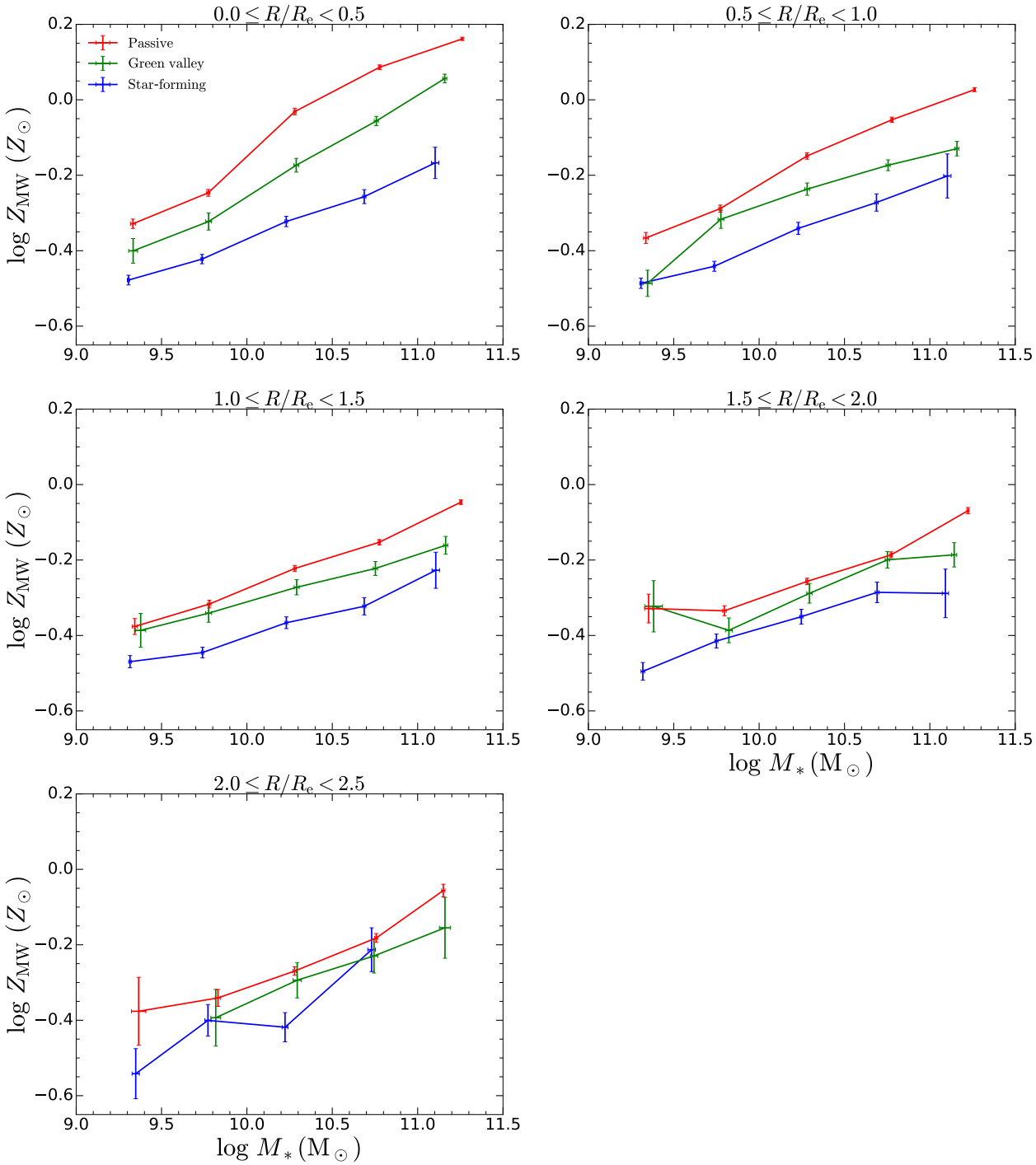

Figure 6.9. The spatially-resolved mass-weighted stellar mass–stellar metallicity relation for star-forming (blue), green valley (green) and passive (red) galaxies. Each panel corresponds to a different radial interval, increasing from left to right and from top to bottom, ranging from the innermost regions ($0 \leq R/R_e < 0.5$, top-left) to the outermost regions ($2 \leq R/R_e < 2.5$, bottom-left) in galaxies.

our analysis. The stellar populations at different R/R_e are likely to be mixed (due to projection effects) in spaxels in highly inclined systems. Furthermore, beam smearing effects will be more severe since the apparent size of the galaxy on the sky is smaller. We investigate how inclination cuts affect the radial-dependence of the stellar metallicities of galaxies in Appendix C.5. Briefly, we find that the qualitative trends discussed here are all preserved, with only minor quantitative changes (0–0.04 dex).

It should also be noted that, while we bin galaxies in relatively narrow stellar mass ranges, we do find that passive galaxies tend to be slightly more massive (in terms of the median stellar mass) than star-forming galaxies in each panel of Fig. 6.10. The offset is usually ~0.05 dex but is up to 0.1 and 0.15 dex in the two highest stellar mass panels, respectively. As the stellar metallicity of passive galaxies tends to increase with stellar mass, this effect tends to exacerbate the stellar metallicity difference between star-forming and passive galaxies slightly, with a usual offset in stellar metallicity of ~0.02 dex, up to ~0.04 dex in the highest stellar mass panel.

Fig. 6.10 clearly shows that passive galaxies are more metal-rich than star-forming galaxies of the same stellar mass and at the same radial distance (in terms of R_e). However, passive galaxies tend to be more compact (i.e. they have a smaller R_e) than star-forming galaxies of the same stellar mass (see e.g. Cappellari et al. 2013; Cappellari 2013; van der Wel et al. 2014; Van Dokkum et al. 2015; Cappellari 2016b). So, a given R/R_e corresponds to a different physical distance for star-forming and passive galaxies. In other words, in order to compare star-forming and passive galaxies at the same physical distance, one would have to compare a higher R/R_e for passive galaxies with a lower R/R_e for star-forming galaxies. Thus the stellar metallicity difference between star-forming and passive galaxies, at a fixed physical radial distance R, is smaller than the stellar metallicity difference at a fixed R_e, due to the negative stellar metallicity gradients in galaxies. Nevertheless, as shown in Fig. 6.10, we find that even the outermost regions of passive galaxies are more metal-rich than the innermost regions of star-forming galaxies, so there will still be a substantial stellar metallicity difference between star-forming and passive galaxies at a given physical radial distance, despite this effect. While we acknowledge that this effect complicates the comparison between star-forming and passive galaxies and decreases the stellar metallicity difference, we will simply be studying the difference in stellar metallicity at fixed R/R_e throughout this work.

The radial variation of the stellar metallicity difference between star-forming and passive (green valley) galaxies is shown in red (green) in Fig. 6.11. As discussed in Chapters 4 and 5, the stellar metallicity difference between star-forming and passive galaxies is a proxy for the prevalence of starvation as a mechanism for quenching star formation in galaxies. Therefore, the decline in the stellar metallicity difference with radial distance could be indicating that, while starvation plays a prominent role in quenching the central regions of galaxies, it plays an

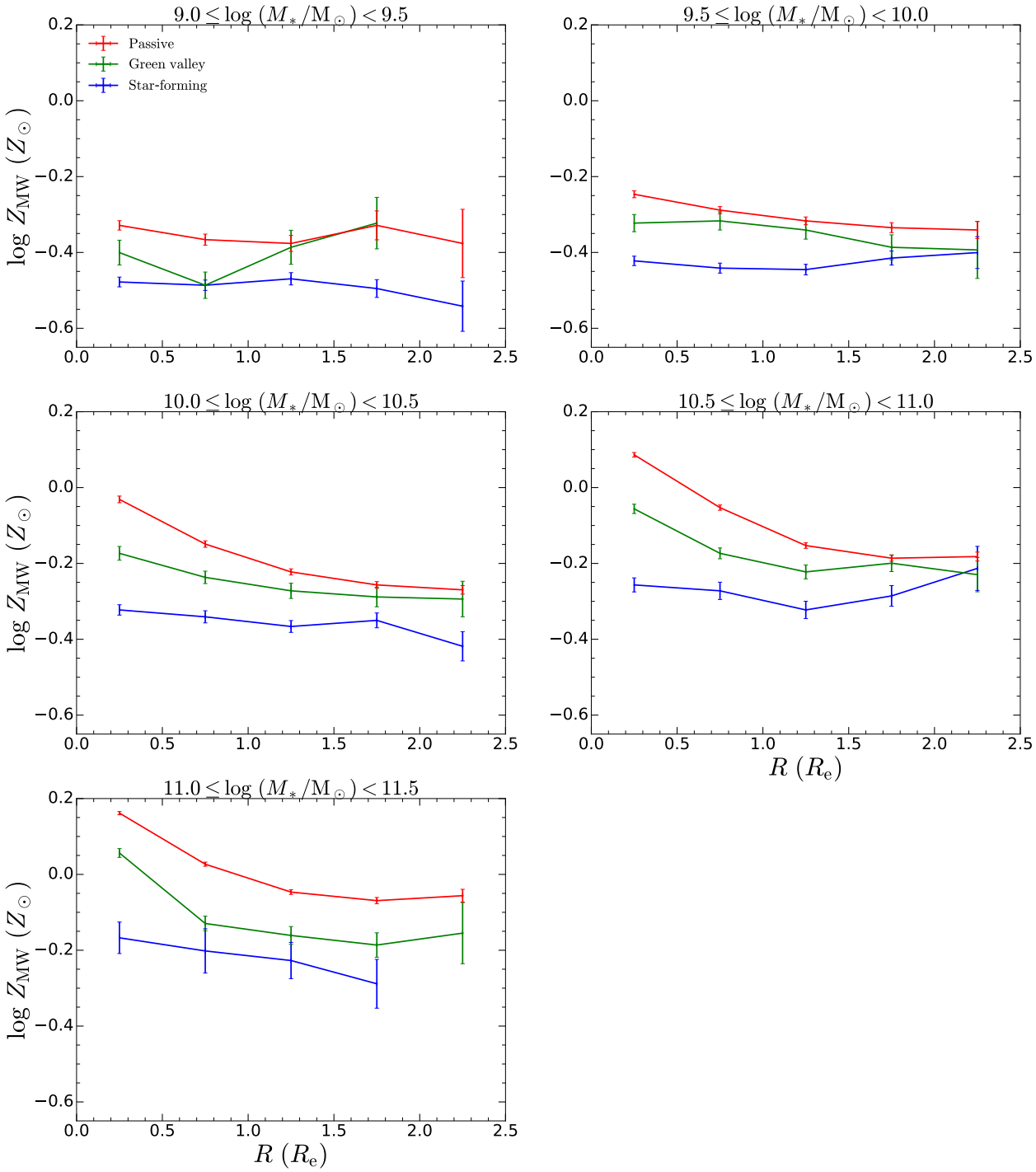

Figure 6.10. The mass-weighted radial stellar metallicity relation for star-forming (blue), green valley (green) and passive (red) galaxies. Galaxies are binned in radial distance (in units of the effective radius R_e), with each panel corresponding to a different stellar mass interval, increasing from left to right and from top to bottom, ranging from low stellar masses ($9 \leq \log(M_*/\mathrm{M}_\odot) < 9.5$, top-left panel) to high stellar masses ($11 \leq \log(M_*/\mathrm{M}_\odot) < 11.5$, bottom-left panel).

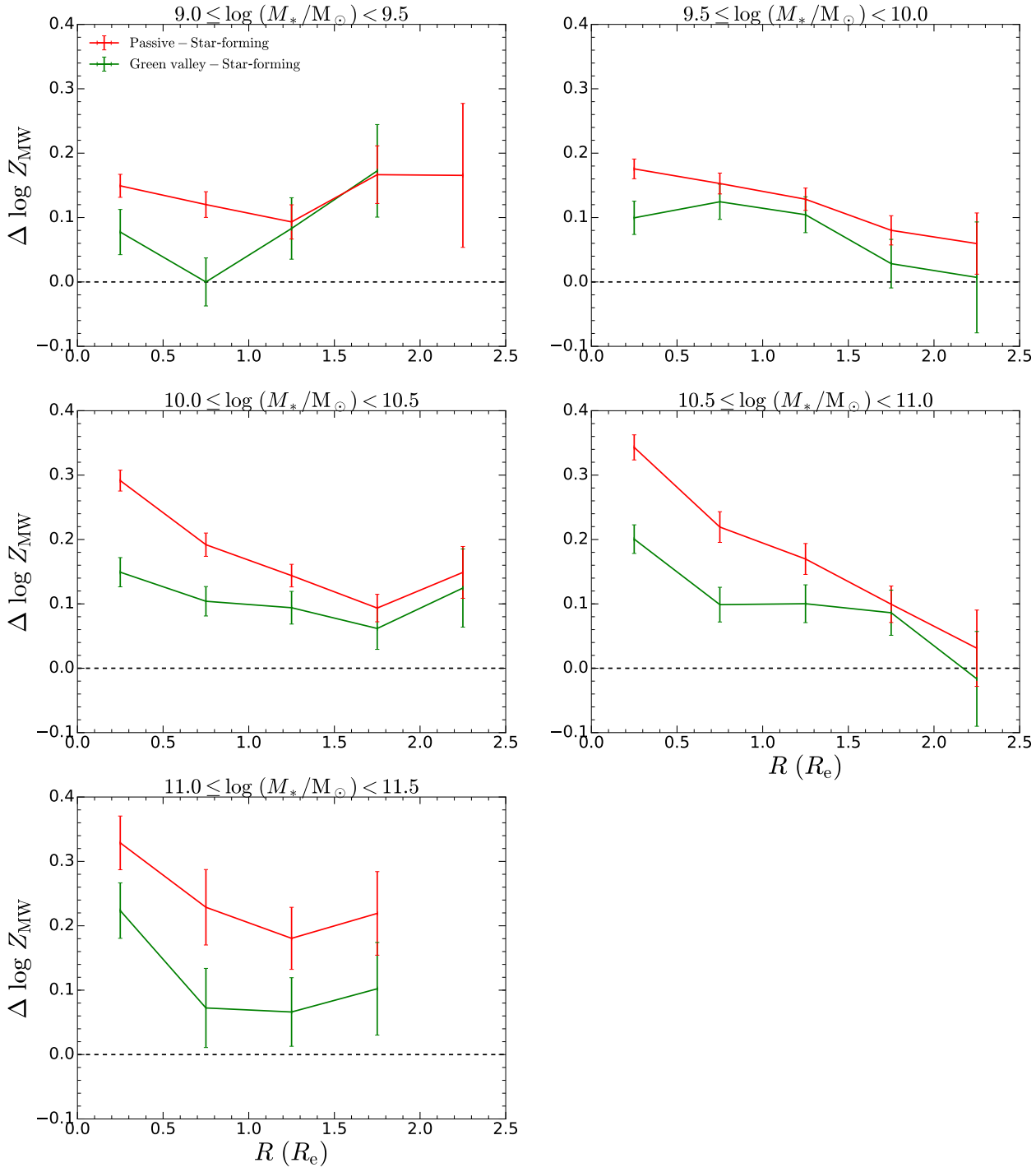

Figure 6.11. The mass-weighted stellar metallicity difference between star-forming and passive galaxies (red), and star-forming and green valley galaxies (green). Galaxies are binned in radial distance (in units of the effective radius R_e), with each panel corresponding to a different stellar mass interval, increasing from left to right and from top to bottom, ranging from low stellar masses ($9 \leq \log(M_*/\mathrm{M}_\odot) < 9.5$, top-left panel) to high stellar masses ($11 \leq \log(M_*/\mathrm{M}_\odot) < 11.5$, bottom-left panel).

increasingly less important role in quenching the outskirts of galaxies. In terms of our chemical evolution model, this would suggest that the 'effective' mass-loading factor $\lambda_{\rm eff}$ increases with radial distance, with quenching being more starvation-dominated in the centre and relatively more outflow-dominated in the outskirts. This conclusion seems reasonable for two reasons. First, the depth of the gravitational potential well, which determines how strongly the outflowing gas is bound to the galaxy (see e.g. Fluetsch et al. 2019), is at its deepest at the centre and becomes shallower with increasing radial distance. Second, the central regions of galaxies are less likely to be replenished with a fresh supply of gas if the accreting gas is deposited with high angular momentum onto the external regions of the galaxy disc (Peng & Renzini 2020; Renzini 2020).

Alternatively, the stellar metallicity differences may decrease with radial distance because the gas fractions in star-forming galaxies tend to decrease with radial distance. In this case, even if starvation is the dominant quenching mechanism at all radii, the stellar metallicity increase during quenching will be smaller in the outer regions because there is relatively less gas available to convert into new metal-rich stars.

Chemical evolution models can be used to distinguish between these two scenarios. We intend to undertake this analysis in future work. Our chemical evolution model discussed in Chapter 3 will be used, and will be updated to take into account the radial variation of metallicity, gas fraction and gas depletion time in galaxies. We will use the mass-weighted radial stellar metallicity relation found in this work to specify the initial stellar and gas-phase metallicities in the models. Furthermore, we will use observations of the radial variation of the atomic and molecular gas content in galaxies to specify how both the gas fraction and gas depletion time vary with radial distance in the models. Any uncertainties in the radial variation of the gas fractions will result in uncertainties on the radial variation of the 'effective' mass-loading factor $\lambda_{\rm eff}$, as this will affect how much unneeded, excess gas can be ejected from the galaxy. Additionally, any uncertainties in the radial variation of the gas depletion times will result in uncertainties on the radial variation of both the duration of quenching $t_{\rm quench}$ and the e-folding timescale $\tau_{\rm q}$, as the gas depletion time sets the clock for the temporal evolution in the models.

6.3.1.2 Stellar age

We show the mass-weighted radial stellar age relation for star-forming, green valley and passive galaxies in Fig. 6.12. We find that the stellar ages of star-forming, green valley and passive galaxies tend to either decrease or are relatively flat with increasing radial distance. Passive galaxies are older than star-forming galaxies at all radii and at all masses, with green valley galaxies usually having stellar ages that are intermediate between star-forming and passive galaxies.

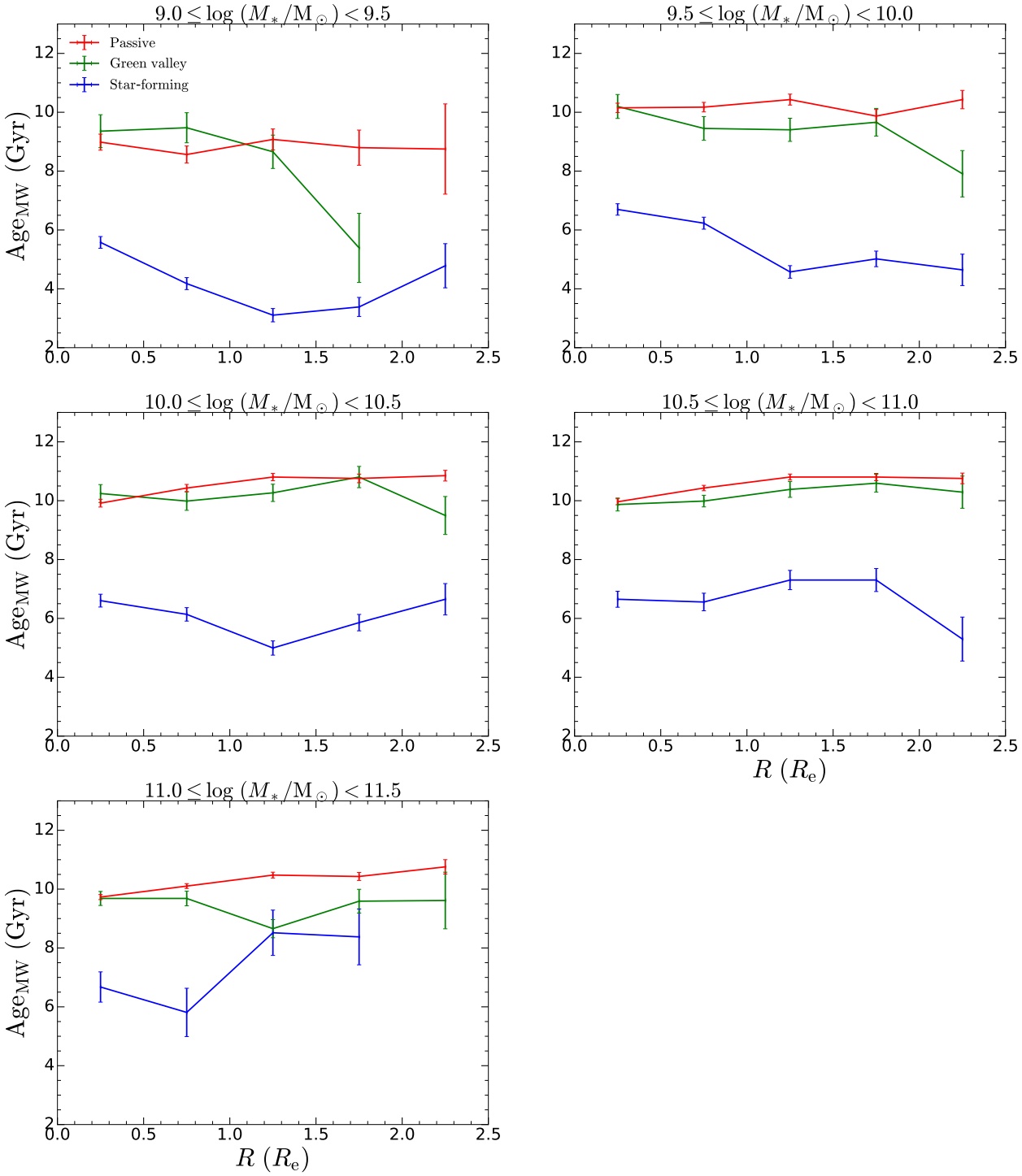

Figure 6.12. Similar to Fig. 6.10, but now showing the mass-weighted radial stellar age relation.

We show the light-weighted radial stellar age relation in Appendix C.6.2, finding qualitatively similar results to the trends seen here.

6.3.2 Environmental dependence

In Chapter 5 and in Section 6.2.3 we found that, after separating star-forming, green valley and passive galaxies, the imprint of environment on the central and global stellar populations of galaxies is weak, with satellites only being marginally more metal-rich and older than centrals of the same stellar mass. In this section we compare the stellar populations in centrals and satellites on a radial basis to establish whether these trends also manifest themselves on a spatially-resolved basis. In particular, we wish to investigate whether the aforementioned trends indeed hold true at *all* radii in galaxies, and also whether the radial variation of the stellar metallicity difference between star-forming and passive galaxies differs for centrals and satellites.

6.3.2.1 Stellar metallicity

We show the mass-weighted radial stellar metallicity relation for centrals (dashed) and satellites (solid) in Fig. 6.13. It is clear that both passive centrals and satellites tend to be more metal-rich than star-forming centrals and satellites, respectively, with the green valley central/satellite population being intermediate between the star-forming and passive populations. Furthermore, the stellar metallicities of centrals and satellites both tend to decrease with increasing radial distance. Finally, the stellar metallicity differences between star-forming and green valley/passive galaxies decreases with radial distance for both centrals and satellites. This is true for centrals (at all masses) and for satellites (at high masses), which suggests that the radial variation of the relative role of different quenching mechanisms (starvation vs. outflows or gas removal) only depends weakly on environment, even for (massive) satellite galaxies. This, for instance, suggests that ram pressure stripping (which should accelerate the gas removal) generally only plays a minor role in the quenching process. The exception are satellite galaxies in the two lowest mass bins, for which the stellar metallicity difference between star-forming and passive satellites remains constant and relatively small at all radii. This suggests that starvation (in this case likely associated with 'strangulation') and gas removal processes (probably a combination of outflows and ram pressure stripping) act uniformly across the discs of low-mass satellites, likely as a consequence of the shallow gravitational potential well of these galaxies.

Now comparing the radial variations for centrals and satellites, we find, similar to our analysis in Chapter 5 and our global analysis in Section 6.2.3, that the environment leaves only a weak imprint on the stellar metallicities of galaxies, with the stellar metallicities of central

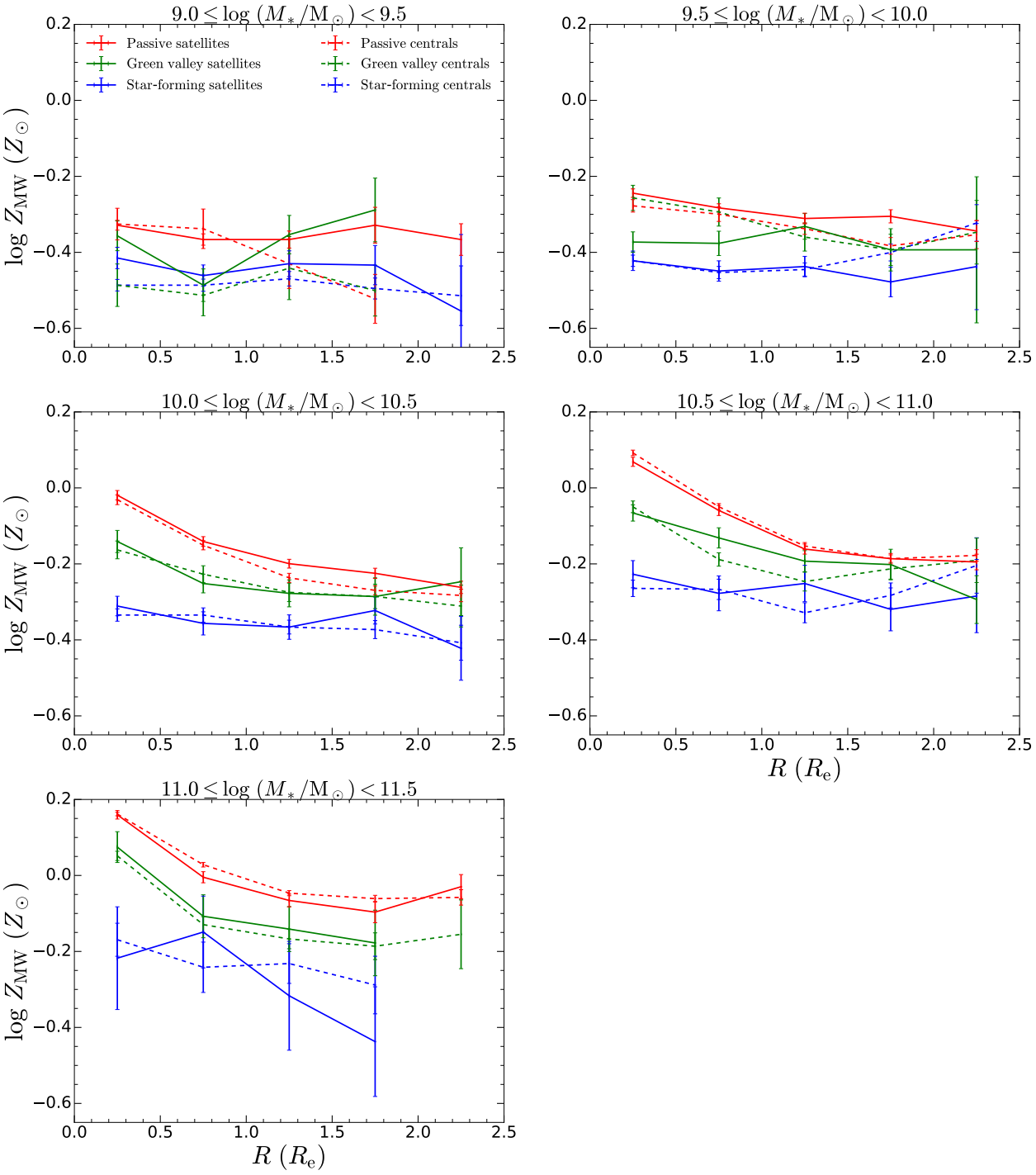

Figure 6.13. Similar to Fig. 6.10, but now also further dividing the galaxy population into centrals (dashed) and satellites (solid).

and satellite galaxies being comparable at all masses and at all radii. Similar to Chapter 5 and Section 6.2.3, passive satellites tend to be more metal-rich than passive centrals of the same stellar mass. The offset between passive centrals and satellites tends to decrease with increasing stellar mass (down to ~0 for $\log(M_*/\mathrm{M}_\odot) \geq 10.5$) and also tends to increase with increasing radial distance (for $\log(M_*/\mathrm{M}_\odot) < 10.5$). However, in contrast to Chapter 5 and Section 6.2.3, we do not find any indication that star-forming and green valley satellites tend to be more metal-rich than star-forming and green valley centrals of the same stellar mass, with the stellar metallicity offset between centrals and satellites often changing sign (i.e. from a metallicity enhancement to a metallicity deficit) seemingly randomly from one radial bin to the next.

We show the light-weighted radial stellar metallicity relation for centrals and satellites in Appendix C.7.1, finding largely the same trends as discussed here.

6.3.2.2 Stellar age

We show the mass-weighted radial stellar age relation for centrals and satellites in Fig. 6.14. The underlying differences between centrals and satellites are relatively small at all masses and at all radii. The substantial offset in stellar age between star-forming centrals and star-forming satellites that was seen in Fig. 6.6 is clearly also present in the radial stellar age relations, with star-forming satellites tending to be older than star-forming centrals at all masses and at all radii.

The light-weighted radial stellar age relation for centrals and satellites is shown in Appendix C.7.2, where we find similar trends to those seen using the mass-weighted ages.

6.4 Summary and conclusions

We have harnessed the spatially-resolved power of the SDSS-IV MaNGA integral field spectroscopic galaxy survey to investigate how quenching operates within galaxies. We find the following:

(i) By integrating all the light in each MaNGA galaxy out to 1.5–2.5 R_e, we derive the global stellar population parameters for ~5000 galaxies in the local Universe, which we analyse to provide a global view of galaxy quenching. We obtain the following results:

- Similar to Chapter 4, but now studying the global properties of galaxies, we find that passive galaxies are substantially more metal-rich than star-forming galaxies of the same stellar mass, with green valley galaxies having stellar metallicities that are intermediate between star-forming and passive galaxies. Thus, starvation is likely to be a key driver of the global quenching of star formation in galaxies.

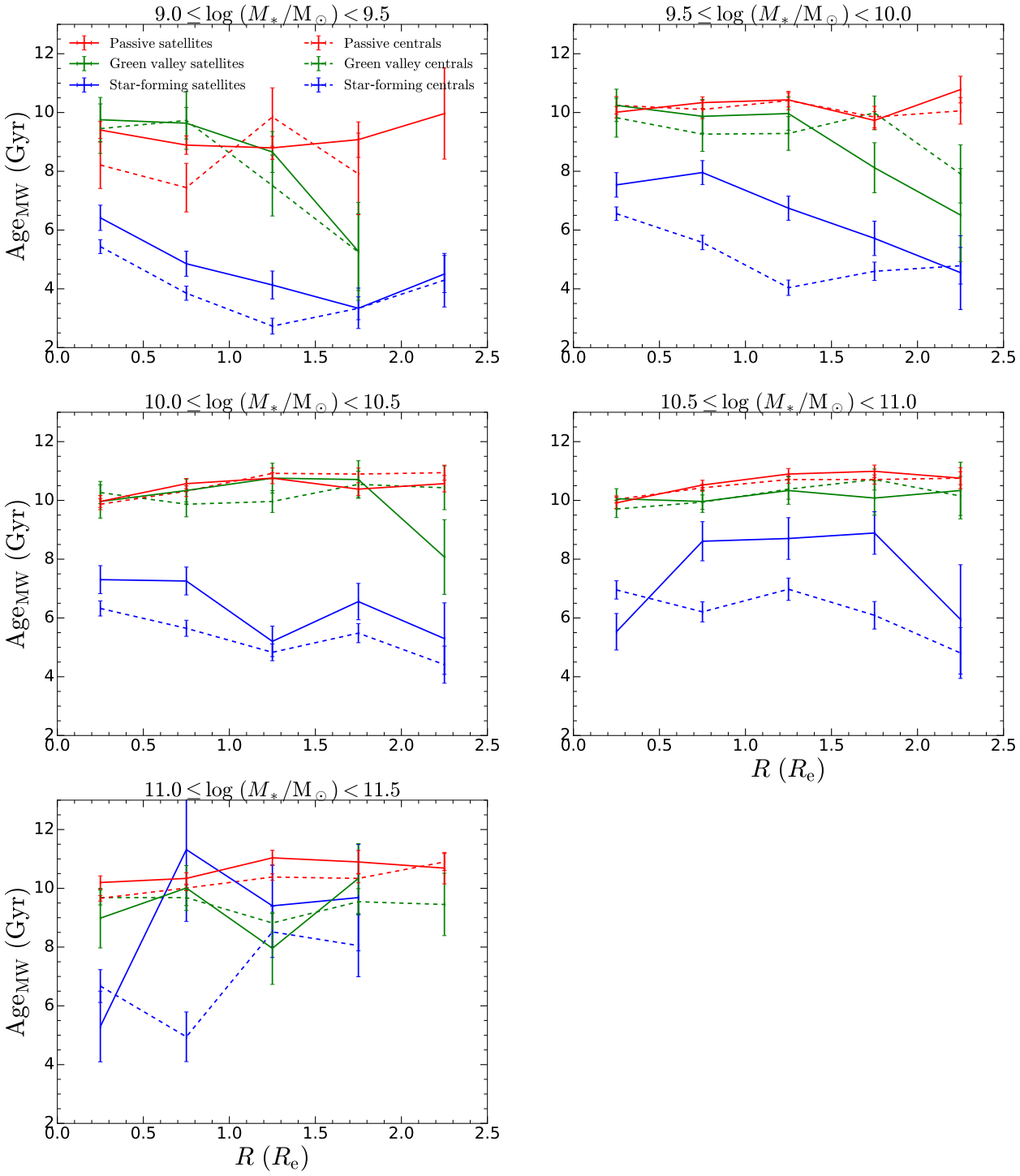

Figure 6.14. Similar to Fig. 6.12, but now also further dividing the galaxy population into centrals (dashed) and satellites (solid).

- Owing to the negative stellar metallicity gradients in galaxies, the normalisations of the global stellar mass–stellar metallicity relations for star-forming, green valley and passive galaxies are lower than the central 3″ relations we found using the SDSS Legacy Survey data in Chapter 4.
- We compare the observed stellar metallicity differences between local passive galaxies and their star-forming progenitors with the predictions of our chemical evolution model to put quantitative constraints on the quenching process at high-redshift. Due to the lower normalisations of the global stellar mass–stellar metallicity relations, we find that the 'effective' mass-loading factors $\lambda_{\rm eff}$ during quenching are now larger than what was found in Chapter 4. Hence our analysis of the global properties of galaxies has revealed that outflows are more important than what we had inferred from our analysis of the central regions of galaxies. Indeed, our model now indicates that galaxies are outflow-dominated at almost all masses (up to $\log(M_*/{\rm M}_\odot) = 10.75$), with only the most massive galaxies still being starvation-dominated. Thus, while starvation is likely to be the prerequisite for quenching, outflows are primarily responsible for depleting the gas reservoirs of galaxies at almost all masses during quenching.
- We also analyse the observed stellar metallicity difference between local green valley and star-forming galaxies to put quantitative constraints on the quenching process in the local Universe. Our models indicate that green valley galaxies have typically been quenching through starvation, with outflows dominating the gas depletion process at all masses, for ∼4 Gyr. This timescale is now in much better agreement (compared to our findings in Chapter 4) with our alternative estimate for the time elapsed since the onset of quenching, given by the global mass-weighted stellar age difference between local star-forming and local green valley galaxies, which is also roughly flat with stellar mass, typically at 3.5–4 Gyr.
- We also investigate the environmental dependence of the global stellar population properties of galaxies. We find, similar to Chapter 5, that satellites are both more metal-rich and older than centrals of the same stellar mass. However, after separating star-forming, green valley and passive galaxies, we find that the true environmental dependence of stellar metallicity and age is in fact much weaker, with star-forming, green valley and passive satellites being only marginally more metal-rich and older than, or in some cases equivalent to, star-forming, green valley and passive centrals of the same stellar mass.
- Thus, our results confirm that the key mass-and environment-dependent trends in galaxy quenching found in Chapters 4 and 5 using the single fibre SDSS Legacy

Survey data hold true *globally*, and hence are not just restricted to the central regions in galaxies.

(ii) By dividing each MaNGA galaxy into a series of 0.5 R_e-wide annuli, we determine the radial variation of the stellar population parameters in galaxies to provide a spatially-resolved view of galaxy quenching. We obtain the following results:

- We find that passive galaxies are significantly more metal-rich than star-forming galaxies at *all* radii, indicating that starvation is a primary driver of quenching at *all* radii in galaxies.
- Furthermore, we find that star-forming, green valley and passive galaxies all exhibit negative stellar metallicity gradients, with the gradients in passive and green valley galaxies tending to be steeper than those of star-forming galaxies. As a result, we find that the stellar metallicity difference between star-forming and passive galaxies decreases with increasing radial distance, which likely indicates (and will be verified in future work) that, while starvation plays a prominent role in quenching the central regions of galaxies, it plays an increasingly less important role in quenching their outskirts.
- We also compare the stellar populations in centrals and satellites on a radial basis, and we find, after separating star-forming, green valley and passive galaxies, that the stellar metallicities and ages of central and satellite galaxies are comparable at all masses and at *all* radii. Thus the environment truly only leaves a weak imprint on the stellar populations of galaxies, not only in the central regions (see Chapter 5) and on the global properties (see Section 6.2.3), but at *all* radii in galaxies.
- Finally, we find that the stellar metallicity differences between star-forming and passive galaxies decrease with radial distance for both centrals (at all masses) and satellites (at high masses). This suggests that the radial variation of the relative role of different quenching mechanisms (starvation vs. gas removal) only depends weakly on environment even for (massive) satellite galaxies, potentially indicating that ram pressure stripping generally only plays a minor role in the quenching process. However, for low-mass satellite galaxies, we instead find that the stellar metallicity difference between star-forming and passive galaxies remains constant and relatively small at all radii, which suggests that starvation and gas removal processes act uniformly across the discs of low-mass satellites, likely as a consequence of the shallow gravitational potential well of these galaxies.

Chapter 7

Conclusions

7.1 Summary

In this thesis we have extensively built on the promising technique pioneered by Peng et al. (2015) that assesses the relative role of different quenching mechanisms through comparisons of the level of chemical enrichment in star-forming and passive galaxies. Leveraging on the statistical power of large spectroscopic galaxy surveys, and focussing on the chemical transformation that takes place during quenching, we have aimed to unveil the primary quenching mechanisms in galaxies. In particular, by utilising the statistical power of the SDSS Legacy Survey, by further developing and refining our chemical evolution model by properly taking into account the effect of different progenitors of local galaxies, by delving deeper into the imprint of environment on the stellar populations of galaxies, and by harnessing the spatially-resolved power of the integral field spectra from the SDSS-IV MaNGA galaxy survey, we have investigated the nature of the primary quenching routes in galaxies, how galaxy quenching depends on both the internal properties of galaxies (i.e. stellar mass) and external factors (i.e. environment), how galaxy quenching has evolved across cosmic time and how quenching operates on a radial basis within galaxies.

In Chapter 4, we investigated the role of mass in galaxy quenching. Leveraging on the statistical power of the SDSS Legacy Survey, we analysed the chemical properties of 80 000 galaxies in the local Universe to assess the relative role of starvation and outflows in driving galaxy quenching. In particular, we analysed the stellar metallicities of star-forming, green valley and passive galaxies to distinguish between different quenching mechanisms. We find

that the significant difference in stellar metallicity between passive galaxies and their star-forming progenitors implies that for galaxies at all masses, quenching must have involved an extended phase of starvation. However, some form of gas ejection has to be introduced into our models to best match the observed properties of local passive galaxies, indicating that, while starvation is likely to be the prerequisite for quenching, it is the combination of starvation and outflows that is responsible for quenching the majority of galaxies. Closed-box models indicate that the duration of the quenching phase is 2–3 Gyr with an e-folding time of 2–4 Gyr, after which further star formation is prevented by an ejective/heating mode. Alternatively, leaky-box models find a longer duration for the quenching phase of 5–7 Gyr and an e-folding time of $\sim$1 Gyr, with outflows becoming increasingly important with decreasing stellar mass. Finally, our analysis of local green valley galaxies indicates that quenching is slower in the local Universe than at high-redshift.

In Chapter 5, we continued our analysis of the SDSS Legacy Survey dataset, investigating the role of environment in galaxy evolution and galaxy quenching. Echoing earlier works, we find that satellites are both more metal-rich (< 0.1 dex) and older (< 2 Gyr) than centrals of the same stellar mass. However, after separating star-forming, green valley and passive galaxies, we find that the true imprint of environment on the stellar populations of galaxies is in fact much weaker, with star-forming, green valley and passive satellites being only marginally more metal-rich (< 0.03 dex) and older (< 0.5 Gyr) than star-forming, green valley and passive centrals of the same stellar mass. We show that the strong environmental effects found when galaxies are not differentiated result from a combination of selection effects brought about by the environmental dependence of the quenched fraction of galaxies, and thus we strongly advocate for the separation of the star-forming, green valley and passive populations of galaxies when the environmental dependence of galaxy properties are investigated. We also study further environmental trends separately for both central and satellite galaxies. We find no further environmental effects for star-forming galaxies, neither for centrals nor for satellites. In contrast, the stellar metallicities of green valley and passive satellites increase weakly with increasing halo mass, increasing local overdensity and decreasing projected distance from their central; this effect is interpreted in terms of moderate environmental starvation ('strangulation') contributing to the quenching of satellite galaxies. Finally, we find a unique feature in the stellar mass–stellar metallicity relation for passive centrals, where galaxies in more massive haloes have larger stellar mass at constant stellar metallicity; this effect is interpreted in terms of the dry merging of passive central galaxies and/or progenitor bias.

In Chapter 6, we utilised the spatially-resolved spectra from the SDSS-IV MaNGA integral field spectroscopic galaxy survey to investigate how quenching operates on a radial basis within galaxies. By integrating all the light in each MaNGA galaxy out to 1.5–2.5 $R_{\rm e}$, we investigated

the mass- and environment-dependence of the global stellar population parameters for ~5000 galaxies in the local Universe. Our results confirm that the key mass- and environment-dependent trends in galaxy quenching found in Chapters 4 and 5 using the single fibre SDSS Legacy Survey data hold true globally, and hence are not just restricted to the central regions in galaxies. However, due to the negative stellar metallicity gradients in galaxies, we do find quantitative differences with the studies in Chapters 4 and 5, as the normalisation of the global stellar metallicities are lower. Most notably, our models now indicate that, while starvation is likely to be the prerequisite for quenching, outflows are primarily responsible for depleting the gas reservoirs of galaxies at all masses during quenching. In addition, we divided each MaNGA galaxy into a series of 0.5 R_e-wide annuli to investigate the radial variation of the stellar population parameters of galaxies. We find that passive galaxies are substantially more metal-rich than star-forming galaxies at *all* radii, with the stellar metallicity difference between star-forming and passive galaxies decreasing with increasing radial distance. Therefore, starvation is a primary driver of quenching at *all* radii in galaxies, with our observational results likely indicating (and will be confirmed in future work) that, while starvation plays a prominent role in quenching the central regions of galaxies, it plays an increasingly less important role in quenching their outskirts.

7.2 Outlook for the future

Thus, we have utilised the statistical power of the SDSS to unveil the primary quenching mechanisms in galaxies as a function of mass, environment, redshift and radial distance. But this thesis only marks the beginning of our study of galaxy quenching. There are still a plethora of promising paths that we intend to pursue in the future.

First, our analysis of MaNGA galaxies revealed that the stellar metallicity difference between star-forming and passive galaxies decreases with increasing radial distance. There are two possible explanations for this result. Firstly, since the stellar metallicity difference between star-forming and passive galaxies serves as a proxy for the prevalence of starvation as a quenching mechanism, this result may indicate that, while starvation plays a prominent role in quenching the central regions in galaxies, it plays an increasingly less important role in quenching their outskirts. However, the amount of chemical enrichment that actually takes place during starvation depends on the relative amount of new metal-rich stars that are formed, which in turn depends on the size of the available gas reservoir (i.e. the gas fraction). Therefore, an alternative explanation is that starvation does in fact play a prominent role in quenching star formation at all radii in galaxies, with the decrease in stellar metallicity difference with radial distance being due to the decrease in the typical gas fractions in galaxies with increasing radial distance.

We intend to use our chemical evolution model to distinguish between these two competing scenarios, by taking into account the radial variation of gas-phase metallicity, stellar metallicity, gas fraction and star formation efficiency in galaxies. In particular, we will use the radial variation of the stellar mass–stellar metallicity relations obtained from our analysis of MaNGA galaxies to specify the initial gas-phase and stellar metallicities in the model. In addition, we will use observations of the gas content in galaxies to specify the radial variation of the initial gas fractions and star formation efficiencies in the model.

Second, our analysis thus far has focussed on the stellar metallicities of galaxies, as these can be reliably measured for both star-forming and passive galaxies, therefore yielding insights into the amount of chemical enrichment that takes place during quenching. In contrast, gas-phase metallicities have traditionally only been studied in star-forming galaxies, as gas-phase metallicity calibrations for non-star-forming regions (that can therefore be applied to study passive galaxies) have only recently become available (Kumari et al. 2019). We intend to use these new calibrations to compare the gas-phase metallicities in star-forming and passive galaxies, which will put further valuable constraints on the role of different physical processes both during and after the quenching process. This analysis is already being done in an ongoing work, to which the author of this thesis has been contributing, using the single fibre SDSS Legacy Survey data (Kumari et al. 2020, in prep.), but the author of this thesis also plans to extend the analysis using the spatially-resolved SDSS-IV MaNGA data.

Third, our analysis thus far has focussed on the chemical transformation that takes place during quenching. However, as alluded to almost a century ago by the early-type–late-type dichotomy discovered by Hubble (Hubble 1926, 1936), and as further consolidated by recent large spectroscopic galaxy surveys (e.g. Strateva et al. 2001), the morphological transformation that seems to take place during the transition from star-forming to passive is likely to be another key component of the quenching process, which our analysis has not yet taken into account. We intend to use the morphological classifications from the Galaxy Zoo project (Lintott et al. 2008) to further separate the SDSS Legacy Survey and MaNGA galaxies into discs and spheroids, to better understand the crucial connection between the morphological and chemical transformations that take place during quenching.

Furthermore, numerical simulations indicate that this morphological transformation is likely to be driven by the major mergers of galaxies (e.g. Toomre 1977; Barnes 1988, 1992, but see also the alternative explanations discussed in Chapters 1 and 3) which simultaneously transform galaxies from discs into spheroids, and temporarily boost and then shut down star formation in galaxies (see e.g. Ellison et al. 2008a; Hopkins et al. 2008; Moreno et al. 2019). We intend to further develop our chemical evolution model to take the effects of major mergers into account. In particular, we intend to incorporate the boost in star formation efficiency that major mergers

tend to induce, and also take into account the additional gas mass and stellar mass that is provided in a merger, together with the dilution of the gas-phase metallicity and reduction in stellar metallicity that results from the mixing of the gas and stars from the two merging galaxies.

In addition, recent studies (see e.g. the discussion in Cappellari 2016a) have shown that the morphological transformation of galaxies is likely to be further connected to the kinematical transformation that seems to take place during quenching, with galaxies transforming from rotation-supported discs into dispersion-dominated spheroids. Thus, we also intend to use kinematical classifications (Emsellem et al. 2007, 2011; Cappellari 2016a) of galaxies in the MaNGA survey to tie together the link between the chemical, kinematical, morphological and structural evolution that takes during the transition from star-forming to passive.

Fourth, our key observational result is that passive galaxies are substantially more metal-rich than star-forming galaxies of the same stellar mass, which is qualitatively consistent with the starvation scenario. This key signature of starvation, together with our other observational findings, such as the weak dependence of stellar metallicity on environment, the tentative evidence for the dry merging of passive central galaxies, and the decrease in the stellar metallicity difference between star-forming and passive galaxies with radial distance provide new, valuable constraints on models of galaxy evolution and quenching. Indeed, using our chemical evolution model, which incorporates the key physical processes of star formation, metal production, gas inflow and outflow, we quantitatively confirmed the starvation scenario. However, it should be noted that these physical processes were only implemented in a relatively simple manner and we made a number of additional simplifying assumptions in the analysis. Thus, we intend to further investigate the starvation scenario, by comparing our key observational findings with the outputs of cosmological hydrodynamical simulations, such as Illustris (Vogelsberger et al. 2014b), IllustrisTNG (Nelson et al. 2019) and EAGLE (Schaye et al. 2015). In particular, by identifying which of these simulations best reproduces our observational findings, we aim to further unveil the nature of the physical mechanisms (which are implemented in a different way in each of the simulations) that are responsible for galaxy quenching, as a function of mass, environment, redshift and radial distance.

Finally, we have leveraged on the statistical power of the largest spectroscopic galaxy survey of our time, the Sloan Digital Sky Survey, to unveil the primary quenching mechanisms in galaxies. Our analysis thus far has therefore been centred on galaxies in the local Universe. However, the era of large spectroscopic galaxy surveys has only just begun. New surveys, utilising the world's most powerful telescopes with state-of-the-art instrumentation, are beginning to be undertaken at higher redshift. We intend to utilise the data from these completed, ongoing and future spectroscopic galaxy surveys to extend our analysis, as we aim to chart the

chemical evolution of galaxies and determine the mass- and environment-dependence of galaxy quenching across cosmic time.

More specifically, we intend to use data from both the SDSS-IV Extended Baryon Oscillation Spectroscopic Survey (eBOSS, Dawson et al. 2016) and the Large Early Galaxy Astrophysics Census (LEGA-C, van der Wel et al. 2016) survey to investigate both the chemical content of galaxies and galaxy quenching at intermediate redshifts ($z \sim 0.7$). We intend to use the data from both surveys, as the datasets are complementary.

The eBOSS survey has obtained low S/N (~5) optical–NIR spectra (3600–10 000 Å in the observed frame) at $R \sim 2000$ for a large sample of galaxies: 300 000 passive galaxies at $0.6 < z < 1.0$ and 175 000 star-forming galaxies at $0.6 < z < 1.1$. We intend to stack star-forming and passive galaxies in bins of stellar mass and redshift to increase the S/N of the spectra.

In contrast, the LEGA-C survey, which has been conducted using VIMOS on the Very Large Telescope (VLT), has obtained high quality (S/N > 10) optical–NIR spectra (3600–10 000 Å in the observed frame) at $R = 200$–2500 for a relatively small sample of galaxies: 2700 galaxies (including both star-forming and passive galaxies) at $0.6 < z < 1$, down to stellar masses of $10^{10}\,M_\odot$.

Perhaps the most exciting prospect for the future is pushing our study of galaxy quenching ever further still, to the peak of cosmic star formation history at $z \sim 2$, using the Multi-Object Optical and Near-Infrared Spectrograph (MOONS) on the VLT. With First Light set for 2021, VLT-MOONS is a next-generation optical–NIR (0.64–1.8 μm) spectrograph that can simultaneously gather the light from 1001 distant galaxies at once (Cirasuolo et al. 2014). Utilising this incredible multiplexing capability, together with the light-gathering power of the VLT, as well as the very generous 190 nights of observing time, the GTO MOONS extragalactic survey, known as MOONRISE (MOONS Redshift-Intensive Survey Experiment), will obtain spectra for ~700 000 galaxies at $0.9 < z < 2.6$. Observing in the rest-frame optical and therefore sampling the same nebular and stellar diagnostics that are observed in surveys of local galaxies, together with its unprecedented statistics, MOONRISE truly is the spiritual successor of the SDSS. Standing on the shoulders of giants, MOONRISE will peer well beyond the galaxies in our cosmic back garden, as it aims to perform a SDSS-like survey of galaxies at cosmic noon.

We intend to use the data from the MOONRISE survey, together with our chemical enrichment-based method for assessing the relative role of different quenching mechanisms, to determine the mass- and environment-dependence of galaxy quenching during the peak epoch of galaxy formation. Using nebular emission lines such as Hα and [O II] to determine star formation rates, we will use the bimodality in the star formation rate–stellar mass plane to clas-

sify galaxies as star-forming and passive. Galaxies will then be stacked in bins of stellar mass, environment and redshift, and the resulting spectra will be fit to derive the stellar metallicities of both star-forming and passive galaxies at $z \sim 2$. In doing so, we aim to unveil the primary quenching mechanisms in galaxies during the peak epoch of galaxy formation.

And thus, just as the Sloan Digital Sky Survey heralded in a new era in astronomy, marking the dawn of the age of large spectroscopic galaxy surveys, now the torch will be passed, and we sit, watching, waiting for the MOONRISE, as we shift our gaze across the heavens towards cosmic noon.

BOTH STARVATION AND OUTFLOWS DRIVE GALAXY QUENCHING

A.1 Introduction

This appendix supplements Chapter 4, where we utilised the statistical power of the SDSS Legacy Survey to investigate the role of mass in galaxy quenching. In particular, we analysed the stellar metallicity differences between star-forming and passive (and also green valley) galaxies, using our chemical evolution model (described in Chapter 3) to assess the relative roles of starvation and outflows in driving galaxy quenching. In Chapter 4 (and also Chapter 6), our chemical evolution model incorporated both the molecular and atomic gas components in galaxies. In this appendix we investigate how our model predictions and conclusions change when only the molecular gas component is included.

A.2 Molecular gas relations

As described in Chapter 3, we used the integrated Schmidt-Kennicutt (SK) law, given by equation (3.1), to parametrise star formation in our models. The total gas mass, which includes both the atomic and molecular components, as well as the total gas depletion time were used in the SK law in Chapter 4 (and 6). In this section, we investigate how our model predictions and conclusions change when only the molecular gas component is considered. In this case, the law for star formation becomes

$$\Psi = \epsilon_m m, \tag{A.1}$$

where ϵ_m is the star formation efficiency for molecular gas and m is the molecular gas mass. ϵ_m is related to $t_{\rm depl,m}$, the molecular gas depletion time, through $\epsilon_m = 1/t_{\rm depl,m}$.

There are two main differences between models that use the total gas mass and models that only use the molecular component. Firstly, molecular gas reservoirs are smaller than the total gas reservoirs. Hence outflows with a given outflow rate Λ will be more effective at quenching star formation in models that only contain molecular gas. This means that leaky-box models that only contain molecular gas will have more difficulty in reproducing the large stellar metallicity differences that have been observed. As a result, these models will tend to disfavour quenching through outflows and $\lambda_{\rm eff}$ will be smaller. Secondly, molecular gas depletion timescales are shorter than total gas depletion timescales. Models that only contain molecular gas will process and enrich the gas in the ISM more rapidly. As a result, the stellar metallicity increases more quickly and so the quenching timescales derived from our analysis of stellar metallicity differences tend to be shorter. These differences between the total gas and molecular gas models are most apparent for low-mass galaxies, as these tend to have relatively larger atomic-to-molecular gas mass ratios than the more massive galaxies. The model predictions for low-mass galaxies are therefore more strongly affected by the removal of the atomic gas component.

A.2.1 Passive galaxies (quenching at high-z)

We compare the observed stellar metallicity differences between star-forming and passive galaxies with the predictions from gas regulator models that only contain molecular gas. Our results using a closed-box model with $\lambda_{\rm eff} = 0$ is shown in Fig. A.1. We find that our models are able to reproduce the observations, and the derived quenching timescales are shorter than what was seen in Fig. 4.5. We also show the quenching timescales and constraints on $\lambda_{\rm eff}$ derived using our leaky-box model in Fig. A.2. The derived quenching timescales are shorter, and the mass-loading factors are smaller than what was seen in Fig. 4.7.

A.2.2 Green valley galaxies (quenching in the local Universe)

We now study the stellar metallicity differences between star-forming and green valley galaxies. Our results for the closed-box model are shown in Fig. A.3. The quenching timescales are typically shorter than what was seen in Fig. 4.8. The predictions from the leaky-box model are shown in Fig. 4.10. The derived quenching timescales are shorter, and the mass-loading factors are smaller than what was seen in Fig. 4.10. When using only molecular gas masses, both our closed-box and leaky-box models struggle to reproduce the observed stellar metallicity differences at the high-mass end.

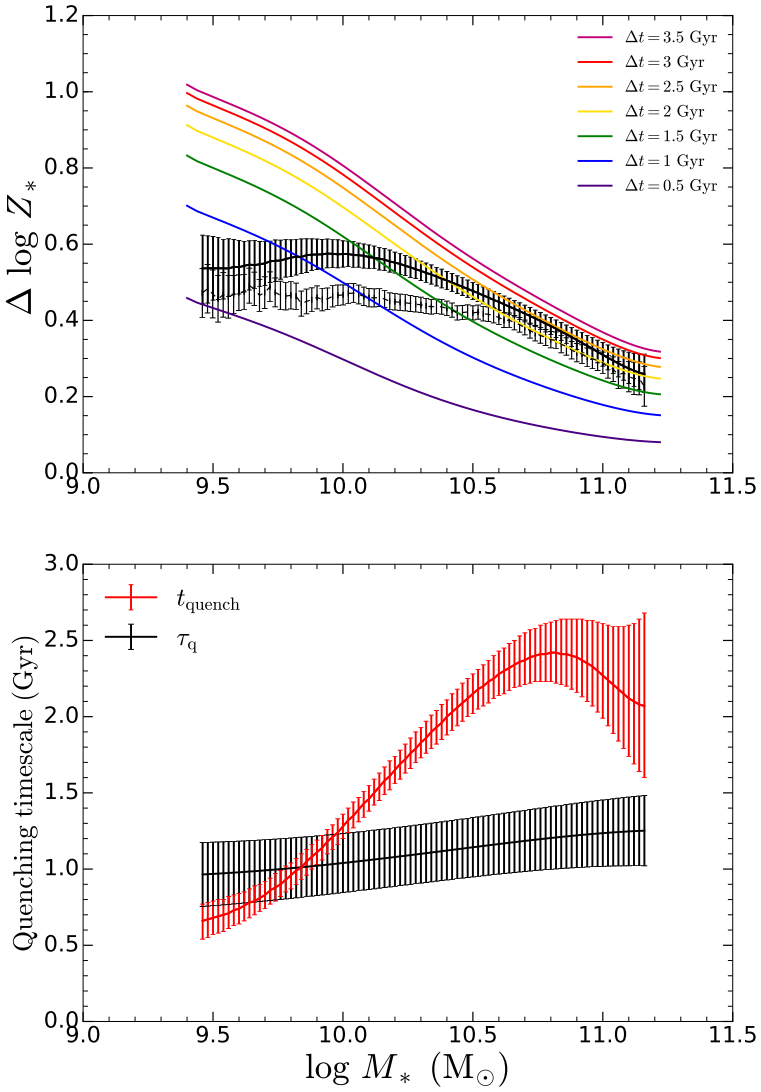

Figure A.1. Similar to Fig. 4.5, where we study the stellar metallicity differences between star-forming and passive galaxies using a closed-box model with $\lambda_{\rm eff} = 0$, but now we only use the molecular gas component in our models.

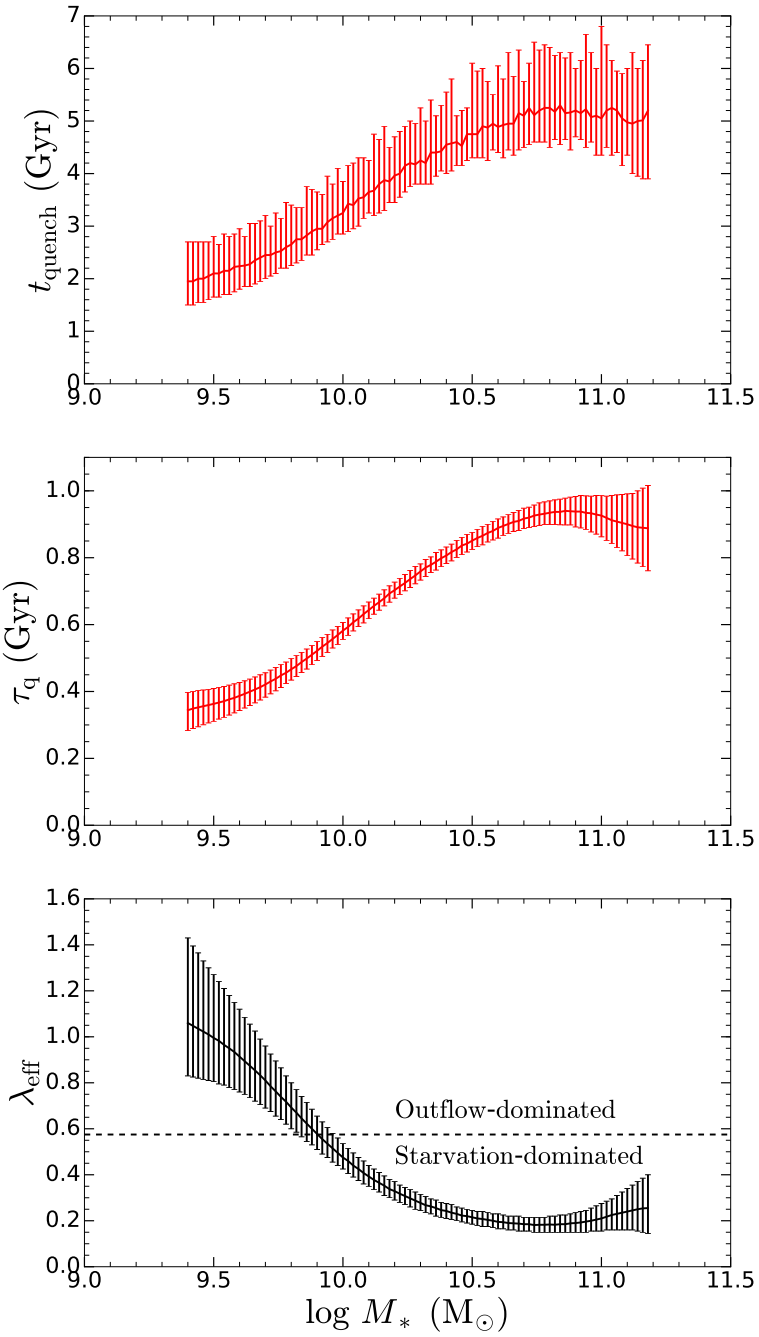

Figure A.2. Similar to Fig. 4.7, but now we only use the molecular gas component in our models.

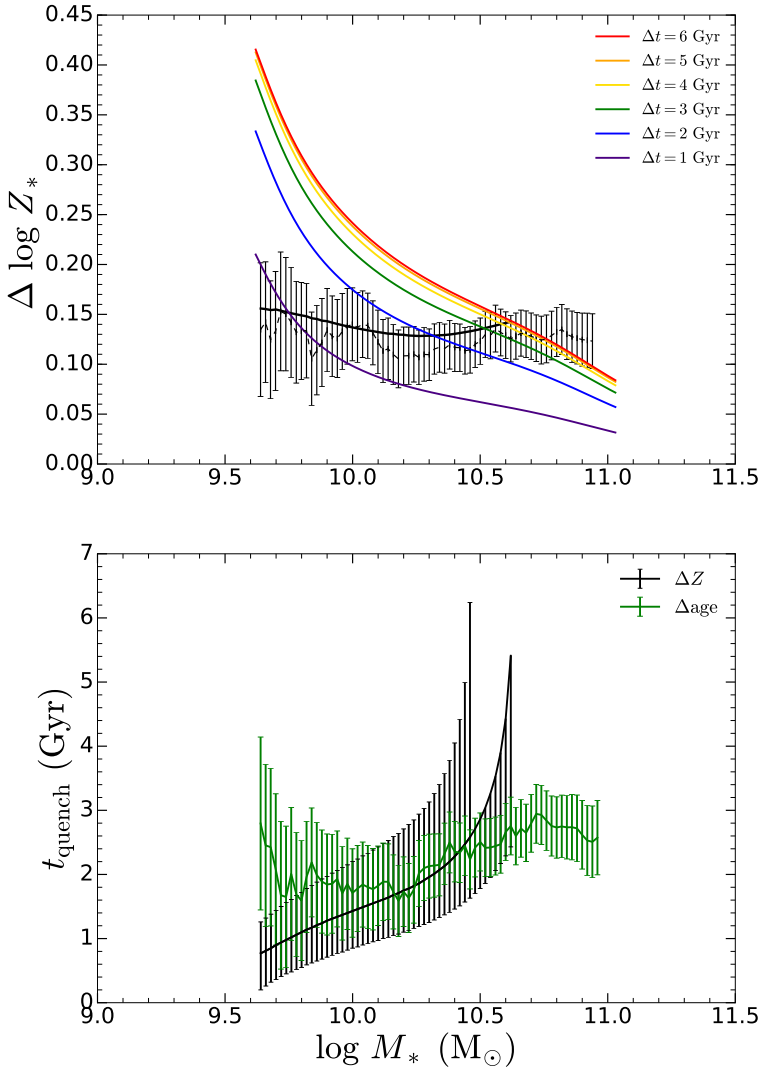

Figure A.3. Similar to Fig. 4.8, where we study the stellar metallicity differences between star-forming and green valley galaxies using a closed-box model with $\lambda_{\rm eff} = 0$, but now we only use the molecular gas component in our models. In the cases when the upper limit on the stellar metallicity difference ΔZ_* cannot be reproduced by our model, only the lower limit on the quenching timescale $t_{\rm quench}$ is shown.

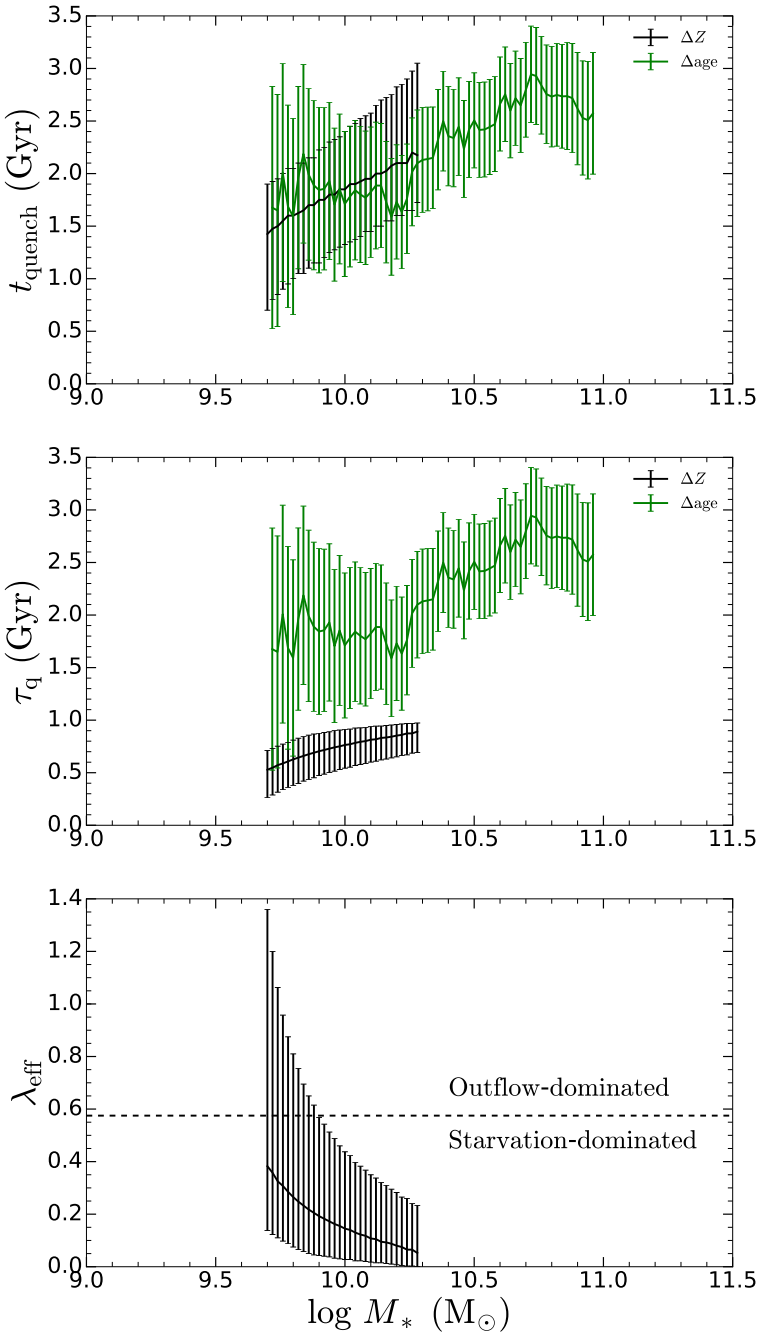

Figure A.4. Similar to Fig. 4.10, but now we only use the molecular gas component in our models.

APPENDIX B

THE WEAK IMPRINT OF ENVIRONMENT ON THE STELLAR POPULATIONS OF GALAXIES

B.1 Introduction

This appendix supplements Chapter 5, where we utilised the statistical power of the SDSS Legacy Survey to investigate the role of environment in galaxy evolution and galaxy quenching.

In Chapter 5 we analysed the environmental dependence (in terms of the central–satellite dichotomy, as well as halo mass, local overdensity and projected distance) of the mass-weighted stellar mass–stellar metallicity and the mass-weighted stellar mass–stellar age relations for star-forming, green valley and passive galaxies. In this appendix we instead briefly study the environmental dependence of the light-weighted stellar mass–stellar metallicity and the light-weighted stellar mass–stellar age relations.

Furthermore, in Chapter 5, we also investigated environmental quenching, by analysing the environmental dependence of the stellar metallicity difference between star-forming and passive galaxies. Given the lack of environmental trends that we had found for star-forming satellites (and centrals), we assumed that the stellar metallicities of star-forming satellites (and centrals) do not depend on environment, i.e. star-forming galaxies were not binned into quartiles of halo mass, local overdensity or projected distance in our environmental quenching analysis. In this appendix we relax this assumption, as we now also divide star-forming galaxies into quartiles of the aforementioned environmental parameters.

This appendix is structured as follows. In Sections B.2 and B.3, we investigate the light-

weighted stellar mass–stellar metallicity relation, and the light-weighted stellar mass–stellar age relation, respectively, for both centrals and satellites. In Section B.4 we revisit our investigation of the environmental dependence of the mass-weighted stellar metallicity difference between star-forming and passive galaxies, as we now also divide star-forming galaxies into quartiles of the aforementioned environmental parameters.

B.2 Light-weighted stellar mass–stellar metallicity relation

Our analysis in the main body of the text was centred on the mass-weighted stellar mass–stellar metallicity relation, using stellar metallicities that were obtained using the spectral fitting code FIREFLY. In order to investigate whether our results are affected by the weighting scheme or spectral fitting procedure adopted, we study, in this section, the light-weighted stellar mass–stellar metallicity relation, using stellar metallicities that have been obtained using two different spectral fitting procedures. First, using a full spectral fit of the optical continuum using FIREFLY. Second, using a simultaneous fit of five metallicity- and age-sensitive optical spectral absorption features (for details see Gallazzi et al. 2005). We note that the latter set of stellar metallicities was used in the environment analysis of Pasquali et al. (2010).

We show the light-weighted stellar mass–stellar metallicity relation using the FIREFLY metallicities in Fig. B.1. Similar to what was seen for the mass-weighted stellar mass–stellar metallicity relation in Fig. 5.1, satellites are typically more metal-rich than centrals of the same stellar mass. This result applies when studying the overall central and satellite population (left panel, in black) and also when studying the star-forming (right panel, blue), green valley (green) and passive (red) populations separately. We also find, as was seen for the mass-weighted stellar metallicities, that the metallicity difference between the overall population of centrals and satellites is larger than that for the star-forming, green valley and passive subpopulations. However, while the light-weighted central–satellite stellar metallicity differences (typically 0–0.02 dex) for star-forming, green valley, and passive galaxies are comparable to the mass-weighted differences (typically 0–0.03 dex), the light-weighted differences for the overall population are much smaller than the mass-weighted differences. This comes about because the stellar metallicity difference between star-forming, green valley and passive galaxies is smaller when using light-weighted metallicities over mass-weighted metallicities (for a more in-depth discussion of this, see Chapter 4), and so the quenched fraction effect only introduces a small, additional metallicity offset between the overall central and satellite populations for the light-weighted metallicities.

Furthermore, we find that the metallicity difference between the overall population of centrals and satellites decreases with increasing stellar mass. In contrast, the metallicity

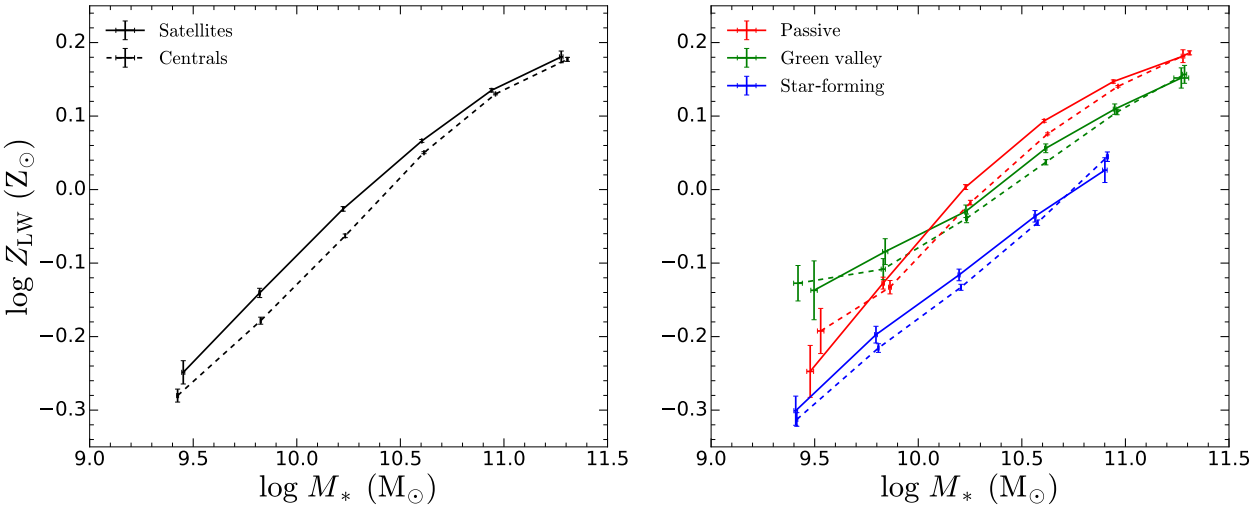

Figure B.1. Similar to Fig. 5.1, but now using light-weighted stellar metallicities from FIREFLY.

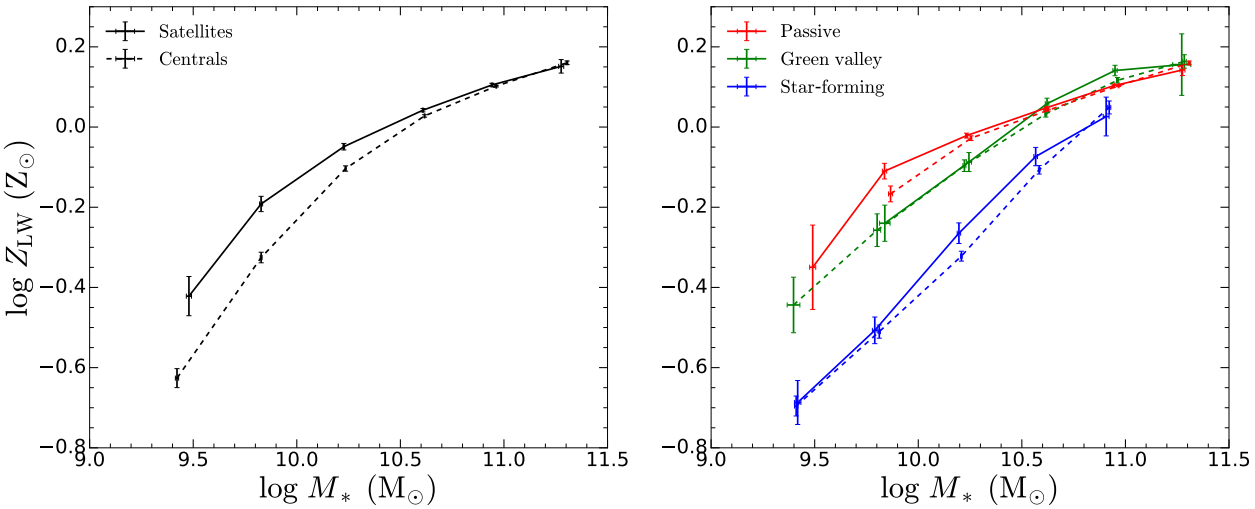

Figure B.2. Similar to Fig. 5.1, but now using light-weighted stellar metallicities from Gallazzi et al. (2005).

difference for star-forming and green valley galaxies is roughly independent of stellar mass, and declines more weakly with mass for passive galaxies. These trends are all consistent with what was seen in our analysis of the mass-weighted stellar mass–stellar metallicity relation. Thus the choice of metallicity weighting used does not affect the qualitative aspects of our results.

The light-weighted stellar mass–stellar metallicity relation using the Gallazzi et al. (2005) metallicities is shown in Fig. B.2. Qualitatively, we find the same trends as with the FIREFLY metallicities. Satellites are more metal-rich than centrals, the quenched fraction effect exaggerates the true metallicity difference between centrals and satellites, and the quenched fraction

effect also misrepresents the true stellar-mass dependence of the metallicity difference between centrals and satellites. Thus, the choice of spectral fitting procedure used also does not appear to affect the qualitative aspects of our results. However, we do find that the quantitative aspects of our results are changed, especially for the stellar metallicity difference between the overall population of centrals and satellites, which we find to be much larger when using the Gallazzi et al. (2005) metallicities. This comes about because the normalisations of the stellar mass–stellar metallicity relations based off of FIREFLY and Gallazzi et al. (2005) are different (which is discussed in detail in 4.4.1). Since the stellar metallicity difference between star-forming, green valley and passive galaxies is much larger when using the Gallazzi et al. (2005) metallicities, the quenched fraction effect introduces a much larger, additional metallicity offset between the overall central and satellite populations, which is why we see such a large gap between centrals and satellites in the left panel of Fig. B.2.

B.3 Light-weighted stellar mass–stellar age relation

In this section we study the light-weighted stellar mass–stellar age relation, using stellar ages obtained using FIREFLY and from Gallazzi et al. (2005), to test whether our results are affected by the weighting scheme or spectral fitting procedure used.

We show the light-weighted stellar mass–stellar age relation using the FIREFLY ages in Fig. B.3. Qualitatively, we find similar trends to what was found with the mass-weighted stellar mass–stellar age relation. Satellites tend to be older than centrals of the same stellar mass, both for the overall population (shown in the left panel) and for star-forming (blue, shown in the right panel), green valley (green) and passive (red) galaxies, the quenched fraction effect exaggerates the true (shown on the right) age difference between centrals and satellites, and the quenched fraction effect also misrepresents the stellar-mass dependence of the true stellar age difference between centrals and satellites. Since the gap in stellar age between star-forming, green valley and passive galaxies is larger when using light-weighted over mass-weighted ages, the quenched fraction effect is stronger for light-weighted ages and so the age difference between the overall central and satellite populations are larger than in the mass-weighted case.

The light-weighted stellar mass–stellar age relation using the Gallazzi et al. (2005) ages is shown in Fig. B.4. The trends obtained are qualitatively consistent with what was found using the light-weighted FIREFLY ages, so the choice of spectral fitting procedure adopted does not appear to affect the qualitative aspects of our results.

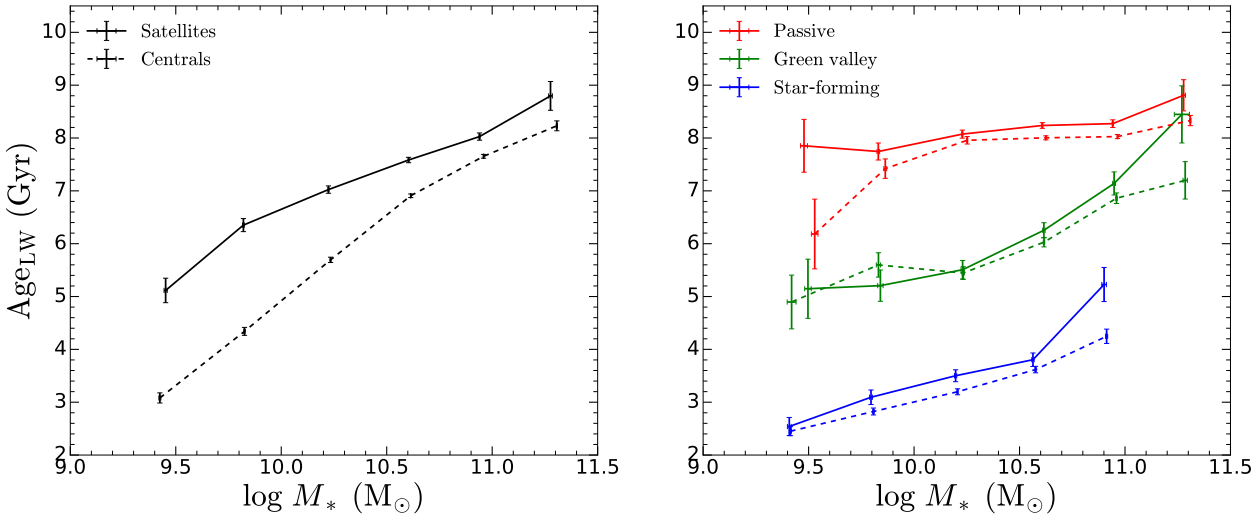

Figure B.3. Similar to Fig. 5.4, but now using light-weighted stellar ages from FIREFLY.

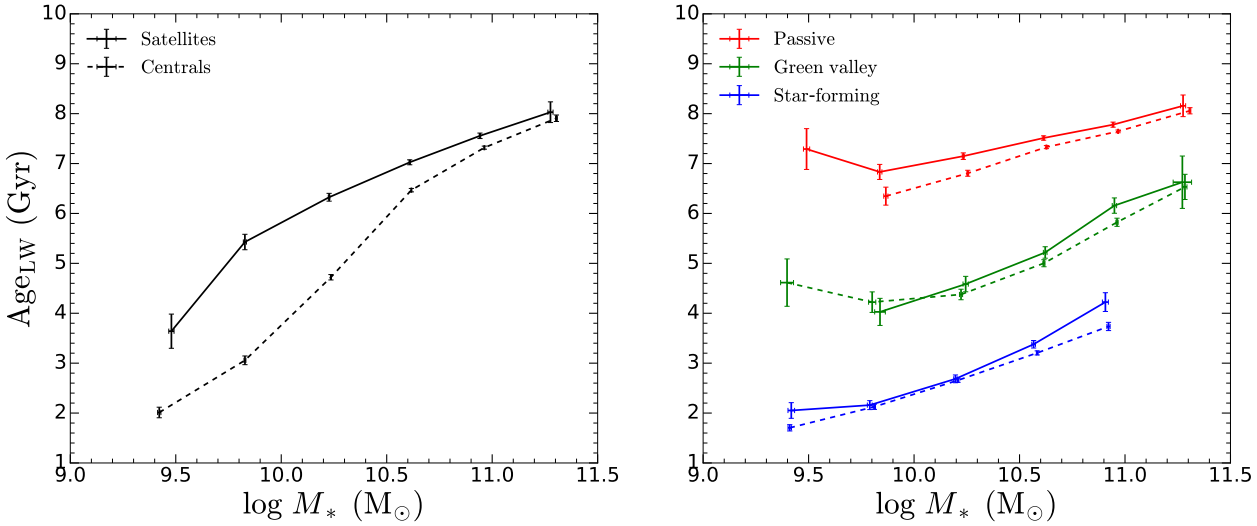

Figure B.4. Similar to Fig. 5.4, but now using light-weighted stellar ages from Gallazzi et al. (2005).

B.4 Stellar metallicity differences using star-forming satellite quartiles

In the main body of the text we made the assumption, given the findings in Section 5.2, that the mass-weighted stellar mass–stellar metallicity relation for star-forming satellites does not depend on environment. In this section we relax this assumption, by now also dividing the star-forming satellite population into quartiles of environment.

We show how the mass-weighted stellar metallicity difference between star-forming and passive galaxies depends on group halo mass (top panels), overdensity (middle panels) and projected distance (bottom panel) for both centrals (left panels) and satellites (right panels) in Fig. B.5.

For centrals, we find that there is no clear trend between the stellar metallicity difference and environment, neither for the halo mass quartiles in the top-left panel, nor for the overdensity quartiles in the middle-left panel. The various quartiles are all consistent with each other within the error bars, and there is no indication of the stellar metallicity difference either increasing or decreasing with increasing halo mass or overdensity.

For satellites, we also also find no clear trend between the stellar metallicity difference and environment, neither for the halo mass quartiles in the top-panel, nor for the overdensity quartiles and projected distance quartiles in the middle-right and bottom-right panels.

Evidently the scatter in the scaling relations for star-forming satellites, together with the relatively large error bars, wash out the trends seen with environment in Section 5.3. Even with the excellent statistics of SDSS DR7, the error bars on the stellar metallicity differences become too large to cleanly separate and distinguish between the various quartiles, which makes a characterisation of the dependence on environment difficult.

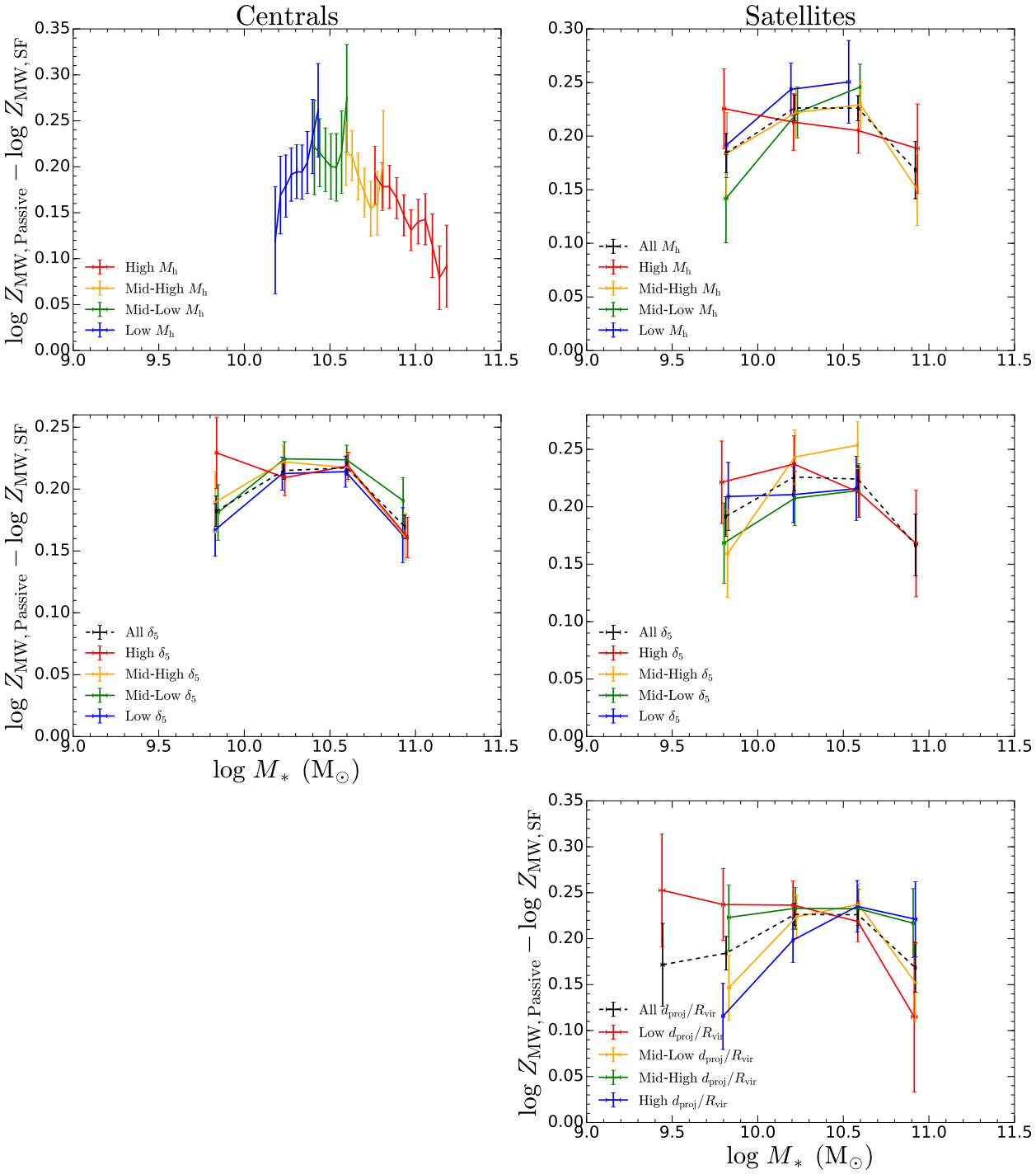

Figure B.5. Similar to Fig. 5.13, but now relaxing the assumption that the stellar metallicity of star-forming satellites does not depend on environment. Rather than use the scaling relations for the entire population of star-forming satellites (shown by the curves named 'All' in Figs. 5.5, 5.9 and 5.11), star-forming satellites are now also divided into quartiles of environment.

APPENDIX C

A Global and Spatially-Resolved View of Galaxy Quenching

C.1 Introduction

This appendix supplements Chapter 6, where we harnessed the spatially-resolved power of the SDSS-IV MaNGA integral field spectroscopic galaxy survey to investigate how quenching operates on a radial basis within galaxies.

In Chapter 6, we integrated the light in each MaNGA galaxy out to ~1.5–2.5 R_e to investigate both the mass- and environment-dependence of the global mass-weighted stellar population parameters (i.e. stellar metallicities and stellar ages) of galaxies. In this appendix we instead briefly investigate the global light-weighted stellar mass–stellar metallicity and stellar mass–stellar age relations.

Additionally, we used our chemical evolution model to determine the relative importance of starvation and outflows in quenching star formation, using global SFRs that were calculated by summing the Bluck et al. (2020) hybrid Hα-D4000-based SFRs on a spaxel-by-spaxel basis. In this appendix we instead use the total SFRs from Brinchmann et al. (2004), which were used in our SDSS Legacy Survey analysis in Chapter 4.

Furthermore, in Chapter 6, we also divided each MaNGA galaxy into a series of 0.5 R_e-wide annuli to investigate the radial variation of the mass-weighted stellar population parameters in galaxies. In this appendix we instead briefly study the radial variation of the light-weighted stellar population parameters.

We did not apply inclination cuts to the MaNGA sample in our analysis in Chapter 6. In this appendix, we investigate whether the radial stellar metallicity trends that we find are sensitive to the inclination cut applied.

This appendix is structured as follows. In Section C.2, we study the global light-weighted stellar mass–stellar metallicity and stellar mass–stellar age relations. In Section C.3, we investigate how our model predictions and conclusions are affected by the choice of SFR indicator. In Section C.4, we study the environmental dependence of the global light-weighted stellar mass–stellar metallicity and stellar mass–stellar age relations. In Section C.5, we investigate whether the mass-weighted radial stellar metallicity relation for star-forming galaxies is sensitive to the inclination cut applied. In Section C.6, we study the light-weighted radial stellar metallicity and radial stellar age relations. Finally, in Section C.7, we study the environmental dependence of the light-weighted radial stellar metallicity and radial stellar age relations.

C.2 Global light-weighted scaling relations

In Section 6.2.1 we studied the global mass-weighted stellar mass–stellar metallicity and stellar mass–stellar age relations. Here we instead investigate the global light-weighted stellar mass–stellar metallicity and stellar mass–stellar age relations to verify whether the findings in Chapter 4 (where we studied spectra of the central 3″ of galaxies) apply only to the central regions of galaxies, or instead hold globally: from the innermost to the outermost regions of galaxies. While mass-weighted quantities trace the cumulative evolution of a galaxy, light-weighted quantities are instead more sensitive to recent evolution, as young stellar populations are brighter and therefore contribute relatively more light-per-mass than older populations.

C.2.1 Stellar metallicity

We show the global light-weighted stellar mass–stellar metallicity relation for star-forming (blue), green valley (green) and passive (red) galaxies in the top panel of Fig. C.1. Similar to what was found in Chapter 4, the light-weighted stellar metallicities of star-forming, green valley and passive galaxies tend to increase with increasing stellar mass. Additionally, green valley and passive galaxies tend to be more metal-rich than star-forming galaxies of the same stellar mass. Therefore, our results here echo what was already found using the mass-weighted stellar metallicities in Section 6.2.1. Namely, that the relatively enhanced level of chemical enrichment in passive galaxies is therefore not just confined to the central regions, indicating that starvation is likely to be driving the global quenching of star formation in galaxies.

Interestingly, low-mass green valley galaxies tend to be slightly more metal-rich than passive galaxies of the same stellar mass, a result that was also found in Chapter 4. This feature is not

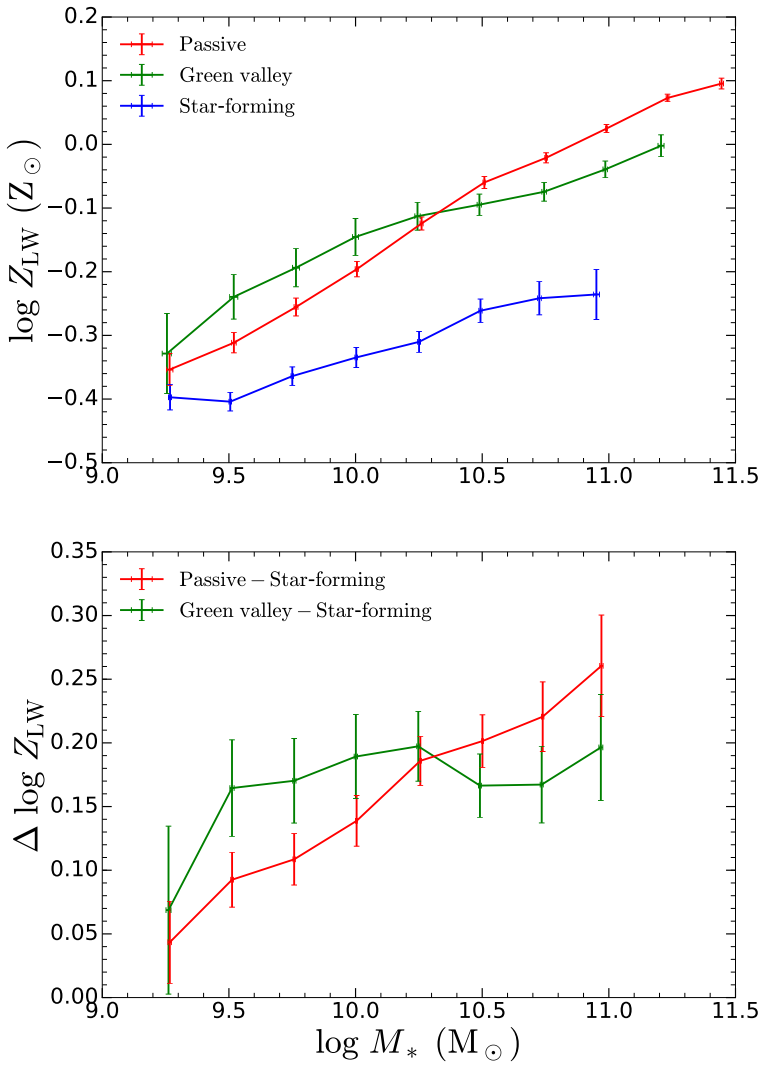

Figure C.1. Similar to Fig. 6.1, but now showing the global light-weighted stellar mass–stellar metallicity relation.

present in the mass-weighted stellar mass–stellar metallicity relation shown in Fig. 6.1. Since passive galaxies no longer actively form stars, their light-weighted and mass-weighted stellar metallicities (and ages) are rather similar. In contrast, green valley galaxies are in the process of quenching but still actively form stars, with light-weighted stellar metallicities that tend to be higher than the mass-weighted stellar metallicities. As these green valley galaxies near the completion of quenching, their mass-weighted stellar metallicities will be comparable to those of passive galaxies. However, their light-weighted stellar metallicities will be larger than those of passive galaxies of the same stellar mass. With time, these recently formed stellar populations will fade in brightness, until the light-weighted and mass-weighted stellar metallicities become equal.

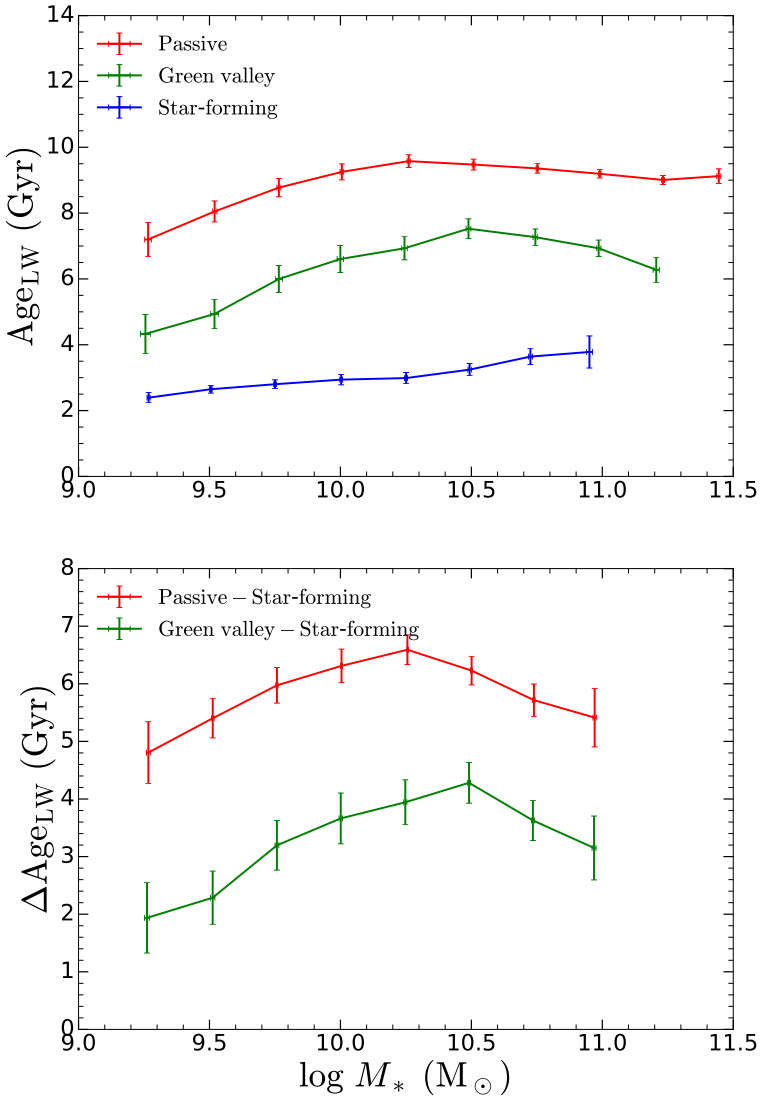

Figure C.2. Similar to Fig. 6.2, but now showing the global light-weighted stellar mass–stellar age relation.

C.2.2 Stellar age

We show the global light-weighted stellar mass–stellar age relation in the top panel of Fig. C.2. Similar to our findings in Chapter 4, the stellar ages of star-forming, green valley and passive galaxies tend to increase with increasing stellar mass. Furthermore, passive galaxies tend to be older than star-forming galaxies of the same stellar mass, with green valley galaxies having light-weighted stellar ages intermediate between those of star-forming and passive galaxies.

C.3 Quenching mechanisms: dependence on SFR indicator

In Section 6.2.2 we determined the relative importance of starvation and outflows in quenching star formation, using global SFRs that were calculated by summing the Bluck et al. (2020) hybrid Hα-D4000-based SFRs on a spaxel-by-spaxel basis. Here we instead use the global SFRs from Brinchmann et al. (2004) (which were used in our analysis in Chapter 4), which were calculated by aperture-correcting the Hα/D4000-based in-fibre SFRs. Since the global SFRs for passive galaxies calculated using the Brinchmann et al. (2004) method are higher than those calculated using the Bluck et al. (2020) method, the durations of quenching $t_{\rm quench}$ that we find in this section are shorter than those found in Section 6.2.2.

C.3.1 Passive galaxies (quenching at high-z)

We show the results from our model-based analysis in Fig. C.3. Both the e-folding timescales and mass-loading factors are similar to what was seen in Fig. 6.4. However, the duration of quenching is shorter, and is roughly flat with stellar mass at 4–5 Gyr (instead of 6–7 Gyr).

C.3.2 Green valley galaxies (quenching in the local Universe)

We show the results from our model-based analysis in Fig. C.4. Both the e-folding timescales and mass-loading factors are similar to what was seen in Fig. 6.5. However, the time elapsed since the onset of quenching is shorter at 2–3 Gyr (instead of ~4 Gyr), and is often inconsistent with the $t_{\rm quench}$ estimates obtained from the global mass-weighted stellar age difference between local star-forming and local green valley galaxies.

C.4 Environmental dependence of global light-weighted scaling relations

In Section 6.2.3 we studied the environmental dependence of the global mass-weighted stellar mass–stellar metallicity and stellar mass–stellar age relations. In this section we instead study the environmental dependence of the global light-weighted stellar mass–stellar metallicity and stellar mass–stellar age relations.

C.4.1 Stellar metallicity

We show the global light-weighted stellar mass–stellar metallicity relation for centrals (dashed) and satellites (solid) in the left panel of Fig. C.5. We find, similar to our analysis in Chapter 5, that satellites tend to be more metal-rich than centrals of the same stellar mass. However, as shown

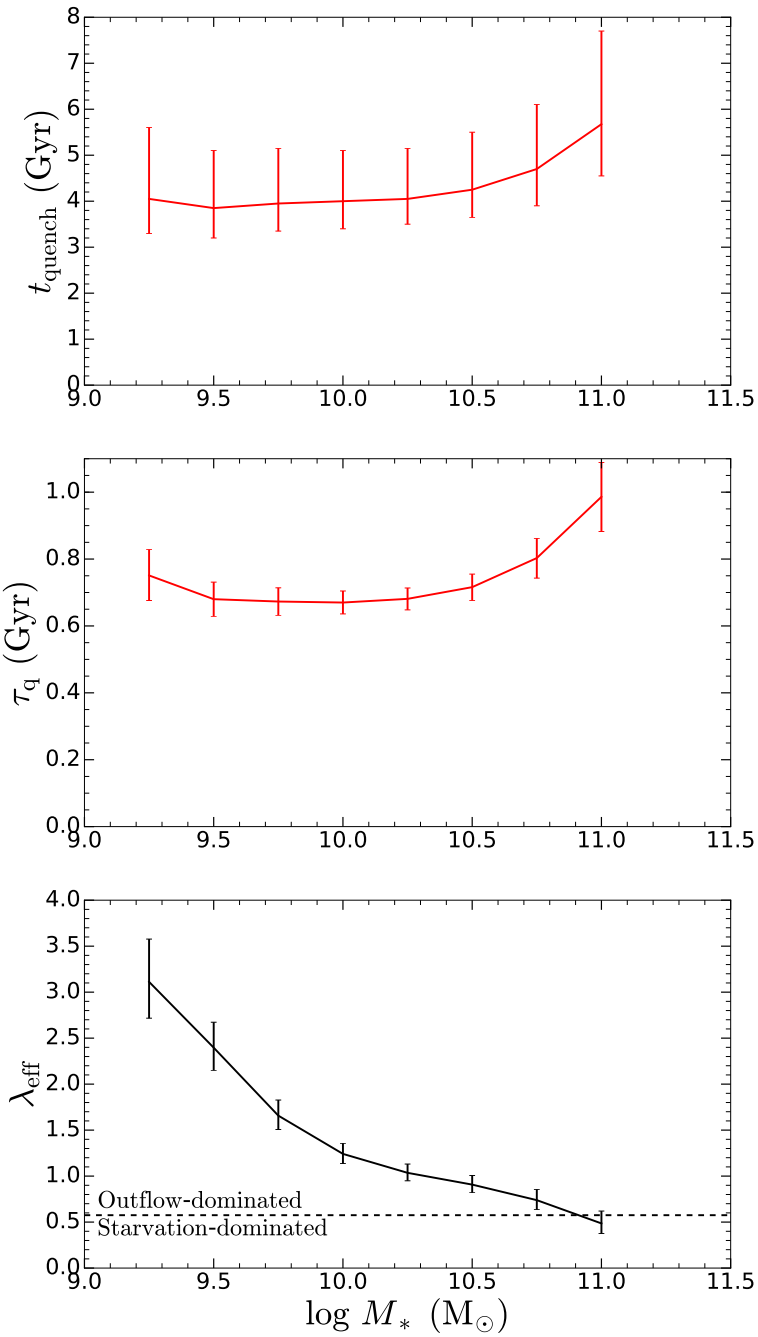

Figure C.3. Similar to Fig. 6.4, but now using global SFRs from Brinchmann et al. (2004) instead of using global SFRs that were computed using the Bluck et al. (2020) hybrid Hα-D4000 approach.

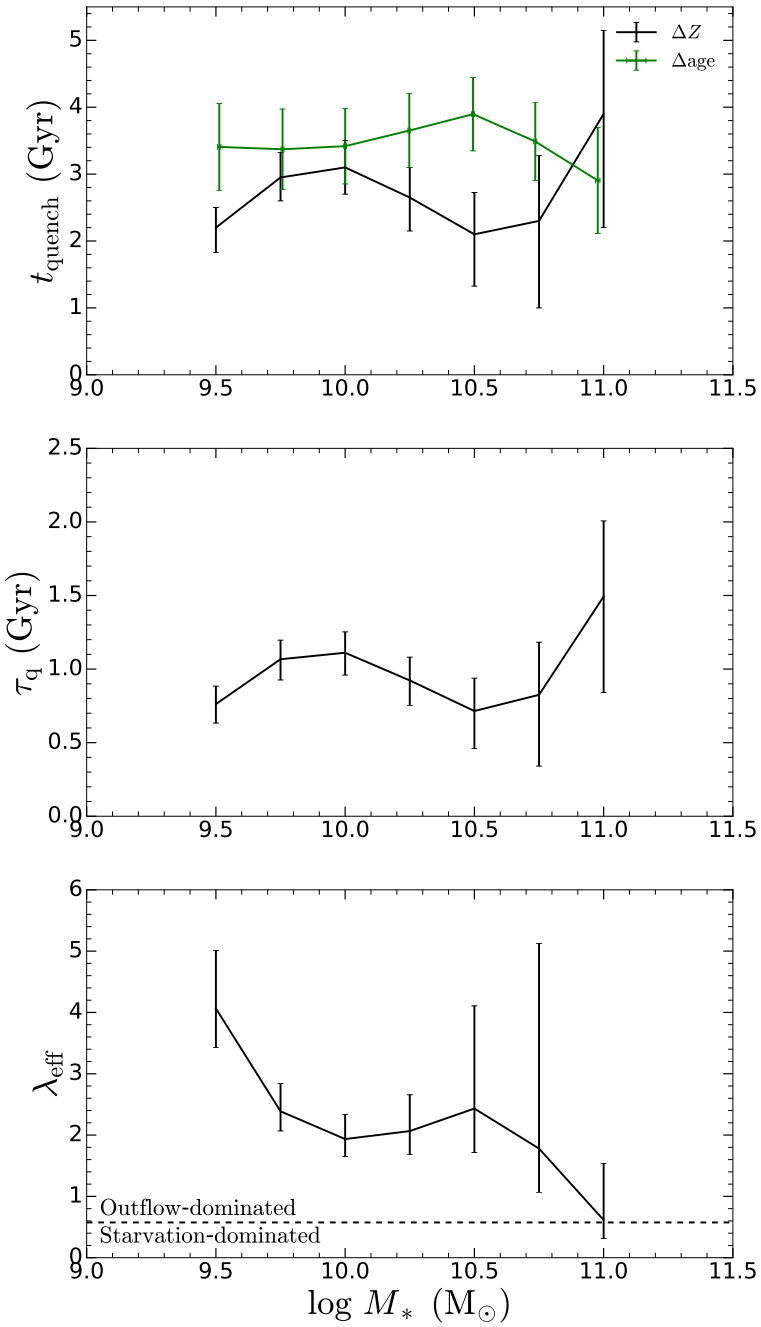

Figure C.4. Similar to Fig. 6.5, but now using global SFRs from Brinchmann et al. (2004) instead of using global SFRs that were computed using the Bluck et al. (2020) hybrid Hα-D4000 approach.

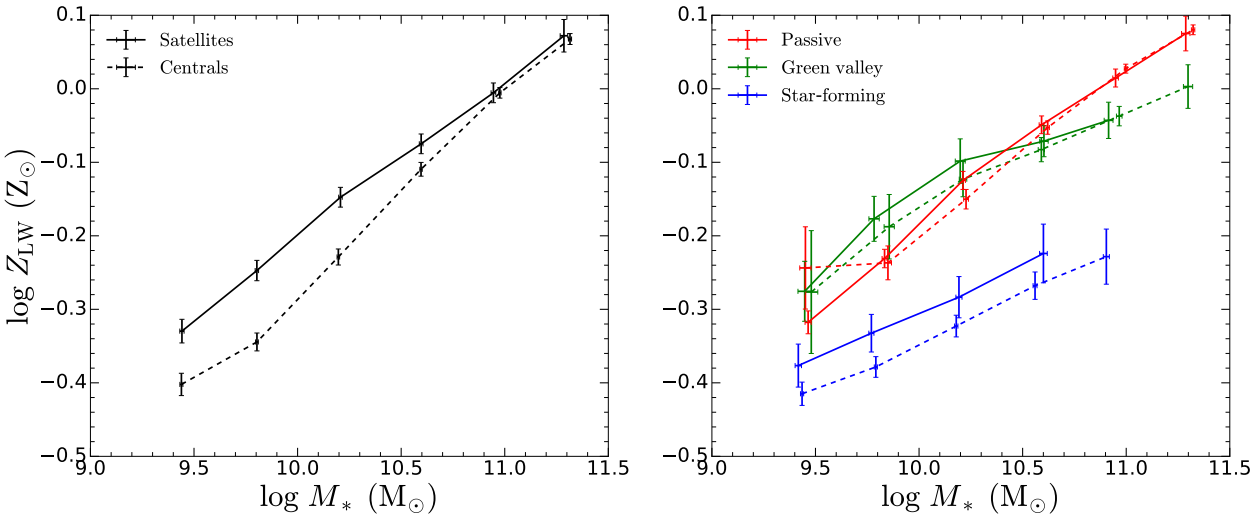

Figure C.5. Similar to Fig. 6.6, but now showing the global light-weighted stellar mass–stellar metallicity relation.

in the right panel of Fig. C.5, after separating into star-forming (blue), green valley (green) and passive (red) galaxies, we find that the true, inherent dependence of stellar metallicity on environment is much weaker than what is seen when studying the overall populations of centrals and satellites. Star-forming satellites, green valley satellites and passive satellites are only marginally more metal-rich than star-forming centrals, green valley centrals and passive centrals of the same stellar mass.

C.4.2 Stellar age

We show the global light-weighted stellar mass–stellar age relation for centrals (dashed) and satellites (solid) in the left panel of Fig. C.6. Again, similar to our analysis in Chapter 5, we find that satellites tend to be older than centrals of the same stellar mass. However, the true imprint of environment on the stellar ages of galaxies is in fact much smaller, as shown in the right panel of Fig. B.3. While star-forming satellites, green valley satellites and passive satellites tend to be older than star-forming centrals, green valley centrals and passive centrals of the same stellar mass, this difference is much smaller than what was seen for the overall populations of centrals and satellites in the left panel of Fig. C.6.

C.5 Inclination cuts

In Section 6.3.1 we studied the radial dependence of the stellar metallicities in star-forming, green valley and passive galaxies, without applying any cuts on inclination. Since beam

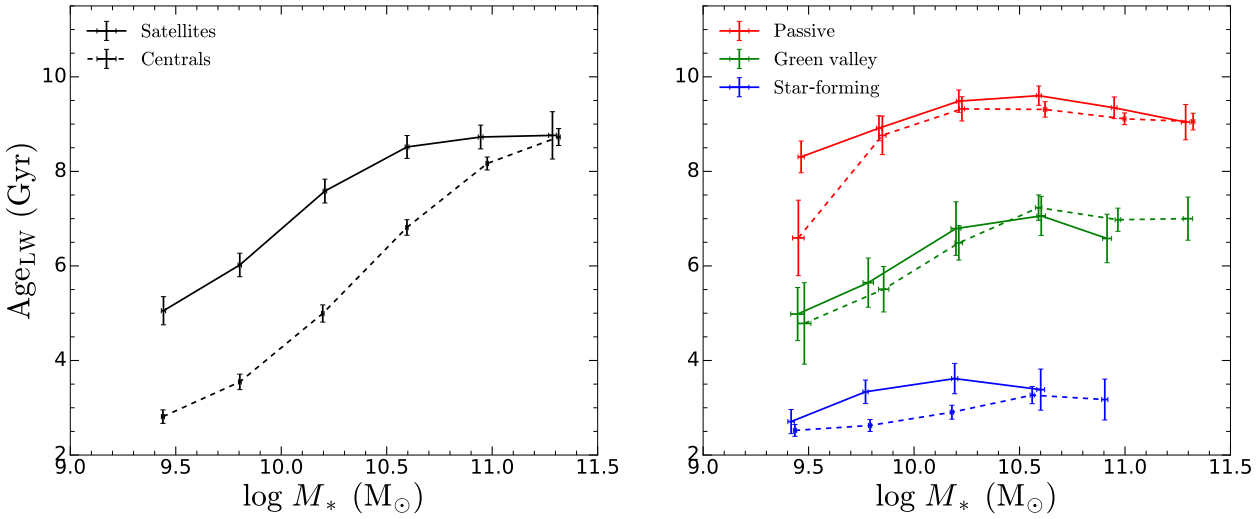

Figure C.6. Similar to Fig. 6.8, but now showing the global light-weighted stellar mass–stellar age relation.

smearing effects are more severe, and stellar populations at different R/R_e can be mixed (due to projection effects) in spaxels in highly inclined galaxies, the observed radial variation of the stellar metallicities in these galaxies may not be reliable. In this section we cut all star-forming galaxies that have inclination angles greater than 60°. We use the b/a elliptical Petrosian axis ratios provided by the NASA-Sloan Atlas catalogue (Blanton et al. 2011), and convert these into inclination angles i assuming a constant oblateness $q = 0.13$ (Giovanelli et al. 1994) using

$$\cos^2 i = \frac{(b/a)^2 - q^2}{1 - q^2}. \tag{C.1}$$

While the majority of star-forming galaxies can described as thick discs, green valley and passive galaxies are likely to have elliptical morphologies. Thus we do not estimate inclination angles, nor apply an inclination cut for green valley and passive galaxies.

We show the radial variation of the stellar metallicities of star-forming (blue), green valley (green) and passive (red) galaxies in Fig. C.7. We show both the full sample of star-forming galaxies (solid) and the sample excluding highly inclined ($i > 60°$) star-forming galaxies (dashed). The qualitative trends are clearly the same, with only minor quantitative changes (0–0.04 dex) after the inclination cut is applied.

C.6 Light-weighted radial scaling relations

In Section 6.3.1 we studied the mass-weighted radial stellar metallicity and radial stellar age relations. In this section we instead study the light-weighted relations.

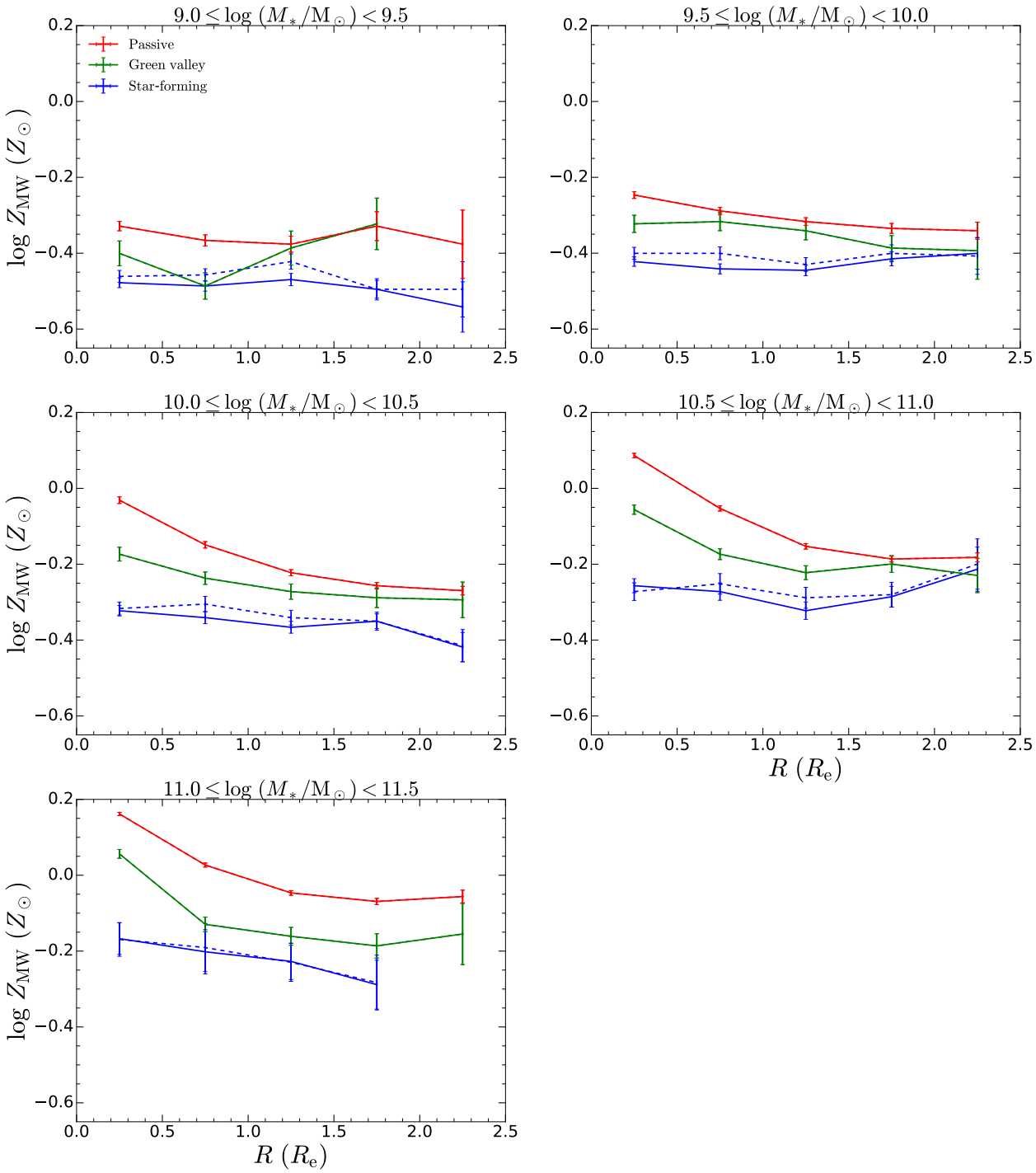

Figure C.7. Similar to Fig. 6.10, but we now show the mass-weighted radial stellar metallicity relation for both the full sample of star-forming galaxies (solid) and the sample excluding highly inclined ($i > 60°$) star-forming galaxies (dashed).

C.6.1 Stellar metallicity

We show the light-weighted radial stellar metallicity relation for star-forming (blue), green valley (green) and passive (red) galaxies in Fig. C.8. Our results echo what was found using the mass-weighted stellar metallicities in Fig. 6.10. Namely, green valley and passive galaxies are more metal-rich than star-forming galaxies at *all* radii and at all masses. Furthermore, the stellar metallicity difference between star-forming and green valley/passive galaxies tends to decrease with increasing radial distance.

C.6.2 Stellar age

We show the light-weighted radial stellar age relation for star-forming, green valley and passive galaxies in Fig. C.8. Similar to our results for the mass-weighted stellar ages, the stellar ages of star-forming, green valley and passive galaxies tend to either decrease or remain flat with stellar mass. Additionally, passive galaxies are older than star-forming galaxies at all radii and at all masses, with green valley galaxies having stellar ages that are intermediate between star-forming and passive galaxies.

C.7 Environmental dependence of light-weighted radial scaling relations

In Section 6.3.2 we studied the environmental dependence of the mass-weighted radial stellar metallicity and radial stellar age relations. In this section we instead study the environmental dependence of the light-weighted relations.

C.7.1 Stellar metallicity

We show the light-weighted radial stellar metallicity relation for centrals (dashed) and satellites (solid) in Fig. C.10. Our results largely mirror what was found using the mass-weighted stellar metallicities in Fig. 6.13. The stellar metallicities of centrals and satellites both decrease with radial distance, with the stellar metallicity difference between star-forming and green valley/passive galaxies tending to decrease with increasing radial distance. In addition, the underlying differences between centrals and satellites tend to be small, indicating that the environment only leaves a weak imprint on the stellar metallicities of galaxies, at *all* radii.

C.7.2 Stellar age

We show the light-weighted radial stellar metallicity relation for centrals and satellites in Fig. C.11. We obtain similar results to what was found using the mass-weighted stellar ages

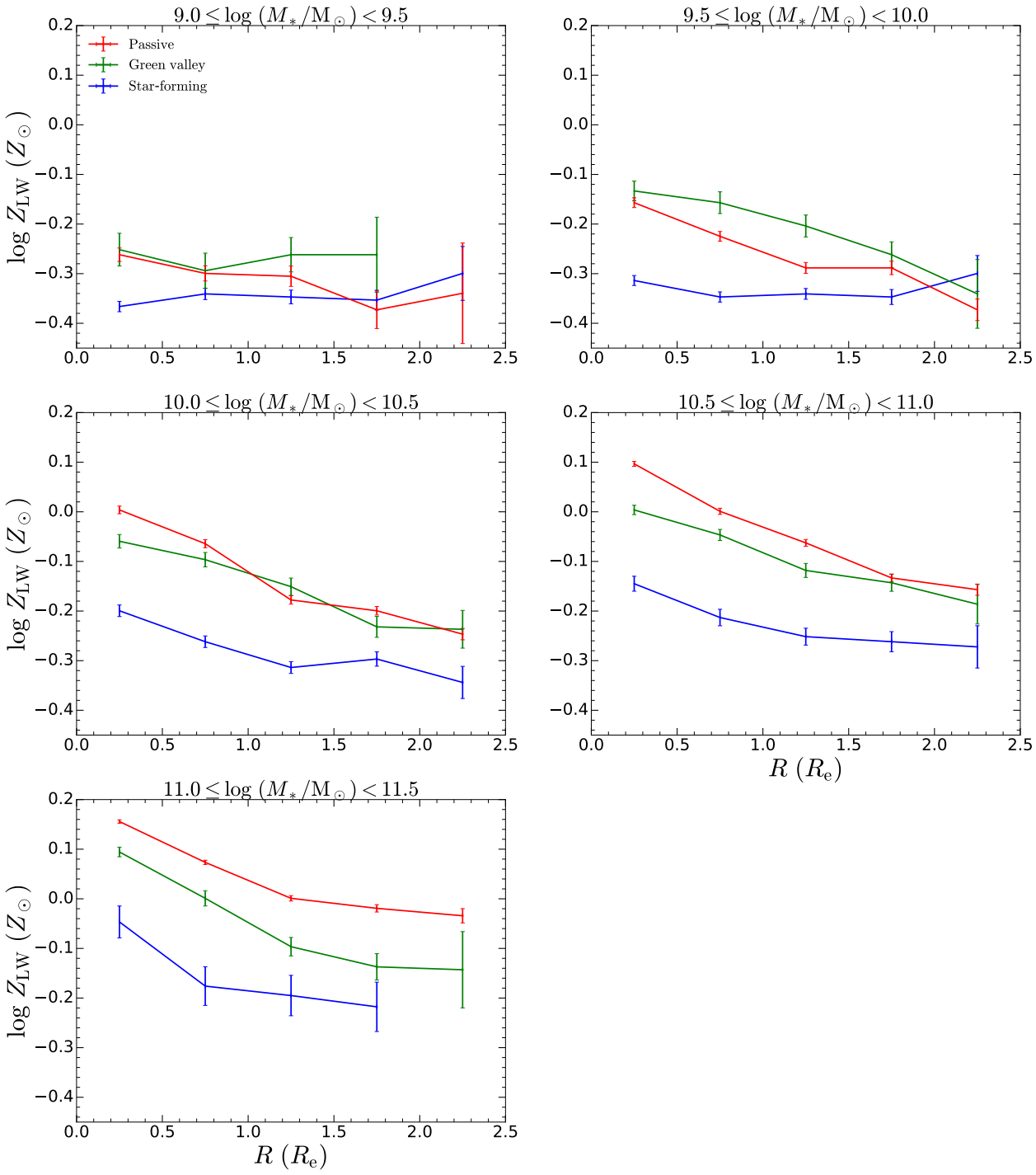

Figure C.8. Similar to Fig. 6.10, but now showing the light-weighted radial stellar metallicity relation.

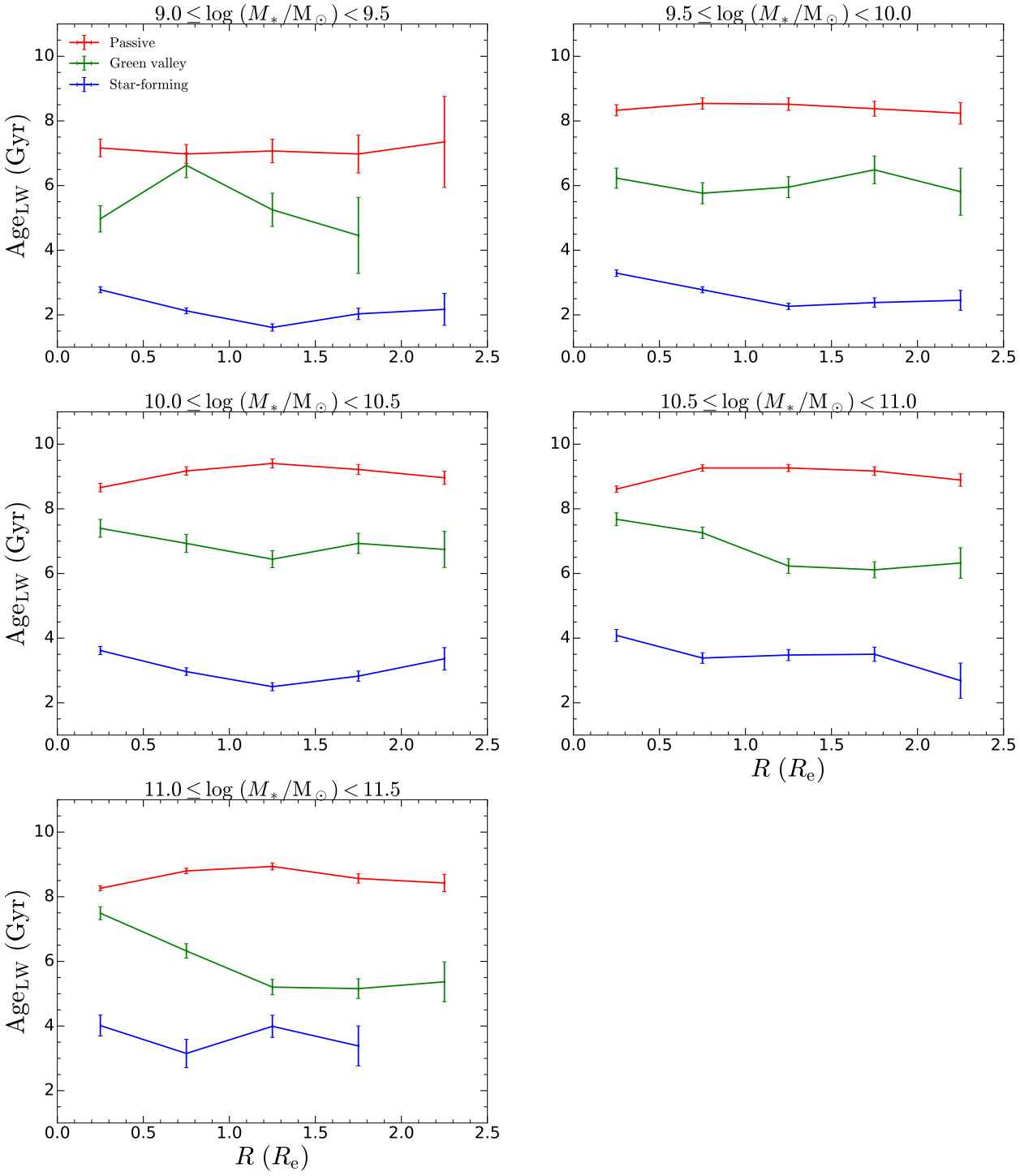

Figure C.9. Similar to Fig. 6.12, but now showing the light-weighted radial stellar age relation.

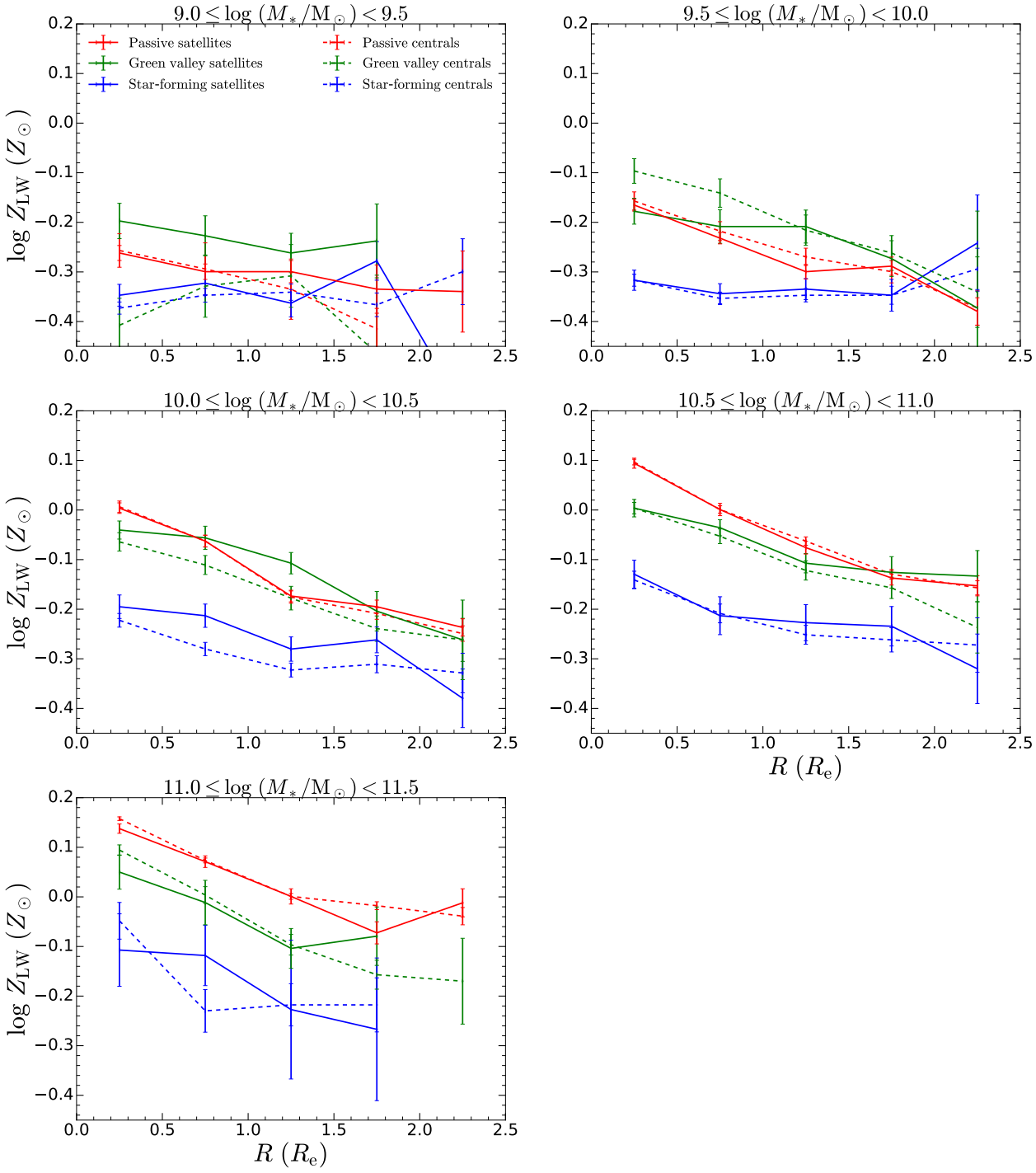

Figure C.10. Similar to Fig. 6.13, but now showing the light-weighted radial stellar metallicity relation.

in Fig. 6.14, with the underlying differences between centrals and satellites being small at *all* radii in galaxies.

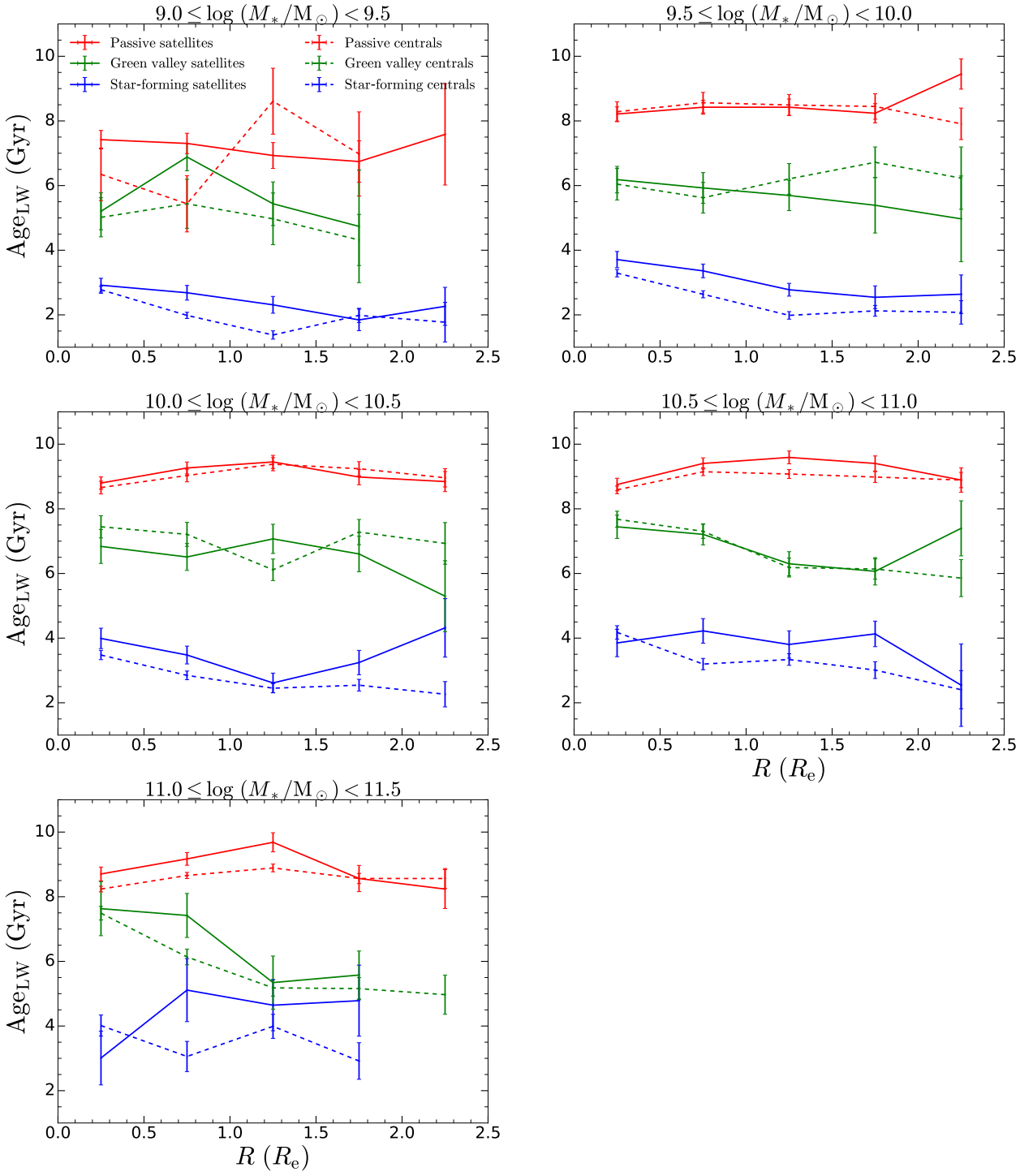

Figure C.11. Similar to Fig. 6.14, but now showing the light-weighted radial stellar age relation.

Bibliography

Abadi M. G., Moore B., Bower R. G., 1999, MNRAS, 308, 947

Abazajian K. N., et al., 2009, Astrophys. J. Suppl. Ser., 182, 543

Adelman-McCarthy J. K., et al., 2006, Astrophys. J. Suppl. Ser., 162, 38

Almeida J. S., Sanchez-Menguiano L., 2019, ApJL, 878, L6

Amendola L., et al., 2013, Living Rev. Relativ., 16

Andrews B. H., Martini P., 2013, ApJ, 765, 140

Aragon Calvo M. A., Neyrinck M. C., Silk J., 2019, Open J. Astrophys., 2

Asplund M., Grevesse N., Sauval A. J., Scott P., 2009, ARA&A, 47, 481

Aumer M., White S. D. M., Naab T., Scannapieco C., 2013, MNRAS, 3164, 3142

Bahé Y. M., Schaye J., Crain R. A., McCarthy I. G., Bower R. G., Theuns T., McGee S. L., Trayford J. W., 2017, MNRAS, 464, 508

Baldry I. K., Glazebrook K., Brinkmann J., Ivezic Z., Lupton R. H., Nichol R. C., Szalay A. S., 2004, ApJ, 600, 681

Baldry I. K., Balogh M. L., Bower R. G., Glazebrook K., Nichol R. C., Bamford S. P., Budavari T., 2006, MNRAS, 373, 469

Bañados E., et al., 2018, Nature, 553, 473

Barnes J. E., 1988, ApJ, 331, 699

Barnes J. E., 1992, ApJ, 393, 484

Beckwith S. V. W., et al., 2006, AJ, 132, 1729

Belfiore F., et al., 2017a, MNRAS, 170, 151

Belfiore F., et al., 2017b, MNRAS, 466, 2570

Belfiore F., et al., 2018, MNRAS, 477, 3014

Belfiore F., et al., 2019, AJ, 158, 28

Birnboim Y., Dekel A., 2003, MNRAS, 345, 349

Blanton M. R., et al., 2003, ApJ, 594, 186

Blanton M. R., et al., 2005, AJ, 129, 2562

Blanton M. R., Kazin E., Muna D., Weaver B. A., Price-whelan A., 2011, AJ, 142, 31

Bluck A. F. L., et al., 2019, MNRAS, 485, 666

Bluck A. F. L., Maiolino R., Sánchez S. F., Ellison S. L., Thorp M. D., Piotrowska J. M., Teimoorinia H., Bundy K. A., 2020, MNRAS, 492, 96

Boselli A., Cortese L., Boquien M., 2014, A&A, 564, A65

Boylan-Kolchin M., Springel V., White S. D., Jenkins A., Lemson G., 2009, MNRAS, 398, 1150

Brammer G. B., et al., 2009, ApJ, 706, L173

Breda I., Papaderos P., 2018, A&A, 614, 1

Brinchmann J., Charlot S., White S. D. M., Tremonti C., Kauffmann G., Heckman T., Brinkmann J., 2004, MNRAS, 351, 1151

Brownson S., Maiolino R., Tazzari M., Carniani S., Henden N., 2019, MNRAS, 490, 5134

Bruzual G., Charlot S., 2003, MNRAS, 344, 1000

Bryant J. J., et al., 2015, MNRAS, 447, 2857

Bundy K., et al., 2015, ApJ, 798, 24

Calzetti D., Armus L., Bohlin R., Kinney A., Koornneef J., Storchi-Bergmann T., 2000, ApJ, 533, 682

Cappellari M., 2013, ApJL, 778

Cappellari M., 2016a, ARA&A, 54, 597

Cappellari M., 2016b, ARA&A, 54, 597

Cappellari M., 2017, MNRAS, 466, 798

Cappellari M., Emsellem E., 2004, PASP, 116, 138

Cappellari M., et al., 2013, MNRAS, 432, 1862

Carollo C. M., Cibinel A., Lilly S. J., Pipino A., Bonoli S., Finoguenov A., 2016, ApJ, 818, 0

Catinella B., et al., 2012, A&A, 544, 30

Chabrier G., 2003, PASP, 115, 763

Chang J., Macciò A. V., Kang X., 2013, MNRAS, 431, 3533

Chilingarian I., Prugniel P., Sil'Chenko O., Koleva M., 2007, Proc. Int. Astron. Union, 2, 175

Chisholm J., Tremonti C. A., Leitherer C., Chen Y., 2017, MNRAS, 469, 4831

Choi J., Conroy C., Moustakas J., Graves G. J., Holden B. P., Brodwin M., Brown M. J., Van Dokkum P. G., 2014, ApJ, 792

Cicone C., et al., 2014, A&A, 562, A21

Cid Fernandes R., Mateus A., Sodr L., Stasinska G., Gomes J. M., 2005, MNRAS, 358, 363

Ciotti L., Ostriker J. P., 2007, ApJ, 665, 1038

Ciotti L., Ostriker J. P., Proga D., 2009, ApJ, 699, 89

Cirasuolo M., et al., 2014, Proc. SPIE, 9147, 91470N

Cole S., Lacey C. G., Baugh C. M., Frenk C. S., 2002, MNRAS, 319, 168

Comparat J., et al., 2017, preprint, (arXiv:1711.06575)

Conroy C., 2013, ARA&A, 51, 393

Conroy C., Gunn J. E., 2010, ApJ, 712, 833

Conroy C., Gunn J. E., White M., 2009, ApJ, 699, 486

Conroy C., White M., Gunn J. E., 2010, ApJ, 708, 58

Cooper M. C., Tremonti C. A., Newman J. A., Zabludoff A. I., 2008, MNRAS, 390, 245

Cortese L., Catinella B., Janowiecki S., 2017, ApJL, 848, L7

Cresci G., Mannucci F., Sommariva V., Maiolino R., Marconi A., Brusa M., 2012, MNRAS, 421, 262

Croton D. J., et al., 2006, MNRAS, 365, 11

Cullen F., et al., 2019, MNRAS, 487, 2038

Curti M., Cresci G., Mannucci F., Marconi A., Maiolino R., Esposito S., 2017, MNRAS, 465, 1384

Daddi E., et al., 2007, ApJ, 670, 156

Daddi E., et al., 2010, ApJ, 713, 686

Davé R., Finlator K., Oppenheimer B. D., 2011, MNRAS, 416, 1354

Davé R., Finlator K., Oppenheimer B. D., 2012, MNRAS, 421, 98

Davé R., Rafieferantsoa M. H., Thompson R. J., Hopkins P. F., 2017, MNRAS, 467, 115

Dawson K. S., et al., 2016, AJ, 151, 44

Dayal P., Ferrara A., Dunlop J. S., 2013, MNRAS, 430, 2891

De Rossi M. E., Theuns T., Font A. S., Mccarthy I. G., 2015, MNRAS, 452, 486

De Rossi M. E., Bower R. G., Font A. S., Schaye J., Theuns T., 2017, MNRAS, 472, 3354

Dekel A., Birnboim Y., 2006, MNRAS, 368, 2

Dekel A., Silk J., 1986, ApJ, 303, 39

Dekel A., et al., 2009, Nature, 457, 451

Dekel A., Zolotov A., Tweed D., Cacciato M., Ceverino D., Primack J. R., 2013, MNRAS, 435, 999

Doi M., et al., 2010, AJ, 139, 1628

Dressler A., 1980, ApJ, 236, 351

Drory N., et al., 2015, AJ, 149, 77

Eisenstein D. J., Annis J., Gunn J. E., Szalay A. S., Connolly A. J., 2001, AJ, 122, 2267

Elbaz D., et al., 2007, A&A, 468, 33

Ellison S. L., Patton D. R., Simard L., McConnachie A. W., 2008a, AJ, 135, 1877

Ellison S. L., Patton D. R., Simard L., McConnachie A. W., 2008b, ApJ, 672, L107

Ellison S. L., Simard L., Cowan N. B., Baldry I. K., Patton D. R., McConnachie A. W., 2009, MNRAS, 396, 1257

Emsellem E., et al., 2007, MNRAS, 379, 401

Emsellem E., et al., 2011, MNRAS, 414, 888

Erb D., Shapley A., Pettini M., 2006, ApJ, 644, 813

Faber S. M., 1972, A&A, 20, 361

Fabian A. C., 2012, ARA&A, 50, 455

Fall S., Efstathiou G., 1980, MNRAS, 193, 189

Farouki R., Shapiro S. L., 1981, ApJ, 243, 32

Faucher-Giguère C. A., Kereš D., Ma C. P., 2011, MNRAS, 417, 2982

Feldmann R., Mayer L., 2015, MNRAS, 446, 1939

Ferland G. J., Korista K. T., Verner D. A., Ferguson J. W., Kingdon J. B., Verner E. M., 1998, PASP, 110, 761

Fillingham S. P., Cooper M. C., Wheeler C., Garrison-Kimmel S., Boylan-Kolchin M., Bullock J. S., 2015, MNRAS, 454, 2039

Fillingham S. P., Cooper M. C., Pace A. B., Boylan-Kolchin M., Bullock J. S., Garrison-Kimmel S., Wheeler C., 2016, MNRAS, 463, 1916

Finlator K., Dave R., 2008, MNRAS, 385, 2181

Fluetsch A., et al., 2019, MNRAS, 483, 4586

Forbes J. C., Krumholz M. R., Burkert A., Dekel A., 2014, MNRAS, 443, 168

Fossati M., et al., 2017, ApJ, 835

Freundlich J., et al., 2019, A&A, 622, 1

Gallazzi A., Charlot S., Brinchmann J., White S. D. M., Tremonti C. A., 2005, MNRAS, 362, 41

Gallazzi A., Brinchmann J., Charlot S., White S. D. M., 2008, MNRAS, 383, 1439

Gallazzi A., Bell E. F., Zibetti S., Brinchmann J., Kelson D. D., 2014, ApJ, 788, 72

Genel S., et al., 2008, ApJ, 688, 789

Genzel R., et al., 2015, ApJ, 800, 20

Giovanelli R., Haynes M. R., Salzer J. J., Wegner G., Costa L. N. D., Freudling W., 1994, AJ, 107

Goddard D., et al., 2017a, MNRAS, 465, 688

Goddard D., et al., 2017b, MNRAS, 466, 4731

Gonzalez Delgado R. M., et al., 2015, A&A, 581

Gunn J. E., Gott, J. Richard I., 1972, ApJ, 176, 1

Gunn J., Carr M., Rockosi C., Sekiguchi M., 1998, AJ, 116, 67

Gunn J. E., et al., 2006, AJ, 131, 2332

Guo Y., et al., 2017, ApJL, 841, 8

Halliday C., et al., 2008, A&A, 479, 417

Hashimoto T., et al., 2018, Nature, 557, 392

Heckman T. M., Alexandroff R. M., Borthakur S., Overzier R., Leitherer C., 2015, ApJ, 809, 147

Hopkins P. F., Hernquist L., Cox T. J., Kereš D., 2008, Astrophys. J. Suppl. Ser., 175, 356

Hubble E., 1926, ApJ, 64, 321

Hubble E., 1929, Proc. Natl. Acad. Sci. U. S. A., 15, 168

Hubble E., 1936, Realm of the Nebulae. Yale University Press, New Haven

Hubble E., Humason M. L., 1931, ApJ, 74, 43

Hughes T. M., Cortese L., Boselli A., Gavazzi G., Davies J. I., 2013, A&A, 550

Hunt L., Dayal P., Magrini L., Ferrara A., 2016a, MNRAS, 463, 2002

Hunt L., Dayal P., Magrini L., Ferrara A., 2016b, MNRAS, 463, 2020

Ivezić Ž., et al., 2019, ApJ, 873, 111

Jeans J. H., 1902, Philos. Trans. R. Soc. London Ser. A, 199, 1

Johnston E. J., Aragón-Salamanca A., Merrifield M. R., Bedregal A. G., 2012, MNRAS, 422, 2590

Johnston E. J., et al., 2017, MNRAS, 465, 2317

Kauffmann G., et al., 2003a, MNRAS, 341, 33

Kauffmann G., et al., 2003b, MNRAS, 341, 54

Kauffmann G., White S. D. M., Heckman T. M., Ménard B., Brinchmann J., Charlot S., Tremonti C., Brinkmann J., 2004, MNRAS, 353, 713

Kennicutt R. C., 1998, ApJ, 498, 541

Kennicutt R., Evans N. J., 2012, ARA&A, 50, 531

Kereš D., Katz N., Weinberg D. H., Davé R., 2005, MNRAS, 363, 2

Kewley L. J., Dopita M. A., 2002, Astrophys. J. Suppl. Ser., 142, 35

Kewley L. J., Ellison S. L., 2008, ApJ, 681, 1183

Kewley L. J., Groves B., Kauffmann G., Heckman T., 2006, MNRAS, 372, 961

King A., Pounds K., 2015, ARA&A, 53, 115

Kobulnicky H. A., Kewley L. J., 2004, ApJ, 617, 240

Koleva M., Prugniel P., Ocvirk P., Le Borgne D., Soubiran C., 2008, MNRAS, 385, 1998

Koposov S. E., Belokurov V., Torrealba G., Evans N. W., 2015, ApJ, 805, 130

Kovač K., et al., 2010, ApJ, 708, 505

Kriek M., et al., 2016, Nature, 540, 248

Kroupa P., 2001, MNRAS, 322, 231

Kumari N., Maiolino R., Belfiore F., Curti M., 2019, MNRAS, 485, 367

Lacey C. G., Cole S., 1993, MNRAS, 262, 627

Lagos C. d. P., et al., 2016, MNRAS, 459, 2632

Lara-López M. A., et al., 2010, A&A, 521, L53

Larson R. B., 1974, MNRAS, 169, 229

Larson R. B., Tinsley B. M., Caldwell C. N., 1980, ApJ, 237, 692

Law D. R., et al., 2015, AJ, 150, 19

Law D. R., et al., 2016, AJ, 152, 83

Le Borgne D., Rocca-Volmerange B., Prugniel P., Lançon A., Fioc M., Soubiran C., 2004, A&A, 425, 881

Lee H., Skillman E. D., Cannon J. M., Jackson D. C., Gehrz R. D., Polomski E. F., Woodward C. E., 2006, ApJ, 647, 970

Leitner S. N., Kravtsov A. V., 2011, ApJ, 734

Lequeux J., Peimbert M., Rayo J. F., Serrano A., Torres-Peimbert S., 1979, A&A, 80, 155

Li H., et al., 2018, MNRAS, 476, 1765

Lian J., Thomas D., Maraston C., Goddard D., Comparat J., Gonzalez-Perez V., Ventura P., 2018a, MNRAS, 474, 1143

Lian J., et al., 2018b, MNRAS, 476, 3883

Lian J., Thomas D., Maraston C., 2018c, MNRAS, 481, 4000

Lian J., Thomas D., Li C., Zheng Z., Maraston C., Bizyaev D., Lane R. R., Yan R., 2019, MNRAS, 489, 1436

Lilly S. J., Carollo C. M., Pipino A., Renzini A., Peng Y., 2013, ApJ, 772, 119

Lintott C. J., et al., 2008, MNRAS, 389, 1179

Lonoce I., et al., 2015, MNRAS, 454, 3912

Lower S., Narayanan D., Leja J., Johnson B. D., Conroy C., Davé R., 2020, arXiv e-prints, p. arXiv:2006.03599

Ma X., Hopkins P. F., Faucher-Giguère C. A., Zolman N., Muratov A. L., Kereš D., Quataert E., 2016, MNRAS, 456, 2140

Maier C., et al., 2016, A&A, 590, A108

Maier C., Ziegler B. L., Haines C. P., Smith G. P., 2019, A&A, 621, 1

Maiolino R., et al., 2008, A&A, 488, 463

Man Z.-Y., Peng Y.-J., Shi J.-J., Kong X., Zhang C.-P., Dou J., Guo K.-X., 2019, ApJ, 881, 74

Mannucci F., et al., 2009, MNRAS, 398, 1915

Mannucci F., Cresci G., Maiolino R., Marconi A., Gnerucci A., 2010, MNRAS, 408, 2115

Maraston C., 2005, MNRAS, 362, 799

Maraston C., Strömbäck G., 2011, MNRAS, 418, 2785

Matteucci F., Panagia N., Pipino A., Mannucci F., Recchi S., Della Valle M., 2006, MNRAS, 372, 265

Mcgee S. L., Balogh M. L., Wilman D. J., Bower R. G., Mulchaey J. S., Parker L. C., Oemler A., 2011, MNRAS, 413, 996

Moore B., Katz N., Lake G., Dressler A., Oemler A. J., 1996, Nature, 379, 613

Moreno J., et al., 2019, MNRAS, 485, 1320

Mouhcine M., Baldry I. K., Bamford S. P., 2007, MNRAS, 382, 801

Murray N., Quataert E., Thompson T. A., 2005, ApJ, 618, 569

Muzzin A., et al., 2013, ApJ, 777, 18

Muzzin A., et al., 2014, ApJ, 796

Naab T., Ostriker J. P., 2017, ARA&A, 55, 59

Neistein E., Dekel A., 2008, MNRAS, 388, 1792

Nelson D., et al., 2019, Comput. Astrophys. Cosmol., 6

Noeske K. G., et al., 2007, ApJ, 660, 43

Oesch P. A., et al., 2016, ApJ, 819, 129

Onodera M., et al., 2015, ApJ, 808, 161

Onodera M., et al., 2016, ApJ, 822, 1

Oser L., Naab T., Ostriker J. P., Johansson P. H., 2012, ApJ, 744, 9

Osterbrock D. E., Ferland G. J., 2006, Astrophysics of gaseous nebulae and active galactic nuclei. University Science Books

Oyarzún G. A., et al., 2019, ApJ, 880, 111

Pagel B. E. J., Edmunds M. G., Blackwell D. E., Chun M. S., Smith G., 1979, MNRAS, 189, 95

Panter B., Jimenez R., Heavens A. F., Charlot S., 2008, MNRAS, 391, 1117

Pasquali A., Gallazzi A., Fontanot F., van den Bosch F. C., De Lucia G., Mo H. J., Yang X., 2010, MNRAS, 407, 937

Pasquali A., Gallazzi A., van den Bosch F. C., 2012, MNRAS, 425, 273

Peng Y. J., Maiolino R., 2014a, MNRAS, 438, 262

Peng Y. J., Maiolino R., 2014b, MNRAS, 443, 3643

Peng Y. J., Renzini A., 2020, Mon. Not. R. Astron. Soc. Lett., 491, L51

Peng Y.-j., et al., 2010, ApJ, 721, 193

Peng Y.-j., Lilly S. J., Renzini A., Carollo M., 2012, ApJ, 757, 23

Peng Y., Maiolino R., Cochrane R., 2015, Nature, 521, 192

Petropoulou V., Vílchez J., Iglesias-Páramo J., 2012, ApJ, 749

Petrosian V., 1976, ApJ, 209, L1

Pettini M., Pagel B. E. J., 2004, MNRAS, 348, 59

Pilyugin L. S., 2001, A&A, 369, 594

Pilyugin L. S., 2005, ApJ, 631, 231

Pipino A., Matteucci F., 2004, MNRAS, 347, 968

Pipino A., Matteucci F., 2006, ApJ, 638, 739

Pipino A., Ercole A. D., Matteucci F., 2008, A&A, 484, 679

Pipino A., Lilly S. J., Carollo C. M., 2014, MNRAS, 441, 1444

Planck Collaboration Ade P. A. R., Aghanim N., Arnaud M., Ashdown M., Aumount J., Baccigalupi C., Banday A. J., 2016, A&A, 594, A13

Popping G., Somerville R. S., Trager S. C., 2014, MNRAS, 442, 2398

Press W. H., Schechter P., 1974, ApJ, 187, 425

Pritchet C., 1977, Astrophys. J. Suppl. Ser., 35, 397

Prochaska J. X., Wolfe A. M., 2009, ApJ, 696, 1543

Puchwein E., Springel V., 2013, MNRAS, 428, 2966

Ranalli P., Comastri A., Origlia L., Maiolino R., 2008, MNRAS, 386, 1464

Reddy N. A., Pettini M., Steidel C. C., Shapley A. E., Erb D. K., Law D. R., 2012, ApJ, 754

Renzini A., 2020, Mon. Not. R. Astron. Soc. Lett., 495, L42

Renzini A., Peng Y.-j., 2015, ApJ, 801, L29

Rhee J., Lah P., Chengalur J. N., Briggs F. H., Colless M., 2016, MNRAS, 460, 2675

Rubin V. C., Ford W. K., Thonnard N., 1980, ApJ, 238, 471

Saintonge A., et al., 2011, MNRAS, 415, 61

Salim S., et al., 2007, Astrophys. J. Suppl. Ser., 173, 267

Salpeter E. E., 1955, ApJ, 121, 161

Sanchez-Blazquez P., et al., 2006, MNRAS, 371, 703

Sánchez-Blázquez P., Ocvirk P., Gibson B. K., Pérez I., Peletier R. F., 2011, MNRAS, 415, 709

Sanchez S. F., Kennicutt R. C., Gil de Paz A., van de Ven G., Vilchez J. M., Wisotzki L., Walcher C. J., 2012, A&A, 538, 1

Sanchez S., Perez E., Sanchez-Barrantes M., Gonzalez J. J., Rosalez-Ortega F. F., Cano-Diaz M., Lopez-Coba C., 2016a, Rev. Mex. Astron. y Astrofis., 52, 21

Sanchez S. F., Perez E., Sanchez-Blazquez P., Garcia-Benito R., Ibarra-Mede H. J., Gonzalez J. J., Rosales-Ortega F. F., 2016b, Rev. Mex. Astron. y Astrofis., 52, 171

Santini P., et al., 2014, A&A, 562, A30

Sarzi M., Falcón Barroso J., 2006, MNRAS, 1200, 1151

Savaglio S., et al., 2005, ApJ, 635, 260

Schawinski K., et al., 2014, MNRAS, 440, 889

Schaye J., et al., 2015, MNRAS, 446, 521

Schinnerer E., et al., 2016, ApJ, 833, 112

Schmidt M., 1959, ApJ, 129, 243

Scott N., et al., 2017, MNRAS, 472, 2833

Scoville N., et al., 2017, ApJ, 837, 150

Segers M. C., Crain R. A., Schaye J., Bower R. G., Furlong M., Schaller M., Theuns T., 2016,

MNRAS, 456, 1235
Sérsic J. L., 1963, Influence of the atmospheric and instrumental dispersion on the brightness distribution in a galaxy
Shapley H., 1918, ApJ, 48, 154
Sklias P., Schaerer D., Elbaz D., Pannella M., Schreiber C., Cava A., 2017, A&A, 605, A149
Smee S. A., et al., 2013, AJ, 146
Somerville R. S., Davé R., 2015, ARA&A, 53, 51
Sommariva V., Mannucci F., Cresci G., Maiolino R., Marconi A., Nagao T., Baroni A., Grazian A., 2012, A&A, 539, A136
Spergel D., et al., 2015, arXiv e-prints, p. arXiv:1503.03757
Spinrad H., Taylor B., 1971, Astrophys. J. Suppl. Ser., 22, 445
Springel V., et al., 2005, Nature, 435, 629
Stott J. P., et al., 2013, MNRAS, 436, 1130
Strateva I., et al., 2001, AJ, 122, 1861
Strauss M. A., et al., 2002, AJ, 124, 1810
Sutherland R. S., Dopita M. A., 1993, Astrophys. J. Suppl. Ser., 88, 253
Tabor M., Merrifield M., Aragón-Salamanca A., Fraser-McKelvie A., Peterken T., Smethurst R., Drory N., Lane R. R., 2019, MNRAS, 485, 1546
Tacconi L., Genzel R., 2010, Nature, 463, 781
Tacconi L. J., et al., 2013, ApJ, 768, 74
Tacconi L. J., et al., 2018, ApJ, 853, 1
Thomas D., Maraston C., Bender R., 2003, MNRAS, 339, 897
Thomas D., Maraston C., Bender R., 2005, ApJ, 621, 673
Thomas D., Maraston C., Schawinski K., Sarzi M., Silk J., 2010, MNRAS, 404, 1775
Tinsley B. M., 1980, Fund. Cosmic Phys., 5, 287
Toft S., et al., 2017, Nature, 546, 510
Tojeiro R., Heavens A. F., Jimenez R., Panter B., 2007, MNRAS, 381, 1252
Tojeiro R., Wilkins S., Heavens A. F., Panter B., Jimenez R., 2009, Astrophys. Journal, Suppl. Ser., 185, 1
Tollet É., Cattaneo A., Mamon G. A., Moutard T., van den Bosch F. C., 2017, MNRAS, 471, 4170
Toomre A., 1977, in Tinsley B. M., Larson Richard B. Gehret D. C., eds, Evolution of Galaxies and Stellar Populations. p. 401
Torrealba G., et al., 2019, MNRAS, 488, 2743
Torrey P., et al., 2018, Mon. Not. R. Astron. Soc. Lett., 477, L16
Torrey P., et al., 2019, MNRAS, 5607, 5587

Tremonti C. A., et al., 2004, ApJ, 613, 898

Trussler J., Maiolino R., Maraston C., Peng Y., Thomas D., Goddard D., Lian J., 2020a, MNRAS, 491, 5406

Trussler J., Maiolino R., Maraston C., Peng Y., Thomas D., Goddard D., Lian J., 2020b, arXiv e-prints, p. arXiv:2006.01154

Tumlinson J., Peeples M. S., Werk J. K., 2017, ARA&A, 55, 389

Van Den Bosch F. C., Aquino D., Yang X., Mo H. J., Pasquali A., McIntosh D. H., Weinmann S. M., Kang X., 2008, MNRAS, 387, 79

Van Dokkum P. G., et al., 2015, ApJ, 813, 23

Vazdekis A., Sánchez-Blázquez P., Falcón-Barroso J., Cenarro A. J., Beasley M. A., Cardiel N., Gorgas J., Peletier R. F., 2010, MNRAS, 404, 1639

Vincenzo F., Matteucci F., Belfiore F., Maiolino R., 2016a, MNRAS, 455, 4183

Vincenzo F., Belfiore F., Maiolino R., Matteucci F., Ventura P., 2016b, MNRAS, 458, 3466

Vogelsberger M., et al., 2014a, MNRAS, 444, 1518

Vogelsberger M., et al., 2014b, Nature, 509, 177

Wake D. A., et al., 2017, AJ, 154, 86

Wang M.-Y., et al., 2017, MNRAS, 468, 4887

Wang E., et al., 2018, ApJ, 860, 102

Westfall K. B., et al., 2019, AJ, 158, 160

Wetzel A. R., Tinker J. L., Conroy C., 2012, MNRAS, 424, 232

Wetzel A. R., Tinker J. L., Conroy C., van den Bosch F. C., 2013, MNRAS, 432, 336

Wheeler C., Phillips J. I., Cooper M. C., Boylan-Kolchin M., Bullock J. S., 2014, MNRAS, 442, 1396

White S., Rees M., 1978, MNRAS, 183, 341

Wilkinson D. M., Maraston C., Goddard D., Thomas D., Parikh T., 2017, MNRAS, 472, 4297

Woo J., et al., 2013, MNRAS, 428, 3306

Wu P.-F., Zahid H. J., Hwang H. S., Geller M. J., 2017, MNRAS, 468, 1881

Wuyts S., et al., 2011, ApJ, 742, 20

Yan R., et al., 2016, AJ, 152, 197

Yang X., Mo H. J., Van Den Bosch F. C., Jing Y. P., 2005, MNRAS, 356, 1293

Yang X., Mo H. J., van den Bosch F. C., Pasquali A., Li C., Barden M., 2007, ApJ, 671, 153

Yang X., Mo H. J., van den Bosch F. C., 2008, ApJ, 676, 248

Yang X., Mo H. J., van den Bosch F. C., 2009, ApJ, 695, 900

Yang X., Mo H. J., Van Den Bosch F. C., Zhang Y., Han J., 2012, ApJ, 752

Yates R. M., Kauffmann G., 2014, MNRAS, 439, 3817

Yates R. M., Kauffmann G., Guo Q., 2012, MNRAS, 422, 215

York D. G., et al., 2000, AJ, 120, 1579

Zahid H. J., Kewley L. J., Bresolin F., 2011, ApJ, 730

Zahid H. J., et al., 2014, ApJ, 792, 75

Zahid H. J., Kudritzki R.-P., Conroy C., Andrews B., Ho I.-T., 2017, ApJ, 847, 18

Zheng W., et al., 2012, Nature, 489, 406

Zheng Z., et al., 2017, MNRAS, 465, 4572

Zwicky F., 1933, Helv. Phys. Acta, 6, 110

Zwicky F., 1937, ApJ, 86, 217

van de Voort F., Bahé Y. M., Bower R. G., Correa C. A., Crain R. A., Schaye J., Theuns T., 2017, MNRAS, 466, 3460

van der Wel A., Holden B. P., Zirm A. W., Franx M., Rettura A., Illingworth G. D., Ford H. C., 2008, ApJ, 688, 48

van der Wel A., et al., 2014, ApJ, 788, 19

van der Wel A., et al., 2016, Astrophys. J. Suppl. Ser., 223, 29